Chemical evolution of inner regions of protoplanetary disks around T Tauri stars

A thesis submitted to The University of Manchester for the degree of
Doctor of Philosophy
in the Faculty of Engineering and Physical Sciences

2014

Andrey Paska

School of Physics and Astronomy

Contents

List of Figures

List of Tables

The University of Manchester

ABSTRACT OF THESIS submitted by Andrey Paska
for the Degree of Doctor of Philosophy and entitled
Chemical evolution of inner regions of protoplanetary disks around T Tauri stars.
May 2014

This thesis has investigated the chemical evolution of the inner regions ($r \leq 10$ AU) of a modelled protoplanetary disk surrounding a low-mass T Tauri star; a phase our own solar system underwent some 4.5–4.6 billion years ago. A 1+1-dimensional physical model of a radially-accreting protoplanetary disk was combined with a chemical model consisting of gas-phase reactions extracted from the RATE95 UMIST database for Astrochemistry, and to this, a network of gas-grain interaction and deuterated reactions were added.

Influenced by the knowledge that radionuclides may have been abnormally abundant in our early solar system compared with the interstellar medium, and that the energy expelled from their decay is sufficient to ionize molecules, a 1-dimensional simulation along the disk midplane was performed, comparing the chemistry with and without radionuclides, as a function of the radionuclide ionization rate. The molecules C_4H_2, HC_3N, C_3H, HCN, CH_4, C_2H_2 and N_2 were found to be particularly sensitive. Of these, HCN and C_2H_2 have already been detected in protoplanetary disks.

Motivated by observations which suggest that T Tauri systems vary from faster to slower accretion rates, the chemical distributions of two disks with stellar accretion rates of 10^{-7} $M_\odot$ yr^{-1} and 10^{-8} $M_\odot$ yr^{-1} were compared. Allowing the mass accretion rate (and thus physical conditions) to vary in time, starting from 10^{-7} $M_\odot$

yr^{-1}, and evolving to a mass accretion rate of 10^{-8} $M_\odot$ yr^{-1}, the molecules CN, HCN, H_2CO and NH_3 were found to be particularly sensitive when compared to a standalone 10^{-8} $M_\odot$ yr^{-1} simulation.

With the use of a 1-D CASA LTE algorithm for ALMA, the sensitivities of HCN and H_2CO were transcribed into integrated intensity differences, as a function of emissivity and optical depth. The largest differences were associated with the largest feasible transitions of HCN and H_2CO; J = 8-7 and J_K = 10_{010}-9_{09} respectively, but could not be converted into potentially observable integrated fluxes due to the restrictions of this model. Both molecules were found to trace different regions of the disk.

Using the stellar accretion rate-to-age linear relation evaluated from observations, the calculation times for the 10^{-7} $M_\odot$ yr^{-1} and 10^{-8} $M_\odot$ yr^{-1} were re-evaluated, of which CN and NH_3 emerged as the most sensitive molecules. Thus, CN and NH_3 may be a possible tracer of calculation time, and disk age.

Declaration

I declare that no portion of the work referred to in the thesis has been submitted in support of an application for another degree or qualification of this or any other university or other institute of learning.

Copyright statement

In scientific fact, those who refuse to go beyond fact rarely get as far as fact.

Thomas Huxley

The people who work in the scientific field, need help to convey what it is about.

Edward Norton

Believe those who are seeking the truth. Doubt those who find it.

Andre Gide

Dedication

To my father.

Acknowledgements

There are many wonderful people to whom I must give acknowledgement to during the course of this work. I begin with those who directly aided me to its completion.

First and foremost, I would like to thank my supervisor, Dr. Andrew Markwick, for giving me this opportunity to undertake research in a truly awe-inspiring area of astronomy. I have been fortunate enough to live in an era where technology has flourished enough to begin understanding astrochemistry. I acknowledge the computational aspects and facilities he provided for me in this work, in addition to the many discussions of programming-related issues which were faced.

I would like to thank Dr. Paul Woods, who kindly withstood my pestering and patiently guided me through many initial steps of programming, early discussions of the literature, found time to thoroughly proof-read sections of my early work... and importantly being a great buddy to travel around Toledo and Madrid with. I thank you very much Paul.

I would like to thank Dr. Catherine Walsh, whom after Andrew's unfortunate accident, took on the private role of big sister. Her vast knowledge of the subject, strong work ethic and patience to discuss important concepts so clearly, aided me through many later aspects of this work. I would personally like to acknowledge her kindness in using her 1-D ALMA CASA disk algorithm, which a major portion of this work is based on. Without the friendship we developed over the last few years, this work would not have been possible.

I would also like to thank Prof. Tom Millar, whose unparalleled knowledge of

the subject, close association with my supervisor Andrew and supervisor to Catherine at the time provided guidance on numerous occasions.

I would also like to thank Dr. Hideko Nomura for providing the physical disk models to my supervisor Andrew, who then passed them on to me. Her discussions in-person whilst touring around Toledo outside conference hours, and by email were always helpful and insightful.

I would finally like to thank Prof. Richard Davis as my advisor, Prof. Albert Zijlstra and Prof. Gary Fuller.

...And then there are the rest of you who have played an important part in my life during the completion of this work. The personal ones. A big thanks go to my friends Dr. Neil James Young, who had to put up with me for two great years as a flatmate, and Dr. Scott Lewis, with whom I spent many an occasion discussing the smaller, funnier things in life when work was challenging.

I must also thank Nichol Cunningham, Dr. Lizette Guzman Ramirez, Matthew Kinder, David Cornaby, Peter Daymond, Dr. Mark McColloch, Dr. Mark Purver, Melis Irfan, Alex Sergides, Roman Belyy, Jill MacDonald, Tim Crinion, Mun-Wei Looi, Arun Asokan, Maralyn Fulker and Natalie Fulker for making life pleasurable. And to anyone else I may have left out and aided me along the way, you have all made this possible. Thank you.

Last and especially of all, I would like to thank my father, who has been a constant source of support for me. Having completed a Ph.D himself, he knew and understood the challenges that lay before me. For this I am truly grateful.
This thesis was typeset with LaTeX.

Abbreviations List

PPD – Protoplanetary disk

PDR – Photon-dominated region

WML – Warm molecular-layer

MHD – Magnetohydrodynamic turbulance

MRI – Magnetorotational instability

ODE – Ordinary differential equation

MMSN – Minimum-mass solar nebula

SLN – Short-lived radionuclide

LLN – Long-lived radionuclide

CHAPTER 1

Introduction

1.1 Overview

Astrochemistry is the study of chemistry in interstellar space. It is fundamental in understanding current and evolutionary states of interstellar phenomena, achieved by observing both the unique discrete spectra of the various molecules contained within. These phenomena are otherwise very difficult or in some cases, impossible to analyze by other means. Particular examples include probing areas of high-mass star formation through masers (e.g. Pestalozzi et al. 2002), and T-Tauri stars with their associated circumstellar and protoplanetary disks (e.g. Dutrey et al. 1997a), all of which are encased in photon-absorbing dust.

Whilst the birth and death of stars have significant implications for the future

structure of galaxies and daughter stars of higher metallicity, the latter stages of star formation can result in a protoplanetary disk of complex chemistry and eventually a system of planets. It is for this reason motivationally that protoplanetary disks are fascinating objects to study; the stepping stone for planetary systems to form, and perhaps life itself to develop. We, as astrochemists are constantly attempting to piece together how and why.

This thesis focuses on the topic of protoplanetary disks around T Tauri stars during a period which our own solar system evolved from, around 4.6 billion years ago, prior to the planet-forming era. During this time, the T Tauri star is thought to actively feed on, or accrete material from its surrounding protoplanetary disk, when the typical age of the system is between 1 and 10 million years old (e.g. Hartmann et al. 1998). Specifically, this thesis presents calculated chemical data from the inner ($r \leq 10$ AU) planet-forming region of a modelled protoplanetary disk surrounding a 0.5 $M_\odot$ T Tauri star. It is organized into five chapters. To provide a flavour of how and where protoplanetary disks fit in to the cycle of stellar birth and death, the remainder of this first chapter briefly outlines the current understanding of the dynamical and chemical transition towards the protoplanetary disk stage, starting from dark clouds, to molecular clouds and finally to the penultimate pre-stellar core phase. The second chapter describes the combined physical and chemical components/parts of the protoplanetary disk model used to calculate the chemical results in detail. The third chapter discusses the potential ionizing effects of decaying radionuclides; in particular, ^{26}Al, thought to have been up to six times more abundant in our early solar system than in the interstellar medium, and the subsequent enhancement in ion-neutral chemical reactions in the densest disk regions with their presence as a function of ionization rate, where all other forms of ionizing radiation, with the exception of cosmic-rays are significantly attenuated. The fourth chapter presents the results of an investigation which chemically simulates evolution from a higher, 10^{-7} $M_\odot$ yr^{-1} stellar accretion rate earlier in time, to a lower, 10^{-8} $M_\odot$

yr^{-1} later epoch. This thesis is then concluded with a detailed discussion of future work in the field of astrochemistry, and a summary of the main points covered in this thesis.

1.2 The chemistry of protoplanetary disks – why do we have to model?

Protoplanetary disks (PPDs) are circumstellar disks of gas and dust ranging from 200 – 1000 AU in radius, and temperatures of 10 – 3000 K, rotating around a young central protostar – a phase our own solar system went through some 4.6 billion years ago. They are vital objects in the low-mass star formation process, firstly because they allow for accretion onto the Young Stellar Object (YSO), and secondly because they transport angular momentum away from the YSO.

Observations of molecular clouds and star-forming regions are used to set constraints on the type of chemistry evolving in the later PPD. PPDs contain a wide variety of molecular species, neutral atoms and atomic ions. Our current knowledge of the chemistry they contain is based on the improving observations of extra-solar PPDs in our galaxy, in addition to the extensive study of our own solar system (i.e. the chemical makeup of the Sun, the planets, comets and meteorites). The PPD environment is suitable for complex chemistry to develop over many millions of years.

However, with the exception of data currently extracted from comets (e.g. Mumma & Charnley 2011), our solar system has evolved too far beyond the PPD phase to directly observe its chemical structure, so one has to use numerical models to simulate these conditions.

Of course, for modellers to model anything, they require a certain set of constraints drawn from fundamental physics, experiments in the lab, and PPD data taken from observations made with telescopes such as Spitzer. With the ever-improving spectral and spatial resolutions of these observational devices telling us

something new or different to previous findings, whether it be features or processes, newer models tend to incorporate as much of this information as possible to ensure that chemical calculations and results are both up-to-date and feasible. Section 2.1 provides a brief chronological overview of some of these PPD models over the last decade.

At the same time, the results from models are used to pin down the next set of interesting features or processes to be observed and studied. Since these features and processes cannot be observed directly (the exception being ”disk gaps” - see Section 4.2), chemical tracers are instead established, where the abundance of certain observable molecules, or the molecular abundance ratio may be shown to correlate with the prominence of a given modelled process (see Table 1 Semenov 2011). The results of chapter 3 and chapter 4 in this thesis are two such examples.

Figure 1.1: *Left*: Artist impression of a typical PPD surrounding a star (http://keckobservatory.org/gallery/detail/25/). *Right*: Hubble Space Telescope (HST) Wide Field and Planetary Camera 2 image of protoplanetary disks (or “proplyds”) observed around five YSOs in the Orion Nebula M42; 29 December 1993 (http://messier.seds.org/more/m042_hst.html).

1.3 A brief history of interstellar chemistry

1.3.1 Progenitor chemistry

Hydrogen is the most abundant element in the universe. The most abundant allotrope of hydrogen is its molecular form, H_2, followed by its more reactive radical form, atomic hydrogen (H). In combination with its low proton affinity, H_2 will react rapidly with everything bar He^+ (Herbst & Klemperer 1973). Arguably two of the most important interstellar reactions involving H_2 are its destruction to form the hydronium (H_3^+) ion:

$$H_2^+ + H_2 \longrightarrow H_3^+ + H,$$

which goes on to drive ion-neutral reactions, and its formation on grain-surfaces (see Section 2.2.2) from atomic hydrogen:

$$H + H + \text{grain} \longrightarrow H_2 + \text{grain}.$$

After H_2, the next most abundant molecules in the interstellar medium are carbon monoxide (CO) (e.g. Dickman 1978), whose atomic C radical formed from ionization is extremely reactive, and helium (He), which although is inert in nature becomes reactive once ionized by cosmic-rays (Herbst & Klemperer 1973). All other molecules now known to exist in the interstellar medium make up the relatively minuscule remaining fraction.

1.3.2 Observations

The study of interstellar molecules is still a relatively recent subject in astrophysics (see Rank et al. 1971, for a review). The characteristic 21 cm (1420.4 MHz) line of H_2 was only first observed in 1951 (Ewen & Purcell 1951). In fact, towards the later 1930s, CH^+, CH and CN had already been discovered from high-resolution observations of bright blue stars in the ultraviolet (UV) part of the electromagnetic

Table 1.1: Typical diffuse cloud, dark and molecular cloud, and protoplanetary disk parameters.

Parameter	Diffuse	Dark and Molecular	PPDs
Temperature, T	100 K	10-50 K	10-3000 K
Molecular density, n	10^2 cm^{-3}	10^2-10^6 cm^{-3}	10^3-10^{15} cm^{-3}
Hydrogen Allotrope	Atomic	Molecular	Molecular
Visual Extinction, A_v (Mag)	2	≥ 5	0.01-1000
Ionization Fraction, $X(e^-)$	10^{-4}	10^{-8}	10^{-15}-10^{-3}

spectrum. In 1963, OH was discovered in the radio as was NH_3 in 1968. By 1971, the total number of detected molecular species reached almost 20. Today the most up-to-date chemical databases (e.g. Smith et al. 2004; Woodall et al. 2007; Wakelam 2009), together with the inclusion of isotopologues and deuterated species, span over 600 species, including CH_4 and various organic molecules such as the alcohol methanol (CH_3OH) and formaldehyde (H_2CO). More complex molecules such as ethane, (C_2H_6) ethanol (C_2H_5OH) and glycine (e.g Ohishi 2008) will inevitably be added to future chemical databases.

1.4 From dark clouds to protoplanetary disks

PPDs are just one period of many phases in the cosmic recycling process of stars. This sub–section highlights some of the important processes that take place at each step along the way to the formation of a T Tauri star and its associated PPD. Table 1.1 compares the approximate values of some typical parameters associated with diffuse, dark and molecular clouds (taken from Millar 2005) and protoplanetary disks.

When a star with mass less than 9 $M_\odot$ runs out of hydrogen to fuse, it undergoes a red giant phase, joining the Asymptotic giant branch (AGB), incurring significant mass loss during the outgrowth. The core becomes a white dwarf whilst the outer

layers diffuse outwards to form a planetary nebula. The material contained within is enriched with various elements heavier than H and He and excited by emitted radiation from the core. This enrichment is the principal process for increasing metallicity in the next generation of forming stars. The spectrum observed can include 'forbidden lines' (e.g. Simpson 1975) due to regions of extreme low density where electrons excite to metastable states; environments not possible to reach at higher densities. The material cools over time (10^4 years) and forms a diffuse cloud. The likelihood of these nebulae evolving into potential star forming regions can be quantitatively estimated by modifying the general form of the Virial theorem:

$$P = -\frac{1}{3}\frac{E_G}{V}, \tag{1.1}$$

where P is the volume-averaged pressure, E_{G} the gravitational energy and V the volume (e.g. Collins 1978; Phillips 1994), and forming an equation for the *Jeans mass*; the minimum or critical mass, M_c, necessary for localized gravitational collapse to occur. It is given by the inequality:

$$M_c > \left(\frac{5k_BT}{G\mu m_H}\right)^{3/2}\left(\frac{3}{4\pi\rho_c}\right)^{1/2}, \tag{1.2}$$

as in Phillips (1994), or more usefully:

$$M_c > 7.598\times10^{21}T^{3/2}\mu^{-3/2}\rho_c^{-1/2}, \tag{1.3}$$

where T is the gas temperature, μ the mean molecular weight of H_2 (~ 2.8) and ρ_c the critical density. For a cloud that exceeds this mass threshold, given the known temperature, molecular weight and critical density parameters, it is likely that the cloud in question will become *fragmented*, regions of the cloud collapsing under gravity due to general inhomogeneity, eventually forming a dense core. Given enough material to accrete, a star can form in these fragmented centres (Phillips 1994).

1.4.1 Diffuse clouds

Diffuse clouds are the first evolutionary step leading to star formation. Their low densities (10^2 cm^{-3}) and visual extinctions ($\sim$ 2 Mag) enable interstellar radiation (optical, UV and cosmic-rays) to completely penetrate through their interior since H_2 and dust are unable to self-shield effectively. Hence they consist mostly of atomic and ionized hydrogen; H and H^+ (Millar 2005), and the ionization fraction, X, given as a function of electron density $n(e^-)$ and hydrogen density $n(H)$:

$$X(e^-) = \frac{n(e^-)}{n(H)}, \tag{1.4}$$

is large for diffuse clouds ($\sim 10^{-4}$). This high degree of ionization is also the reason for their relatively warm temperature, $\sim$ 100 K. The high ionic abundance leads to rapid reactions between atomic ionic radicals such as C^+, S^+, and neutral molecules, whilst the high electron abundance enhances atomic hydrogen recombination, and reformation of H_2 on dust grains. Diffuse clouds undergo significant atomic ion population loss over time to diatomic species such as CN, CN^+, OH, CH and CH^+ (Solomon & Klemperer 1972; Millar 2005). The fully-penetrating, intense radiation-field though the cloud prevents the buildup of larger molecules such as hydrocarbons at this stage of evolution.

1.4.2 Dark clouds and giant molecular clouds (GMCs)

As the cloud cools, the temperature drops and the cloud contracts. As density rises, so does molecular surface shielding from penetrating radiation (A_v increases from $\sim$ 2 to $\sim$ 5 Mag). Consequently the overall ionization fraction reduces from around 10^{-4} to 10^{-8}. There comes a point where UV radiation cannot penetrate the interior of a cloud appreciably, and only cosmic rays can. Chemistry is therefore principally driven by cosmic-ray ionization reactions involving H_2, CO and He, and also by proton-transfer reactions involving the hydronium ion H_3^+ (Herbst & Klemperer 1973; Woodall et al. 2007). Low temperatures $\sim$ 10 K can be achieved due to the

balancing of cosmic-ray heating and molecular emission cooling (e.g. Goldsmith & Langer 1978), which in turn induces freeze-out onto grain surfaces (see Section 2.4.2). As a result, the dominant hydrogen allotrope switches back to H_2. The low temperature, high density and high extinction conditions of dark clouds, in combination with the prevalence of ion-neutral reactions initially induced by cosmic rays, all favour the formation of more complex, volatile molecules over time (giant molecular clouds, or GMCs).

1.4.3 Pre-stellar core collapse

Typical GMCs, with the required parameters to exceed the Jeans mass, undergo density gradient fragmentation consisting of dense clumps $\sim 10^3$-10^5 cm^{-3} around 1 pc in diameter, encased in a 10^2-10^3 cm^{-3} inter-clump medium (Evans 1999). Clumps themselves consist of denser $> 10^5$ cm^{-3} cores of ~ 0.1 pc diameter (Markwick & Charnley 2004). These clumps are thought to undergo gravitational collapse and form pre-stellar cores. Cores then grow by accreting material from their surrounding envelopes. Ultimately, an accreting core's ability to continue to collapse is dependent on its ability to radiate away stored gravitational potential energy, which is achieved through molecular excitation and emission. During this phase, the cloud parameters change. Collapse increases density and, if the collapsing system is considered isothermal (where the heating from gravitational compression balances the radiative heat loss; see Gaustad 1963), the Jeans mass will decrease. But what initiates collapse, and the dynamics involved are still uncertain.

Cores are not thought to collapse freely, and are instead impeded to some extent by the presence of resistive magnetic and turbulent processes. The precise details remain debated in the literature, with differing opinions as to the exact timescales of collapse in the presence of these processes which oppose gravity (see Markwick & Charnley 2004, for a review). Two theories are currently proposed. Briefly, the Standard Model (see Shu et al. 1987) points to an initial stuttering phase caused by

magnetohydrodynamical (MHD) turbulence (highlighted in Section 3.3) which then decays away (via ambipolar diffusion) after several million years, followed by free-fall core collapse. This extends the total collapse timescale to $\sim 10^7$ years, which is longer than the apparent 1-4 million year age limit of T Tauri stars still encased in molecular cloud gas which signifies the end of this stage of evolution (Hartmann et al. 2001). The Driven Supersonic Turbulence (DST) model was instead suggested by some as a means to satisfy the core-collapse time-frame criterion, decaying more rapidly than MHD turbulence, with a larger proportion of the collapse occurring under free-fall (e.g. Larson 2003).

The extent of core density increase with core radius over time has also been debated. The Singular Isothermal Sphere (SIS) density model (see Shu 1977) suggests a $\rho \propto r^2$ distribution which leads to core collapse from the inside out. However some MHD studies have questioned its feasibility (e.g. Desch & Mouschovias 2001), with observations (e.g. Bergin et al. 2002) instead fitting closer to the Bonner-Ebert uniform-density sphere distribution of the Larson-Penston (LP) model (see Larson 1969 and Penston 1969). The chemical evolution of both radial-density core collapse schemes has been modelled and compared in the past (e.g. Aikawa et al. 2001; Rodgers & Charnley 2003).

Initially a pre-stellar core is cold enough for molecular species to be frozen-out onto grains and depleted from the gas, particularly for outer regions of the envelope. Here, most C, N and O species are hydrogenated, where molecules such as CO_2 (e.g. Pontoppidan et al. 2008), CH_4 (e.g. Öberg et al. 2008a,b), NH_3 (e.g. Bottinelli et al. 2008) and CH_3OH (e.g. Gibb et al. 2004; Watanabe et al. 2006; Boogert et al. 2008) can form on grain surfaces. As the core evolves, and envelope material is accreted inward, temperatures do eventually increase and molecules are desorbed into the gas. At the same time, the higher density increases molecular collision rates, and certain molecules such as HCO^+ and N_2H^+ are depleted, which can be traced (van Zadelhoff 2002).

1.4.4 Star formation

The next phase involves the formation to a low-mass (0.5 - 2 $M_\odot$) star when the conditions (temperature, pressure, density) are high enough for hydrogen fusion to begin. To do so, they traverse through a pre main sequence (PMS) path, often termed the Hayashi track (Hayashi 1961). Probing the evolution directly from the pre-stellar core to low-mass star phase is impossible since the surrounding envelope of gas and dust efficiently absorbs the optical and UV light emitted from the central object, rendering it optically invisible; it is only once the star begins hydrogen fusion, and the envelope and later disk is cleared away, that they become optically visible. Instead, the pre-stellar phases are probed indirectly, where dust grains are heated to an equilibrium temperature where the emission and absorption per grain become equal, and emit in the more continuous infra-red and sub-mm regions of the electromagnetic spectrum, often termed spectral energy distributions (SEDs). The evolutionary phases are often categorized into four classes (Class-0 to Class-III), each associated with distinct SEDs (e.g. Figure 1.1 in van Zadelhoff 2002). Figure 1.2 displays an annotation of the these classes.

In summary, Class-0 represents the initial pre-stellar core collapse phase highlighted in Section 1.4.3. It is also termed the main accretion phase, and is defined by the epoch when a collapsing central core accretes from a much larger and more massive spherical envelope, around the size of $\sim$ 10000 AU (Shu 1982; van Zadelhoff 2002). Class-I, known as the late-accretion phase, begins around 10^4 to 10^5 years after Class-0, and is associated with an enveloped optically thick molecular cloud approximately $\frac{1}{10}$ the mass of the now central protostar, where a powerful bi-polar outflow jet has cleared away the majority of the envelope mass. It also signifies the initial formation of a centrifugally-supported disk near the centre, where the angular momentum L of the rotating envelope forces accretion of material into a flattened plane perpendicular to L (Terebey et al. 1984). Class-II (10^5 - 10^6 years after Class-0) signifies the advanced formation and flattening of a well-mixed protostellar disk

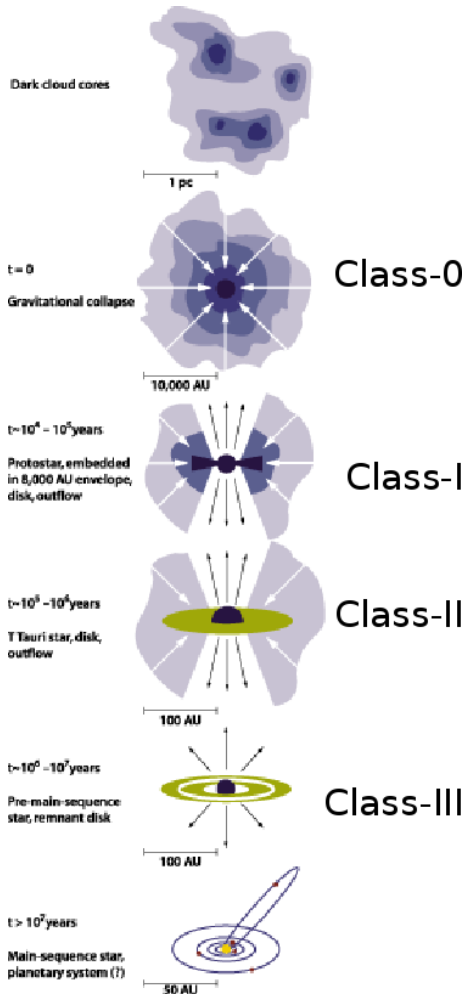

Figure 1.2: The evolution of a pre-main sequence star. Taken from Shu (1982), with class phase annotations added.

of gas and dust typically between 200 - 1000 AU in radius, and the consequent widening and dissipation of the main outflow cavity. At this stage the central object has evolved into a classical-line T Tauri star (CTTS), which may be optically visible depending on the angular view with respect to Earth. By Class-III (10^6 - 10^7 years after Class-0) the CTTS becomes a typically-referred weak-line central T-Tauri star (WTTS). Stellar accretion slows considerably, and localized accretion and coagulation processes within the disk gradually result in the transition from a

debris disk containing little gas, to one containing planetesimals which, by completely sweeping-up the surrounding disk material, will go on to form planets and comets (Shu 1982; van Zadelhoff 2002; Markwick & Charnley 2004). Later epochs represent the phases of optically-visible main-sequence stars which have ceased accreting, and an associated system of orbiting planets housed in a fully cleared disk $\sim$ 50 - 100 AU in radius.

This thesis particularly focuses on the chemical constituents of PPDs which exist between the Class-II and Class-III stages, where the process of stellar accretion is beginning to slow, and grain-settling and coagulation has not yet taken place (i.e. gas and dust are well-mixed).

1.5 PPDs

Early observations of CO towards Class-II T Tauri stars (e.g. Cohen 1983; Adams et al. 1988; Keene & Masson 1990; Koerner et al. 1993; Lay et al. 1994; Guilloteau & Dutrey 1994; Dutrey et al. 1994) in our galaxy revealed chemical material rotating in a disk structure around them. Since then, other molecules have been observed in many T Tauri disks. A summary of molecular species detected so far in various T Tauri disks is shown in Tables 4.1 and 4.2 of Section 4.3. Like in pre-stellar cores, observations of molecules in PPDs are established from a molecular line emission spectrum (SEDs), primarily in two wavelength regimes. Infra-red (IR) wavelength emission originates from vibrational transitions of gas-phase molecules in warm ($T \geq 200$ K) environments. Sub-mm wavelength emission is generated from molecular excitation and relaxation of rotational energy levels, in colder astrophysical environments such as dark and molecular clouds (10 K $\leq T \leq$ 200 K).

1.5.1 Physical structure

The physical disk structure of PPDs has also been interpreted from their SEDs. Geometrically flat, pancake-shaped disks (e.g. Lynden-Bell & Pringle 1974; Friedjung 1985) were initially proposed as a means of explaining how a disk of constant depth is heated by radiation from the central star. These assumed that the disk height was very much smaller than the disk radius, and most of the disk material was confined to the rotation plane. However, Rydgren & Zak (1987) first noted IR luminosity excesses larger than previous flat spectral measurements made with the IRAS observatory. Adams et al. (1987) suggested this could only be explained by an intrinsic heating process from within the disk itself which results in the flaring or puffing-up of the warmer upper layers of the outer region, and hence a larger interaction area with the incident stellar radiation from which the resulting excess emission is detected. A flared disk model was first proposed by Kenyon & Hartmann (1987) and most notably considered in Chiang & Goldreich (1997) with particular reference to the observed GM Aur system. Nowadays most 2-D models consider a physically-flared disk (such as the model used in this thesis; see Section 2.2). Figure 1.3 in van Zadelhoff (2002) compares the SED profiles for a flat and a flared disk.

1.5.2 Chemical structure

Molecular observations have led to a common 2-D chemically-stratified structure for PPDs, first proposed in Aikawa & Herbst (1999). Briefly, this consists of three vertical zones: a photon-dominated surface layer, a warm-molecular layer and a cold, icy midplane (Figure 1.3). The photon-dominated surface layer is directly exposed to stellar UV and X-rays, and interstellar UV and cosmic rays. Chemistry here is typically governed by photodissociation and ionization reactions; particularly in the hot ($T \leq 1000$ K) inner $1 - 2$ AU region, made up of simple atoms and cations such as H^+, C, C^+, O and N. Deeper down, the warm-molecular layer is

typically composed of H_2, CO and hydrogenated molecular species such as NH_3, HCN, H_2O, H_2CO and CH_3OH, which persist because of the increased shielding from the upper layers of the disk. Regions of the outer midplane ($r \geq 20$ AU, $T \sim 10$ - 20 K) are cold enough for most species to freeze out onto dust grains. At smaller radii, temperatures become sufficient to desorb molecules into the gas; the exact point of which is termed the snow-line, and is different for each molecule (see Section 4.2). When $T \geq 1000$ K ($r = 1$ AU), dust itself begins to evaporate (e.g. Markwick et al. 2002) and is commonly termed the inner dust rim (e.g. Dullemond & Monnier 2010). Hotter regions are thought to consist of atomic gas and plasma.

So far there have been no sub-mm observations of the inner ($r \leq 10$ AU) regions of disks, which are associated with the deeper, planet-forming zones (e.g. Bergin 2009). The Atacama Large Millimeter Array (ALMA), initiated in 2013, will have both the spectral and angular resolution to probe these $r \leq 10$ AU regions of various T Tauri systems in the sub-mm range (van Dishoeck & Jørgensen 2007; van Dishoeck 2009). There are likely to be many more complex and less abundant molecules which have not yet been detected, particularly more exotic organics such as direct precursors to amino acids, which are currently seen in comets (e.g. Kobayashi et al. 1995; Charnley et al. 2010). Cooler regions around the midplane are likely areas for such molecules to form on grains, which may then be accreted inward to hotter regions where they are desorbed into the gas. It is hoped that ALMA will detect these.

1.5.3 Accretion

A PPD is an essential feeding source for the central protostar to condense, grow and evolve. The extent of gas and dust accreted from the surrounding disk to the central star is quantified by a stellar accretion rate, measured in solar masses per year ($M_\odot$ yr^{-1}). Various observations of PPDs around T Tauri stars in Taurus and Chamaeleon I molecular clouds have determined that stellar accretion rates vary between 10^{-7}

$M_\odot$ yr^{-1} and 10^{-10} $M_\odot$ yr^{-1} for disks between the ages of 1 and 10 million years old, after which accretion halts, and the star enters the Main Sequence (Hartmann et al. 1998). The physical structures of two such stellar accretion rates, 10^{-7} $M_\odot$ yr^{-1} and 10^{-8} $M_\odot$ yr^{-1}, are considered in this thesis.

A given star cannot absorb all the angular momentum associated with accreted disk material since it would gain unrealistically fast spin rates which do not coincide with current ideas of stellar evolution (Lynden-Bell & Pringle 1974). Instead, the accreted material's angular momentum is transferred "outward" to the rest of the disk. Processes which allow angular momentum transfer imply that disks are turbulent, viscous, fluid-behaving mediums, rotating in a differential manner. These intrinsic processes generate heat known as viscous dissipation (discussed further in Section 2.3.2), in addition to the conventional heating processes from stellar and interstellar radiation.

1.5.4 Dynamics: magnetohydrodynamic turbulence (MHD)

Many works have noted that molecular viscosity alone is too inefficient at redistributing angular momentum to justify the large accretion rates observed in disks, and that some form of additional intrinsic turbulence must be responsible (e.g. Gammie 1996). Several forms have been proposed in the literature (e.g. Lin & Papaloizou 1980; Klahr 2004; Shalybkov & Rüdiger 2005), but the most regarded is magnetohydrodynamical (MHD) turbulence, which is induced by magnetorotational instability (MRI; Balbus & Hawley 1991; Hawley & Balbus 1991). The general MRI criterion was first theorized in Velikhov (1959), and is generated when the magnetic field tension, between radially-adjacent gas layers rotating apart, increases over time as the angular velocity decreases with radius and angular momentum is transferred outward through the disk, generating MHD turbulence. Balbus & Hawley (1991) were the first to note that even a relatively weak primordial magnetic field was able to induce MRI in a differentially rotating Keplarian-based PPD.

The degree of chemical ionization in PPDs is crucial in producing MRI. Briefly, MRI is thought to be promoted in the plasma-rich upper regions of the disk, where the presence of a primordial magnetic field (present in pre-stellar dense cores (e.g. Girart et al. 2006) and important in star formation (e.g. Shu et al. 1987)) permeating throughout the disk is able to interact with the rich sea of electrons and cations. The extent of MRI is reliant on the "coupling" strength of the magnetic field to the plasma, which itself depends on the electron and cation abundance relative to neutral species which have not been ionized. This degree of coupling between the plasma and magnetic field is therefore often quantified by the ionization fraction given in Equation (1.4), or an extended version defined in Gammie (1996):

$$x(e) = \frac{n_{\rm e}}{n_{\rm H}} \sim \left(\frac{\zeta}{\beta n_{\rm H}}\right)^{1/2}, \tag{1.5}$$

where ζ is the photoionization rate, and β is a typical dissociative recombination coefficient, $\eta = 8.7 \times 10^{-6}\ T^{-1/2}$ cm^3 s^{-1} (Glassgold et al. 1986). Others also prefer to define the coupling degree in terms of a magnetic Reynolds number, $\mathrm{Re_M}$, also defined in Gammie (1996) as:

$$\mathrm{Re_M} = \frac{V_{\rm A} H}{\eta}. \tag{1.6}$$

Here, $V_{\rm A} \sim \alpha^{1/2} c_s$ is the Alfven speed as a function of the viscosity parameter α and the sound speed c_s, H is the disk scale height defined by $H = c_s/\Omega$, where Ω is the Keplerian velocity as a function of radius, and η is the magnetic resistivity:

$$\eta = (6.5 \times 10^3) x(e) \quad \mathrm{cm^2 s^{-1}}, \tag{1.7}$$

as derived in Hayashi (1981).

1.5.5 Dead zones

MHD turbulence from MRI does not always occur everywhere in PPDs. Theoretical models of PPDs have shown turbulence to exist only in regions where $x(e)$ or $\mathrm{Re_M}$ is

above a critical level; that is, where the gas is sufficiently ionized that it couples to the magnetic field. Most authors define this critical value in terms of $x(e)$, between the values 10^{-12} (e.g. Semenov et al. 2004; Willacy & Woods 2009; Walsh et al. 2012) and 10^{-13} (e.g. Gammie 1996), and $\mathrm{Re_M} \geq 100$ (e.g. Sano & Stone 2002; Ilgner & Nelson 2006b). Many works have found "dead zones" (e.g. Gammie 1996) located in the most dense inner midplane region, where the ionization fraction is so low ($x(e) < 10^{-12}$ or $\mathrm{Re_M} \leq 100$) that the majority of the gas is decoupled from the magnetic field, and inward stellar accretion flow may be inhibited (e.g. Sano et al. 2000; Fromang et al. 2002a; Semenov et al. 2004; Ilgner & Nelson 2006a,b,c; Turner et al. 2007; Turner & Sano 2008; Zhu et al. 2009; Willacy & Woods 2009; Umebayashi & Nakano 2009; Dzyurkevich et al. 2010; Fogel et al. 2011; Vasyunin et al. 2011; Walsh et al. 2012). Dead zones may not be completely "dead" in the full sense since a small fraction of waves from the surrounding turbulent zones may penetrate the dead zone, and still generate small rates of accretion (Turner & Sano 2008). This may well be the case when vertical-mixing processes are considered in models.

Dead zones vary in size and location depending on the model. In some works, a general increase in the outer dead zone boundary radius at the midplane, r_{crit}, with disk mass was found since the number of charged particles at the midplane decreases with surface density. Sano et al. (2000) studied the dead zone in three models (0.3, 3 and 10 times the minimum-mass solar nebula (MMSN) density distribution) and established an enlargement with surface density. Willacy & Woods (2009) found a marked increase in the size of the dead zone at the midplane (from an outer "critical" radius $r_{\mathrm{crit}} \sim 8$ AU to 18 AU - the orbit of Uranus) between their $\alpha = 0.01$ and $\alpha = 0.025$ models (the latter of which is more applicable to the solar system mass). Studies have also concluded a link between dead zone and dust grain size, whereby smaller grains recombine with more free electrons, due to their combined larger surface area, than larger ones. Turner & Sano (2008) compared a

MMSN protostellar disk with $r = 1$ μm grains and no grains and found the dead zone to disappear altogether in the latter. There has also been suggestion of a decrease in dead zone size with increasing photoionization rate, with separate studies on cosmic rays (e.g. Gammie 1996), X-rays (e.g. Igea & Glassgold 1999; Chiang & Murray-Clay 2007) and radionuclides (e.g. Finocchi & Gail 1997; Sano et al. 2000; Umebayashi & Nakano 2009). Umebayashi & Nakano (2009) noted a sizable increase ($r_{\rm crit} \sim 17$ AU to ~ 30 AU - the orbit of Neptune) after updating the basic vertically-incident cosmic-ray attenuation expression to one which assumed isotropic incidence (see Section 3.2).

Inclusion of heavy metals such as Na, K and Mg, which thermally ionize under inner PPD conditions ($T \geq 10^3$ K), is also thought to contract the dead zone (Fromang et al. 2002b; Ilgner & Nelson 2006b). Ilgner & Nelson (2006b) showed that although heavy metal ions such as Mg^+ are relatively slower in sweeping-up free electrons than molecular ions, if implemented with a high enough abundance ($\sim 10^{-10} - 10^{-8}$), turbulent diffusion can have a notable effect in reducing the size of the dead zone, or remove it altogether. A 1+1D mixing model in Semenov et al. (2004) showed that the HCN/HNC emission line ratio may be a suitable tracer of such disk diffusion.

The lack of MHD turbulence in dead zones may have important ramifications for the formation of planets, since these modelled dead zones happen to exist around the proposed planet-forming region of disks. Matsumura et al. (2007) discussed the role in which dead zones have in halting the inward accretion of Jovian-sized planets. Unlike turbulent regions where chemistry is kept to an ionic, atomic and basic molecular level, dead zones likely consist of a complex hydrocarbon chemistry, where the formation of more delicate organics and pre-biotics is a distinct possibility. But many authors have also highlighted the potentially episodic nature of MRI activation over time. Sano et al. (2000) and Zhu et al. (2009) argued that as dust sinks towards the midplane and coagulation proceeds over time into planetesimals,

the disk becomes less dense, which may allow for deeper radiative penetration, and subsequent MRI activation in previous dead zone regions at a later stage of evolution. This may account for the observed stellar luminosity enhancements in FU Orionis, attributed to changes in standard accretion rates from 10^{-7} $M_\odot$ yr^{-1} to 10^{-4} $M_\odot$ yr^{-1} over a space of 100 yr or so (e.g. Hartmann & Kenyon 1996).

The exact mechanisms which affect MRI are debated, and consist of calculations simulating ohmic dissipation, Hall diffusion and ambipolar diffusion. Whilst some studies (Turner et al. 2007; Bai & Goodman 2009) have investigated purely the role of ohmic dissipation in MRI, where magnetic energy is dissipated due to the normalization of electrons and ions in a plasma to the speed of sound, c_s, other works (e.g. Chiang & Murray-Clay 2007; Perez-Becker & Chiang 2011) have emphasized the effects of ambipolar diffusion in suppressing MRI and MHD turbulence, due to the sheer ubiquitous presence of neutral H_2 in disks. For this reason they argue that they should be incorporated into calculations of MRI activity in modelled disks (e.g. Walsh et al. 2012). Ambipolar diffusion is an energy-expelling process where drifting neutral gas (i.e. H_2) is collisionally coupled to the sea of ions in the plasma which itself is bound to the magnetic field, hence the neutral gas and magnetic field are indirectly coupled. The extent of neutral coupling to ions in the plasma, i.e. the extent to which H_2 can accrete by MRI, is commonly described by a dimensionless ambipolar diffusion parameter, Am:

$$\mathrm{Am} = \frac{x(e) n_{\mathrm{H_2}} \beta_{in}}{\Omega}, \tag{1.8}$$

where $\beta \sim 1.9 \times 10^{-9}$ cm^3 s^{-1} is the average rate coefficient for ion-neutral collisions, Ω is the Keplerian angular velocity and n_{H_2} the number density of neutral gas assumed to consist mostly of H_2. For the neutral medium to be considered unstable, H_2 must collide with enough ions "within the e-folding time of the instability, $1/\Omega$" (Chiang & Murray-Clay 2007); that is, where Am exceeds a critical value, Am^{crit}, of 100 (Hawley & Stone 1998; Sano & Stone 2002). More recent works (e.g. Bai 2011) have revised $\mathrm{Am}^{crit} \sim 1$, based on a strong coupling limit satisfied in PPDs

where ion resistivity is low and ion-electron recombination times are lower than the orbital period, $2\pi/\Omega$. Walsh et al. (2012) recently compared ohmic dissipation and ambipolar diffusion effects in their model and found that ambipolar dissipation further suppressed MRI in disk regions of lower density, which corresponded to a dead zone enlargement in the outward radial direction. They also compared the older Hawley & Stone (1998) Am = $\mathrm{Re_M}$ = 100 criterion with $\mathrm{Am^{crit}}$ = 1 and established that the suppression of MRI is reduced from affecting most of their disk to just affecting the midplane. In both cases, they found that UV and X-ray photochemistry had little effect on Am and $\mathrm{Re_M}$ values at the midplane.

Since MRI turbulence, disk ionization and dust settling are coupled, modelling MHD turbulence in a self-consistent manner as a function of time has so far proved a arduous computational task. Simulations of 1+1D turbulent diffusion in disks have been made (e.g. Ilgner et al. 2004; Semenov et al. 2004; Ilgner & Nelson 2006b; Semenov & Wiebe 2011; Heinzeller et al. 2011; Walsh et al. 2012) and localized 3-D shearing boxes (e.g. Hawley & Stone 1998; Turner et al. 2007; Turner & Sano 2008; Zhu et al. 2009) have also been attempted. So far, no full dynamical simulation of an entire disk has been achieved which couples dynamics, radiation and chemistry. From a chemical perspective, reaction networks have been restricted to basic schemes which assume only a few ions and grains with ionization and recombination reactions. Grains have been assumed to be negatively charged such that cations directly recombine or dissociatively recombine on grain surfaces, which is valid where the number density exceeds 10^{12} cm^{-3}, which is generally true for the inner $r < 20$ AU disk midplane in most models. Simulations incorporating a greater variety of charged grain compositions (PAH's) and anionic molecules (e.g. CN^-) should be considered as future work since they may affect the recombination rates in different areas of the disk. As of now, no MHD simulation utilizing a more complex chemical network has been implemented, and it is hoped to be achieved in the future.

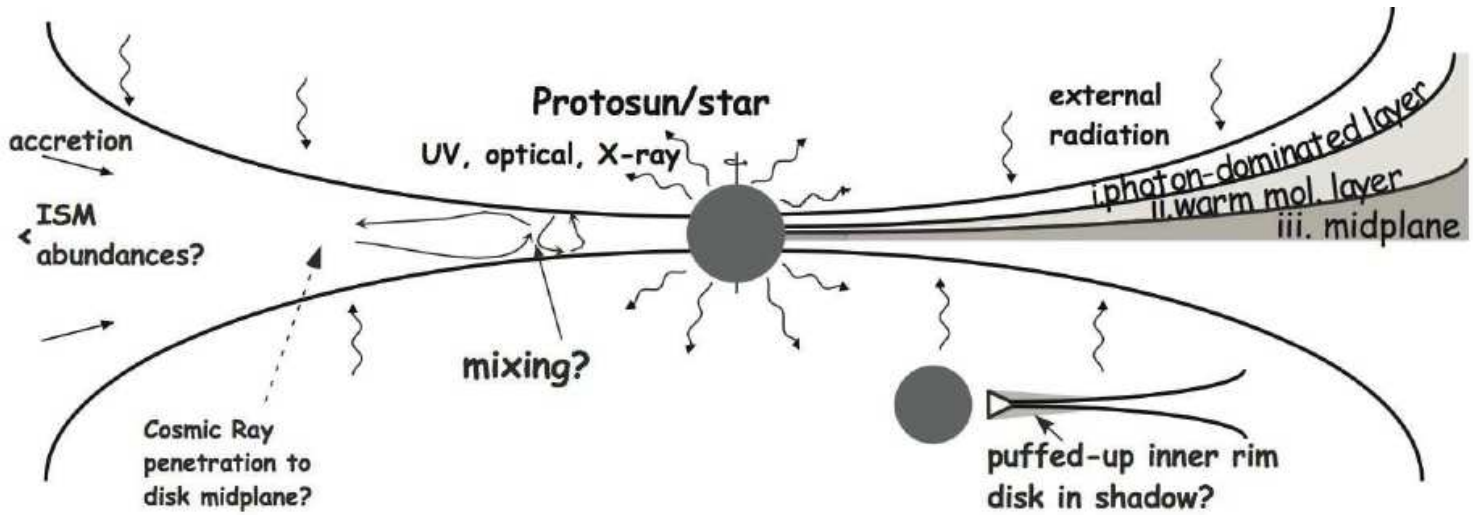

Figure 1.3: A possible chemical structure of our early protoplanetary disk (edge-on view), taken from Bergin et al. (2007). The disk is divided into three layers; from top to middle: a photon-dominated surface layer, a warm molecular layer, and a midplane.

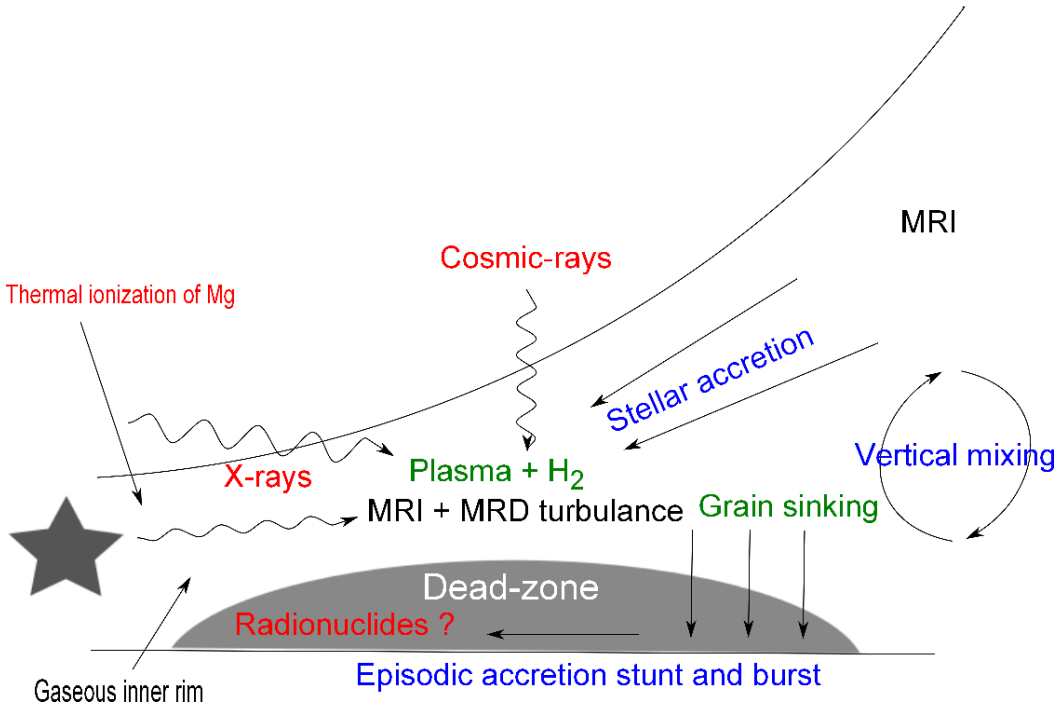

Figure 1.4: The common two-tier ionization scheme of inner PPDs. In the upper disk, X-rays and cosmic-rays ionize gas above a critical ionization level ($\geq 10^{-12}$) to produce a plasma soup of ions and electrons coupled to the magnetic field. MRI is thought to generate MHD turbulence, which transports angular momentum outward and allows for stellar accretion inward. At the same time, H_2 becomes collisionally coupled to ions in the plasma (ambipolar diffusion) which may suppress MRI. X-ray and cosmic rays are increasingly attenuated towards the midplane to a depth where the ionization fraction drops below the critical value needed to maintain MRI. This region is known as the dead zone. Many factors may affect its size or presence altogether as the disk evolves, such as grain settling and coagulation, thermal ionization of heavy metals, turbulent mixing and radionuclide ionization.

CHAPTER 2

Model

2.1 Preamble

Spectral observations of dark clouds and pre-stellar cores set the initial constraints of chemistry present in PPDs, and the physical and chemical modelling of PPDs then helps piece together the dynamical processes and chemical evolution which occur over time. Chemical models incorporate a database of known chemical reactions which consist of interaction information. These are based on rate-coefficients, deduced either from theory, laboratory experiments or from observational data. This chapter outlines the physical and chemical model of a PPD used to calculate the results in chapter 3 and 4 of this thesis, and explains the basic physical processes which are incorporated.

2.2 Introduction

Astrochemical modelling of interstellar clouds began over 60 years ago (e.g. Bates & Spitzer 1951), based then on a few basic ion-neutral reactions in the gas-phase, cosmic-ray ionization (Herbst & Klemperer 1973) and grain-surface chemistry (e.g. Hollenbach & Salpeter 1971), simply because models were constrained by a lack of computing power and knowledge of reaction-rates. PPD modelling has been a rather recent innovation; starting around 30 years ago (e.g. Lewis et al. 1979) before really taking off some 10 – 15 years ago, when computers became powerful enough to handle the vast quantity of calculations required.

2.2.1 PPD model comparisons

Table 2.1 lists some of these recent PPD models, along with their physical and chemical characteristics applied for specific investigations, which are discussed in the relevant papers. The columns in Table 2.1 are defined as thus:

- Physics (**P**): the physical disk description; Semi-Analytical (S); Bell et al. (1997)(B); MMSN (Hayashi 1981)(H); Steady Accretion Disk (Lynden-Bell & Pringle 1974)(A); D'Alessio (1998; 1999; 2001)(D); Chiang & Goldreich (1997; 1999)(C); Nomura (2002)(N); Dullemond & Dominik (2004)(DD); Nomura & Millar (2005)(NM)

- Chemistry (**Ch**): Prasad & Huntress (1980)(PH); Mitchell (1984) & Baulch et al. (1992)(MB); Grain-surface reactions, excluding gas-grain interaction i.e. H_2 formation or ion recombination (S); UMIST database (Millar et al 1997; Le Teuff et al. 2000; Woodall et al. 2006)(U); Ohio State database (Terzieva & Herbst 1998; Smith et al. 2004)(O); Deuterium fractionation reactions (D); NIST chemical kinetics database (N); Cernicharo (2004)(C); Jansen et al. (1995)(J); Various (V)

- Dimension (**D**): 1-D mid-plane model (1); 1+1D vertical (2)
- Ionization (**I**): Cosmic-ray (C); UV (U); X-ray (X); Lyman-α (L); Radionuclide ionization (R)
- Gas-grain interaction (**G**): Freeze-out and thermal/non-thermal desorption
- Dust destruction (**D**): Yes (Y) or No (N)
- Observables (**Ob**): Column density (CD); D/H ratios (D:H); Line profiles from calculations (L)
- Coupling between dynamics and chemistry (**Cp**): Yes (Y) or No (N).

Table 2.1:

A list of recent PPD models for comparison (updated from Markwick & Charnley 2004). The columns are defined as thus: Column title, Author(s) and column notations as discussed in Section 2.2.1.

Model	P	Ch	D	I	G	D	Ob	Cp
Aikawa et al. (1996)	H	PH	1	U,C	Y	N	CD	N
Bauer et al. (1997)	S	MB	1	-	N	Y	No	N
Finocchi & Gail (1997)	S	MB	1	C,R	N	Y	No	N
Willacy et al. (1998)	B	U,S	1	C,R	Y	N	No	N
Aikawa & Herbst (1999a)	H	O	2	X,C,U	Y	N	CD	N
Aikawa & Herbst (1999b)	A	O,D	1	C	Y	N	D:H	N
Aikawa et al. (1999)	A	U	1	C	Y	N	No	N
Willacy & Langer (2000)	C	U,S	2	U,C,R	Y	N	CD	N
Aikawa & Herbst (2001)	H	O,D	2	X,C,U	Y	N	CD,D:H	N
Aikawa et al. (2002)	D	O	2	U,C	Y	N	CD,L	N
Markwick et al. (2002)	B	U	2	X,C,U,R	Y	N	CD	N
van Zadelhoff et al. (2003)	D	O	2	U,C	Y	N	L	N
Millar et al. (2003)	N	U	2	U,C,R	Y	N	CD	N
Ilgner et al. (2003)	B	U	2	U,C,R	Y	N	No	Y
Ilgner et al. (2004)	A	U	2	–	Y	Y	No	N
Jonkheid et al. (2004)	D	J,U	2	C,U	Y	Y	L	N
Semenov et al. (2004)	D	U	2	C,U,X,R	Y	N	CD	N
Semenov et al. (2005)	DD	U	2	C,U,R	N	N	CD,L	N
Semenov et al. (2006)	D	U	2	C,U,X,R	Y	N	CD	N
Ilgner & Nelson (2006a; b; c)	A	V	2	X	Y	N	–	N
Woods & Willacy (2007)	D	U	2	C,U,X,R	Y	N	CD	N
Agundez et al. (2008)	D	U,N,C	2	C,U,X	Y	Y	CD,L	N
Semenov et al. (2008)	D	U	2	C,U,X	Y	Y	L	N
Willacy & Woods (2009)	D	U,D	2	C,U,X,R	Y	N	CD,D:H	N
Nomura et al. (2009)	NM	U	2	C,U,X	Y	N	CD,L	N
Umebayashi & Nakano (2009)	H	S	2	C,U,X,R	Y	N	CD	N
Walsh et al. (2010)	NM	U,S	2	C,U,X,R	Y	N	CD	N
Semenov et al. (2010)	D	O,S	2	C,U	Y	N	–	N
Heinzeller et al. (2011)	NM	U,S	2	C,U,X	Y	N	CD,L	N
Semenov et al. (2011)	D	O,S	2	C,U,X,R	Y	N	CD	N
Fogel et al. (2011)	D	O,S	2	C,U,L,X	Y	N	CD,L	N
Walsh et al. (2012)	NM	U,S	2	C,U,L,X	Y	N	CD,L	N
This work	N	U,S	2	C,U,R	Y	N	CD,D:H,L	N

2.2.2 Coupled and uncoupled PPD models

PPD models which calculate chemistry as a function of time consist firstly of an underlying physical grid which describes the physical and dynamical structure of a PPD in terms of fundamental parameters such as density, temperature and photoionization rate, which are calculated iteratively, or self-consistently, by one or two-dimensional radiative transfer equations. Secondly, they consist of a listed network of chemical reactions in the form of binding energies and activation temperatures which enable reaction rate-coefficients to be calculated. Such models are termed "uncoupled", since both parts are treated separately, i.e. the local physical parameters are calculated first, and input into the rate-coefficient calculations of the chemical model. Since the understanding (from an observational point of view) is that PPDs are complex interactions between chemistry, dynamics and radiation, models should ultimately "couple" all three simultaneously. Sadly, with exception of small-scale coupled "slab" simulations (e.g. Turner et al. 2007), no such coupled simulation of an entire PPD has yet been achieved, due in part to the enormous computational power required to simulate the more realistic 3-D behavior, and the limited theoretical understanding of this coupling in different regions of PPDs (termed the "triangle of pain"; see Markwick & Charnley 2004).

There are, however, two major advantages of uncoupled models. The first is that both physical and chemical parts can be made as independently complex as possible (Markwick et al. 2002), and secondly, simulations complete in a faster time than a coupled one. The model used in the investigations of this thesis is uncoupled. In the proceeding section (Section 2.3), the physical part is discussed in detail, and is placed in context with other models in Table 2.1 which use other surface density prescriptions. The chemical part then discussed the following section (Section 2.4). The physical structure of two stellar accretion rates, 10^{-7} $M_\odot$ yr^{-1} and 10^{-8} $M_\odot$ yr^{-1} are considered. This is discussed in Section 2.3.5. As a benchmark, Appendix A compares some chemical results from the combined model used here with a previ-

ous investigation which utilized the same physical model from Nomura (2002).

2.3 Physical model

For both of these stellar accretion rate prescriptions, the physical structure resembles an axisymmetric disk surrounding a typical central T Tauri star, with parameters $M_* = 0.5\ M_\odot$, radius $R_* = 2\ R_\odot$ and $T_* = 4000$ K. This section is split into four further subsections. In the first subsection (2.3.1), the spatial grid distribution for the modelled PPD is discussed. In subsection 2.3.2, the two heating processes are explained, and an expression for their heating rates with respect to temperature is established. In subsection 2.3.3, the vertical structure of the disk is outlined, from the assumption of hydrostatic equilibrium. In subsection 2.3.4, radiative equilibrium is assumed and the resulting two-dimensional radiative transfer equations are set-up and defined, and in subsection 2.3.5, the resulting density and temperature distributions calculated from the equations in 2.3.3 and 2.3.4 are discussed. Finally in 2.3.6, the method of accretion adopted in this model is explained, along with an approximation for the accretion velocity and time period of calculation at each radial grid point.

2.3.1 Grid space

Both the spatial and physical structure, provided by Andrew Markwick (private communication) is taken from the model derived in Nomura (2002) and Millar et al. (2003), consisting of a 1 + 1 (radial and vertical) dimensional grid of ~ 7500 points, which models the inward flow of accretion by essentially following the chemical composition of a gas parcel from the outer to inner region. Although the entire grid available for simulation is between 0.01 and 100 AU, the model starts from a maximum radius of $r = 25$ AU and ends at 1 AU. This was decided since firstly the temperature at the midplane beyond a distance of 25 AU rises due to the nature

of the radiative calculation used, i.e. reprocessed radiative heating begins to have a more significant effect than viscous dissipation at heating the disk (see Section 2.3.3 and Millar et al. 2003). Simulating the disk from beyond r = 25 AU therefore results in profile abnormalities of gas-grain abundances at the midplane. Secondly, modelling between r = 1 and 0.01 AU is excluded since both dust destruction and three-body gas-phase reactions have been shown to be important in these regions, which this model does not simulate for the purposes of computational speed. Nevertheless, this model simulates the important areas of interest with regards to this thesis since the aim of the investigations in Chapters 3 and 4 is to aid the understanding of chemical evolution in potentially habitable planet-forming regions, which are thought to lie between the radii of 1 and 10 AU for stars like our own.

Figure 2.1 is a schematic illustration of the grid structure used. The number of vertical grid points, N_z, increases with radius to map out the prescribed flaring of the disk as has been observed from various SEDs (see Chiang & Goldreich 1997). For simplicity, vertical-mixing is ignored and only radial accretion is assumed since most of the disk mass resides at the midplane (a thin-disk approximation; see Ilgner et al. 2004). This translates to the vertical grid point step–size, Δz, remaining constant at each radius, which differs from the more common cases of scale–height–based Lagrangian accretion simulations discussed in Ilgner et al. (2004), and used in recent models such as Nomura et al. (2009), Willacy & Woods (2009) and Walsh et al. (2010, 2012). In these cases, Δz reduces with decreasing radius such that N_z remains constant. The advantage there is that one is able to analyze the vertical chemical distribution in more detail at low disk radii compared to the thin-disk approximation, but has the disadvantage of requiring greater computational power and time. The simulations undertaken in this work strike a sufficient balance between detail and computational speed.

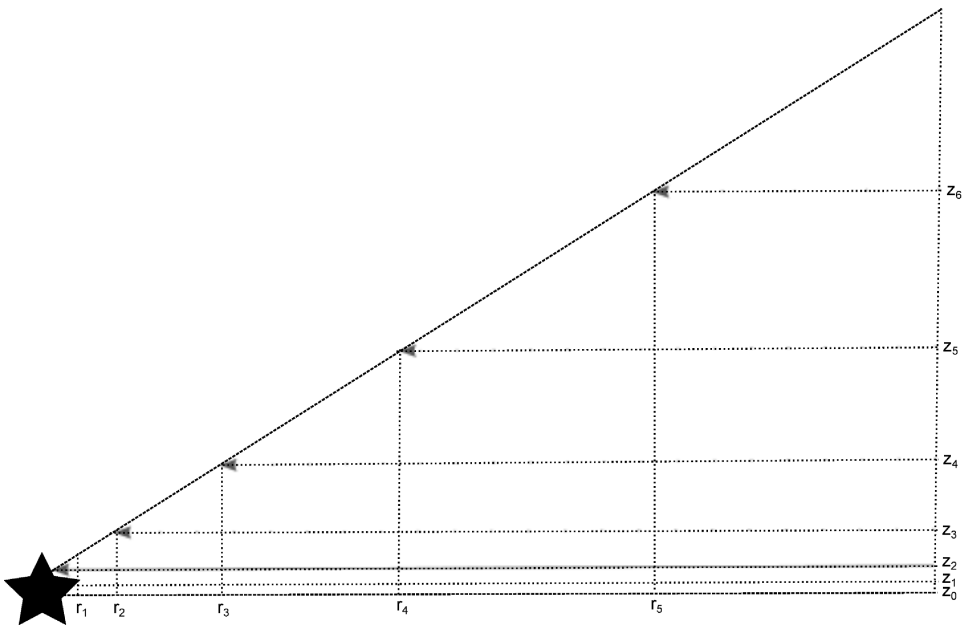

Figure 2.1: Schematic depicting the grid distribution (not to scale). The radial grid point step size, Δr, between a point (r_n, z_n) and (r_{n+1}, z_{n+1}) increases with radius and is identical for all heights at a given value. The same is true for the vertical grid point step size, Δz. The arrows indicate the direction of simulated accretion along lines of constant z since there is no vertical component of the accretion flow. A simulation begins at r = 25 AU and finishes at r = 1 AU.

2.3.2 Heating processes

Two sources of heating are considered; viscous dissipation from the midplane, and stellar radiation from the T Tauri star. Each is discussed in turn. X-ray heating is *not* considered in this model or thesis.

2.3.2.1 Viscous dissipation

In chapter 1, the idea of turbulence as an intrinsic process in the disk, and its justification for allowing stellar accretion was summarized. Turbulence in MRI regions

is thought to generate intrinsic heat known as viscous dissipation, which warms the surrounding medium. The turbulence modelled here, as in Nomura (2002), is quantified according to the α-viscous model, first discussed in Shakura & Sunyaev (1973). The resulting heating rate due to viscous dissipation, $Q_{\rm vis}$, is:

$$Q_{\rm vis} = \frac{9}{4}\Sigma\alpha c_{\rm s}^2\Omega, \tag{2.1}$$

where Σ is the gas surface density at a particular disk radius r (see Section 2.3.3), α is the viscosity parameter set to 0.01 for both 10^{-7} $M_\odot$ yr^{-1} and 10^{-8} $M_\odot$ yr^{-1} prescriptions, $c_{\rm s}$ is the sound speed at the midplane and Ω is the rotational frequency. Heat from viscous dissipation is modelled to emanate vertically from the midplane, where densities are highest. The explicit derivation of $Q_{\rm vis}$ as a function of these parameters is shown in Appendix B.

2.3.2.2 Stellar radiation

The second source is radiative heating from the hypothetical stellar source at $r = z =$ 0 AU. Gravitational energy is released as radiation from the hypothetical stellar surface as the star contracts. Assuming the source is a black–body, the corresponding thermal heating rate is given by:

$$Q_{\rm star} = \sigma T_*^4, \tag{2.2}$$

where σ is the Stefan–Boltzmann constant, and the stellar temperature $T_* = 4000$ K as defined previously. Equations (2.1) and (2.2) together quantitatively describe the total heating rate, $Q_{\rm tot}$, which is used to calculate the temperature distribution:

$$Q_{\rm tot} = Q_{\rm vis} + Q_{\rm star} = \frac{9}{4}\Sigma\alpha c_{\rm s}^2\Omega + \sigma T_*^4. \tag{2.3}$$

The resulting energy and heating transport mechanism is purely radiative. Convective transport is not considered since this model excludes vertical mixing (Nomura 2002).

2.3.3 Vertical structure

To calculate the vertical structure of the disk, hydrostatic equilibrium is assumed in the vertical direction, given by the equation:

$$\frac{dP}{dz} = c_s^2 \frac{d\rho}{dz} = -\rho g_z, \tag{2.4}$$

where P and ρ are the pressure and density respectively, and g_z is the acceleration due to gravity in the vertical direction, itself calculated from an expression incorporating the Kepler angular velocity, $\Omega(r)$:

$$g_z = \Omega(r)^2 z = \left(\frac{GM_*}{r^3}\right)^{3/2} z. \tag{2.5}$$

The height of the disk at each radius is constrained by the minimum limit of the gas density integral in the z–direction, which is set to where the gas density reduces to 3.8×10^{-22} g cm^{-3}, the typical molecular cloud gas density (Nomura 2002).

For a given radius r, the gas column density, $\chi(z)$, is given by the integral of all gas densities at each vertical grid-point up to a height z in the vertical column:

$$\chi(z) = \int_{-z}^{+z} \rho(z)\, dz. \tag{2.6}$$

The gas surface density, $\Sigma(r)$, as in Nomura (2002) is defined as the gas column density from the midplane up to the disk surface, z_∞:

$$\sum(r) = \int_0^{z_\infty} \rho(z)\, dz, \tag{2.7}$$

(noting that in other models, surface density is usually calculated from $+z_\infty$ to $-z_\infty$, in which case Equation (2.1) would contain a constant of $\frac{9}{8}$ instead of $\frac{9}{4}$. This can be rectified by multiplying the surface density by 2 since the disk is considered axisymmetric). In this model, the gas surface density distribution at each radial grid point is established by firstly equating the gravitational energy of accreting mass to the heating process from viscous dissipation (i.e. conservation of energy):

$$\frac{3GM_*\dot{M}}{8\pi r^3}\left[1 - \left(\frac{R_*}{r}\right)^{1/2}\right] = \frac{9}{4}\Sigma\alpha c_s^2\Omega, \tag{2.8}$$

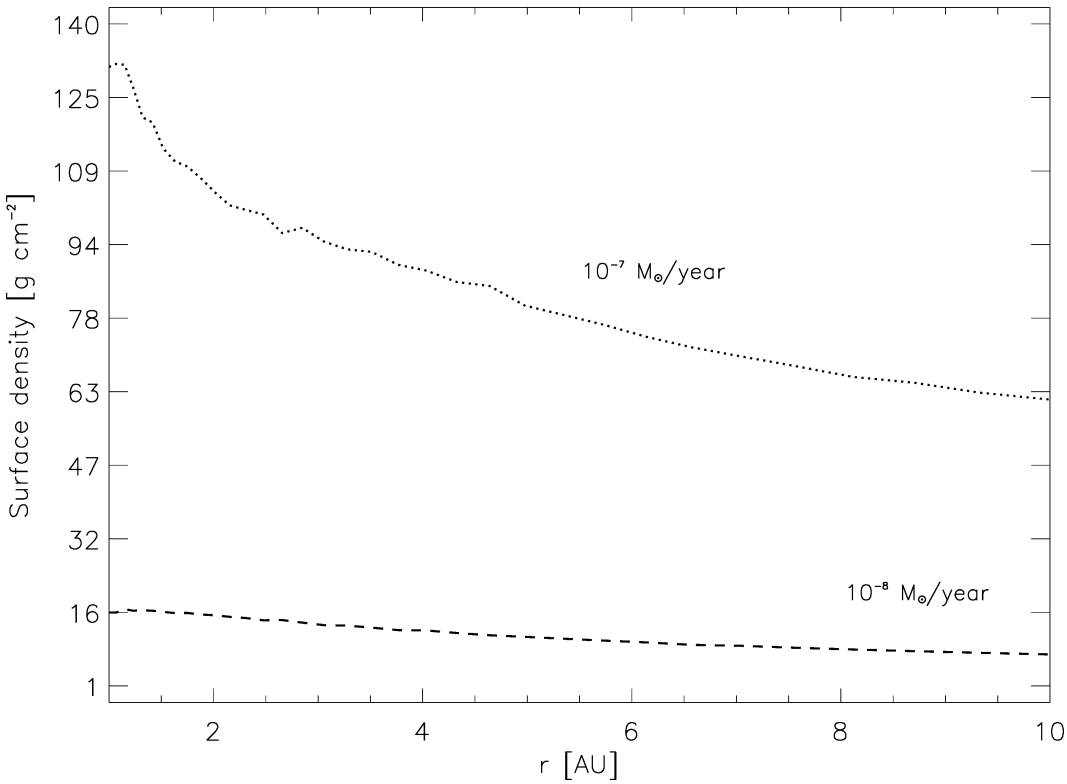

Figure 2.2: Surface density profiles for both 10^{-7} $M_\odot$ yr^{-1} and 10^{-8} $M_\odot$ yr^{-1} modelled disks.

where $\dot{M}$ is the stellar accretion rate and G is the gravitational constant (Millar et al. 2003), and secondly rearranging in terms of Σ:

$$\Sigma = \frac{1}{6}\frac{GM_*\dot{M}}{\pi r^3 \alpha c_s^2 \Omega}\left[1 - \left(\frac{R_*}{r}\right)^{1/2}\right] \quad \text{gcm}^{-2}. \tag{2.9}$$

This is derived in Appendix B. Figure 2.2 shows the resulting surface density distributions for two stellar accretion rates considered, between the radii of 1 and 10 AU (it must be noted that the author of Nomura (2002) incorrectly stated that their surface density distribution was based on the MMSN, when in reality Equation (2.9) was followed as correctly interpreted in Millar et al. (2003) (H. Nomura; private communication)).

The surface density distributions of this model are lower than other models which consider either 10^{-7} $M_\odot$ yr^{-1} or 10^{-8} $M_\odot$ yr^{-1}. Models that incorporate the

D'Alessio, Lynden-Bell & Pringle and Nomura & Millar physical prescriptions in Table 2.1 (labelled "D", "A" and "NM" in the Physics column) follow the same distribution as in Equation (2.9), and in most cases a 10^{-8} $M_\odot$ yr^{-1} disk. At a radius of 1 AU, these models achieve a surface density of $\sim$ 100 g cm^{-2} as opposed to just 17 g cm^{-2} in this model, and at 10 AU their values are $\sim$ 30 g cm^{-2}, larger than $\sim$ 8 g cm^{-2} here. Those that follow the Minimum-Mass Solar Nebula prescription (MMSN) (labelled "H" in Physics column and discussed in Sections 3.2.1 and 3.5.2.5 of this thesis) achieve even higher surface density values $\sim$ 1700 g cm^{-2} at a radius of 1 AU (see Fig. 7 in D'Alessio et al. 1998 for a comparison between the MMSN and Equation (2.9) prescription) in both 10^{-7} $M_\odot$ yr^{-1} and 10^{-8} $M_\odot$ yr^{-1} models. A comparison between the MMSN model and the 10^{-7} $M_\odot$ yr^{-1} disk is revisited in Chapter 3.

2.3.4 Radiative equilibrium and transfer

This model considers stellar UV radiation as the main external heating source. The extent of photon propagation through the disk is determined by the opacity values of the modelled gas and dust distribution. Some models (e.g. Willacy & Woods 2009) assume that the gas and dust are completely decoupled in their thermal nature (i.e. by following different temperature distributions). The model here assumes that they have the same temperature distribution over the entire disk (i.e. $T_{\rm gas} = T_{\rm dust}$). For simplicity, dust grains in both stellar accretion rate prescriptions are fixed at a diameter of 0.4×10^{-6} m, or 0.4 microns, with a gas–to–dust ratio of 0.01. Dust is assumed to evaporate into its constituent chemical components such as C, H_2O and Si, specifically in the $T > 2300$ K regions of this model (Nomura 2002). But since these temperatures are only reached once inside the minimum 1 AU radius ($r \sim 0.1$ AU) dust is inferred to coexist and be well-mixed with the gas.

Both the gas and dust absorption properties in the model are quantitatively defined by the monochromatic dust absorption opacity, κ_ν (see Eqs. 15a – 19 in Adams

& Shu 1985), and

$$\frac{1}{\kappa_{\mathrm{R}}} \equiv \frac{\int_0^\infty \frac{1}{\kappa_\nu}\frac{\partial B_\nu}{\partial T}\, d\nu}{\int_0^\infty \frac{\partial B_\nu}{\partial T}\, d\nu}, \tag{2.10}$$

for the gas opacity, equal to the Rosseland mean opacity, κ_{R}, which, in terms of gas density ρ and temperature T as determined in Bell & Lin (1994) becomes:

$$\kappa_{\mathrm{R}} = \kappa_i \rho^a T^b, \tag{2.11}$$

where κ_i, a and b are values associated with the eight known second-order states of gas (see Nomura 2002). Radiative scattering is omitted for simplicity.

The two heating rates defined in Section 2.3.2 are functions of respective "source" temperatures, which are used to determine the temperature and density distributions of the model. The stellar temperature, T_* is fixed at 4000 K. But since the source of viscous heating is located at the disk midplane, the sound speed and corresponding viscous temperature, T_{vis}, are functions of disk radius. Radiative equilibrium, where all emitted and absorbed radiation is balanced, is assumed at all points in the disk. The equation is given by:

$$4\pi \int_0^\infty \kappa_\nu B_\nu(T(r,\Theta)d\nu = \int_0^\infty \kappa_\nu J_\nu(r,\Theta)d\nu, \tag{2.12}$$

where ν is the photon frequency, B_ν is the Planck function, and J_ν is a result of integrating the total mean specific intensity, I_ν over all solid angles:

$$J_\nu(r,\Theta) = \frac{1}{4\pi}\int_0^{2\pi}\int_{-1}^{1} I_\nu(r,\Theta,\mu,\phi)d\mu d\phi. \tag{2.13}$$

The various angular definitions are given in Section 2.3 of Nomura (2002) and Appendix C of this thesis. I_ν (and therefore J_ν) is then calculated via the two-dimensional radiative transfer equation. If one assumes a path length, s, for a ray propagating from a radiative source to a point in the disk, then:

$$\frac{dI_\nu}{ds} = \rho\kappa_\nu(S_\nu - I_\nu), \tag{2.14}$$

where S_ν is the specific source function. I_ν is itself calculated from the sum of three specific intensity components:

$$I_\nu = I_\nu^* + I_\nu^{\rm vis} + I_\nu^{\rm th}, \tag{2.15}$$

where I_ν^* and $I_\nu^{\rm vis}$ represent, respectively, the specific intensity of radiation from the stellar source, and the viscous dissipation process at the midplane of the disk. The third term represents the specific intensity of thermal dust grain emission (Nomura 2002). The reader is referred to Section 2.3 of Nomura (2002) and Appendix C for the equations of each component in terms of source temperature, κ_ν and B_ν by utilizing a spherical coordinate system adopted to describe the radiation field. The resulting calculations of the density and temperature distributions are solved self-consistently with Equation (2.12) for the disk, and is explained in Appendix AI of Nomura (2002). Briefly, I_ν is calculated at each grid point by means of a derived "short-characteristics" solving method involving Equation (2.14) (see Dullemond & Turolla 2000, and Appendix A2 in Nomura 2002). The temperature at each grid point is then estimated via the Newton-Raphson iteration method. Finally the density distribution is calculated by inserting the iterated temperature values. The resulting density and temperature distributions are discussed in the following section.

2.3.5 Density and temperature distribution

Figure 2.3 shows the density and temperature distributions of both 10^{-7} $M_\odot$ yr^{-1} and 10^{-8} $M_\odot$ yr^{-1} disks from a number of perspectives. The 10^{-7} $M_\odot$ yr^{-1} disk is generally warmer, more dense and optically thick than the 10^{-8} $M_\odot$ yr^{-1} disk. The 10^{-7} $M_\odot$ yr^{-1} disk is more flared since its outer surface region is more intensely irradiated from the denser inner region (Nomura 2002). Temperatures for both disks range from as low as $\sim$ 10 K for $r \geq 5$ AU at the midplane, to $\sim$ 1100 K and 560 K at the 10^{-7} $M_\odot$ yr^{-1} and 10^{-8} $M_\odot$ yr^{-1} disk surface respectively, due to direct irradiation

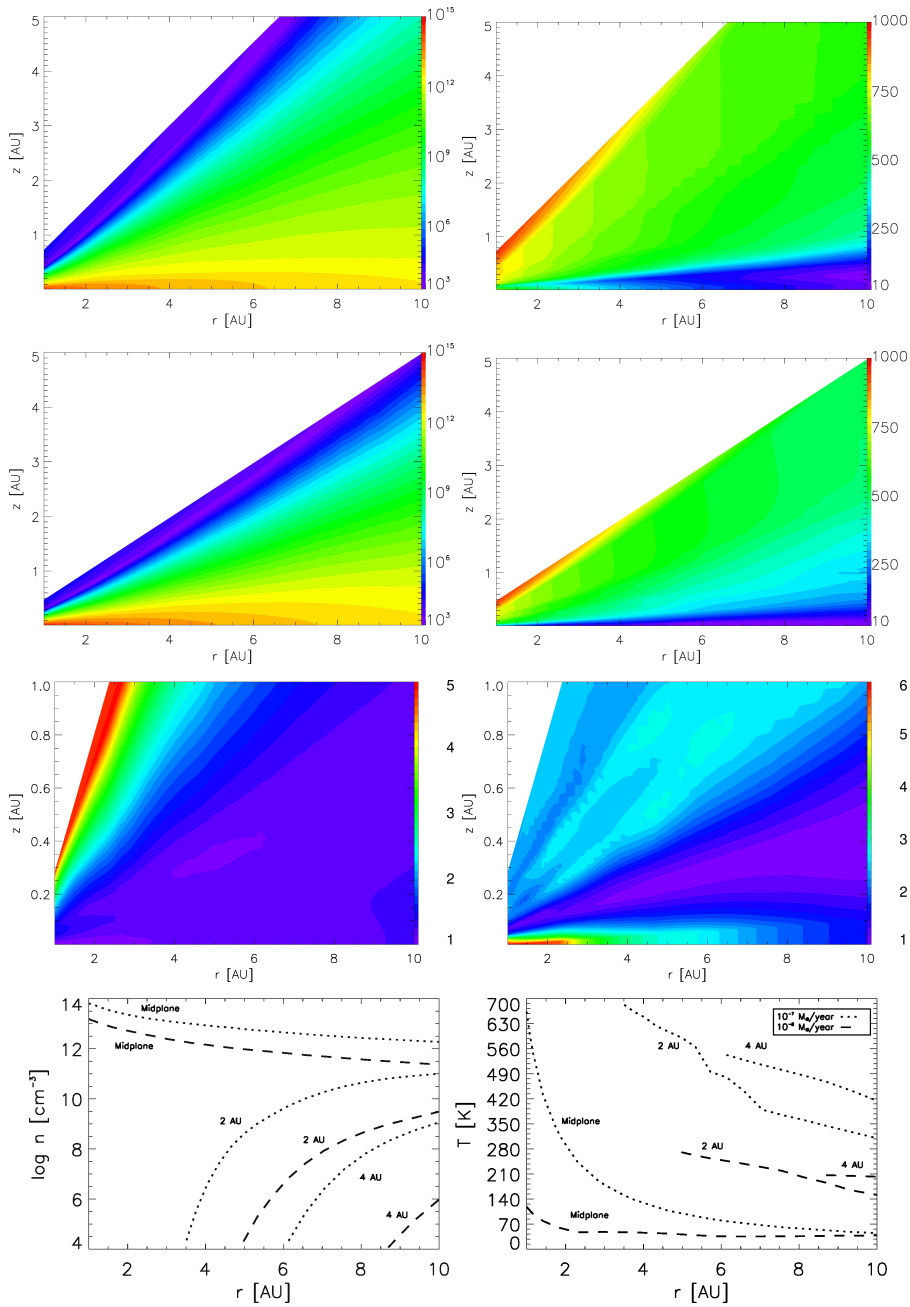

Figure 2.3: Number density in cm^{-3} (left column) and gas temperature in K (right column) as functions of disk radius and height, for models assuming a mass accretion rate of 10^{-7} $M_\odot$ yr^{-1} (1st row) and 10^{-8} $M_\odot$ yr^{-1} (2nd row). The third row shows 10^{-7} $M_\odot$ yr^{-1} / 10^{-8} $M_\odot$ yr^{-1} number density sensitivity with logarithmic scale (left) and temperature sensitivity with linear factor scale (right). The bottom row shows number density (left) and temperature (right) isoheight profiles at the midplane (z = 0 AU), 2 AU and 4 AU.

from the central star (Millar et al. 2003). Viscous heating is more significant in the $r \sim 1 - 2$ AU 10^{-7} $M_\odot$ yr^{-1} midplane region, reaching 663 K; in contrast to 180 K in the 10^{-8} $M_\odot$ yr^{-1} disk.

2.3.6 Accretion time

Chapter 1 highlighted the importance of accretion in PPDs and overviewed turbulence from MRI as a viable mode of angular momentum transport which paves the way for accretion to occur. A derivation of the stellar mass accretion rate, $\dot{M}$, as a function of parameters such as the surface density, Σ, and the viscosity parameter, α, for a gas parcel migrating radially inward in "steady" modelled protoplanetary disk (in hydrostatic equilibrium) such as this one, is shown in Appendix B. Briefly, the expression as derived in Pringle (1981) is given by:

$$\dot{M} = 2\pi R \,.\, \Sigma \,.\, v_{\mathrm{R}} \quad \mathrm{M_\odot yr^{-1}}, \tag{2.16}$$

where R is the disk radius and v_{R} is the accretion velocity at a radius R, usually expressed in units of cm s^{-1}. Note that v_{R} is a negative value by definition, but this is omitted here for simplicity. Assuming that the accretion rate at each radial grid point is consistent with the stellar accretion rate, then the accretion time, τ_{R}, taken for a gas parcel to migrate from an outer disk radius R with surface density Σ, to an inner disk radius R' can be approximated by:

$$\tau_R(R) \sim \frac{\Delta R}{v_R} \sim \frac{2\pi R \Delta R \Sigma(R)}{\dot{M}} \quad \mathrm{yr}, \tag{2.17}$$

where $\Delta R = R$ - R'. Values of τ_R are then calculated for all 57 radial grid points between 1 and 25 AU, for both 10^{-7} $M_\odot$ yr^{-1} and 10^{-8} $M_\odot$ yr^{-1} modelled disks. A total timescale is calculated by summing over all individual accretion times for all radial grid points. A parcel beginning at a radius of 25 AU (the starting point), will be accreted to 1 AU in 1.78×10^5 years for the 10^{-7} $M_\odot$ yr^{-1} disk, and 1.81×10^5 years for the 10^{-8} $M_\odot$ yr^{-1} disk. Since the focus in this thesis is between 10 and 1

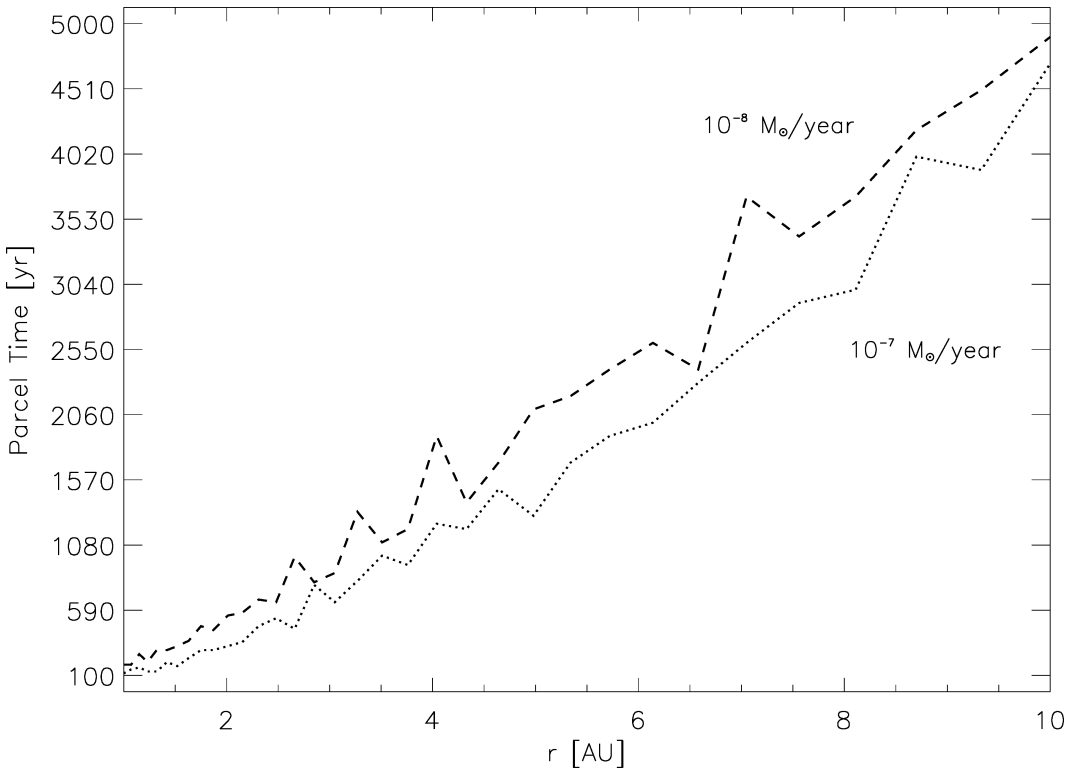

Figure 2.4: Parcel accretion time profiles as calculated from Equation (2.2) for both 10^{-7} $M_\odot$ yr^{-1} and 10^{-8} $M_\odot$ yr^{-1} modelled disks.

AU (i.e. 34 radial grid points), the durations are 4.24×10^4 years and 5.28×10^4 years respectively. This is equivalent to an average accretion velocity, $v_{\rm av}$, of 64 cm s^{-1} in the 10^{-7} $M_\odot$ yr^{-1} disk and 63 cm s^{-1} in the 10^{-8} $M_\odot$ yr^{-1} disk. Willacy & Woods (2009) and Nomura et al. (2009) both estimate $v_{\rm av} \sim 40$ cm s^{-1} in their 10^{-8} $M_\odot$ yr^{-1} $\alpha = 0.01$ disk models; some $\sim \frac{1}{3}$ slower, due to their larger surface density distributions. Figure 2.4 depicts the accretion time profiles, whilst Table 2.2 presents the accretion times at each radial grid point, between the radii of 1 and 10 AU, as calculated from Equation (2.17).

Table 2.2: Time duration values for a gas parcel at each radial grid point between 1 and 10 AU, for both stellar accretion rate prescriptions.

Radial grid point	Radius (AU)	10^{-7} $M_\odot$ yr^{-1}		10^{-8} $M_\odot$ yr^{-1}	
		Time (yr)	No.vert grid points	Time (yr)	No.vert grid points
1	1.00	1.16(02)	54	1.81(02)	49
2	1.07	1.44(02)	56	1.80(02)	50
3	1.15	1.60(02)	57	2.60(02)	52
4	1.23	1.30(02)	58	2.00(02)	53
5	1.32	1.30(02)	59	2.90(02)	54
6	1.42	2.00(02)	61	2.90(02)	55
7	1.52	1.70(02)	62	3.20(02)	57
8	1.63	2.30(02)	63	3.60(02)	58
9	1.75	2.90(02)	65	4.70(02)	59
10	1.87	2.90(02)	66	4.40(02)	60
11	2.01	3.20(02)	67	5.50(02)	62
12	2.15	3.50(02)	68	5.70(02)	63
13	2.31	4.70(02)	70	6.70(02)	64
14	2.48	5.30(02)	71	6.50(02)	65
15	2.66	4.50(02)	72	9.90(02)	67
16	2.85	7.80(02)	74	8.00(02)	68
17	3.05	6.50(02)	75	8.70(02)	69
18	3.27	8.10(02)	76	1.33(03)	70
19	3.51	1.00(03)	77	1.10(03)	71
20	3.76	9.30(02)	79	1.20(03)	73
21	4.04	1.24(03)	80	1.90(03)	74
22	4.33	1.20(03)	81	1.40(03)	75
23	4.64	1.50(03)	82	1.70(03)	76
24	4.98	1.30(03)	84	2.10(03)	78
25	5.34	1.70(03)	85	2.20(03)	79
26	5.72	1.90(03)	86	2.40(03)	80
27	6.14	2.00(03)	87	2.60(03)	81
28	6.58	2.30(03)	89	2.40(03)	82
29	7.05	2.60(03)	90	3.70(03)	84
30	7.56	2.90(03)	91	3.40(03)	85
31	8.11	3.00(03)	93	3.70(03)	86
32	8.70	4.00(03)	94	4.20(03)	87
33	9.33	3.00(03)	95	4.50(03)	89
34	10.0	4.70(03)	96	4.90(03)	90

2.4 Chemical model

A chemical network consists of one or more files containing lists of chemical reactions known to occur between a given species and others. Each listed reaction has associated values (usually related to molecular binding energies or activation temperatures) which are used to calculate the rate of the chemical reaction, known as a rate coefficient, k, usually expressed in units of cm^{-3} s^{-1}. The larger the k value associated with a given reaction, the more rapid the reaction. Chemical evolution in protoplanetary disks is governed by a complex combination of reaction types. Typical k values for reactions which are known to occur are shown in Table 2.3. The chemical model adopted in this thesis consists firstly of a network of

Table 2.3: Typical gas-phase reaction types occurring in interstellar environments and protoplanetary disks. Radiative dissociation is also known as photodissociation.

Reaction type	Equation	Typical k values (cm^3s^{-1})
Neutral-neutral	$A+BC \rightarrow AB+C$	10^{-17}
Ion-neutral	$A^+ + BC \rightarrow AB^+ + C$	10^{-15}
Charge exchange	$A^+ + BC \rightarrow A + BC^+$	10^{-9}
Dissociative recombination	$AB^+ + e^- \rightarrow A+B$	$\sim 10^{-13}$
Radiative dissociation	$AB + h\nu \rightarrow A+B$	10^{-12}
Radiative recombination	$A^+ + e^- \rightarrow A + h\nu$	10^{-18}
Radiative association	$A+B \rightarrow AB + h\nu$	10^{-17}
Cosmic-ray ionization	$A + c.r \rightarrow A^+ + e^-$	10^{-17}

gas-phase species and their reactions taken from the Rate95 version of the UMIST database initially provided by Andrew Markwick (private communication). To this, a deuterated network is added whose rate coefficients are taken from Roberts & Millar (2000b) and Roberts et al. (2002b), also provided by Andrew Markwick (private communication). Reactions include two-body neutral-neutral and ion-neutral

reactions, UV and cosmic-ray photochemistry, and cosmic-ray particle ionization. These are discussed in Section 2.4.1. Secondly, gas-grain interactions are included, which involve the processes of thermal desorption of species into the gas-phase from grains, adsorption freeze-out from the gas onto the grain, and dissociative recombination of atomic and molecular cations on grain-surfaces. This is discussed in Section 2.4.2.

2.4.1 Gas-phase network

The gas-phase chemistry in this model is gathered from a reduced version of the Rate95 network (Millar et al. 1997). This consists of a 3894 gas-phase reaction coefficients, involving 395 chemical species, comprised of 7 elements: H, He, C, N, O, S and Fe. Fluorine (F), phosphorus (P), sodium (Na) and magnesium (Mg) are all omitted to reduce computational time. The rate coefficients are calculated from a subset of α, β and γ coefficients and these vary in value and definition depending on the chemical reaction type.

2.4.1.1 Rate coefficient calculations

The reactions in the data file are written in the form:

$$\mathrm{R1, R2, P1, P2, P3}, \alpha, \beta, \gamma$$

where R1 and R2 are the reactants, and P1, P2 and P3 are the products. The following paragraph briefly describes the equations used to calculate the rate coefficients for: (i) two-body gas-phase reactions, (ii) cosmic ray particle ionization (R2 = CRP), (iii) cosmic ray-induced photoreactions (R2 = CRPHOT) and (iv) UV photoreactions (R2 = PHOT), all considered in this chemical model:

(i) Two-body reactions between gas-phase species usually result in two products, e.g.

$$H_2 + OH \longrightarrow H_2O + H,$$

but some result in just one,

$$H^+ + e^- \longrightarrow H,$$

or even three,

$$He^+ + OH \longrightarrow O^+ + H + He.$$

For two-body reactions (R1, R2 = species X, species Y),

$$k = \alpha \left(\frac{T}{300}\right)^{\beta} \exp - \left(\frac{\gamma}{T}\right) \quad \mathrm{cm^3 s^{-1}}, \tag{2.18}$$

where α is the average binding or activation energy required for the reaction to occur, T is the gas temperature, β is a power law value assigned to T, and γ the probability that a given photon will influence the reaction taking place, usually per cosmic ray ionization rate.

(ii) Cosmic ray ionization in the form of high–energy particles, e.g.

$$O + CRP \longrightarrow O^+ + e^-,$$

$$k = \alpha \quad \mathrm{s^{-1}}, \tag{2.19}$$

where α is the cosmic ray ionization rate, set to the canonical value of 1.3×10^{-17} $\mathrm{s^{-1}}$ with respect to H_2. (iii) Cosmic ray induced photoreactions, e.g.

$$C_4H_2 + CRPHOT \longrightarrow C_4H + H,$$

$$k = \alpha \left(\frac{T}{300}\right)^{\beta} \frac{\gamma}{(1-\omega)} \quad \mathrm{s^{-1}}. \tag{2.20}$$

where α, T and γ have the same meanings, and ω represents the dust-grain albedo, set to equal 0.6 (e.g. Woodall et al. 2007). (iv) Photoreactions due to the interstellar UV field, e.g.

$$CH_2 + PHOTON \longrightarrow CH + H,$$

$$k = \alpha' \exp - (\gamma' A_v) \quad \mathrm{s}^{-1}, \tag{2.21}$$

where α' is the ionization rate in the unshielded interstellar UV field, γ' a parameter used to take into account the extinction of dust at UV wavelengths (Woodall et al. 2007) and A_v is the extinction at visible wavelengths by interstellar dust, per total H nuclei ($\sim 2n[\mathrm{H_2}]$) at a given grid point, calculated from:

$$A_v = \frac{\tau}{3 \times 10^{21}} \quad \mathrm{mag}, \tag{2.22}$$

where τ is the optical depth.

2.4.1.2 Deuterated species

Deuterated species, which consist of heavier forms of hydrogen by housing a proton and neutron in the nucleus, have been known to exist in the interstellar medium for quite some time. They act as interesting tracers in the ISM since molecular $\frac{\mathrm{D}}{\mathrm{H}}$ abundance ratios are found to be higher (e.g. $\sim 10^{-2}$ in TMC-1) than the cosmic, atomic $\frac{\mathrm{D}}{\mathrm{H}}$ ratio, $\sim 1.5 \times 10^{-5}$, due in principle to zero-point energy differences between the forward and reverse reactions of the following cations with HD, in low $T \sim 10 - 100$ K environments:

$$\mathrm{H_3}^+ + \mathrm{HD} \Longleftrightarrow \mathrm{H_2D}^+ + \mathrm{H_2},$$
$$\mathrm{CH_3}^+ + \mathrm{HD} \Longleftrightarrow \mathrm{CH_2D}^+ + \mathrm{H_2},$$
$$\mathrm{C_2H_2}^+ + \mathrm{HD} \Longleftrightarrow \mathrm{C_2HD}^+ + \mathrm{H_2}.$$

This is discussed in Roberts & Millar (2000a), Roberts & Millar (2000b) and Roberts et al. (2002b). The rate coefficients used in this model are taken from Roberts & Millar (2000b) (e.g. Table 1, p2). The rate coefficient for forward reactions is given by:

$$k = \alpha \left(\frac{T}{300}\right)^{\beta} \quad \mathrm{cm^3 s^{-1}}, \tag{2.23}$$

whereas for reverse reactions:

$$k = \alpha \left(\frac{T}{300}\right)^{\beta} \exp\left(-\frac{\gamma}{T}\right) \quad \mathrm{cm^3 s^{-1}}, \tag{2.24}$$

where all terms have the same definitions as those in the gas-phase rate coefficient equation (Equation 2.18) in Section 2.4.1.1. This model incorporates around 7000 reactions involving deuterated species, including these three forward and reverse reactions.

2.4.2 Gas-grain interaction

In cold ($T \sim 10$ K) and dense ($n \sim 10^{15}$ cm^{-3}) environments, species in the gas-phase can freeze onto the surfaces of larger-sized dust grains. Grains can act as mediators for transporting complex chemistry from outer to inner PPD regions which would otherwise be destroyed in gas-phase chemical reactions. At the same time, they also act as catalysts for dissociative surface recombination of cations, and enable surface reactions such as chemisorption and physisorption to occur. The exact composition of dust grains is debated; popular candidates are silicates such as olivine, graphite and amorphous carbon (e.g. Adams & Shu 1985).Two gas-grain interaction processes are included in the chemical model, provided and implemented by Andrew Markwick (private communication). The first is thermal desorption, i.e.

$$\text{A-grain} \longrightarrow \text{A (gas)}.$$

where grains are heated to the point where the molecule escapes into the gas. The extent of thermal desorption from grain surfaces is dependent on a species' molecular binding energy, E_{D}, usually given in units of K, the temperature of the environment, and the molecule's mass. The thermal desorption (or evaporation) rate, k_{evap}, as in Watson (1976), Tielens & Hagen (1982) and Tielens & Allamandola (1987), used in this model is given by:

$$k_{\mathrm{evap}} = \nu_0 \exp\left(\frac{-E_{\mathrm{D}}(T)}{T_{\mathrm{grain}}}\right) \quad \mathrm{s}^{-1}, \tag{2.25}$$

where ν_0 is the characteristic adsorbate vibrational frequency (s^{-1}) established from the harmonic oscillator expression given in Hasegawa et al. (1992):

$$\nu_0 = \left(\frac{2n_s E_D}{\pi^2 m}\right)^{1/2} \quad s^{-1}, \tag{2.26}$$

where n_s is the surface density of sites on grains (1.5×10^{-15} cm^{-2}), E_D the adsorption binding energy for a given species in K, T_{grain} the grain temperature (= T_{gas}) and m the species mass. Other methods of ν_0 evaluation are discussed in Tielens & Allamandola (1987).

The second considered process is adsorptive freeze-out, i.e.

$$\text{A (gas) + grain} \longrightarrow \text{A-grain},$$

which also includes dissociative surface recombination for ions, i.e.

$$\text{AB}^+ \text{ (gas)} \longrightarrow \text{A-grain + B-grain}.$$

Freeze-out is additionally dependent on the density and cross-sectional area of grains. In this model it is assumed that grains are negatively charged, and therefore act as a sink for cations in the gas (e.g. Umebayashi & Nakano 1980, 1981; Semenov et al. 2004; Walsh et al. 2012). The freeze-out rate, k_{freeze}, for a given species X, as adopted from Umebayashi & Nakano (1980) and Willacy & Woods (2009) is given by:

$$k_{freeze} = S_X C_X (\pi a^2 n_g) v_X \quad s^{-1}, \tag{2.27}$$

where the sticking coefficient, S_X, is set to equal 1.0 for all species (Hasegawa et al. 1992), a is the grain radius (0.2 μm), n_g is the number density of grains (= 1.0 $\times 10^{-2} n_{H_2}$), v_X is the root mean square of the total thermal velocity of X in three dimensions ($\sim (3k_B T/m)^{1/2}$) and C_X is given by the expression:

$$C_X = 1 + \frac{16.71 \times 10^{-4}}{aT_{grain}}, \tag{2.28}$$

as in Rawlings et al. (1992), which represents a additional factor for increasing k_{freeze}, when cations (X^+) dissociatively recombine on grains, since cations will be

more attracted to them than neutrals (Umebayashi & Nakano 1980; Markwick et al. 2002; Willacy & Woods 2009). C_X is set to 1 for neutral species.

2.4.3 Initial abundances

Chemical models of PPDs require a input list of initial chemical abundances associated with epochs prior to PPDs such as dark clouds or pre-stellar cores, in order to calculate the chemical evolution. To most accurately reflect the pre-PPD evolutionary state, the initial abundance chemistry used here (Tables 2.4 and 2.5) is taken from a pre-stellar core model provided by Andrew Markwick (private communication) and discussed in Markwick-Kemper (2005), which has been simulated for 10^6 years at a constant temperature of 10 K. As treated in Willacy & Woods (2009), the binding energies for deuterated species (Table 2.5) are set to be 21 K more than their hydrogenated equivalents, which is the zero-point energy difference (in terms of temperature) between hydrogen and deuterium atoms. The full chemical listing of the reduced network is provided in Appendix D, alongside their initial abundance values.

2.4.4 Model process

The resulting density, temperature and optical depth values are listed alongside their radial and vertical grid points in files termed rhoTM-7.dat and rhoTM-8.dat, which denote the 10^{-7} $M_\odot$ yr^{-1} and 10^{-8} $M_\odot$ yr^{-1} disks. To this, column density and surface density values were determined separately, and added to these files by the author of this thesis. For each grid point in turn, mediator codes extract physical parameters from the data files, along with the input abundances, and the rate coefficients are calculated. The resulting final chemical abundances are then calculated at each grid point. This model uses the LSODE (Livermore Solver for Ordinary Differential Equations) calculator (provided by Andrew Markwick; private communication) to

Table 2.4: List of various initial abundances in our model relative to H_2, taken from the output of a dense-core model at 10 K (Markwick-Kemper 2005), and their adsorption binding energies. Frozen species, on grain surfaces, are generally more abundant than their gaseous equivalent, because of significant freezeout by the typical age of a dark cloud (10^5 yr). As the simulated gas parcel in the disk moves inward where temperatures increase, species desorb from grain surfaces.

Species	Gas $n(x)/n_{H_2}$	Grain $n(x)/n_{H_2}$	E_D (K)	Reference
H	2.5(-11)	9.2(-17)	350	1
H_2	1	3.07(-06)	315	8
C	6.0(-12)	1.2(-16)	800	1
N	6.8(-11)	1.3(-15)	800	1
N_2	9.3(-06)	1.3(-10)	790	2
O	2.1(-10)	3.9(-15)	800	1
O_2	9.6(-12)	8.0(-16)	1210	1
S	1.4(-10)	7.8(-15)	1100	1
Fe	1.0(-08)	8.8(-08)	4200	1
HCO	1.7(-11)	4.3(-15)	1510	1
HCO^+	4.1(-15)	4.3(-15)*	–	1
CO	6.8(-05)	4.1(-08)	855	2
CO_2	2.3(-07)	5.4(-09)	2990	3
OH	2.0(-13)	2.3(-17)	1259	4
CN	6.8(-14)	1.0(-15)	1510	1
HCN	1.7(-06)	1.1(-09)	1760	1
H_2O	2.4(-05)	2.4(-03)	4800	5
H_2CO	1.9(-08)	1.2(-11)	1760	1
NH_3	4.6(-09)	4.9(-10)	2790	5
CH_4	1.4(-07)	6.97(-12)	1090	6
CH_3OH	9.4(-10)	9.6(-09)	4930	5

*HCO^+ assumes its neutral form when frozen onto grain surfaces. **References:** (1) Tielens & Allamandola (1987); (2) Öberg et al. (2005); (3) Walsh et al. (2012); (4) Allen & Robinson (1977); (5) Brown & Bolina (2007); (6) Herrero et al. (2010); (7) Sandford & Allamandola (1993); (8) Ruffle & Herbst (2000).

Table 2.5: List of various initial deuterated abundances in our model relative to H_2, taken from the output of a dense-core model at 10 K (Markwick-Kemper 2005), and their adsorption binding energies.

Species	Gas $n(x)/n_{H_2}$	Grain $n(x)/n_{H_2}$	E_D (K)
D	1.6(-15)	5.4(-21)	621
D_2	1.9(-06)	1.0(-11)	357
HD	1.6(-05)	7.7(-11)	336
D_2O	7.5(-12)	7.7(-10)	4840
HDO	1.1(-08)	1.1(-06)	4820
DCO	2.3(-15)	5.8(-19)	1530
HDCO	4.0(-12)	2.6(-15)	1781
D_2CO	3.1(-16)	2.0(-19)	1802
CD_3OH	4.9(-19)	5.1(-18)	4993
CD_3OD	1.9(-22)	1.9(-21)	5014
CD	3.4(-21)	9.2(-24)	671
DCN	1.4(-10)	8.8(-14)	1781
NHD	4.4(-13)	1.0(-17)	881
NHD_2	5.5(-15)	5.9(-16)	2832
ND_3	9.6(-19)	1.0(-19)	2853
CD_4	7.8(-14)	4.1(-18)	1174

explicitly evaluate the reaction rate ODEs for each molecule, and thus determine their abundance at each timestep. The basic ODE expression for a given species i with abundance n_i is a sum of the rates of formation subtracted from the sum of the rates of destruction, expressed here by:

$$\frac{dn(i)}{dt} = \sum_{j,k} k_{jk} n_j n_k - \sum_{l,m,n} k_{in} n_l n_m, \tag{2.29}$$

where n_j and n_k represent the abundance of species reacting to form i, and n_l and n_m are species produced from reactions involving i and another species n. The model process results in the production of two data files for each grid point - one with a list of final calculated abundances whose format is identical to that of the initial abundance input file, and secondly a list of abundances at each timestep of each grid

point, depicting the numerical change in the chemical abundances. The latter output file is particularly useful in tracing the chemical evolution at a particular grid point under fixed physical conditions. RTOL (Relative Tolerance) and ATOL (Absolute Tolerance) values, which essentially represent the tolerances of the LSODE program iteratively calculating changes in abundances from one timestep to the next, are set to 10^{-9} and 10^{-11} respectively. Values lower than this result in a simulation which may be more accurate but takes too long to complete, whilst larger values lead to inaccuracies in results and LSODE calculation failures. The chosen values represent an adequate balance between stability, simulation time and accuracy.

2.4.4.1 Model design

Figure 2.5 depicts a summary of the major components of the model, and a describes how the model operates to simulate the accretion process from one grid point to the next. For a given grid point, the list of initial abundances (box 1), physical data for a given stellar accretion disk (box 2) and chemical network listing all included reactions (box 3) are called within a perlscript code called "make point" (box 4), which determines the rate coefficients for each reaction based on the density, temperature, optical depth and column density. This perlscript code was initially provided by Andrew Markwick (private communication), and added to by the author of this thesis to read in the vertical column and surface density, and include both a cosmic-ray attenuation expression and desorption rate (see Chapter 3).

The resultant rate coefficients, along with a list of the density, temperature and optical depth value for the current grid point extracted from the physical data file (box 6), an ODE network of the entire chemical database, and the LSODE package[1] (boxes 7 and 8 respectively, both written in Fortran and provided by Andrew Markwick) are called into a master Fortran script "disk.f" (provided by Andrew Markwick) which computes the chemical evolution over a number of assigned time

[1] Hindmarsh et al. (1983)

steps. This produces the two output files, “evol.dat” (box 9) and “output.dat” (box 10), which are both duplicated and one copy renamed to represent the grid point just calculated. The calculation is repeated for each grid point in the disk, and calculations along the same height and next radial grid point in, use the output abundances from the previous radial grid point out, as input. In this way, accretion is modelled from the outer r = 25 AU disk to the inner r = 1 AU disk.

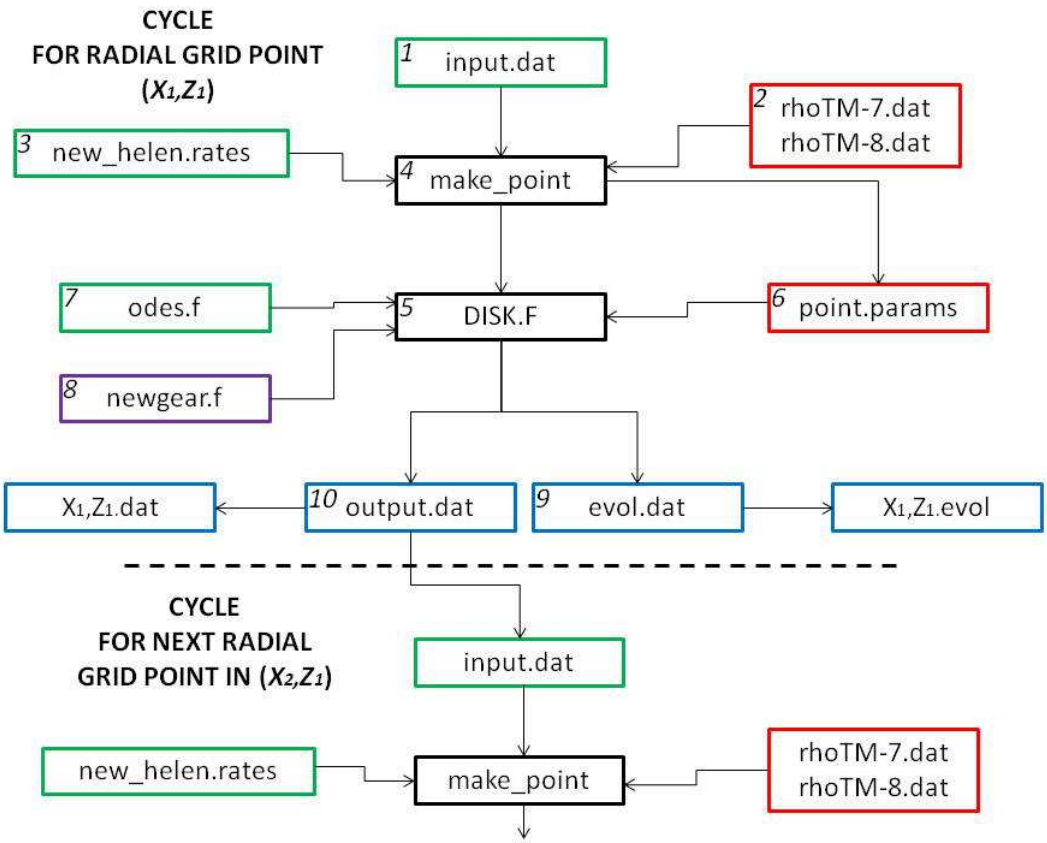

Figure 2.5: Flow chart depicting the major components of the model accretion process.

2.4.4.2 Modelling the calculation time

Figure 2.6 presents a schematic of the full calculation process over the entire disk grid. Once the accretion time has elapsed over the entire grid, an additional calcu-

lation time is added to each grid point until every point has been run for the same length of time. Since accretion times decrease with radius, more isolated calculation time is added to decreasing radial grid points. The 10^{-7} $M_\odot$ yr^{-1} and 10^{-8} $M_\odot$ yr^{-1} accretion disks are chosen to be calculated up to a time of 1.78×10^5 and 1.81×10^5 years respectively, which represent the times taken for the gas to accrete from a radius of 25 AU to inside 1 AU. The chemical results presented in Chapters 3 and 4 thus represent states of the disk snapshot in time at 1.78×10^5 and 1.81×10^5 years; the exception being Section 4.5, which re-evaluates the calculation time in accordance with observations.

2.5 Summary

In this chapter, the physical and chemical components of an uncoupled 1+1D protoplanetary disk model has been described, involving the disk structures of two stellar accretion rates: 10^{-7} $M_\odot$ yr^{-1} and 10^{-8} $M_\odot$ yr^{-1}. The physical model is taken from Nomura (2002). The physical structures resemble an axisymmetric disk surrounding a typical T Tauri star with parameters $M_* = 0.5\ M_\odot$, radius $R_* = 2\ R_\odot$ and $T_* =$ 4000 K. Two heating sources are considered: stellar heating, and viscous dissipation from the midplane. The physical model is flared and radial accretion is assumed according to the thin-disk approximation (see Ilgner et al. 2004). Figure 2.7 displays a summary of the disk processes considered in this model. The α-viscous parameter of 0.01 is adopted, and the density and temperature distributions (Figure 2.3) are iteratively calculated from the two-dimensional radiative transfer equation under the assumptions of hydrostatic and radiative equilibrium (see Nomura 2002). Disk gas and dust are well-mixed and assumed to have identical temperature distributions. The surface density distribution is determined by equating an expression for the gravitational energy of radially accreting mass to the expression for the viscous heating process (Equation 2.8). The two files which represent the physical model,

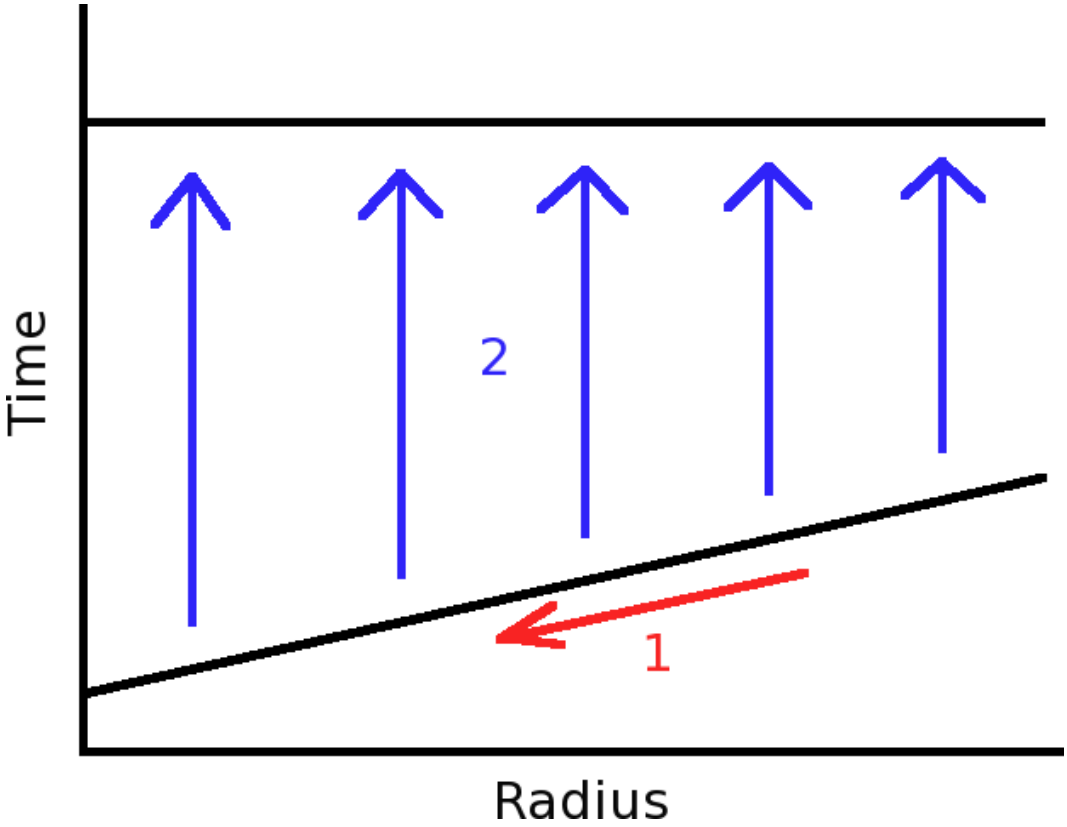

Figure 2.6: Schematic of the full calculation process over the entire disk grid. Both stellar accretion disks are initially calculated under the accretion timescales discussed in Section 2.3.6 (Phase 1). Then, for the 10^{-7} $M_\odot$ yr^{-1} accretion disk, every grid point is run in isolation for an additional time until every point has been run for a total of 1.78×10^5 years, and for the 10^{-8} $M_\odot$ yr^{-1} accretion disk, 1.81×10^5 years (Phase 2). These represent the times taken for gas to accrete from a radius of 25 AU to inside 1 AU.

rhoTM-7.dat and rhoTM-8.dat, contain data on the grid distribution and the physical parameters such as density, temperature, optical depth, vertical and horizontal column densities at each grid point.

The chemical model consists of an initial abundance file taken from a pre-stellar core model (see Markwick-Kemper 2005), and a reduced Rate95 gas-phase chemical network of 3894 gas-phase reaction coefficients, to which deuterated (Roberts &

Millar 2000a) and grain-surface species (e.g. Hasegawa et al. 1992) are added. Gas-phase reactions include two-body interaction, photo (UV) chemistry and cosmic ray ionization. The unattenuated cosmic-ray ionization rate, per H_2 molecule, is set to 1.3×10^{-17} s^{-1}. Gas-grain interactions include freeze-out and thermal desorption, and dissociative recombination of cations on grain-surfaces. In total, there are 9659 reactions.

The LSODE calculator is used to evaluate the chemical abundances from the ODEs of formation and destruction for each species at each timestep. RTOL and ATOL values of 10^{-9} and 10^{-11} respectively are used and provide a adequate balance between calculation accuracy and stability. The physical and chemical parts of the model are brought together to produce outputs of chemical abundances at each grid point.

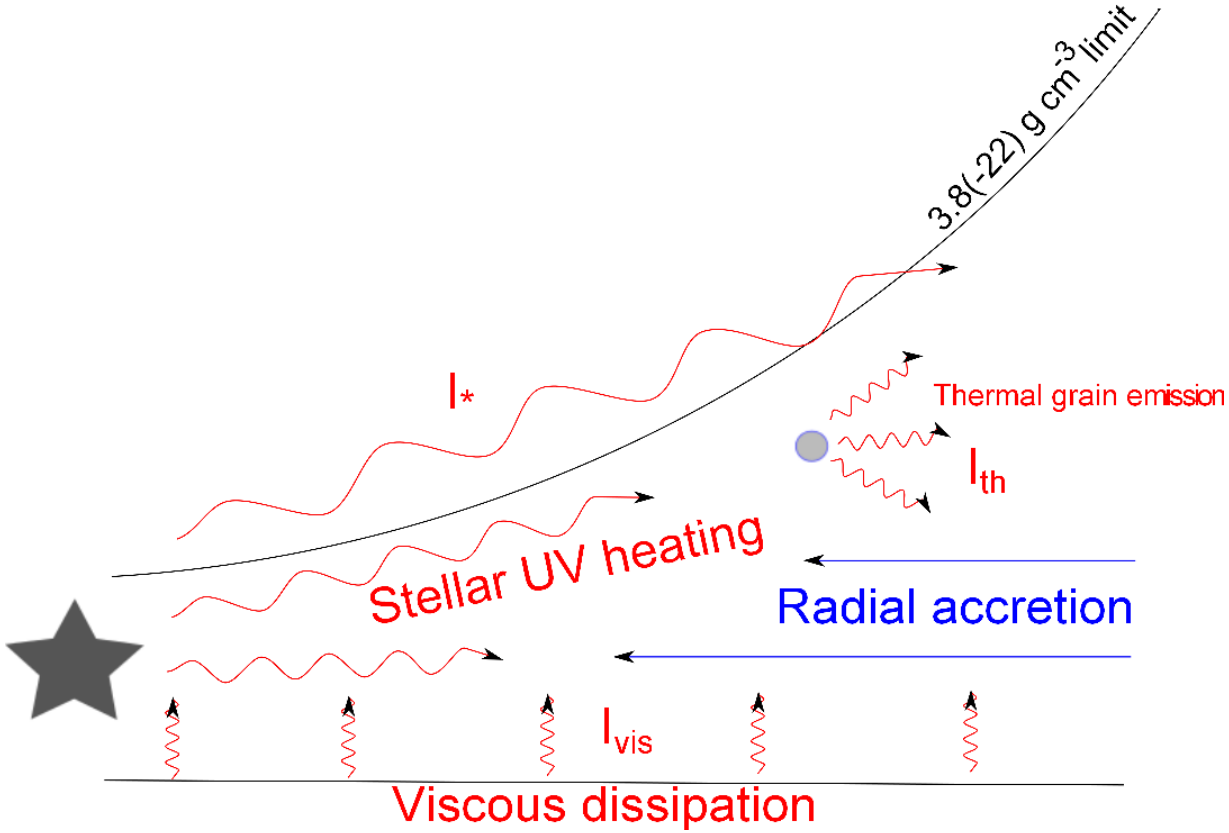

Figure 2.7: Summary of heating processes in this model.

CHAPTER 3

Ionization processes from radionuclides

3.1 Overview

The main external sources of radiation which drive ionization are stellar X-rays, UV and interstellar cosmic-rays. As Chapter 2 explained, this particular model considers specifically the chemical effects of interstellar UV, as a function of visual extinction, A_V, and cosmic–rays, as a function of ionization rate, ζ, relative to H_2. Other models also consider stellar UV and X-ray photochemistry. So far it has been unclear how much of an effect radionuclides, an internal source, had in influencing chemical processes in PPDs, amongst other potential later effects such as a source of

localized internal heating during the planetesimal era, which may have influenced the formation of the inner rocky planets in our solar system. Not only is there evidence to suggest that radionuclides were present in our own early solar system, but the most ionizing radionuclide, ^{26}Al in particular was thought to have been up to six times more abundant in our early solar system than in the local interstellar medium.

This chapter discusses the potential influence of radionuclides in this model, focusing particularly on ^{26}Al. Radionuclides are modelled in such a way as to supplement the ionization effects of cosmic–rays, thought to be the only other radiative source able to penetrate the inner midplane regions, where these heavy-element radionuclides quickly settled down to. Before assessing the effects of radionuclides in this way, one must address how the attenuation of cosmic-rays are modelled, and how they compare with UV and X-rays attenuating as they propagate through a PPD.

3.2 Attenuation of ionizing sources

The ionization potential of a source is quantitatively given by its ionization rate per second, with reference to a particular species; usually H_2. X-rays have been theoretically shown to have a significant effect on inner disk chemistry, with unattenuated ionization rates of 10^{-13} – 10^{-15} s^{-1}; more so than stellar UV (e.g. Igea & Glassgold 1999; Markwick et al. 2002). Cosmic-rays, highly energetic ($\sim$ 1 GeV) non-thermal particles consisting mainly of protons and nuclei such as Fe, have a commonly–assigned characteristic unattenuated ionization rate of 1.3×10^{-17} s^{-1}. Other cosmic-ray ionization rate values estimated in the past include 6.8×10^{-18} s^{-1} (Spitzer 1968), 4.0×10^{-18} s^{-1} (Umebayashi & Nakano 1981), 6.0×10^{-17} – 8.0×10^{-16} s^{-1} (van Dishoeck & Black 1986), 4.0×10^{-17} s^{-1} (Cecchi-Pestellini & Aiello 1992) and 2.0×10^{-17} s^{-1} (Finocchi & Gail 1997); some inferred from different regions of the interstellar medium (see Lepp 1992). Later works have generally

adopted rate values from $\sim 10^{-18}$ s^{-1} to larger values of $\sim 10^{-17}$ s^{-1} due to a poor understanding of the low part of the cosmic-ray energy spectrum.

Attenuation is usually referred to as a function of surface density, in g cm^{-2}. Although more energetic, UV and X-rays are attenuated more effectively than cosmic-rays in PPDs. Disk dust readily absorbs UV beyond surface densities of 10^{-3} g cm^{-2} (Umebayashi & Nakano 2009). X-rays in inner disk regions penetrate up to surface depths of ~ 10 g cm^{-2} (Igea & Glassgold 1999), but cosmic-rays penetrate up to much deeper depths of ~ 96 g cm^{-2}, referred to as the characteristic cosmic-ray attenuation length, $\lambda_{\rm CR}$ (Umebayashi & Nakano 1981).

It has been postulated that cosmic-rays are attenuated significantly enough to have negligible influence on ionizing gas in the inner disk midplane, or that they are even unable to penetrate at all (Igea & Glassgold 1999; Umebayashi & Nakano 2009). This is principally dependent on the surface density distribution where the surface density exceeds 96 g cm^{-2}, which varies between models.

Figure 2.3 displayed the radial surface density profiles for the 10^{-7} M$_\odot$ yr^{-1} and 10^{-8} M$_\odot$ yr^{-1} models used in this work inside a radius of 10 AU and shows that the surface density only exceeds 96 g cm^{-2} in the 10^{-7} M$_\odot$ yr^{-1} disk inside 3 AU. 10^{-8} M$_\odot$ yr^{-1} surface density values are too low for cosmic-rays to be attenuated enough to have negligible influence in ionizing chemistry, and cosmic-rays penetrate the entire inner 10^{-8} M$_\odot$ yr^{-1} disk. Therefore one concludes that attenuation is only significant in the 10^{-7} M$_\odot$ yr^{-1} disk.

Figure 3.1 shows the H_2 gas column density distribution for the 10^{-7} M$_\odot$ yr^{-1} disk. The surface contours of 10^{-3} and 10 g cm^{-2} are also shown, depicting, respectively, the approximate attenuation surfaces of UV and X-rays. The black region represents values which exceed 96 g cm^{-2}, to which cosmic-rays are attenuated.

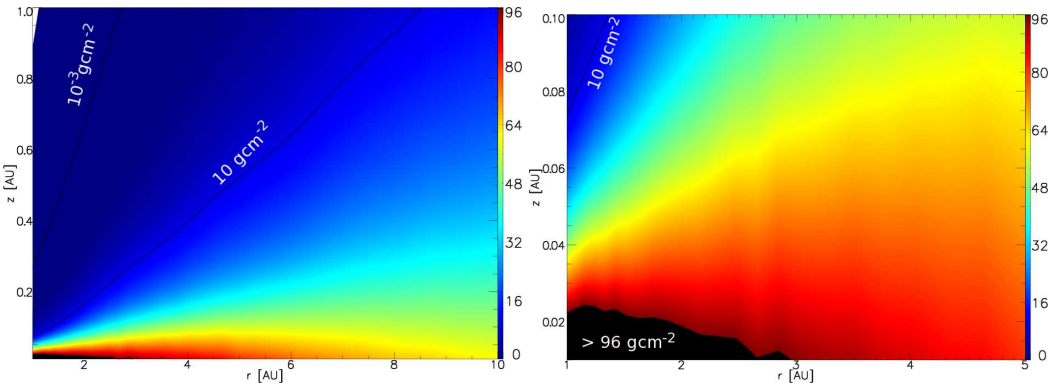

Figure 3.1: Total gas column density distributions for the 10^{-7} $M_\odot$ yr^{-1} accretion disk. The surface contours of 10^{-3} and 10 g cm^{-2} are also shown, depicting the approximate attenuation thresholds of UV and X-rays respectively. The black region represents values which exceed 96 g cm^{-2}

3.2.1 Cosmic-ray attenuation modelling

There are currently three different prescriptions of modelling cosmic–ray attenuation to be found in the literature, which all describe how an initial unattenuated cosmic-ray rate value $\zeta^0_{\rm CR}$ attenuates to a smaller value $\zeta_{\rm CR}$, as a function of radius r and height z. The first, proposed in Umebayashi & Nakano (1981) and used in Finocchi & Gail (1997) is a basic, "plane–parallel" slab approximation:

$$\zeta_{\rm CR}(r,z) = \zeta^0_{\rm CR} \exp\left(\frac{\chi(r,z)}{115}\right) + 1 \quad {\rm s}^{-1}, \tag{3.1}$$

which was originally adopted for molecular cloud modelling. The second, more popular prescription is an updated plane-parallel approximation (see Semenov et al. 2004) adapted to protoplanetary disks:

$$\zeta_{\rm CR}(r,z) = \frac{\zeta^0_{\rm CR}}{2}\left[\left(\exp\frac{(-\chi_1(r,z))}{\lambda_{\rm CR}}\right) + \left(\exp\frac{(-\chi_2(r,z))}{\lambda_{\rm CR}}\right)\right] \quad {\rm s}^{-1}. \tag{3.2}$$

These two prescriptions effectively assume cosmic–rays which are vertically incident from above and below the disk where χ is the gas column density at a radius r and height z, and χ_1 and χ_2 are above and below the point (r, z) respectively. The

third prescription is a more complex, "isotropic" approximation, originally derived in Umebayashi & Nakano (2009):

$$\begin{aligned}\zeta_{\rm CR}(r,z) &\approx \frac{\zeta^0_{\rm CR}}{2}\left\{\exp\left(-\frac{\chi(r,z)}{\lambda_{\rm CR}}\right)\right\}\left[1+\left(\frac{\chi(r,z)}{\lambda_{\rm CR}}\right)^{3/4}\right]^{-4/3} \\ &+ \exp\left(-\frac{\Sigma(r)-\chi(r,z)}{\lambda_{\rm CR}}\right)\times\left[1+\left(\frac{\Sigma(r)-\chi(r,z)}{\lambda_{\rm CR}}\right)^{3/4}\right]^{-4/3} \quad {\rm s}^{-1}, \quad (3.3)\end{aligned}$$

which is a function of the column density, χ, at a point (r, z) and also surface density, Σ, as a function of r. This expression is based on the assumption that cosmic-rays penetrate the disk isotropically, i.e. from all directions. The derivation can be found in the Appendix of Umebayashi & Nakano (2009), and is summarized in Appendix E of this thesis.

Figure 3.2 compares the distributions of the second (Semenov et al. 2004) plane-parallel cosmic-ray attenuator with the Umebayashi & Nakano (2009) isotropic attenuator for the 10^{-7} $M_\odot$ yr^{-1} accretion disk. Both attenuators similarly reduce cosmic-rays to a minimum value of 3.16×10^{-18} s^{-1} at a midplane radius of 1 AU, but the isotropic case clearly attenuates cosmic-rays over more of the disk than the plane-parallel one. This is because the isotropic case also attenuates the non-parallel flux contribution of cosmic-rays, which make up a fraction of the total flux. Umebayashi & Nakano (2009) therefore found that the isotropic attenuator expands their modelled dead zone compared to the plane-parallel attenuator. PPD models which still consider the plane-parallel assumption may in fact be underestimating the extent of cosmic-ray attenuation. Note that Equation (3.3) was originally derived for a minimum-mass solar nebula (MMSN) geometrically-thin disk with no flaring characteristics, i.e.:

$$\Sigma(r) = 1.7 \times 10^3 \left(\frac{r}{1{\rm AU}}\right)^{3/2} \quad {\rm gcm}^{-2}. \quad (3.4)$$

Nevertheless, adapting to a flared disk model such as this one still produces a reasonable attenuation distribution. This is because the flared portion of the disk does little to attenuate cosmic-rays, since the bulk of the gas density resides around the

midplane ($r >> z$).

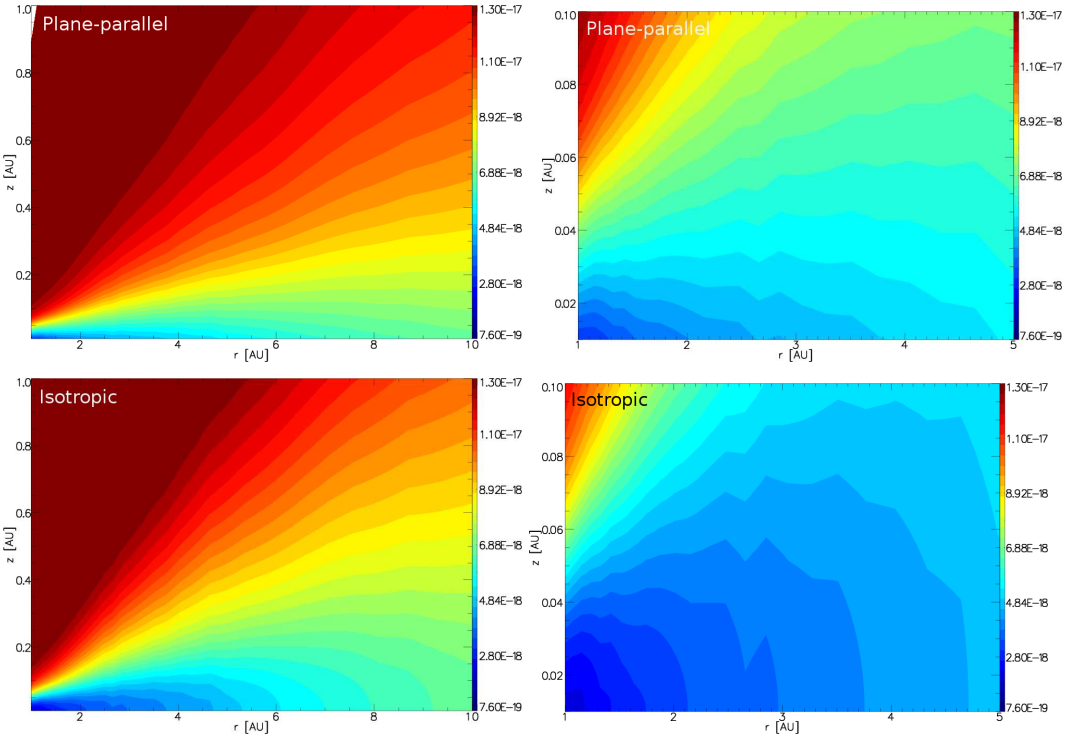

Figure 3.2: Plane-parallel (top row) and isotropic (bottom row) cosmic-ray attenuation distributions for the 10^{-7} $M_\odot$ yr^{-1} accretion disk. The distribution is constrained between 1.3×10^{-17} s^{-1} (the unattenuated cosmic-ray ionization rate) and 7.6×10^{-19} s^{-1} (the total radionuclide ionization rate).

Despite this similarity, the attenuation strength between the MMSN model and this one is vast, in that the gas density is much higher in the MMSN model. At a radius of 1 AU for example, the MMSN surface density value is 1700 g cm^{-2}, whilst the value from this 10^{-7} $M_\odot$ yr^{-1} accretion disk is 137 g cm^{-2}. Cosmic-rays are attenuated to a much larger extent in the MMSN model than in this one.

3.3 Radionuclides

Some studies have suggested that the primary radiation in the $\Sigma > 96$ g cm^{-2} region could be generated from another source from within the disk itself: radionuclides (e.g. Umebayashi & Nakano 1981; Finocchi & Gail 1997; Umebayashi & Nakano 2009). The most important of these is ^{26}Al, the most ionizing radionuclide. Although now extinct, ^{26}Al contributed around 91% of the total ionization of all radionuclides combined in the early solar system (Umebayashi & Nakano 2009). Studies have indicated that ^{26}Al may been around six times more abundant in our early solar system than interstellar abundance measurements suggest. This is inferred from combined geological and astrophysical evidence regarding our own solar system's formation 4.6 billion years ago (e.g. Lee et al. 1977; Umebayashi & Nakano 1981; Amelin et al. 2002; Gilmour & Middleton 2008). The most up-to-date "total" radionuclide ionization rate, $\sim 7.6 \times 10^{-19}$ s^{-1} (Umebayashi & Nakano 2009) is around a factor of 100 less than the unattenuated cosmic-ray rate, but these rates become more competitive near the midplane where cosmic-rays are attenuated > 96 g cm^{-2} (e.g. Finocchi & Gail 1997; Willacy & Woods 2009; Umebayashi & Nakano 2009).

Radionuclides are commonly split into two groups: short-lived radionuclides (SLNs) with half-lives ≤ 2 Myr, which are now extinct in the solar system, and the long-lived radionuclides (LLNs) with half-lives larger than this, and as a result are still present in the solar system today. A list of these SLNs and LLNs and their data, taken directly from the collated tables in Umebayashi & Nakano (2009) are shown in Tables 3.1, 3.2 and 3.3.

Table 3.1: A list of various short-lived radionuclides with their respective ionization rates (per H_2 molecule) of known abundances in the primitive solar nebula (taken from Umebayashi & Nakano 2009). Total energy emission of some radionuclides, denoted by E_{tot} may give two values separated by a comma, which corresponds to the respective decay channel if more than one exists. Those with energies and ionization rates of 0 mean that further work must be done in determining these values.

SLN	Decay mode	Half-life, $t_{1/2}$ (yr)	E_{tot} (keV)	Stable isotope	Abundance w.r.t stable isotope	$\zeta^{H_2}{}_R$ (s^{-1})
^{10}Be	β^-	1.5×10^6	209	^{9}Be	9.5×10^{-4}	4.1×10^{-24}
^{26}Al	β^+, EC	7.4×10^5	3304, 1978	^{27}Al	(5-7) $\times 10^{-5}$	(7.3–10) $\times 10^{-19}$
^{36}Cl	β^-, β^+	3.0×10^5	272, 1063	^{35}Cl	4.6×10^{-6} to 1.6×10^{-4}	6.4×10^{-22} to 2.5×10^{-20}
^{41}Ca	EC	1.0×10^5	0	^{40}Ca	1.4×10^{-8}	0
^{53}Mn	EC	3.7×10^6	0	^{55}Mn	5.1×10^{-6} to 2.8×10^{-5}	0
^{60}Fe	β^-	1.5×10^6	2741	^{56}Fe	5×10^{-7} to 1×10^{-6}	(3.0-5.9) $\times 10^{-20}$

Table 3.2: A list of various short-lived radionuclides with their respective ionization rates (per H_2 molecule), "whose abundances in the primitive solar nebula are unknown", instead utilizing a reference nuclide to determine an associated abundance (taken from Umebayashi & Nakano 2009). Total energy emission of some radionuclides, denoted by E_{tot} may give two values separated by a comma, which corresponds to the respective decay channel if more than one exists.

SLN	Decay mode	Half-life, $t_{1/2}$ (yr)	E_{tot} (keV)	Reference nuclide	Associated abundance	$\zeta^{H_2}{}_R$ (s^{-1})
^{93}Zr	β^-	1.5×10^6	51	^{93}Nb	3.1×10^{-11}	1.1×10^{-21}
^{98}Te	β^-	4.2×10^6	1543	^{98}Ru	1.5×10^{-12}	5.5×10^{-22}
^{126}Sn	β^-	1.1×10^5	2885	^{126}Te	3.8×10^{-11}	9.7×10^{-19}
^{236}Np	β^-, EC	1.5×10^5	46438, 4882	^{232}Th	2.1×10^{-12}	1.4×10^{-19}
^{237}Np	Np-series (α, β)	2.1×10^6	44640	^{209}Bi	5.7×10^{-12}	1.2×10^{-19}

Table 3.3: A list of various long-lived radionuclides with their respective ionization rates (per H_2 molecule) of known abundances in the primitive solar nebula (taken from Umebayashi & Nakano 2009). Total energy emission of some radionuclides, denoted by E_{tot} may give two values separated by a comma, which corresponds to the respective decay channel if more than one exists.

LLN	Decay mode	Half-life, $t_{1/2}$ (yr)	E_{tot} (keV)	Abundance w.r.t hydrogen nucleus	$\zeta^{H_2}{}_R$ (s^{-1})
^{40}K	β^-, EC	1.28×10^9	534, 1461	2.2×10^{-10}	1.1×10^{-22}
^{232}Th	Th-series (α, β)	1.41×10^{10}	40135	1.8×10^{-12}	5.3×10^{-24}
^{235}U	Ac-series (α, β)	7.04×10^8	44584	2.4×10^{-13}	1.6×10^{-23}
^{238}U	U-series (α)	4.47×10^9	47969	7.7×10^{-13}	8.5×10^{-24}

3.3.1 Radionuclide ionization rate

As derived in Umebayashi & Nakano (1981) and Umebayashi & Nakano (2009), the ionization rate of a given radionuclide X per H_2 molecule, is estimated from the expression:

$$\zeta_{\mathrm{R}}^{\mathrm{H}_2}(\mathrm{X}) \sim \frac{E_{\mathrm{em}}(\mathrm{X})}{W_{\mathrm{H}_2}} \frac{w(\mathrm{X})x(\mathrm{X})}{0.5 + x(\mathrm{He})} \quad \mathrm{s}^{-1}. \tag{3.5}$$

The ionization rate is a function of: (i) its abundance x(X) relative to H_2, (ii) x(He); the abundance of He relative to H_2 (= 0.84), (iii) the average energy E_{em} emitted by decay, released in the form of α particles, electrons and photons, and (iv) its decay rate constant w(X), updated in Umebayashi & Nakano (2009) to be:

$$w(\mathrm{X}) \equiv \frac{\ln 2}{t_{1/2}(\mathrm{X})}, \tag{3.6}$$

This is in contrast to the previous expression derived in Umebayashi & Nakano (1981) and used in Finocchi & Gail (1997):

$$w(\mathrm{X}) \equiv \frac{1}{t_{1/2}(\mathrm{X})}. \tag{3.7}$$

For example, the values extracted for ^{26}Al from Table 3.1 ($t_{1/2} = 7.4 \times 10^5$ yr, E_{em} = 3.3 MeV), together with estimating $x(^{26}\mathrm{Al}) \sim 1.75 \times 10^{-10}$ when the $x(^{26}\mathrm{Al})/x(^{27}\mathrm{Al})$ ratio = 5×10^{-5} is considered (see Section 3.4.3 and Umebayashi & Nakano 2009) gives an ionization rate of $\sim 7.0 \times 10^{-19}$ s^{-1}.

3.3.2 ^{26}Al decay

Radionuclides undergo general α, β and γ radioactive decay processes (of typical depth ranges 0.005, 0.2 and 8 g cm^{-2} respectively) with sufficient energy to ionize chemical species within the range of emission (Umebayashi & Nakano 2009). The most ionizing radionuclide, ^{26}Al is an SLN with a half life, $\tau_{1/2} = 7.4 \times 10^5$ yr and mean lifetime $\tau \sim 1.04$ Myr (Wang et al. 2009). It has two decay channels; both resulting in an excited daughter nucleus ^{26}Mg:

- β^+ decay:

$$^{26}\mathrm{Al} \rightarrow {}^{26}\mathrm{Mg}^* + \mathrm{e}^+ + \nu_\mathrm{e},$$

- Electron capture (EC):

$$^{26}\mathrm{Al} \rightarrow + \mathrm{e}^- \rightarrow {}^{26}\mathrm{Mg}^* + \nu_\mathrm{e},$$

with an 82% to 18% yield respectively (Finocchi & Gail 1997). This is followed by relaxation:

$$^{26}\mathrm{Mg}^* \rightarrow {}^{26}\mathrm{Mg} + \gamma.$$

On top of this smaller yield, Finocchi & Gail (1997) established that the ionization potential of the EC-decay channel is negligible compared with the β^+ channel since most of energy is carried away by the emitted neutrino. The remaining channels present three ionization processes > 13.6 eV. The positron emitted from β^+ decay can either collisionally ionize directly within a range ~ 0.1 g cm^{-2}, or annihilate with another to form a pair of photons with an ionization range of ~ 5 g cm^{-2}. The other is the γ-ray photon emitted from $^{26}\mathrm{Mg}^*$ which has an energy of either 1130, 1809 or 2938 MeV. Each photon is larger than the positron energy, 470 keV, thus ^{26}Mg relaxation has the greatest ionization potential from ^{26}Al decay (Umebayashi & Nakano 2009). The 1809 MeV photon is particularly important since it is unique to ^{26}Al decay, and its emission line has been largely observed from many high-mass star and supernovae regions of the galactic bulge, proving the existence of active nucleosynthesis in the ISM (e.g. Mahoney et al. 1982; Diehl et al. 2006, 2008). These same observations are used to establish the ISM ^{26}Al abundance, relative to the stable ^{27}Al isotope. The value is currently estimated at $\sim 8.4 \times 10^{-6}$, which correlates to a mean ISM ^{26}Al ionization rate of $\sim 9.2 \times 10^{-20}$ s^{-1} (Diehl et al. 2006).

3.3.3 Evidence for radionuclides

The presence of extinct radionuclides in our early solar system have been studied and debated extensively (e.g. Podosek & Swindle 1988); particularly for ^{26}Al, concerning measurements from Calcium-Aluminium-rich (CAI) inclusions embedded in chondritic meteorites. The discovery of these CAIs, such as in the Allende meteorite (Lee et al. 1977) lead scientists to believe that ^{26}Al existed in an epoch ($\sim$ 2 Myr) prior to planetesimal formation. Specifically, Lee et al. (1977) reported a large ^{26}Mg excess which could not be accounted for by direct injection of fossil ^{26}Mg from the ISM, and must be the remains of ^{26}Al decay. They established a CAI "canonical" ^{26}Al/^{27}Al isotopic ratio of 5.1×10^{-5}. Since then, over 1500 studies of ^{26}Mg excess in embedded CAIs of many meteorites (Umebayashi & Nakano 2009), using more sophisticated spectroscopic techniques, have concluded similar enhancements with an average canonical ratio of 4.5×10^{-5}, which is six times larger than the ISM value. Combining with the old decay rate constant from (Umebayashi & Nakano 1981), this coincides with a mean ionization rate of 6.1×10^{-19} s^{-1} (noting the factor of 10 error in Umebayashi & Nakano 1981 which was highlighted in Finocchi & Gail 1997). Using the newer Umebayashi & Nakano (2009) decay constant resulted in a rate value of 7.0×10^{-19} s^{-1}, which is approximately eight times larger than the ISM rate. In fact, one study of CAIs in another meteorite, Leoville 144A (Young et al. 2005) argued for a "supra-canonical" value $\sim 6 - 7 \times 10^{-5}$, which translated to an ionization rate as high as 1.0×10^{-18} s^{-1}. However this has since been disputed due to debates over the exact epoch in which CAIs formed in relation to their encased chondrules (e.g. Gounelle 2006). Nevertheless, studies of ^{36}Cl, ^{60}Fe and ^{41}Ca infer similar meteoritic enhancements over their ISM values (e.g. Huss & Meyer 2009). Evidence suggests that the early solar nebula may have been abnormally rich in ionizing radionuclides such as ^{26}Al.

There are current debates as to whether an internal phenomenon from within the

early solar nebula can explain the radionuclide abundance excess, or if they were "injected" during an early "CAI-forming" window from an external source (see MacPherson et al. 1995 and Boss 2012 for reviews). The excess ratios of ^{10}Be and ^{36}Cl for example, may point to, and in theory can be explained by internal cosmogenic spallation, where solar energetic particles (SEPs) accelerated by a more active protosun than today sufficiently irradiated and induced proton capture in stable isotopes with similar proton numbers (e.g. Wasserburg et al. 2006; Huss & Meyer 2009). On the other hand, ^{60}Fe excesses are better explained with the theory of external nucleosynthesis production in Wolf-Rayet stars, supernovae and asymptotic giant-branch (AGB) stars which were then injected as CAIs formed (e.g. Wadhwa et al. 2007), although the initial amount of ^{60}Fe present in the primitive solar nebula has since been disputed (Moynier et al. 2011). Recent theoretical work from Boss & Keiser (2010) and Boss & Keiser (2012), using 3-D axisymmetric models of cloud core triggering and SLN injection processes, concluded that supernovae were more efficient at injecting SLNs to the established meteoritic abundances, than AGB and Wolf-Rayet stars, due to the shockwave dynamics of the injection process. It has generally been considered that ^{26}Al and ^{41}Ca excesses were also nucleosynthesized and externally injected like ^{60}Fe, but this has recently been disputed since an as of yet unobserved pre and post-injection correlation with the ^{17}O/^{16}O ratio in meteorites should also exist, which is larger in supernovae, and AGB and Wolf-Rayet stars (Gounelle & Meibom 2007; Ellinger et al. 2010).

The current general consensus is that a combination of these internal and external phenomena are probable to account for all SLN excesses. Furthering the external source idea, if the narrow 2 Myr gap between CAI and chrondule formation is to be believed, along with the inhomogeneity of ^{26}Al in the galactic plane, then our solar system probably formed relatively close to these candidates. Exactly how close is a matter of debate since it becomes difficult to account for the current understanding of the structure and composition of the solar nebula which would

have been modified or even destroyed altogether in the presence of the powerful stellar winds and tidal forces generated by these candidates.

3.3.4 ^{26}Al production

Identifying the exact mechanisms of radionuclide production is important to unlocking the secrets of their origins. Radionuclides are essentially nucleosynthesized via ^{3}He. Unfortunately, little experimental data exists on ^{3}He-induced reactions, so theoretical cross-sections are established from reaction codes such as the TALYS nuclear reaction simulator (see Fitoussi et al. 2008). Fitoussi et al. (2008) in particular used TALYS to compare the current fusion cross-sections of all known fusion processes leading to ^{26}Al formation. The dominant fusion reaction for ^{26}Al production involves ^{24}Mg:

$$^{24}\mathrm{Mg} + {}^{3}\mathrm{He} \rightarrow {}^{26}\mathrm{Al}^{*} + \mathrm{p},$$

whereby the excited ^{26}Al decays from the 3^{+} state to its 5^{+} ground state, releasing a 417 keV γ-photon:

$$^{26}\mathrm{Al}^{3+} \rightarrow {}^{26}\mathrm{Al}^{5+} + \gamma,$$

with $\tau_{1/2}$ = 6.3452 s (Fitoussi et al. 2008). Various lab models have studied the 417 KeV γ-line emission from this fusion reaction. Another mechanism, highlighted in (MacPherson et al. 1995) is:

$$^{25}\mathrm{Mg} + \mathrm{p} \rightarrow {}^{26}\mathrm{Al} + \gamma,$$

which is thought to occur at temperatures of 3.5×10^{7} K. Processes capable of producing ^{26}Al at these temperatures are:

- Hydrostatic H-burning regions in the core of $M \geq 20\ M_{\odot}$ stars,
- H-H burning regions in the H-shell of low and intermediate $M \leq 9\ M_{\odot}$ stars,
- "Explosive" ($T \sim 2 \times 10^{8}$ K) H, C and Ne-burning regions in supernovae(MacPherson et al. 1995).

3.3.5 Heating from radionuclides

Most of the heavier SLN radionuclides such as ^{26}Al, ^{41}Ca and ^{60}Fe were refractory and siderophillic, and so in theory would sink to the disk midplane faster than surrounding gas and dust. Dust grains coalesce over time by mutual collision whilst spatially distributing towards the midplane via sedimentation, trapping and encasing the radionuclides inside (Umebayashi & Nakano 2009). In addition to other possible heating mechanisms (see Hewins & Newsom 1988) these radionuclides may have been a substantial heating source inside planetesimals by melting the silicate content within, contributing to the differential (achondritic) nature of some meteorites found on Earth, and possibly the formation of the inner planets themselves (Urey 1955). Gilmour & Middleton (2009) went as far as to suggest a trend between the ^{26}Al excess abundance and the advancement rate of "technological civilizations". The authors highlight on the idea that the heat generated from ^{26}Al decay beyond the snow-line (the epoch of which occurs up to a "snow moment") increases the devolatisation of gas accreted in planetesimals, slowing down the overall core formation rate of gas giants and eventual size. Therefore, solar systems with higher ^{26}Al abundances contain gas giants that are perhaps less-massive than those with lower ^{26}Al abundances which formed faster. At the same time, high ^{26}Al abundances also result in volatile-poorer terrestrial planets than systems with lower ^{26}Al abundances, categorizing the Earth as volatile-poor. Early epoch inward migration theories of gas-giants would also suggest a sweeping-up of volatile reservoirs in the terrestrial zones before those planets formed which is more rapid in the low ^{26}Al regime. However, these discussions do not account for the potentially large heat losses incurred during accretion which do not go into heating the accreting-volatiles themselves.

3.4 Investigation: cosmic-rays vs radionuclides

So far, the attenuating effects of cosmic-rays, and the presence of radionuclides have been outlined. Figure 3.3 compares the midplane profiles of the cosmic-ray ionization rate using the isotropic attenuator, and total radionuclide ionization rate fixed at 7.6×10^{-19} s^{-1} in the 10^{-7} M$_\odot$ yr^{-1} accretion disk. It shows that attenuation is insufficient to reduce the cosmic-ray ionization rate to a value below that of the radionuclides. Its lowest value is 3.16×10^{-18} s^{-1} at 1 AU, which is still 4 times larger than the radionuclide rate. In contrast, a MMSN model is dense enough to attenuate cosmic-rays sufficiently below that of the radionuclides. At the same point, the MMSN surface density value is 1700 g cm^{-2}, resulting in a cosmic-ray ionization rate of $\sim 1.27 \times 10^{-26}$ s^{-1}, i.e. 6×10^{7} times smaller than the total radionuclide rate. Umebayashi & Nakano (2009) specifically found the ionization rate of cosmic-rays to drop below the radionuclides at a radius of 3.3 AU in their disk, which is around 140 g cm^{-2}. This value is not far from the maximum surface density value in this 10^{-7} M$_\odot$ yr^{-1} accretion disk; 137 g cm^{-2} at r = 1 AU.

Irrespective of this fact, the effects of radionuclides on the chemistry in these regions may still be apparent. This investigation compares the chemical effects at the midplane (i.e. in 1-D), where the cosmic-ray attenuation is strongest, by adding and omitting the radionuclides. The simplest method for investigating their potential effect involves adding the radionuclide ionization rate to that of cosmic-rays at each point, and comparing to the chemical output of attenuation itself with the radionuclides omitted.

3.4.1 Radionuclide ionization rate addition

In this investigation, cosmic-rays are assumed to penetrate the disk isotropically, and they are attenuated at each point according to Equation (3.3) derived in Umebayashi & Nakano (2009). The total radionuclide ionization rate is assumed to equal

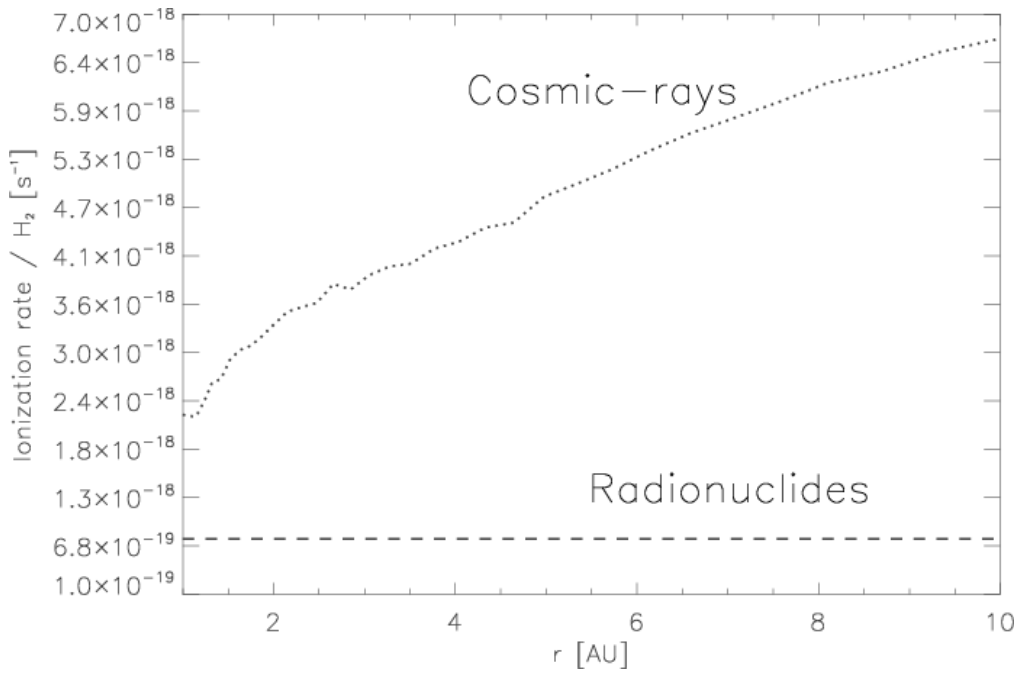

Figure 3.3: Ionization rate profiles along the midplane of cosmic-rays which are isotropically attenuated, and the radionuclides which are fixed at 7.6×10^{-19} s^{-1}.

7.6×10^{-19} s^{-1}, of which 91% is contributed by ^{26}Al, the most ionizing radionuclide with an ionization rate of 7.0×10^{-19} s^{-1} if the ^{26}Al/^{27}Al canonical ratio of 5×10^{-5} is considered. The ionization rate is thus:

$$\zeta_{\rm T} = \zeta_{\rm CR} + \zeta_{\rm R} \quad {\rm s}^{-1}, \tag{3.8}$$

where the terms denote, respectively, the ionization rates of cosmic-rays and the radionuclides.

3.4.1.1 Results

Table 3.4 compares the midplane ionization rate abundance ratio ($n_{\rm X}(\zeta_{\rm T})$ / $n_{\rm X}(\zeta_{\rm CR})$, where $n_{\rm X}$ is the relative abundance of a species X) of some species at a radius of 1, 3, 5 and 10 AU, with and without radionuclides based on this simplistic treatment. In principle, changes in chemistry and ratio values are dictated by thermal desorption from grains, followed by either:

Table 3.4: Abundance ratio values (ζ_T / ζ_{CR}) for various species at the midplane for r = 1 AU, 3 AU, 5 AU and 10 AU. Species are split between those that show abundance increase with radionuclides (ratio > 1), those which show no change (ratio = 1), and those which decrease (ratio < 1). The most abundant species, H_2, H, He, CO, H_2O and HCN are hardly affected with ratios ~ 1.

Species	1 AU	3 AU	5 AU	10 AU
CHD_2OH^+	1.32	1.20	1.16	1.00
CH_3CN^+	1.31	1.20	1.16	1.02
CH_3OH^+	1.29	1.20	1.16	1.00
G-C_2D	1.27	1.14	1.11	1.10
C_2D	1.27	1.14	1.13	1.13
C	1.23	1.16	1.05	1.02
G-C	1.23	1.15	1.05	1.02
C_4H	1.22	1.17	1.07	1.00
G-C_4H	1.22	1.17	1.07	1.00
C_2H	1.20	1.15	1.06	1.00
G-C_2H	1.20	1.15	1.06	1.00
G-S	1.13	1.08	0.99	1.01
S	1.13	1.08	0.99	1.01
CO_2^+	1.09	1.00	1.00	1.01
CO_2	1.07	1.00	0.99	1.01
H_2CO	1.02	1.01	1.01	1.00
HCN	1.01	0.99	1.00	1.00
H^+	1.00	1.00	1.00	1.00
He^+	1.00	1.00	1.00	1.00
H_2^+	1.00	1.00	1.00	1.00
H_3^+	1.00	1.00	1.00	1.00
H_2O	1.00	1.00	1.00	1.00
H_2O^+	1.00	1.00	1.00	1.00
HDO	1.00	1.00	1.00	1.00
CO	1.00	1.00	1.00	1.00
CO^+	1.00	1.00	1.00	1.00
CN	1.00	1.00	1.00	1.00
C^+	1.00	1.00	1.00	1.00
Fe	1.00	1.00	1.00	1.00
Fe^+	1.00	1.00	1.00	1.00

Table 3.4 (continued): Abundance ratio values (ζ_T / ζ_{CR}) for various species at the midplane for r = 1 AU, 3 AU, 5 AU and 10 AU.

Species	1 AU	3 AU	5 AU	10 AU
CH_3OH	0.99	1.00	1.00	1.03
$CH_3OH_2^+$	0.99	1.00	1.00	1.03
G-CH_3OH	0.99	1.00	1.00	1.00
C_2H_2	0.98	0.97	1.00	1.01
G-C_2H_2	0.98	0.97	1.00	1.00
G-O_2	0.98	0.81	0.85	1.06
O_2	0.98	0.81	0.85	1.06
G-NH	0.92	0.99	0.96	1.01
NH	0.92	0.99	0.96	1.01
G-N	0.90	1.03	1.05	1.03
N	0.90	1.03	1.04	1.02
NO	0.89	1.01	1.02	1.03
GNO	0.88	1.01	1.01	1.03
C_3H_2	0.87	0.89	0.91	1.00
G-C_3H_2	0.87	0.88	0.90	1.00

- direct ionization, i.e.

$$A \longrightarrow A^+,$$

- two-body reactions followed by ionization and consequent ion-neutral reactions, i.e.

$$A + B \longrightarrow C \text{ followed by } C \longrightarrow C^+,$$
$$C^+ + D \longrightarrow E^+.$$

These may then freeze back out or dissociatively recombine on grains to form a new species, i.e.

$$A^+ \longrightarrow \text{G-A},$$
$$E^+ \longrightarrow \text{G-F} + \text{G-J},$$

depending on the number of recombination channels forming a certain molecule on the grain, and the value of C_X at a given point in the disk (Equation 2.28). Grains

act not only as mediators in preserving species from being processed in the gas, but also act as switchers from one set of reaction channels to another. Neutrals with a greater number of cations which dissociatively recombine to form it, such as C and S, are likely to be enhanced indirectly as a result of the production of more cations with inclusion of the radionuclides. On the other hand, those which have little, or do not have dissociative recombination formation reactions on grains (e.g. N_2, HCN, C_2H_2) will be depleted.

The most enhanced species at 1 AU, with T = 663 K are higher-order hydrocarbon chain ions, CHD_2OH^+, CH_3OH^+, CH_3CN^+, followed by other carbon radicals such as C, C_4H, C_2H and CO_2. Production of hydrocarbon chain ions are mainly driven by rapid endothermic ion-neutral reactions, which are enhanced ~ 30% with the inclusion of the extra ionization potential provided by the radionuclides. Interestingly HCO^+, CH_3CO^+ and C^+ – three ionic species which are dominant in other works, are hardly sensitive at all. The most depleted species (~ 13 %) are nitrogen radicals N, NO and NH, along with C_3H_2, O_2 and C_2H_2. At larger radii and lower temperatures, these enhancements and depletions generally decrease since there are less ions and few species in the gas to ionize or react.

However, towards the disk centre, the increasing temperature enhances the thermal velocity of molecules and cations which, although increases the rate of ion-neutral and two-body reactions, also increases the recombination reactions with free electrons and grains. At the same time the increasing density principally enhances the rate at which gas and grains interact. So although the hydrocarbon cation ratios are enhanced the most, their actual abundances are reduced because the overall ionization fraction decreases.

It is shown that both gas and grain ratio values of neutral molecules increase or decrease by the same number, indicating changes occur exclusively in the gas, whether due to ionization, dissociation or two-body processes. The most abundant neutrals, e.g. CO, H_2O, H_2CO, NH_3 and CH_4 are hardly sensitive since there are a

far greater number of molecules to ionize. In fact it is difficult to trace exact changes from the ratio values alone since differences in actual abundance may weight above the ratio differences. Molecules that are abundant and show small sensitivity may show greater differences compared to less abundant molecules which show high sensitivity. Most of these hydrocarbon ions which show sensitivities have abundances $\leq 10^{-20}$; although $C_3H_2 \sim 10^{-11}$, N $\sim 10^{-15}$ and NH $\sim 10^{-20}$. Table 3.5 presents a list of molecules with the largest differences in abundance. From this

Table 3.5: Abundance difference values ($\zeta_T - \zeta_{CR}$) for various species at the midplane for r = 1 AU, 3 AU, 5 AU and 10 AU. Species are listed in order of most enhanced abundances (positive values) to most depleted abundances (negative values) at 1 AU. H_2, H, He, CO, H_2O and CN are unaffected.

Species	1 AU	3 AU	5 AU	10 AU
C_4H_2	1.0(-09)	9.0(-10)	-1.0(-10)	0
HC_3N	1.0(-09)	2.0(-09)	4.0(-09)	0
C_3H	1.5(-09)	5.3(-12)	1.6(-14)	1.0(-17)
H_2CO	2.7(-10)	2.6(-10)	1.0(-10)	9.7(-12)
C_2H	1.1(-17)	4.6(-16)	1.0(-15)	4.2(-16)
C	1.2(-17)	1.4(-16)	1.0(-15)	4.3(-15)
H_3^+	0	0	0	0
H_2O	0	0	0	0
CO	0	0	0	0
CN	0	0	0	0
C^+	0	0	0	0
He^+	0	0	0	0
C_3H_4	-4.2(10)	-2.9(-10)	-7.3(-11)	0
HNC	-1.6(-09)	-2.3(-09)	-3.0(-09)	0
HCN	-3.0(-09)	-3.0(-09)	-4.0(-09)	0
CH_4	-3.0(-09)	-4.0(-09)	-4.0(-09)	-1.0(-09)
C_2H_2	-3.0(-09)	-1.2(-09)	1.0(-11)	1.2(-16)
N_2	-1.0(-08)	1.0(-08)	-1.0(-08)	-1.0(-08)

perspective, one sees that the most enhanced abundances are in fact the hydrocar-

bon neutrals C_4H_2, HC_3N and C_3H, and the most depleted abundances are CH_4, HCN, C_2H_2 and N_2, all with abundances $\geq 10^{-7}$.

The reasons for some of the differences seen are complex and therefore cannot be explained simply by the enhancements in neutral species with many dissociative recombination channels on grains. For example, the increased ionization rate enhances the photodissociation of C_2H_2 to C_2H. C_2H_2 is also ionized to the radical $C_2H_2^+$ which becomes embroiled in vigorous ion-neutral reactions with H_2 to form higher order hydrocarbon ions $C_2H_3^+$ and $C_2H_4^+$. At the same time C_2H_2 is reformed from electronic recombination of these same hydrocarbon ions, but at a lower rate than its photodissociation and ionization, or the photodissociations of other hydrocarbons C_4H_2 and HC_3N, to C_2H. Both C_2H and C_2H_2 also react to form C_4H_2, which itself photodissociates to C_4H and C_2H. Hence C_2H is enhanced whilst C_2H_2 is depleted. The reason for N_2 depletion is even more complex and therefore not so clear. It likely involves net losses of 3rd or higher order generation species occurring consistently from 1 to 10 AU to other reaction channels which are not recycled back to form N_2.

Figure 3.4 compares the midplane abundance profiles of some sensitive species from Table 3.4, with radionuclides (dotted line), without radionuclides (dashed line) and omitting cosmic-ray attenuation altogether (dot-dashed line). Figure 3.5 compares the abundance enhancement profiles for some of the most sensitive species listed in Table 3.5. For the latter, positive values depict enhancements with radionuclide inclusion, whilst negative values represent depletions.

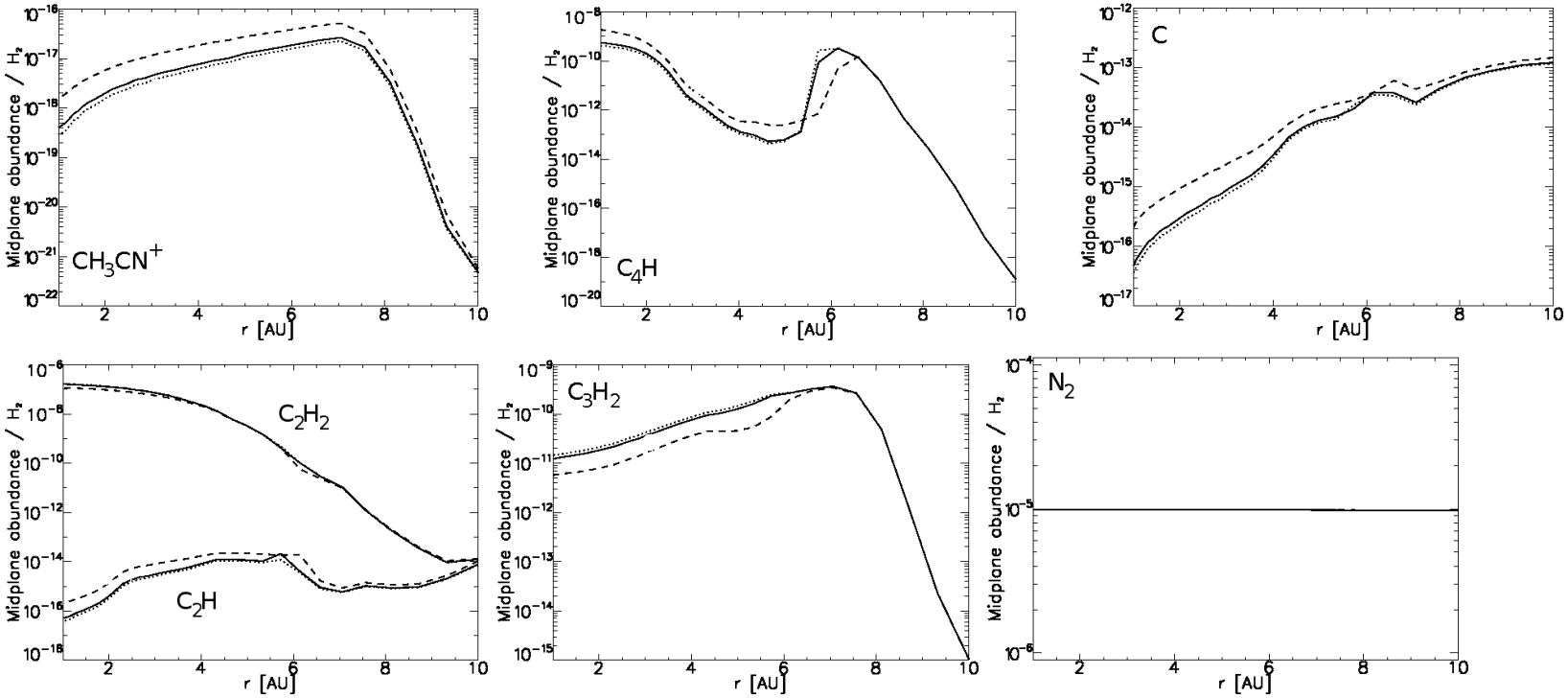

Figure 3.4: Midplane abundance distributions for various species the 10^{-7} $M_\odot$ yr^{-1} accretion disk with radionuclides (solid line), without radionuclides (dotted line) and omitting cosmic-ray attenuation altogether (dashed). The top row represents species which are enhanced with radionuclides (CH_3CN^+, C_4H, C), and the bottom row those which are depleted (C_3H_2, N_2). The bottom–left figure displays C_2H and C_2H_2 profiles, which are related.

3.4.2 Sticking coefficients

Most disk models in the literature adopt either a sticking coefficient S_X of 0.3 (e.g. Markwick et al. 2002; Semenov et al. 2004; Willacy & Woods 2009) or unity (i.e. 1) (e.g. Walsh et al. 2010; Heinzeller et al. 2011; Walsh et al. 2012) where the classical adsorption rate expression from Hasegawa et al. (1992) is used (Equation 2.28). Some have stated that this coefficient is likely to be even smaller than 0.3 in high–temperature regions (e.g. Burke & Hollenbach 1983) located nearer to disk surfaces (Semenov et al. 2004). Table 3.6 highlights some molecules which are most sensitive to a change of $S_X = 1$ to 0.3 for the 10^{-7} $M_\odot$ yr^{-1} accretion disk model with the inclusion of radionuclides. These are presented as ratio values ($S_X = 1.0$ / $S_X = 0.3$). Ratios > 1 represent larger abundances when the model is run with $S_X = 1.0$, whilst values < 1 depict larger abundances when $S_X = 0.3$.

Principally, the sticking coefficient represents a probability of a molecule sticking to the grain. Unity (1) means guaranteed (100%) sticking upon first contact, whilst 0.3 depicts a 30% chance of sticking. Thus, neutrals and cations in the gas are less likely to adsorb back onto grain surfaces in the lower $S_X = 0.3$ case, and grain abundances are notibly reduced.

Grain ratios increase and grain abundances are reduced with decreasing radius (and increasing temperature) in the $S_X = 0.3$ model since the competing thermal desorption returns species into the gas more rapidly, and the gas-grain interaction is less-enhanced with the corresponding density increase.

The most sensitive grain species at a radius of 1 AU are found to be frozen multi-carbon molecules (containing either 2, 3 or 4 carbon atoms), the highest of which is G-C_2. At 3 AU, the most enhanced is G-D_2S, at 5 AU G-O, and at 10 AU it is G-OH.

Since the lower $S_X = 0.3$ value allows species to spend more time in the gas, it also allows for the production of more cations; particularly high order molecular cations which are driven by rapid ion-neutral reactions applicable inside a radius

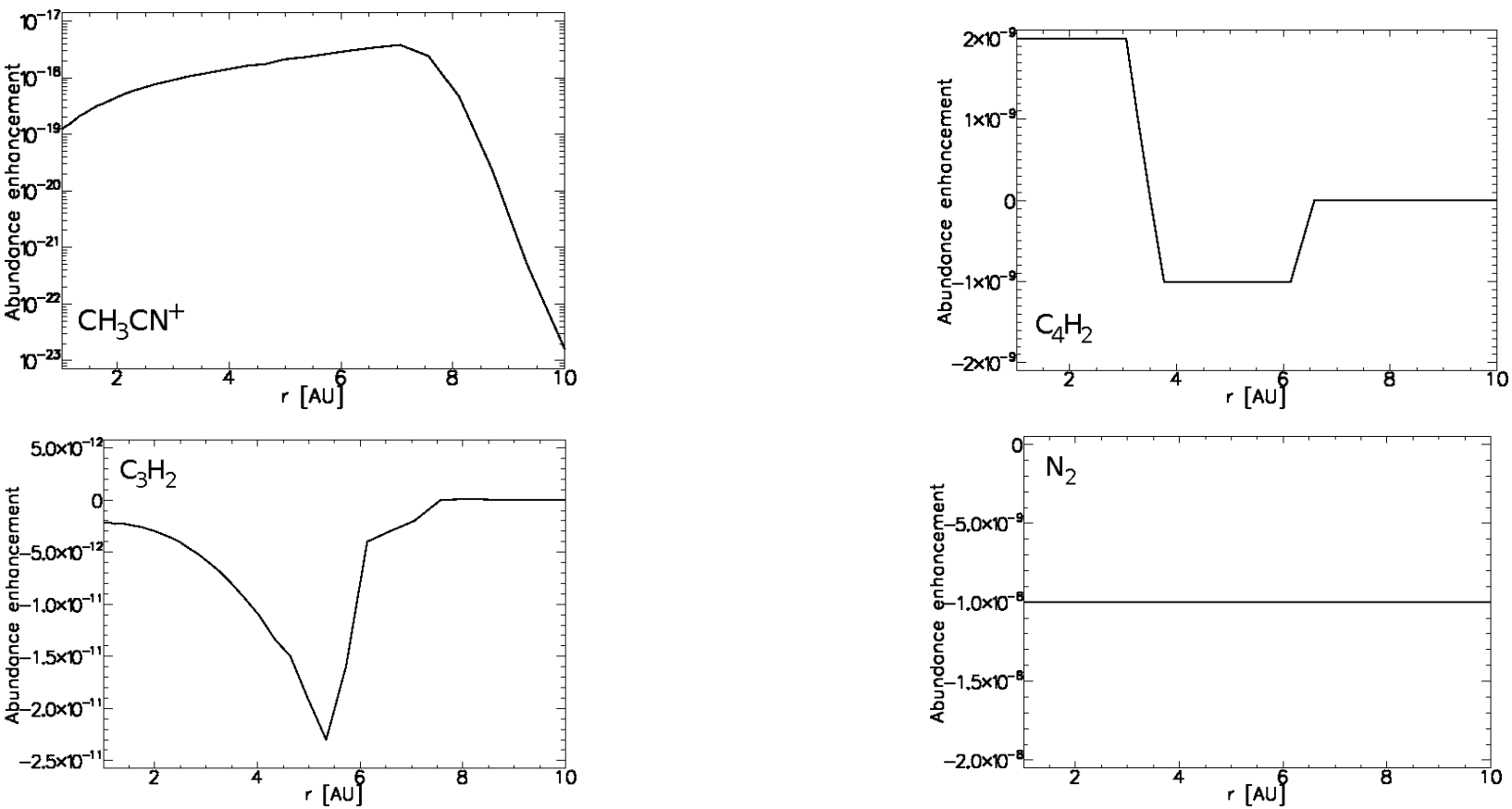

Figure 3.5: Abundance–enhancement profiles along the midplane for CH_3CN^+ (top left), C_4H_2 (top right), C_3H_2 (bottom left) and N_2 (bottom right).

Table 3.6: The midplane ratio values of the top ten most sensitive species which are enhanced (1st row set, > 1) and depleted (2nd row set, < 1) with a change in S_X from 1 to 0.3 for r = 1 AU, 3 AU, 5 AU and 10 AU. Species are listed in order of most enhanced abundances to most depleted abundances at 1 AU. H_2, HD, H_2^+, He and CO are unaffected with ratios of 1.

Species	1 AU	3 AU	5 AU	10 AU
G-C_2	9.59	6.59	0.92	1.36
G-C_4	8.02	8.24	2.41	0.99
G-DC_3N	5.98	5.03	4.31	0.90
G-HC_3N	4.73	4.10	3.63	0.95
G-C_2H_2D	4.48	2.94	3.39	0.70
G-C_3N	4.29	4.18	3.43	1.00
G-C_3	4.14	3.23	0.60	1.13
G-C_3D	4.03	2.77	1.01	0.99
G-C_3O	3.89	3.16	0.74	0.73
G-HCN	3.78	3.83	3.97	1.76
NH_4^+	0.15	0.29	0.28	0.26
NH_3D^+	0.15	0.24	0.18	0.22
$CD_3OH_2^+$	0.14	0.18	0.12	0.33
$NH_2D_2^+$	0.13	0.24	0.23	0.19
$C_3H_5^+$	0.13	0.13	0.17	0.62
$C_3H_4D^+$	0.12	0.10	0.16	0.61
NHD_3^+	0.12	0.34	0.36	0.29
ND_4^+	0.12	0.25	0.22	0.19
HDS_2^+	0.10	0.19	0.09	0.05
$H_2S_2^+$	0.10	0.16	0.09	0.08

of 10 AU. The most sensitive is found to be $H_2S_2^+$ at 1 AU, $C_3H_4D^+$ at 3 AU and DNS^+ at 5 AU, whose abundances are enhanced by an additional 90.3%, 90.4% and 99.3% respectively in the $S_X = 0.3$ model. At 10 AU, cation and gas abundances are low and the most depleted species in terms of sensitivity is G-S_2 (reduced to 4.9×10^{-8} % of the $S_X = 1.0$ value). Ratios generally tend towards unity with increasing

(colder) radii, as chemical abundances in the gas are reduced; thus the difference in S_X becomes less important.

However as before, the greatest ratio differences are not attributed to the greatest differences in abundance. As Table 3.7 shows, the largest abundance differences are weighted towards the more abundant molecules. At 1 AU, the most enhanced is HCN, whilst at 3, 5 and 10 AU it is CO. The most depleted molecule at all four radii is D_2.

Table 3.7: The midplane abundance difference values of the top five most sensitive species which are enhanced (1st row set, > 1) and depleted (2nd row set, < 1) with a change in S_X from 1 to 0.3 for r = 1 AU, 3 AU, 5 AU and 10 AU. Species are listed in order of most enhanced abundances to most depleted abundances at 1 AU. CO, the most enhanced molecule at r = 3, 5 and 10 AU is also shown.

Species	1 AU	3 AU	5 AU	10 AU
HCN	1.2(-07)	1.2(-07)	1.4(-07)	-1.0(-07)
HC_3N	1.0(-07)	1.0(-07)	8.2(-08)	-2.6(-14)
OCS	1.2(-09)	1.1(-09)	2.7(-09)	-1.0(-19)
C_3N	1.1(-09)	9.4(-10)	1.1(-09)	-7.7(-18)
H_2CS	6.1(-10)	7.0(-10)	6.6(-10)	-1.3(-13)
CO	0	2.0(-07)	2.0(-07)	1.0(-07)
HNC	-7.2(-08)	-5.6(-08)	-4.3(-08)	-1.1(-07)
H_2O	-1.0(-07)	0	-7.2(-10)	2.6(-19)
N_2	-1.1(-07)	-1.0(-07)	-1.1(-07)	-1.0(-07)
CH_4	-1.1(-07)	-1.1(-07)	-1.2(-07)	-8.4(-08)
D_2	-3.0(-07)	-3.1(-07)	-3.1(-07)	-3.3(-07)

Figure 3.6 compares the top three most enhanced, and top three most depleted molecular radial profiles, as established at r = 1 AU. The profiles of OCS, CH_4 and D_2 remain more or less the same up to 10 AU. HCN displays a sharp depletion from 9 AU outwards. HC_3N also shows a depletion ~ 6 AU, albeit to a lesser extent. H_2O dips down sharply to a peak abundance difference of -3×10^{-6} between 3 and 5 AU.

These depletions are attributed to the point where they begin to desorb into the gas (i.e. at the snow-line), where adsorption and desorption rates are competitive and similar, and the difference in S_X values is particularly apparent.

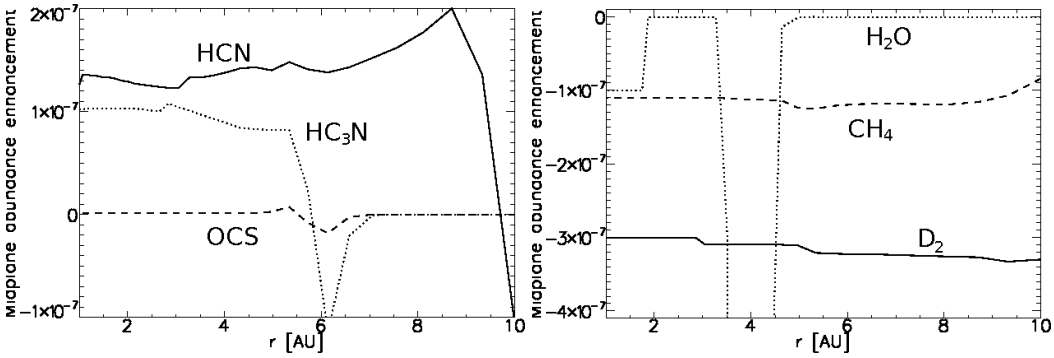

Figure 3.6: The midplane abundance difference distributions of the top three most enhanced species (left) and depleted species (right) as determined at $r = 1$ AU, as a result of changing S_X from 1 to 0.3.

This particular investigation compared the chemical outputs of two simulations with $S_X = 1$ and 0.3; both cases with radionuclides included. It is also likely that chemical differences between radionuclide inclusion and omission will be enhanced in the $S_X = 0.3$ case, since the adsorption and recombination rates on grains are reduced and differences are generated more exclusively in the gas. Tables 3.8, 3.9 and 3.10 compare the abundance ratios and abundance differences of certain molecules at $r = 1, 5$ and 10 AU which show the greatest change between radionuclide inclusion and omission for the $S_X = 1$ and 0.3 models. They are listed in such a way as to present the most sensitive molecule in the network from each of the ratio and abundance difference enhancement and depletion lists. The value from the list in which they peak in is highlighted in bold. Some molecules, such as N_2 at 1 AU and HC_3N at 5 AU, peak in more than one criteria.

The results show that the overall ratio sensitivity is enhanced significantly from tens of a percent in the $S_X = 1$ case to orders of magnitude for $S_X = 0.3$. At $r = 1$ and 5 AU, the most affected are low-abundant hydrocarbon cations ($\leq 10^{-15}$) which

are extensively enhanced, and low-abundant nitrogen and sulphur-bearing diatomic molecules which are most depleted - the latter of which is a shift from low-abundant hydrocarbons which constitute the majority of the ratio depletions in the $S_X = 1$ case (Table 3.4). At 10 AU, the grain abundances are the most enhanced, and increase dramatically from $S_X = 1$ to 0.3. Whilst grain-bound S_2 is the largest with a ratio value of 3.19 in the $S_X = 1$ model, it switches to grain-bound CHD (with a ratio value of 48.1) when $S_X = 0.3$. CD_3 remains the most depleted molecule, with a ratio value of 0.96 when $S_X = 1$ which is decreased further to 0.71 when $S_X = 0.3$.

The abundance differences, attributed to molecules which are abundant (i.e. $\geq 10^{-7}$) are also augmented. At 1 AU the most enhanced molecule switches from C_4H_2 (1.0×10^{-9}) to N_2 (4.0×10^{-8}). The latter is actually the most depleted molecule at 1 AU and the most enhanced at 5 AU and 10 AU in the $S_X = 1$ case. At 1 AU and 5 AU, CO is the most depleted molecule when S_X is set to 0.3, and suggests a strong formation dependency from dissociative recombination on grains since the abundance difference, at both of these radii when $S_X = 1$ is 0. At $r = 5$ AU, HC_3N remains the most enhanced molecule, increasing from an abundance difference of 4.0×10^{-9} when $S_X = 1$ to 6.0×10^{-8} for $S_X = 0.3$. At 10 AU, the most enhanced molecule switches from CH_2 to N_2, whilst the most depleted becomes CH_4 when $S_X = 0.3$.

3.4.3 Cosmic-ray induced desorption

In addition to the thermal heating process from the disk medium, molecular desorption can be induced by radiation which heats grains to the desorption temperature. In this respect, radiative desorption is independent of disk temperature, and is considered a non-thermal process. Radiative desorption has the effect of releasing molecules into the gas at temperatures lower than the local gas temperature required for thermal desorption, and increases the overall desorption rate. Many previous works (e.g. Semenov et al. 2004; Walsh et al. 2010; Heinzeller et al. 2011;

Table 3.8: Tabulated data of molecules at r = 1 AU which show greatest ratio and abundance differences with and without radionuclides between S_X = 1 and 0.3. Columns are defined as thus: **FA1**: S_X = 1 final abundance with radionuclides, **FA0.3**: S_X = 0.3 final abundance with radionuclides, **R1**: S_X = 1 ratio value, **FA0.3**: S_X = 0.3 ratio value, **AD1**: S_X = 1 abundance difference, **AD0.3**: S_X = 0.3 abundance difference. Values highlighted in bold depict that molecule to be the most enhanced or depleted for that particular stat in the entire chemical network.

Species	FA 1	FA 0.3	R 1	R 0.3	AD 1	AD 0.3
CH_2DOH^+	5.2(-25)	2.0(-24)	**1.32**	3.1(+04)	1.3(-25)	2.0(-24)
CH_2DCN^+	3.0(-21)	2.1(-20)	1.31	**1.6(+07)**	7.1(-22)	2.1(-20)
C_4H_2	4.2(-07)	4.7(-07)	1.01	1.02	**1.0(-09)**	9.2(-09)
N_2	9.9(-06)	1.0(-05)	0.99	1.01	**-1.0(-08)**	**4.0(-08)**
C_3H_2	1.2(-11)	5.7(-11)	**0.91**	0.48	-1.2(-12)	-6.2(-11)
G-S_2	7.0(-23)	3.9(-23)	1.10	**0.09**	6.4(-24)	-3.9(-22)
CO	6.5(-05)	6.6(-05)	1.00	0.99	0	**-2.0(-07)**

Table 3.9: Tabulated data of molecules at r = 5 AU which show greatest ratio and abundance differences with and without radionuclides between S_X = 1 and 0.3. Columns are defined as thus: **FA1**: S_X = 1 final abundance with radionuclides, **FA0.3**: S_X = 0.3 final abundance with radionuclides, **R1**: S_X = 1 ratio value, **FA0.3**: S_X = 0.3 ratio value, **AD1**: S_X = 1 abundance difference, **AD0.3**: S_X = 0.3 abundance difference. Values highlighted in bold depict that molecule to be the most enhanced or depleted for that particular stat in the entire chemical network.

Species	FA 1	FA 0.3	R 1	R 0.3	AD 1	AD 0.3
CH_3CN^+	1.3(-17)	4.3(-17)	**1.16**	1.8(+03)	1.8(-18)	4.3(-17)
NO	6.0(-10)	1.7(-10)	1.03	**3.1(+04)**	1.7(-11)	1.7(-10)
HC_3N	6.1(-07)	5.3(-07)	1.01	1.13	**4.0(-09)**	**6.0(-08)**
DSO^+	3.2(-22)	1.7(-20)	**0.64**	66.7	-1.8(-22)	1.7(-20)
G-C_3	5.2(-24)	8.5(-24)	0.95	**1.1(-07)**	-2.6(-25)	-7.9(-17)
N_2	9.9(-06)	1.0(-05)	0.99	1.01	**-1.0(-08)**	4.0(-08)
CO	6.7(-05)	6.7(-05)	1.00	0.99	0	**-2.0(-07)**

Table 3.10: Tabulated data of molecules at r = 10 AU which show greatest ratio and abundance differences with and without radionuclides between S_X = 1 and 0.3. Columns are defined as thus: **FA1**: S_X = 1 final abundance with radionuclides, **FA0.3**: S_X = 0.3 final abundance with radionuclides, **R1**: S_X = 1 ratio value, **FA0.3**: S_X = 0.3 ratio value, **AD1**: S_X = 1 abundance difference, **AD0.3**: S_X = 0.3 abundance difference. Values highlighted in bold depict that molecule to be the most enhanced or depleted for that particular stat in the entire chemical network.

Species	FA 1	FA 0.3	R 1	R 0.3	AD 1	AD 0.3
G-S_2	1.7(-50)	3.3(-41)	**3.19**	19.0	1.2(-50)	3.1(-41)
G-CHD	2.1(-19)	4.6(-20)	1.11	**48.1**	2.1(-20)	4.5(-20)
CH_2	1.8(-09)	1.2(-09)	1.02	1.29	**4.0(-11)**	2.7(-10)
CD_3	1.4(-13)	1.8(-13)	**0.96**	**0.71**	-5.8(-15)	-7.4(-14)
N_2	9.7(-06)	9.8(-06)	0.99	1.01	**1.0(-08)**	**1.0(-08)**
CH_4	3.2(-07)	4.1(-07)	0.99	0.99	-1.0(-09)	**-5.0(-09)**

Walsh et al. 2012) have considered and investigated the influence of UV and X-ray photodesorption processes on disk chemistry, which greatly affect the gas-grain interaction near the disk surface and deeper regions where the disk opacity is low enough for X-rays and UV-photons to penetrate. These works have also considered cosmic-ray induced desorption, but found the process to have minimal effects on inner (r < 10 AU) disk chemistry.

Surface densities at the inner disk midplane are sufficient to attenuate UV and X-rays to nominal levels, but since cosmic-rays can penetrate to the inner midplane depths of the 10^{-7} $M_\odot$ yr^{-1} accretion disk, it is still important to check whether cosmic-ray induced desorption may be an influential desorption process here for this disk, which should be supplemented in some form along with the traditional thermal desorption mechanism. This is usually modelled through the use of a separate network of cosmic-ray induced desorption reactions, e.g.

$$\text{G-CH}_4 + \text{CRPHOT/CRP} \rightarrow \text{CH}_4,$$

or more implicitly by simply adding a calculated desorption rate, $k_{\rm crd}$, to the thermal desorption rate, $k_{\rm therm}$:

$$k_{\rm des} = k_{\rm therm} + k_{\rm crd}.$$

One may expect cosmic-ray induced desorption to increase the fractional abundance of molecules in the gas which may then be prone to the ionization effects of the radionuclides. At the same time its desorption effects will be reduced by the attenuation of cosmic-rays passing through the dense disk medium at the midplane.

To determine the influence of cosmic-ray induced desorption on the chemistry with and without the presence of radionuclides, the implicit method by Leger et al. (1985) and Hasegawa & Herbst (1993) is followed. As summarized in Walsh et al. (2010), the assumption is based on the impulsive heating of grains by the transfer of around 0.4 MeV into each dust grain of radial size 0.1 μm by cosmic-rays consisting of relativistic Fe nuclei impacting with an energy 20 – 70 MeV per nucleon. Supposing that most molecules desorb from grains around 70 K, the expression for cosmic-ray induced desorption is given by:

$$k_{\rm crd} = f(70{\rm K})k_{\rm therm}(70{\rm K})\frac{\zeta_{\rm CR}}{5\times10^{-17}} \quad {\rm s}^{-1}, \tag{3.9}$$

as in Heinzeller et al. (2011). Here $k_{\rm therm}$ is the thermal desorption energy (Equation 2.28) at 70 K, and $f(70\ {\rm K}) = 3.16\times10^{-19}$ is defined as the duty cycle of grains which, is essentially considered as the ratio of the desorption cooling time from 70 K ($\sim 10^{-5}$ s^{-1}) to the time interval between subsequent heatings to 70 K ($\sim 3.16\times10^{13}$ s). Since this model inherently considers grains with radius 0.2 μm, and that the evaporation rate is proportional to the square of the grain radius (see Eq. 22 in Leger et al. 1985), $k_{\rm crd}$ is multiplied by an extra factor of 4.

Another important feature which has thus far not been addressed in the literature is the desorption potential from the radionuclides; in particular ^{26}Al. Gilmour & Middleton (2009) speculated that the abundance of ^{26}Al scales in some form with the evaporation rate of volatiles as planetesimals are heated. Then, perhaps

the same idea can be applied to earlier disk epochs where the size of grains were much smaller. An approximation (albeit a rather crude one) is to further supplement the total desorption rate with an additional value representing the radionuclides as a function of the expression defined in Equation (3.8), and replacing $\zeta_{\rm CR}$ with $\zeta_{\rm R}$ $\sim 7.6 \times 10^{-19}$ s^{-1}. With the basis of ^{26}Al being completely locked away in grains and the grain-size assumed in this model being much less than 1 cm, the emitted radiation from its decay is not attenuated by the encasing grain itself and traverses through the disk medium (e.g. Umebayashi & Nakano 2009). Finocchi & Gail (1997) concluded that the β^+-decay of a single ^{26}Al nucleus releases a single 1.809 MeV photon, plus two other photons from e$^+$–e$^-$ pair annihilation at 0.511 MeV each when the β^+-particle is indeed eventually halted in the disk medium. This is a total energetic potential of $\sim$ 2.8 MeV if one neglects radionuclide attenuation itself, i.e. that the emitted energy does *not* interact with the surrounding gaseous material.

Then if one crudely assumes that the energy interacts only with other neighboring grains (and is therefore purely available for grain heating), and that this energy of 2.8 MeV is completely transferred to the grain, then the duty cycle of grains to 70 K is enhanced by a factor $\sim$ 3.2/0.4 = 8, where:

$$k_{\rm rad} \sim 7\ k_{\rm crd}.$$

Figure 3.7 compares the $S_{\rm X}$ = 1 midplane abundance ratio (top row) and abundance difference profiles of some molecular cations and abundant molecules ($\sim 10^{-7}$) that were shown to be sensitive in Tables 3.4 and 3.5, firstly considering only thermal desorption (left), thermal desorption and cosmic-ray induced desorption (middle), and thermal, cosmic-ray and radionuclide-induced desorption (right). Irrespective of the extra desorption potential, these plots show that there is no enhancement whatsoever with the supplementation of these additional desorption processes.

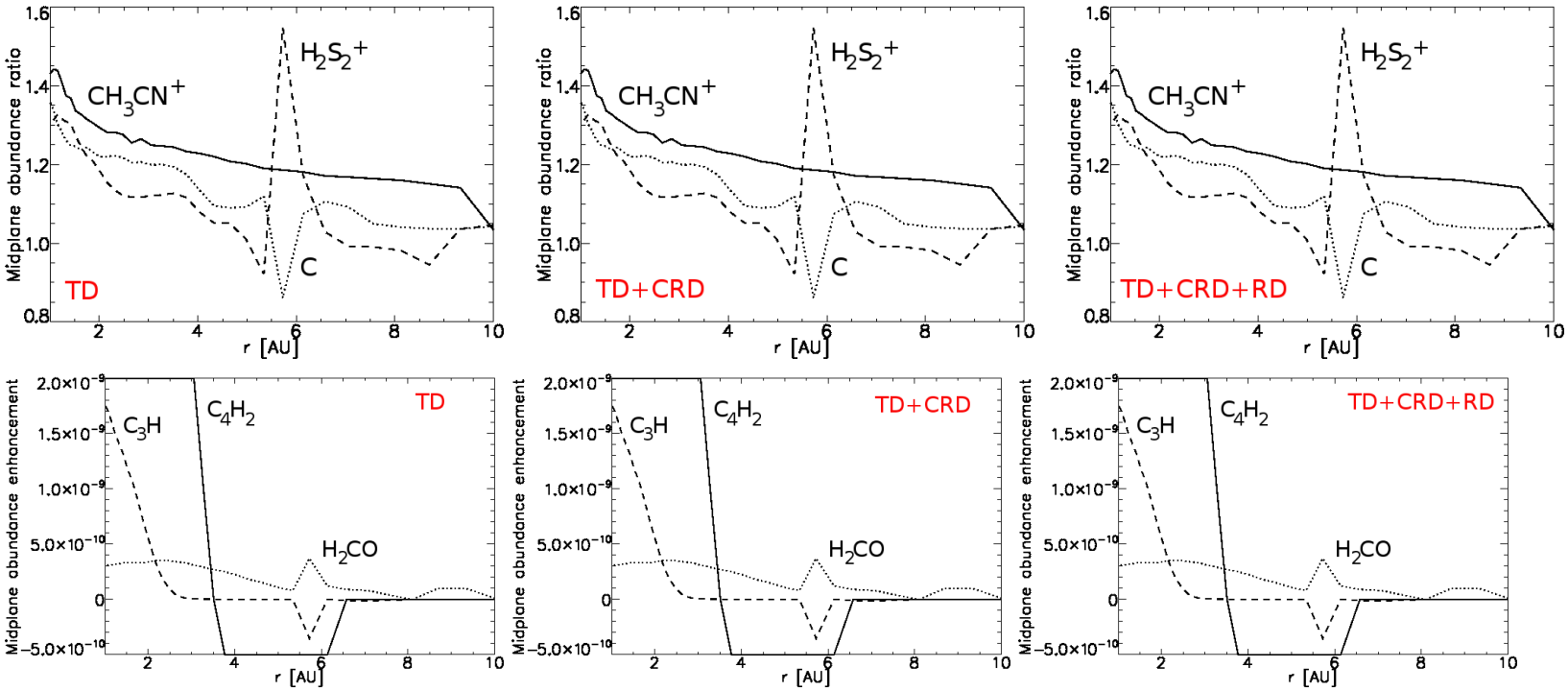

Figure 3.7: $S_X = 1$ midplane abundance ratio profiles of CH_3CN^+, $H_2S_2^+$ and C (top row), and abundance difference profiles of C_4H_2, C_3H and H_2CO (bottom row), firstly considering only thermal desorption (left), thermal desorption and cosmic-ray induced desorption (middle), and thermal, cosmic-ray and radionuclide-induced desorption (right).

3.4.4 Ionization fraction

The two images of Figure 3.8 present the 1+1D ionization fraction distribution for the 10^{-7} $M_{\odot}$ yr^{-1} accretion disk up to a radius of 25 AU (left) and 10 AU (right) with the inclusion of radionuclides, and with a sticking coefficient $S_X = 1$. The white region depicts where the ionization fraction is below 10^{-12}, i.e. a dead-zone. In this accretion model with $S_X = 1$, the dead-zone extends out to a midplane radius just beyond 25 AU.

Figure 3.9 compares the overall S_X=1 and S_X=0.3 ionization fraction profiles at the midplane with and without radionuclides up to a radius 10 AU. In both cases the profiles decrease as the total number of cations in the gas is reduced and lost to higher order hydrocarbon species by ion-neutral and recombination reactions in the gas. The difference between the ionization fraction profiles with radionuclides (solid line) and without (dashed) is negligible (i.e. much less than an order of magnitude) and unnoticeable. However the overall ionization rate in the S_X=0.3 model is enhanced. The enhancement at 10 AU is almost an order of magnitude, converging to around half an order of magnitude at 1 AU.

Lastly, Figure 3.10 depicts the ionic fraction ratios of the important cations C^+, HCO^+, Fe^+ and CH_3OH^+ (as a function of their neutral equivalent) with radionuclides (left image) and without (right image) for S_X=1. The differences in the ionic ratio profiles of C^+/C, HCO^+/HCO, Fe^+/Fe and CH_3OH^+/CH_3OH are seen to be nominal. The cation with the largest ionic/neutral ratio is CH_3CO^+ with a consistent ionic fraction profile of $\sim$ 1.4 in both cases from 1 to 10 AU. This particular profile is beyond the scale of the two figures and therefore cannot be shown.

Since there is no variation whatsoever in the molecular abundances whilst incorporating cosmic-ray induced desorption, the associated ionization fraction distributions also remain the same.

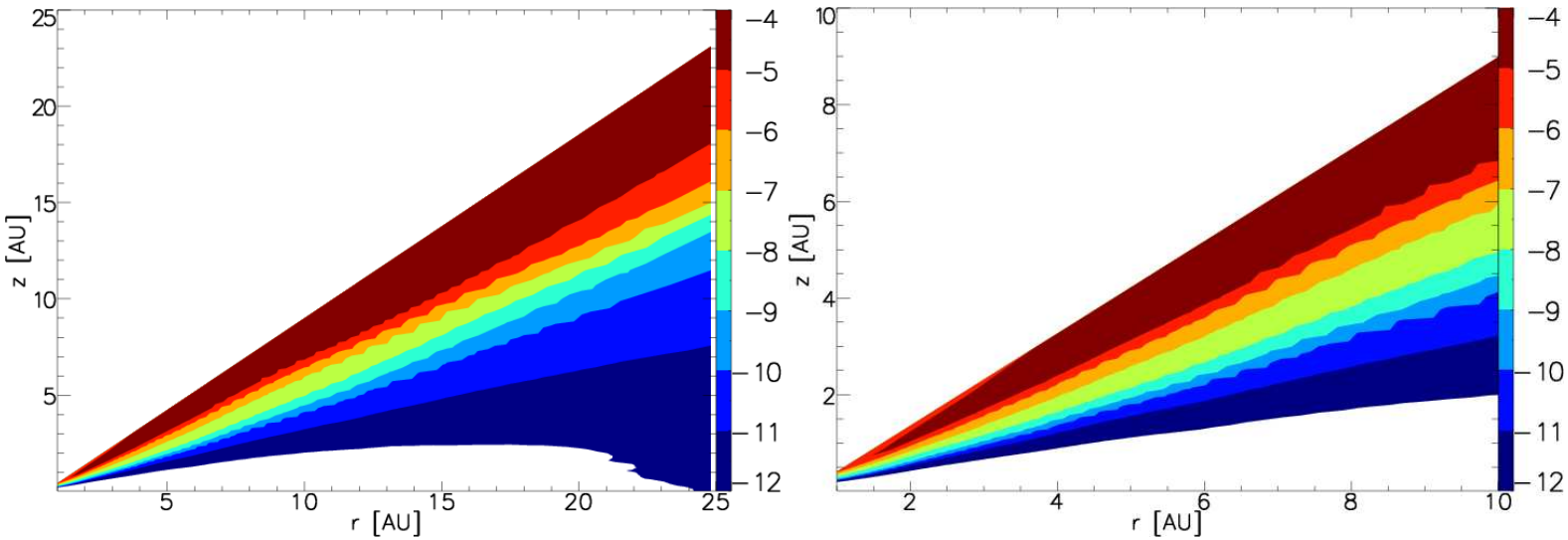

Figure 3.8: The overall 10^{-7} $M_{\odot}$ yr^{-1} ionization fraction distribution inside a radius of 25 AU (left) and 10 AU (right). The white regions represent an ionization fraction less than 10^{-12}.

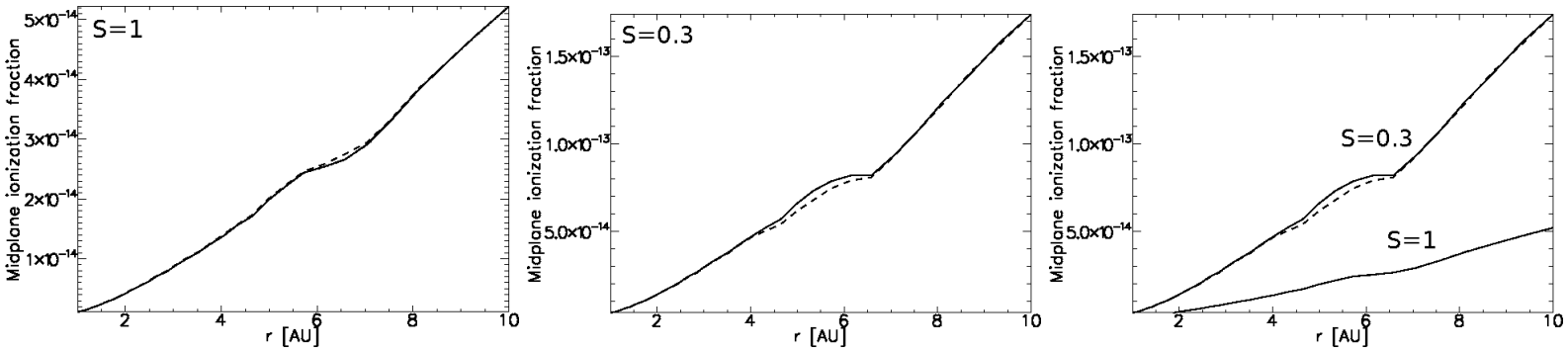

Figure 3.9: Overall ionization fraction profiles for the 10^{-7} $M_\odot$ yr^{-1} accretion disk inside a radius of 10 AU, with radionuclides (solid line), and without radionuclides (dashed line) for $S_X = 1$ (left), $S_X = 0.3$ (middle) and together (right).

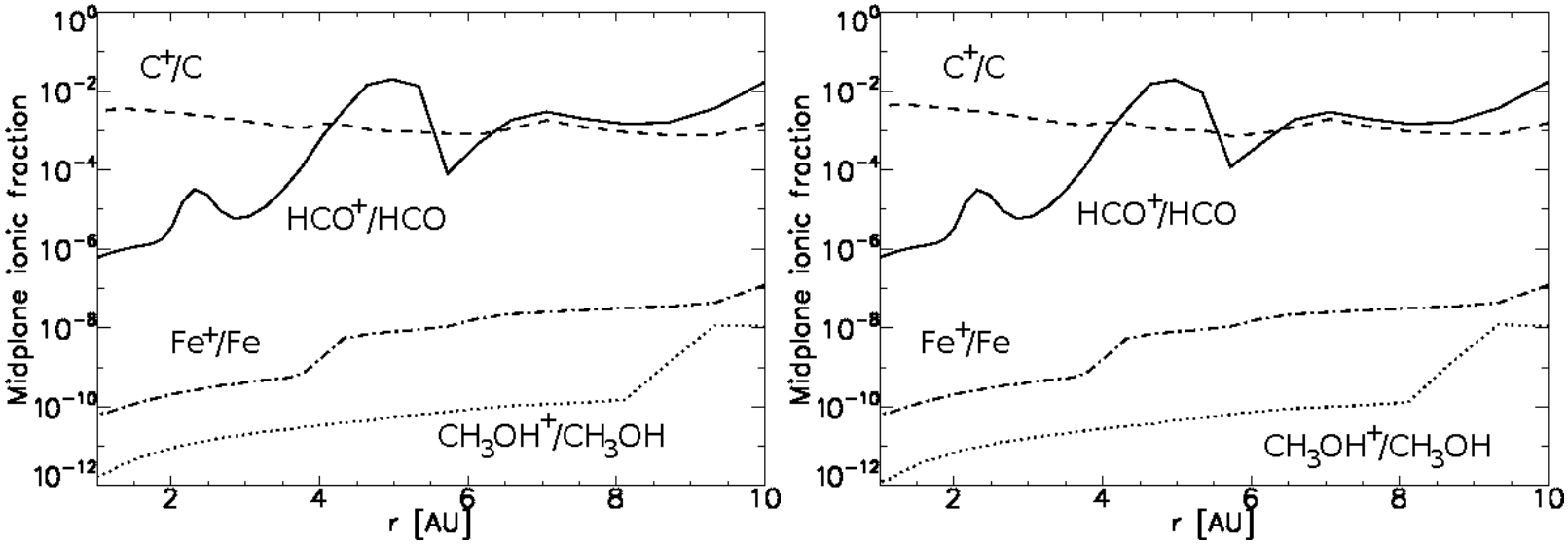

Figure 3.10: $S_X = 1$ ionic/neutral ratio profiles for C^+, HCO^+, Fe^+ and CH_3OH^+ with radionuclides (left) and without (right).

3.5 Discussion

3.5.1 Chemical tracers of radionuclides

The current idea of radionuclide excesses in our own early solar system is certainly proving a motivation for modellers to determine as much information about their potential effects in firstly ionizing chemistry in earlier PPD epochs, where stellar accretion rates are relatively high (10^{-7} $M_\odot$ yr^{-1} – 10^{-10} $M_\odot$ yr^{-1}), where gas and dust are well-mixed, and grains are small ($r < 1$ cm). But also secondly as an internal heating source, increasing the evaporation of volatile species in later epochs, where stellar accretion has ceased, significant dust coagulation has taken place, and planetesimals are forming.

Radionuclides are not directly traceable from PPD observations. One of the main motives of this particular investigation has been to present results which may help answer whether or not the presence of radionuclides, to the excesses established from our own solar system, can be chemically traced in other disks via their effects on chemistry, and thus determining whether our solar system is abnormal and unique in this context. To start with, a potential chemical tracer must be abundant enough to be observable and, based on the 1-D model results presented in this investigation, must emit prominently in the sub-mm regime, associated with the colder midplane regions. This is obviously constrained by the current spatial and spectral resolutions of current sub-mm receivers, restricted to observing only the outer $r > 50$ AU regions of the disk. ALMA, on the other hand will have the resolution to probe inner ($r < 10$ AU) disk regions on on a milli-arcsecond scale, once fully operational.

Ideally a candidate may have already been observed in PPDs. Even though these observations are made at larger radii than considered here, current ideas suggest this material is accreted eventually to the $r < 10$ AU regions. Based on these two criteria, the most abundant molecules already observed in the sub-mm regime, and

which have shown sensitivity in terms of abundance differences are HCN and C_2H_2 (Table 3.5). These have fractional abundances $\sim 10^{-7}$ inside 5 AU, and are depleted $\sim 10^{-9}$. This accounts to an abundance percentage difference of ~ 1 %.

Explicitly predicting whether the difference between the molecular emissions would be detectable requires simulating the observational data which ALMA will take. These differences may be presented in the form of column densities, or integrated intensity fluxes. One generally-used simulating package is CASA (Common Astronomy Software Applications), which is discussed and used in Section 4.5. This requires extending this investigation to a 1+1D simulation, and to much further radii, where the resulting calculated flux becomes intense enough to be detectable. Since this investigation considers only 1-D, this is certainly a case for future work.

3.5.2 Uncertainties and assumptions

In this subsection, some of the uncertainties and assumptions made in this investigation are highlighted.

3.5.2.1 Radionuclide abundances

A major geological dispute still exists in the determination of the fractional abundances of the radionuclides, whereby often more than one fractional abundance value is proposed (see Tables 3.1 – 3.3). This translates to several possible ionization rate values for a particular radionuclide (Equation 3.4). For example, there exist two values of the $^{26}Al/^{27}Al$ ratio; the canonical $(4.5 - 5) \times 10^{-5}$ value, and the supra-canonical 7×10^{-5} value. These correspond to a canonical rate of 7.0×10^{-19} s^{-1} and supra-canonical rate of 1.0×10^{-18} s^{-1}. Although the supra-canonical value is less-regarded than the canonical, which is why it has not been investigated here, incorporating the supra-canonical rate into the model will enhance the ionization further, and enhance the ratio and abundance difference values. These enhancements would also be more significant in the $S_X = 0.3$ model compared to the $S_X =$

1.0 one.

3.5.2.2 Embedded or free radionuclides?

A particular disparity for the future is determining whether the radionuclides should be modelled, whereby they are either completely embedded in grains (Cowie & Songaila 1986; Stepinski 1992) or if a fraction persists freely in the gas (~ 0.1 % in Turner & Sano 2008). So far this has not altered the way in which radionuclides are modelled, since their presence is implemented purely as a function of ionization rate, as in this work. But as the dynamical and chemical effects of radionuclides in disks are better understood over time, the way in which radionuclides are interpreted in future PPD models will become important. Examples include the explicit modelling of isotropic photon trajectories from grains which simulate the emission of energy from embedded radionuclides, including attenuation of which there is already information about (e.g. Section 3.3.2), and individual photochemical reactions involving the 1.809 MeV photon released from ^{26}Mg relaxation, which could be implemented into future chemical networks.

3.5.2.3 Radionuclide desorption

This work has touched on the idea of radionuclides not only ionizing disk chemistry, but also potentially heating grains which are particularly abundant at the midplane. Decaying radionuclides should emit enough energy to heat surrounding grains to temperatures at which molecules frozen on their surfaces, are desorbed into the gas. This investigation has briefly modelled this process as a function of cosmic-ray desorption, which of course is not the most accurate method. But as previously mentioned, explicit dynamical modelling of emitted photon trajectories will improve the understanding of this potentially important desorption process.

3.5.2.4 Cosmic-rays vs stellar winds

Some works (e.g. Khajenabi 2012) have studied exclusively the effects of cosmic-rays enhancing MRI (and MHD) in PPD disks. However there is debate as to whether cosmic-rays are able to penetrate through a disk at all, since some have argued that T Tauri winds are sufficient to blow most of the incident flux away above the inner disk surface (e.g. Igea & Glassgold 1999). Some authors (e.g. Ilgner & Nelson 2006a,b,c, Turner et al. 2007, Turner & Sano 2008, Ilgner & Nelson 2008) prefer to tread carefully with cosmic-rays, and have omitted them altogether from their dynamical calculations of disks. Instead they focus on the effects of X-rays and radionuclides in driving MHD. On the other hand, astrochemists still readily incorporate cosmic-rays into their models. Omitting cosmic-rays entirely from this model would have drastic effects on chemistry, reducing the ionization rate significantly along the midplane. Modelling only radionuclides in this scenario will likely enhance the production of molecular cations slightly, but over time the chemistry will be dominated by high-order hydrocarbons which are not broken-back down by cosmic-rays, which would otherwise be present.

3.5.2.5 Modelled density distribution

Sections 2.3.3 and 3.3.1 touched on the comparisons between the lower surface density distribution considered in this model, and the higher MMSN surface density distribution considered in other works such as Sano et al. (2000) and Umebayashi & Nakano (2009). Other distributions have also been considered when modelling radionuclides, such as the disk structure from Duschl et al. (1996) in the work of Finocchi & Gail (1997):

$$\Sigma(r) = 2500\left(\frac{r}{1\mathrm{AU}}\right)^{-3/5} \quad \mathrm{gcm}^{-2}, \tag{3.10}$$

whose modelled geometrically-thin disk also has a surface density distribution significantly greater than this model. These assumptions ultimately result in different

degrees of cosmic-ray attenuation, which in the Finocchi & Gail (1997) and Umebayashi & Nakano (2009) investigations, locate regions attributed solely to the ionization effects of the radionuclides, unlike in this work. Other density distributions which have not necessarily been used to model the chemical effects of radionuclides, but could be utilized for future comparison include the low-density Brauer et al. (2008a) model:

$$\Sigma(r) = 45\left(\frac{r}{1\mathrm{AU}}\right)^{-4/5} \quad \mathrm{gcm}^{-2}, \tag{3.11}$$

or the modified MMSN high–density Desch (2007) model:

$$\Sigma(r) = 5.1 \times 10^{4}\left(\frac{r}{1\mathrm{AU}}\right)^{-2.2} \quad \mathrm{gcm}^{-2}. \tag{3.12}$$

A detailed comparison of these distributions can be found in Zsom et al. (2010).

3.5.2.6 Maintenance of stellar accretion rate and implication on radionuclide epoch

In reality it is unlikely that a stellar accretion rate of 10^{-7} $M_\odot$ yr^{-1} and 10^{-8} $M_\odot$ yr^{-1} can be maintained with the low surface densities of this model. This is probably attributed to an error in the calculation of the initial gas temperature and density distribution (H. Nomura; private communication). Recent models using either the Lynden-Bell & Pringle or MMSN physical prescriptions (Table 2.1) have larger surface densities, and are more reasonable assumptions of surface densities associated with these stellar accretion rates. The surface densities from this model are instead better representations of an epoch later in the evolution of a protoplanetary disk, where the stellar accretion rate is lower. In reality this has implications for radionuclides, since firstly meteoritic evidence suggests injection took place when the solar nebula was young and the stellar accretion rate was high, and secondly by this stage their effect on the gas may have diminished due to decay, or they may be encased in grains where sufficient coagulation has taken place. So this stellar accretion rate model may be inappropriate for modelling radionuclides during a time when they

were having an effect on disk chemistry. Comparisons between the chemical results discussed in this chapter and those incorporating a more recent physical model with larger surface densities should be investigated in the future, as should a general study of chemical effects with different physical prescriptions.

3.5.2.7 Accretion

This investigation has assumed inward radial accretion along the midplane. In earlier discussions of the literature (Section 1.5.4), it had been argued that inward accretion was likely not uniform. Accretion is most rapid nearer the surface where the disk was magnetorotationally-unstable and prone to MHD turbulence, and the ionization fraction was high ($\sim 10^{-3} - 10^{-4}$), whilst decreasing towards the midplane, upon where the disk eventually becomes magnetorotationally-stable ($x(\mathrm{e}) \leq 10^{-12}$) in an apparent dead-zone, where accretion is stunted or halted during the viscous–phase. However some recent 2-D dynamical models (e.g. Tscharnuter & Gail 2007) have simulated inward accretion in the upper disk layers, with outward transport along the midplane, owing to the influence of turbulent mixing processes. Nevertheless, the chemical evolution of a 1-D specific model which simulates no accretion along the midplane (i.e. starting from the same initial abundance chemistry at each radial grid point) would likely be very different compared to the accreted model considered in this investigation, and is a plausible scenario since the ionization fraction is below 10^{-12} in this modelled disk (Figure 3.8).

3.5.2.8 Turbulent mixing

In Section 1.5.4, the idea of turbulent mixing in disks was summarized. Turbulence is likely a 3-dimensional process which varies considerably throughout a disk, making it computationally challenging to simulate over an entire disk (Semenov 2011). Some models (e.g. Turner et al. 2007; Turner & Sano 2008; Ilgner & Nelson 2008; Dzyurkevich et al. 2010) have already attempted dynamical 3-D simulations of lo-

calized disk "slabs", whilst Tscharnuter & Gail (2007) have modelled over an entire disk in 2-D. Previous models (e.g. Ilgner et al. 2004, Ilgner & Nelson 2006b, Semenov & Wiebe 2011, Heinzeller et al. 2011) have also simulated the influence of basic turbulent vertical-mixing processes on the chemical evolution of 1+1D disks, which transports chemistry to-and-from the midplane. Molecules shown to be sensitive to mixing include NH_3, CO_2, O_2 and C_2H_2, the latter molecule of which was also shown to be sensitive to the presence of radionuclides (Table 3.5). Since it is thought that mixing timescales are shorter than accretion timescales, the chemical composition is likely to change along the midplane if it were incorporated into this model. The ionization fraction may also vary depending on the recombination timescale of free electrons sinking towards the midplane.

3.5.2.9 Ionization fraction

The ionization fraction distribution in Figure 3.8 is primarily determined by the photoprocesses considered in the model. Since stellar UV and X-ray photoprocesses are not explicitly implemented here, the ionization fraction near the surface is underestimated. If these photoprocesses were implemented, the ionization fraction would be enhanced nearer the surface, and the chemistry would alter with it. The higher electron density generated from these additional photoprocesses will slow down the rate at which the magnetic-field is leaked away (Umebayashi & Nakano 1980), and potentially increase MHD in these regions. The ionization fraction is unlikely to change at the midplane, but if turbulent mixing processes were to be considered then one may see an enrichment of molecules at the midplane which are only formed in the surface and warm-molecular layer regions. Consequently, the chemical enhancements and depletions with radionuclides may vary somewhat.

3.5.2.10 Magnetic Reynolds number

This investigation has only briefly discussed the overall ionization fraction in the 10^{-7} $M_{\odot}$ yr^{-1} accretion disk. More thorough, dynamical studies of the Magnetic Reynolds number, discussed in Section 1.5.4, have been made (e.g. Sano et al. 2000; Ilgner & Nelson 2006b; Walsh et al. 2012) and it would be interesting to assess, with regards to this particular model, whether the Re_M alters as a result of the extra ionization potential provided by the radionuclides. One would probably expect little change since the ionization fraction difference with and without radionuclides is minimal, but should be investigated for completeness.

3.5.2.11 Grain charge

At all points in the disk, the electron number density, used to calculate the ionization fraction, is equal to the total cation number density, since charge must be conserved. At the same time, it is assumed that grains act as an anionic sink for cations in the gas. Comparative studies of basic chemical networks which model the charge distribution of grains have been made (e.g. Ilgner & Nelson 2006a) and indicate that grains are the dominant charge carriers at the midplane, where the free electron number density is low. Despite differences between their basic chemical networks, Oppenheimer & Dalgarno (1974) and Umebayashi & Nakano (1980) showed that metallic cations such as Na^+, Mg^+, Ca^+ and Fe^+ are very important in regulating the charge-state distributions of grains. Since this model only considers Fe and Fe^+ and singly-charged cations and grains, adopting some of the more metallic-rich network of Oppenheimer & Dalgarno (1974) may be interesting to see whether the abundance sensitivity with radionuclides is altered in any way.

3.5.2.12 Grain morphology

In this model the grain radius is fixed at 0.2 μm. There has already been much work comparing the chemistry between disk models with different grain sizes (e.g. Turner & Sano 2008, Dullemond et al. 2008, Vasyunin et al. 2011, Dominik & Dullemond 2011) and also the impact this has on the dynamics of the disk (Sano et al. 2000, Turner & Sano 2008, Brauer et al. 2008b). Larger grains reduce the overall surface area available for species in the gas to interact, and disk opacity is reduced, enabling UV and X-ray photons to propagate deeper into the disk. Grain sizes may also vary in different parts of the disk (e.g. Miotello et al. 2012) and settle towards the midplane over time (e.g. Fogel et al. 2011). Increasing the grain size (i.e. up to 1 cm) in this model may result in a similar enhancement in ratio and abundance difference sensitivities when changing from S_X = 1.0 to 0.3, and reduce the size of the dead-zone, or even remove it altogether, as was shown in Sano et al. (2000).

Different grain compositions have also been investigated in the past which differ from the composition considered in this model, which alters both their adiabatic properties and heating efficiency. This model has neglected grain-surface chemistry for simplicity, which would otherwise likely enhance volatile species initially formed on the grain, and which are then returned to the gas to be further ionized by the radionuclides. Other possibilities include the more complex modelling of non-spherical grain morphology as they aggregate (e.g. Voshchinnikov et al. 1999; Ilgner 2012), grain sputtering (e.g. Bringa & Johnson 2004) and "bouncing" after reaching a critical size of a few cm (e.g. Zsom et al. 2010). All of these aspects would alter the radionuclide sensitivities since gas-grain interaction is fundamental to the abundances of molecules residing at the midplane.

3.5.2.13 Chemical completeness

As with other works which consider a reduced chemical network, models cannot make predictions for the chemical evolution of species which are not included in

them. The same goes for reaction types, of which stellar-UV and X-ray photoreactions and desorption, cosmic-ray photodesorption reactions and grain-surface reactions are not included in this model. In addition to the diverse physical approaches in disk modelling, chemical models are generally different (see Section 2.2 and Ilgner & Nelson 2006b) making it difficult to compare between results. This is an argument for making models as chemically complete as possible in future work, if one is able to meet the larger computational demand.

3.6 Summary

In this chapter, the influence on inner disk chemistry at the midplane, by incorporating the effects of radionuclides has been discussed. Namely, the presence of the radionuclides have been modelled purely as a function of their combined ionization rate per H_2 molecule, 7.6×10^{-19} s^{-1}, and added to the cosmic-ray ionization rate which varies as a function of the column density and surface density of the disk. The most ionizing radionuclide is ^{26}Al, found to have been around six times more abundant in our early solar system than in the local interstellar medium, and may have been important in influencing both its early chemistry and dynamics.

Firstly, this investigation has found that the most sensitive species, with the extra ionization rate provided by the radionuclides, at the midplane inside a radius of 5 AU are hydrocarbon cations such as CHD_2OH^+ and CH_3CN^+. However, these abundances are $\leq 10^{-20}$ and the sensitivity, measured as an abundance ratio between radionuclide inclusion and omission, scales inversely with both the actual abundance relative to H_2, and also the abundance difference between radionuclide inclusion and omission, i.e.

$$\text{Ratio} \propto \frac{1}{\text{Difference}} \propto \frac{1}{\text{Abundance}}.$$

From an abundance difference perspective, the molecules showing the greatest change are C_4H_2, HC_3N and C_3H which are all enhanced, and HCN, CH_4, C_2H_2 and N_2

which are all depleted. The abundances of these molecules are much higher than the hydrocarbon cations, $\geq 10^{-7}$. For some molecules such as C_2H and C_2H_2, the chemical enhancements and depletions can be understood relatively easily, whereby the most sensitive channels involve small changes to the reaction rates of similar cation equivalents such as $C_2H_3^+$ and $C_2H_4^+$. For others such as N_2 it is not so clear.

Secondly, a comparison was made specifically between the chemical effects of radionuclide ionization inclusion for a model considering a grain sticking-coefficient of $S_X = 1$ and 0.3. Switching to the lower sticking coefficient value was shown to enhance both the ratio sensitivity and abundance differences of certain molecules such as CH_2DOH^+ and C_4H_2, and notably deplete the abundance of CO.

Thirdly, the ratio and abundance differences from the original model, which considered only thermal desorption, were compared to simulations which incorporated cosmic-ray induced desorption, added purely as a supplement to the thermal desorption rate, and also a "crude" approximation of the potential radionuclide desorption rate at the midplane. Neither of these additional desorption processes were shown to alter any of the original ratio or abundance differences.

Finally the changes to the overall ionization fraction at the midplane were investigated. Although it was found that the difference between the ionization fraction profiles with and without radionuclides was nominal between the $S_X = 1$ and 0.3 models, the overall ionization fraction was enhanced when $S_X = 0.3$. The ionic fraction ratio profiles of C^+, HCO^+, Fe^+ and CH_3OH^+, with and without radionuclides were also shown to be unchanged for the $S_X = 1$ model.

The discussed molecular abundance differences may correspond to, and signify the presence of radionuclides in other protoplanetary disks to the excesses deduced from our own early solar system, with the advent of ALMA potentially probing the deeper inner midplane regions associated with sub-mm emission. The best speculated candidates at this current time are HCN and C_2H_2 which have already been

observed in other disks. Further work, such as extending this investigation to a full 1+1D simulation, incorporating the effects of UV and X-rays (including their photodesorption effects), modelling the heating and chemical desorption effects of the radionuclides from grains, modelling the effects of turbulent diffusion and vertical mixing, monitoring the effects of different grain sizes, calculating the differences in column density values, and integrated intensity flux differences from the CASA ALMA simulator for HCN and C_2H_2, are just a few examples during this exciting period of astrochemical modelling.

CHAPTER 4

Stellar accretion rate influence on inner disk chemistry

4.1 Overview

In the last chapter, the effects of various forms of radiation, on disk chemistry in planet-forming regions were discussed. In particular, the effect that radionuclides such as ^{26}Al may have in photodissociating and ionizing chemistry such as C, C_2H and C_2H_2, in the epoch representing a stellar mass accretion rate of 10^{-7} $M_\odot$ yr^{-1}. However, chemistry between different epochs can vary, given the changes in physical conditions over time. The stellar accretion process is thought to slow over time until, eventually, it stops (Hartmann et al. 1998). As this process slows, in-

creased dust coagulation and localized accretion within the disk itself can result in the formation of planets which sweep up surrounding disk material, the evidence for which is observed in disks with apparent "gaps" (e.g. Varnière et al. 2006). So far, bridging the gap between the basic chemistry observed in protoplanetary disks and the more-complex chemistry which resides in planets such as in our solar system proves a challenge. Accretion is thought to be one important factor, by bringing complex species formed and preserved in the ice such as CH_3OH, H_2CO and CH_4 from the colder outer disk, to the gas-phase in the warmer, inner disk (e.g. Nomura et al. 2009). Given enough time, these complex species will undergo chemical processing to simpler species owing to the hotter and more radiatively-intense conditions of the inner disk. The extent of this chemical mixing as a result of accretion is dependent on: (i) the accretion timescale, $\tau_{\rm acc}$, (ii) the calculation timescale at each grid point, $\tau_{\rm calc}$, (iii) the gas and ice-to-grain interaction timescale; in particular the desorption and adsorption timescales, $\tau_{\rm des}$ and $\tau_{\rm ads}$, which govern whether a species is returned to the gas or not and how rapidly these processes occur, and (iv) the chemical timescale, $\tau_{\rm chem}$, which considers the rate of gas-phase and photoreaction processes for species which are returned to the gas-phase. The latter three timescales, approximately, scale inversely with the corresponding rate-coefficients defined in Sections 2.4.1 and 2.4.2, i.e.

$$\tau_{\rm des} \sim k_{\rm therm}{}^{-1}; \quad \tau_{\rm ads} \sim k_{\rm freeze}{}^{-1}; \quad \tau_{\rm chem} \begin{cases} \sim k_{\rm gas}{}^{-1} & \text{for two-body reactions,} \\ \sim k_{\rm phot}{}^{-1} & \text{for photoreactions.} \end{cases}$$

In this chapter, the general chemistry calculated from the modelled disk with a stellar mass accretion rate of firstly 10^{-7} $M_\odot$ yr^{-1} and secondly 10^{-8} $M_\odot$ yr^{-1} is compared and discussed, particularly focusing on reactions involving species such as CO, CO_2, HCN, H_2O and H_2CO which have been observed in high abundance. A method is discussed for calculating the chemical evolution as a result of allowing the stellar accretion rate to vary from 10^{-7} $M_\odot$ yr^{-1} to 10^{-8} $M_\odot$ yr^{-1}, using a 1st order iteration method by combining their physical parameters. In chemical terms,

we compare the resulting 10^{-8} $M_{\odot}yr^{-1}$ chemical distribution between the chemical input of the dense-core model initial abundances listed in Tables 2.4 and 2.5, and the input from the resulting 10^{-7} $M_{\odot}$ yr^{-1} chemical distribution. The aim is to see which species, if any, are sensitive to the differences in chemical input, and translate these changes to differences in column density values which may or may not be observed by ALMA. The main set of results are "naturalized" simulations, following equation (2.17) in Section 2.3.6. A "normalized" set of results are also calculated, by normalizing $\tau_{\rm calc}$ at each radial grid point from Equation (2.17) according to the stellar mass accretion rate–disk age linear relation, $\log \dot{M}$ = -8.0 - 1.4 $\log t_{\rm age}$ from Hartmann et al. (1998).

4.2 General chemistry

Tables 4.1 and 4.2 highlight the various molecules which have so far been observed in T Tauri disks, in two wavelength regimes. IR observations are associated with hotter ($T \geq 350$ K) disk regions above the midplane, and originate from vibrational transitions of molecules. Sub-mm observations originate predominantly from colder (10 K $\leq T \leq$ 100 K, $r > 50$ AU) environments. Observations up to this point have been limited by the small angular size of protoplanetary disks. The exceptions so far are firstly the W. M Keck Observatory in Hawaii (www.keckobservatory.org) and Spitzer, both IR detectors. The first has been used to observe CO in inner 0.5 – 2 AU disk regions of V836 Tauri some 50 pc away, up to an angular resolution of 0.4", concluding that IR emission from CO arises in the inner hot surface region, directly exposed to both X-ray and UV radiation (see Najita et al. 2008). The second has been used to observe surface-residing CO, OH (Salyk et al. 2008, 2011), CO_2, HCN (Lahuis et al. 2006b) and H_2O (Pontoppidan et al. 2010a; Carr & Najita 2008, 2011) in numerous inner ($r \sim 1$ AU) T Tauri disks. The Atacama Large Millimeter Array (ALMA) has both the spectral and angular resolution to probe $r \leq 10$ AU regions

Table 4.1: IR molecular observations in young protoplanetary disks. Modified from Markwick & Charnley (2004). Acronyms are defined as follows: IRTF (NASA Infra-Red Telescope Facility), Keck (W. M. Keck Observatory), SST (Spitzer Space Telescope).

Detected molecule	**System**	**Reference(s)**	**Observing device**
CO	DQ Tau etc	Najita et al. (2003)	IRTF
	V836 Tau	Najita et al. (2008)	Keck
C_2H_2	IRS 46	Lahuis et al. (2006a)	SST
HCN	IRS 46	Lahuis et al. (2006a)	SST
H_2O	SVS 13	Carr et al. (2004)	IRTF
	AS 205A &	Salyk et al. (2008)	SST
	DR Tau		& Keck
CO_2	IRS 46	Lahuis et al. (2006a)	SST
OH	AA Tauri	Carr & Najita (2008)	SST

of disks in the sub-mm range, and detect exotic organics such as direct precursors to amino acids, which are seen in comets (see Markwick & Charnley 2004). Its full initiation is hoped to begin from 2013, and new ALMA Cycle-0, and Cycle-1 disk data expected soon, may confirm the presence of complex species such as CH_3OH, C_2H_5OH and benzene, from spectral lines in the sub-mm on a milli-arcsecond (inner disk region) scale.

These observations, along with those from pre-disk epochs such as molecular clouds and dense-cores (see Nomura & Millar 2004), have allowed modellers to establish a general chemical structure for protoplanetary disks around T Tauri stars. With the plethora of chemical species considered in this model, the following investigation in this chapter focuses on the most abundant of the species which have been observed; CO, H_2O, HCN and H_2CO, along with other species important in their chemical synthesis.

Previous work on the chemical modelling of inner ($r \leq 10$ AU) regions of pro-

Table 4.2: Sub-mm molecular observations in young protoplanetary disks. Modified from Markwick & Charnley (2004). Acronyms are defined as follows: JCMT (James Clerk Maxwell Telescope), IRAM telescope (Institute for Radio Astronomy in the Millimeter range telescope), OVRO (Ohio Valley Radio Observatory), SMA (Square Millimeter Array), NMA (Nobeyama Millimeter Array).

Detected molecule	System	Reference(s)	Observing device
CO	TW Hya	Kastner et al. (1997)	JCMT
		Dutrey et al. (1997b)	IRAM
	LkCa15 & GM Aur	Qi (2001)	OVRO
	LkCa15 & TW Hya	van Zadelhoff et al. (2001) & van Dishoeck et al. (2003)	JCMT
	TW Hya	Qi et al. (2006)	SMA
	MWC 480, LkCa15 & DM Tau	Piétu et al. (2007)	IRAM
CN	TW Hya	Kastner et al. (1997)	JCMT
	DM Tau & GG Tau	Dutrey et al. (1997b)	IRAM
HCN	TW Hya	Kastner et al. (1997)	JCMT
	DM Tau & GG Tau	Dutrey et al. (1997b)	IRAM
	LkCa15 & TW Hya	van Zadelhoff et al. (2001)	JCMT
		van Dishoeck et al. (2003)	
	LkCa15 & TW Hya	Thi et al. (2004)	JCMT
	TW Hya	Qi et al. (2008)	SMA
HCO^+	TW Hya	Kastner et al. (1997)	JCMT
	DM Tau & GG Tau	Dutrey et al. (1997b)	IRAM
	LkCa15 & TW Hya	van Zadelhoff et al. (2001)	JCMT
	TW Hya	van Dishoeck et al. (2003)	JCMT
	MWC 480, LkCa15 & DM Tau	Piétu et al. (2007)	IRAM
	TW Hya	Qi et al. (2008)	SMA

Table 4.2 (continued): Sub-mm molecular observations in young protoplanetary disks.

Detected molecule	System	Reference(s)	Observing device
CS	DM Tau &	Dutrey et al. (1997b)	IRAM
	GG Tau		
	IRC +10216	Young et al. (2004)	SMA
C_2H	DM Tau &	Dutrey et al. (1997b)	IRAM
	GG Tau		
N_2H^+	LkCa15 &	Dutrey et al. (2007)	IRAM
	DM Tau		
H_2CO	DM Tau	Dutrey et al. (1997b)	IRAM
	GG Tau		
	LkCa15	Aikawa et al. (2003)	NMA
	LkCa15	Thi et al. (2004)	JCMT

toplanetary disks have focused analysis on CO, HCN (Agúndez et al. 2008), H_2CO (Millar et al. 2003) and CH_3OH (Nomura et al. 2009). Benzene (see Woods & Willacy 2007), deuterated species (see Willacy & Woods 2009) and carbon isotope fractionation (see Woods 2009) have also been modelled in the past.

4.2.1 Stratification and timescales

A basic stratification of a protoplanetary disk was discussed in Section 1.4.7, and is generally seen to consist of a hot ($T \geq 1000$ K) photon-dominated surface layer (PDR), a warm-molecular layer and a colder, denser midplane. The general perception amongst models is that the disk chemical structure merges into a warm inner zone "soup" inside a radius of 20 AU, but this convergence only begins $\sim$ 5 AU in this model. Figure 4.1 illustrates how the timescales are related in the stratified disk, and is applicable to both 10^{-7} $M_\odot$ yr^{-1} and 10^{-8} $M_\odot$ yr^{-1} disks considered in this chapter.

In the r = 10 – 25 AU midplane, the high density and low temperatures are sufficient to freeze even the most volatile species such as CO onto dust grains (but not necessarily in the context of the r < 10 AU work presented here - see later). Here,

$\tau_{\rm des} >> \tau_{\rm ads}$, $\tau_{\rm chem} >> \tau_{\rm acc}$ and $\tau_{\rm chem} >> \tau_{\rm calc}$. $\tau_{\rm chem}$ is considered ∞ in comparison to $\tau_{\rm acc}$ and $\tau_{\rm calc}$, since the majority of species are frozen on grains, and not present in the gas to react.

In the radial direction towards innermost ($r \leq 1$ AU) midplane regions, all species are returned to the gas-phase since disk temperatures exceed desorption temperatures ($\tau_{\rm des} < \tau_{\rm ads}$ and column densities are sufficient to shield this region from the radiation-field, and chemical processing of more complex molecules to simpler ones occurs ($\tau_{\rm chem} < \tau_{\rm acc}$ and $\tau_{\rm chem} < \tau_{\rm calc}$). Here, the warm molecular-layer and midplane essentially merge since conditions are similar.

From the colder midplane vertically towards the surface, one sees a return of species to the gas with increasing temperature and decreasing density ($\tau_{\rm des} < \tau_{\rm ads}$), and a consequent increase in the rate of chemical processing. The extent of this processing here is dependent on how much of a given species and its reactants are returned to the gas, i.e. how much less $\tau_{\rm des}$ is than $\tau_{\rm ads}$, and the $\frac{\tau_{\rm chem}}{\tau_{\rm calc}}$ ratio. In general, a species achieves a "steady-state" abundance when $\frac{\tau_{\rm chem}}{\tau_{\rm calc}} \leq 1$, that is, chemical reactions are rapid enough to "finish" processing a species such that its abundance no longer changes over time. Species where $\frac{\tau_{\rm chem}}{\tau_{\rm calc}} > 1$ are not in steady-state.

Chemical models have shown that complex hydrocarbon species are destroyed more rapidly than they are formed upon return to the gas-phase. CH_3OH, in particular is not formed in the gas at all, and its survival in the inner disk has thus been suggested as a tracer of accretion velocity (see Nomura et al. 2009). H_2CO has been shown to trace the vertical temperature profile in the inner disk (see Millar et al. 2003). At the PDR surface, all species are in the gas, and the intense radiation field drives rapid photochemical breakdown of molecules to atoms and ionic species.

In chapter 2, the general physical and chemical processes considered in the model were discussed. In chapter 3, cosmic-ray induced photodesorption was supplemented simply as an addition to thermal evaporation rate originally given in

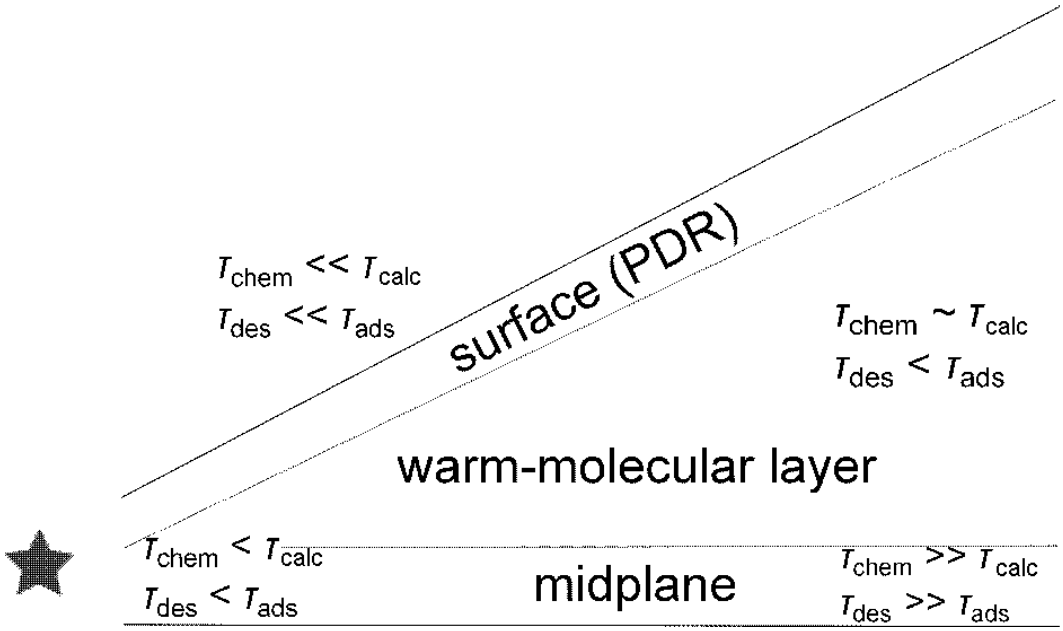

Figure 4.1: Schematic showing the stratification and general corresponding relationships between calculation, chemical, adsorption and desorption timescales at different regions of the disk (not to scale).

Equation (2.25). Since these additional process are not explicitly implemented into the chemical model as a separate set of photoreactions, they are omitted from the work in this chapter, which focuses particularly on the chemical reactions taking place in the 10^{-7} $M_\odot$ yr^{-1} and 10^{-8} $M_\odot$ yr^{-1} disk. In the following two sections (4.3.2 and 4.3.3), the resulting chemical distributions from both 10^{-7} $M_\odot$ yr^{-1} and 10^{-8} $M_\odot$ yr^{-1} disks are compared and discussed, representing snapshots in time of 1.78×10^5 years and 1.81×10^5 years respectively. The first of these sections addresses the general gas-phase reaction route chemistry in the PDR and warm-molecular layer (hereafter WML) for each of the species in Tables 4.1 and 4.2, in addition to CH_3OH and CH_4. The second covers the effects of desorption and adsorption processes at the midplane, which dominate over gas-phase reactions until the gas parcel is accreted to regions where temperatures are large enough to return molecules to the gas.

4.2.2 Comparison of molecular abundances in the PDR and warm-molecular layer

Figures 4.3 to 4.16 display the relative molecular distributions (with respect to H_2) of each of these molecules between the radii of 1 and 10 AU and maximum disk heights for both stellar accretion rates (7.5 AU for 10^{-7} $M_\odot$ yr^{-1} and 5 AU for 10^{-8} $M_\odot$ yr^{-1}). The top row images represent the full abundance variation for that particular molecule, whilst the the relative abundances in the bottom row images are normalized between 10^{-3} and 10^{-12}. The reaction routes for the molecules discussed are found to be identical in both disks, and the differences in chemical distributions are a result of the differences in the physical conditions of 10^{-7} $M_\odot$ yr^{-1} and 10^{-8} $M_\odot$ yr^{-1}. Figure 4.2 highlights the important production and destruction routes involving these species which take place in the PDR and WML.

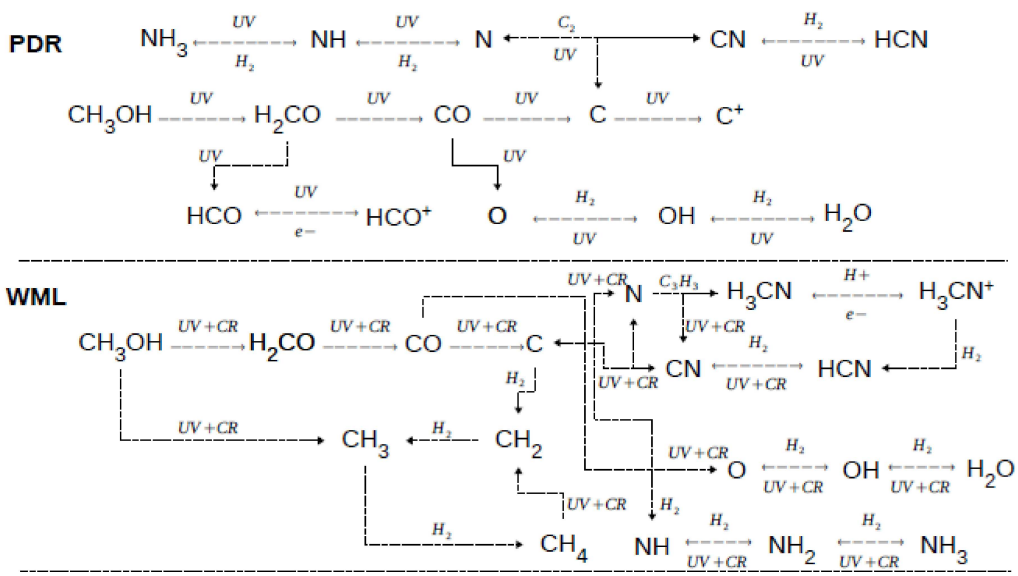

Figure 4.2: A summary of production and destruction reaction routes in the inner $r \leq 10$ AU PDR and WML.

Figure 2.3 detailed the density and temperature sensitivity between 10^{-7} $M_\odot$ yr^{-1} and 10^{-8} $M_\odot$ yr^{-1} disks. In the PDR, the gas density is, on average, 10^3 less in the

10^{-8} $M_\odot$ yr^{-1} disk, and therefore, the amount of H_2 available to react is less. This difference is not as great further down in the warm-molecular layer, but reduced interstellar UV-photon shielding due to the optically thinner 10^{-8} $M_\odot$ yr^{-1} disk and the lower temperature here (~ factor of 2) means that the PDR/WML boundary sits at a lower height in the 10^{-8} $M_\odot$ yr^{-1} disk.

In general, radial accretion to PDR regions which are similar in density and temperature between the disks result in similar depletions to less complex molecules, constituent atoms or ions. Accretion to regions where densities and temperatures are larger (i.e. the $r \leq 4$ AU PDR) in the 10^{-7} $M_\odot$ yr^{-1} disk result in preservation of molecules even up to the inner surface of the disk which are otherwise depleted in the 10^{-8} $M_\odot$ yr^{-1} disk. In most other models which consider stellar UV radiation (e.g. Walsh et al. 2010, Walsh et al. 2012), all molecules are processed on very short chemical timescales to atoms and ions at the PDR, hence the model used here overestimates the abundance of many molecules in these regions, particularly for H_2O, H_2CO and CH_3OH in the 10^{-7} $M_\odot$ yr^{-1} disk. Accretion throughout the warm-molecular layer does little to alter each of the molecules in the 10^{-7} $M_\odot$ yr^{-1} disk, which are influenced more by reactions with other species as opposed to UV-photons. The interstellar UV-field is attenuated more swiftly than cosmic-rays further down in the disk, and at the midplane, cosmic-rays dominate radiative processes with molecules which are mostly in the gas.

CO is the most abundant molecule after H_2 and He in this model, averaging an abundance of 10^{-5} relative to H_2 in both disks (Figure 4.3). CO is formed from the UV photolysis of H_2CO and HCO at the PDR, but is itself photodissociated more rapidly to atomic C and O. Here, the CO abundance drops to 10^{-6}. In the 10^{-7} $M_\odot$ yr^{-1} disk, CO depletion first begins $\sim r \leq 10$ AU at the PDR–WML boundary, where the photodissociative effects from interstellar UV and cosmic-rays are equal. At this point, the increased reservoir of C and O, and the shielding from photons is just sufficient to culture a synthesis of simple molecules such as CN, HCN, H_2O

and CH_4 which all peak here. This becomes more prevalent at smaller r as the rate of synthesis and gas density increases. This synthesis layer occurs closer in ($r \leq 2$ AU) in the 10^{-8} $M_\odot$ yr^{-1} disk. The formation of CO becomes increasingly governed by the photodissociation and endothermic destruction of CO_2 with H_2 further down in the disk, the latter of which also produces H_2O. This channel peaks in the highly shielded, innermost hot disk regions. CO_2 (Figure 4.4) generally traces the distribution of CO, albeit the $r \leq 6$ AU depleted region in the 10^{-7} $M_\odot$ yr^{-1} disk. CO and CO_2 are also formed from dissociative recombination of $HCO_2{}^+$, particularly at the PDR.

The molecular abundances of gas-phase OH, H_2O, and CN and HCN are dictated by the competition between the photodissociative destruction from interstellar UV and cosmic-ray photons, i.e.

$$\mathrm{OH + PHOTON \longrightarrow O + H,}$$
$$\mathrm{H_2O + PHOTON \longrightarrow OH + H,}$$
$$\mathrm{CN + PHOTON \longrightarrow C + N,}$$
$$\mathrm{HCN + PHOTON \longrightarrow CN + H,}$$

and temperature-sensitive endothermic formation reactions via H_2, e.g.

$$\mathrm{O + H_2 \longrightarrow OH + H,}$$
$$\mathrm{OH + H_2 \longrightarrow H_2O + H,}$$
$$\mathrm{CN + H_2 \longrightarrow HCN + H.}$$

The first process is most rapid where gas densities are sufficiently low (10^{-3} – 10^{-6} cm^{-2}), the interstellar UV-flux is unattenuated and adsorption processes are minimal. The second is particularly strong where temperatures are high ($T \geq 300$ K) and there is sufficient H_2 to react with ($n \geq 10^3$ cm^{-2}). In the 10^{-7} $M_\odot$ yr^{-1} disk at the PDR surface between $r = 4$ and 10 AU, the first process "wins" and H_2O and HCN photodissociates to OH and CN and their constituent atoms O, C and N. Inside 4 AU, the endothermic channel dominates due to the higher temperature, hence OH,

H_2O and HCN are abundant here.

In the same region of the 10^{-8} $M_\odot$ yr^{-1} disk, more atomic O is leached away from the $H_2O \leftrightarrow OH$ channel and the endothermic reactions are less rapid. H_2O and OH are therefore less abundant. While H_2O is ubiquitous throughout the entire $r \leq 10$ AU 10^{-7} $M_\odot$ yr^{-1} disk with a relative abundance of $\sim 10^{-4}$, it is only as abundant in a confined layer above the midplane ($z \leq 2$ AU) of the 10^{-8} $M_\odot$ yr^{-1} disk and depleted to $\sim 10^{-9}$ in the gas above this.

As in Walsh et al. (2010), CN exists abundantly in a layer above that of HCN near the surface of the 10^{-8} $M_\odot$ yr^{-1} disk highlighting the prominence of the CN $\leftrightarrow$ HCN channel, but HCN and CN are similarly abundant in the equivalent region of the 10^{-7} $M_\odot$ yr^{-1} disk. Here, CN and hence HCN are formed from C, N and O synthesis as a result of CO and N_2 destruction reactions.

C_2H is principally formed from the photodissociation of C_2H_2. C_2H_2 is most efficiently formed from dissociative recombination reactions involving higher order hydrocarbonic and hydrocyanic ions such as $C_2H_3^+$ and $H_2C_3N^+$. C_2H is abundant in the layer above C_2H_2 in the 10^{-8} $M_\odot$ yr^{-1} disk, with the boundary located at the point where the UV-photodissociation rate is equal to that of cosmic-rays. In the 10^{-7} $M_\odot$ yr^{-1} disk, C_2H_2 coexists with C_2H (apart from the surface) by reason of the increased recombination rate in the denser disk. C_2H acts as a good indicator of the interstellar UV–cosmic-ray photodissociation threshold in the 10^{-7} $M_\odot$ yr^{-1} disk, and likewise with C_2H_2 in the 10^{-8} $M_\odot$ yr^{-1} disk.

H_2CO (Figure 4.9) is predominantly formed from photolysis of CH_3OH (Figure 4.13) which itself is formed only on grain surfaces from $CH_3OH_2^+$. H_2CO is photodissociated to CO, CO_2 and HCO^+ by UV photons in the PDR, and to CO by cosmic-rays in the WML. H_2CO is more abundant in the 10^{-7} $M_\odot$ yr^{-1} disk, and peaks in a layer similar to HCN near the surface. In contrast, the distribution peaks at a smaller radius ($r \leq 4$ AU) in the 10^{-8} $M_\odot$ yr^{-1} disk, and a similar thin band exists just above the midplane.

HCO^+ (Figure 4.12) exists abundantly at the PDR of the 10^{-7} $M_\odot$ yr^{-1} disk, and is generally present where CO is depleted, as is N_2H^+ (Figure 4.16). HCO^+ is formed from photoionization of HCO, H_2CO and endothermic reactions of CO^+ with H_2. HCO^+ is confined to the inner $r \leq 4$ AU PDR, and the synthesis route as a result of CO photodissociation. NH_3 (Figure 4.15) also peaks here, resulting from the endothermic synthesis of N to NH and to NH_2, and is photodissociated back to NH and NH_2 at the PDR.

In summary, the 10^{-7} $M_\odot$ yr^{-1} and 10^{-8} $M_\odot$ yr^{-1} molecular distributions of CO, CO_2, H_2O, HCN, OH, CN, C_2H_2, C_2H, N_2H^+, NH_3, CH_3OH and CH_4 have been presented and their chemical interactions in the gas have been discussed. All of these species, with the exception of NH_3, CH_3OH and CH_4 have been observed in protoplanetary disks. The most abundant molecules are CO, H_2O and HCN. Interesting features include the photodissociation of CO to free C and O in a thin band at the PDR–WML boundary layer, promoting a molecular synthesis layer which produces H_2O, HCN and CH_4 in the 10^{-7} $M_\odot$ yr^{-1} disk. All twelve molecules are generally most abundant in the WML, and are photodissociated to simpler molecules, atoms and ions at the PDR, and depleted at the midplane (see Section 4.3.3). The ubiquity of H_2O, HCN and H_2CO at the r 1–2 AU PDR in the 10^{-7} $M_\odot$ yr^{-1} disk are likely a result of (i) neglecting stellar UV photons, (ii) high grain temperatures ($T_{\rm gas} = T_{\rm grain}$) which increases their rate of freezeout ($k_{\rm freeze} \propto T$), towards the surface and their preservation, and (iii) endothermic reactions with H_2 which peak in the inner PDR. In other models with decoupled gas and grain temperature distributions (e.g. Heinzeller et al. 2011), the grain temperature is not as great in the PDR, and less is frozen back out, leaving molecules to be processed in the high temperature gas.

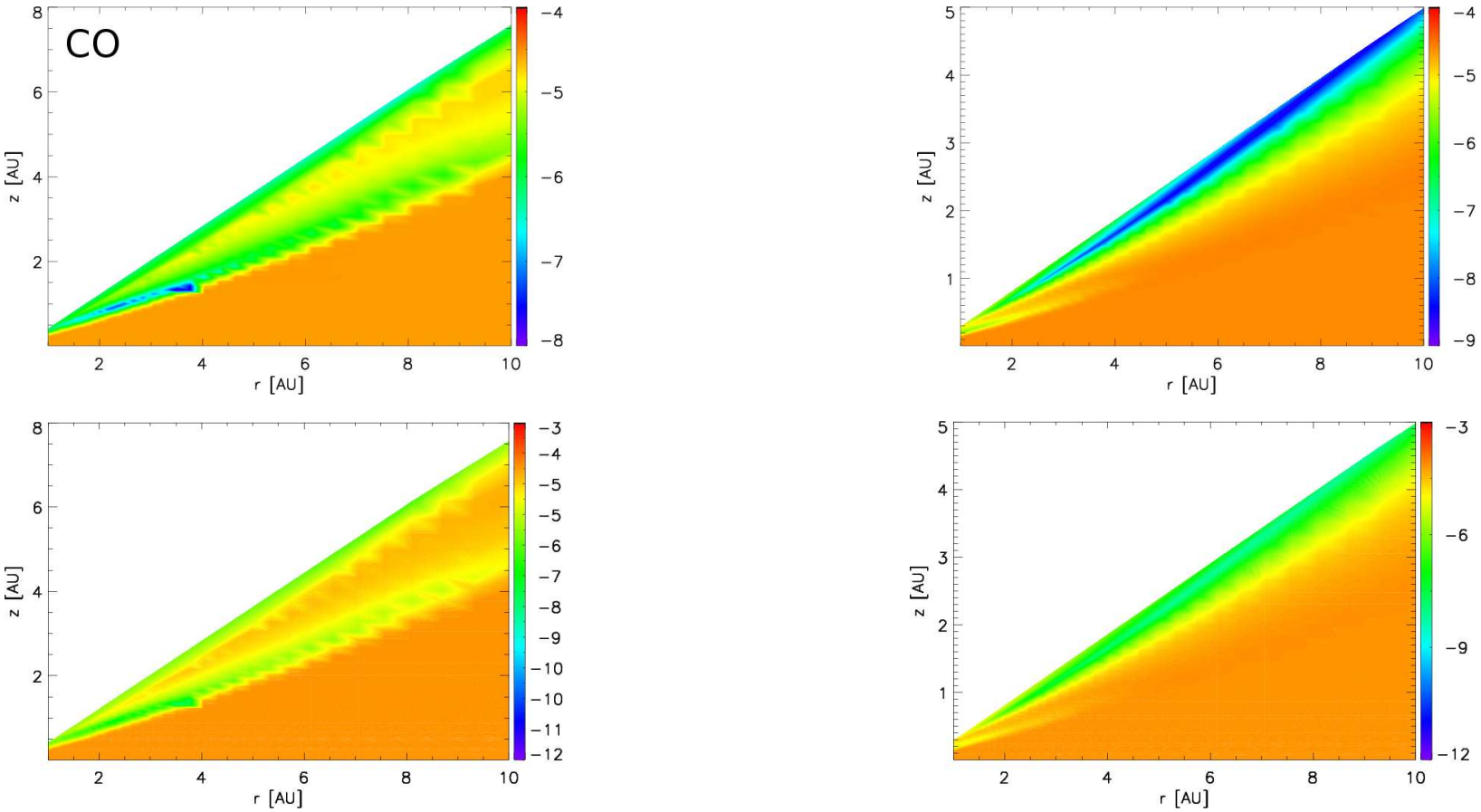

Figure 4.3: Comparison of 10^{-7} $M_\odot$ yr^{-1} (left) and 10^{-8} $M_\odot$ yr^{-1} (right) molecular distributions of CO, with natural maximum abundance variation (top) and constrained abundance variation (bottom).

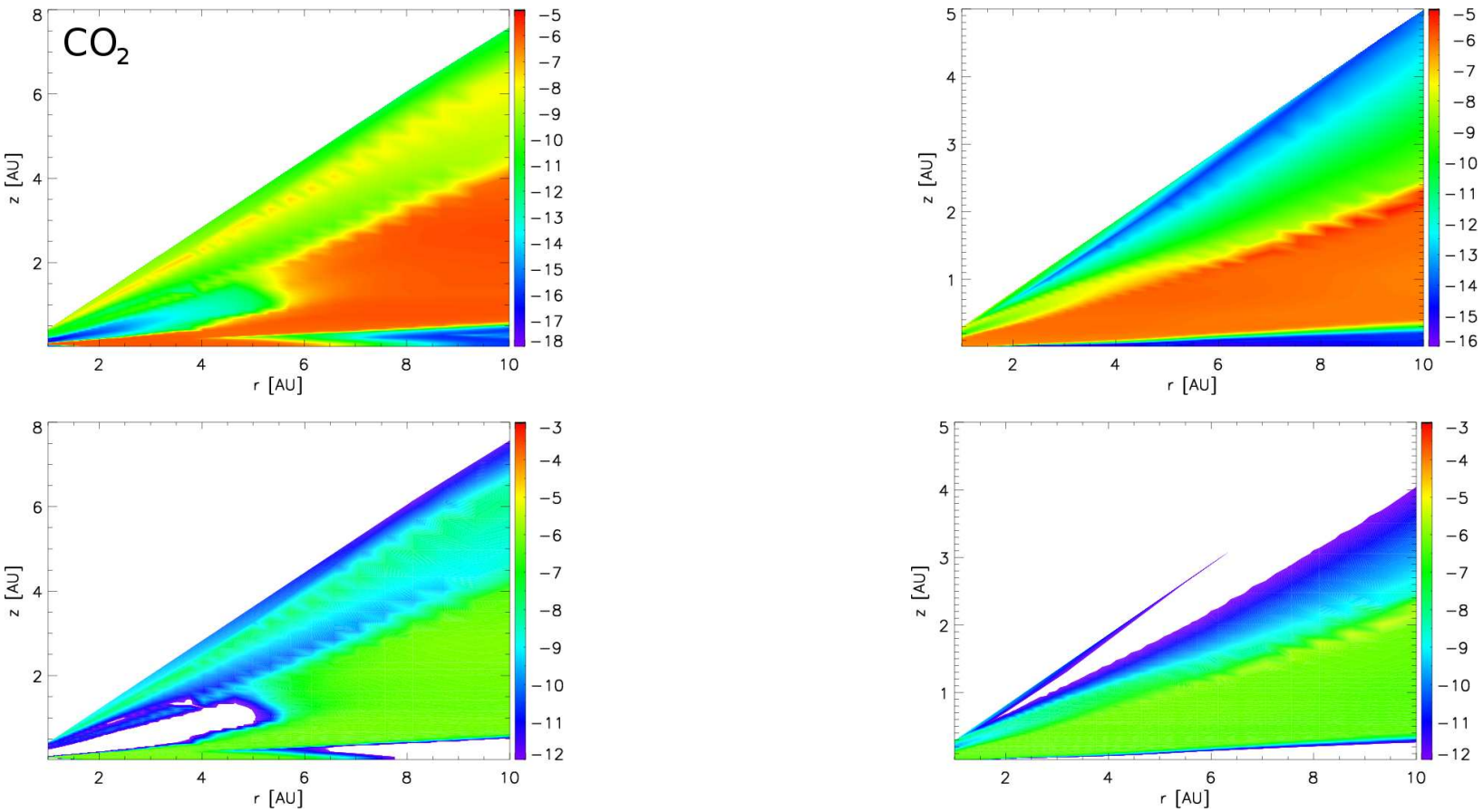

Figure 4.4: Comparison of 10^{-7} $M_\odot$ yr^{-1} (left) and 10^{-8} $M_\odot$ yr^{-1} (right) molecular distributions of CO_2, with natural maximum abundance variation (top) and constrained abundance variation (bottom).

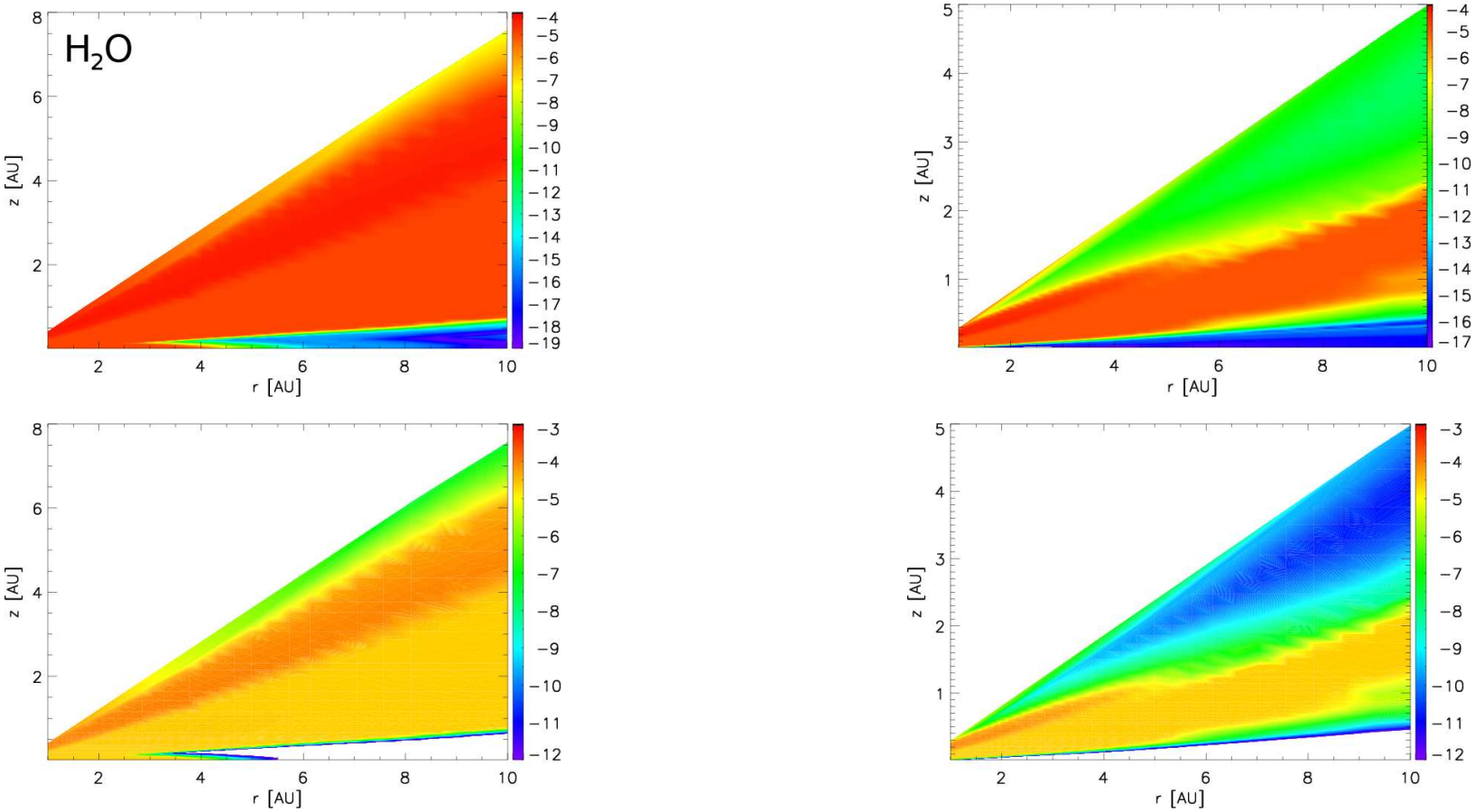

Figure 4.5: Comparison of 10^{-7} $M_\odot$ yr^{-1} (left) and 10^{-8} $M_\odot$ yr^{-1} (right) molecular distributions of H_2O, with natural maximum abundance variation (top) and constrained abundance variation (bottom).

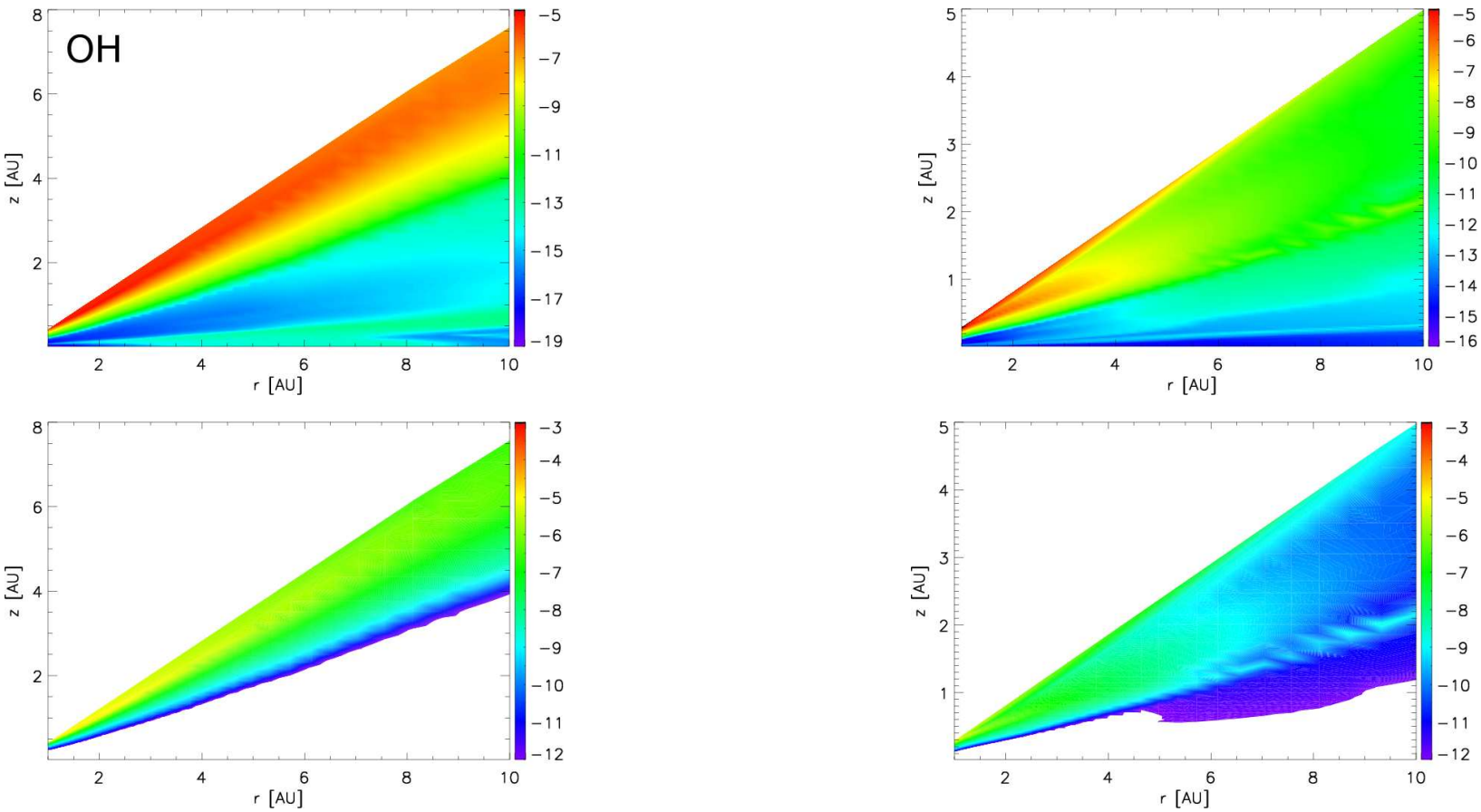

Figure 4.6: Comparison of 10^{-7} $M_\odot$ yr^{-1} (left) and 10^{-8} $M_\odot$ yr^{-1} (right) molecular distributions of OH, with natural maximum abundance variation (top) and constrained abundance variation (bottom).

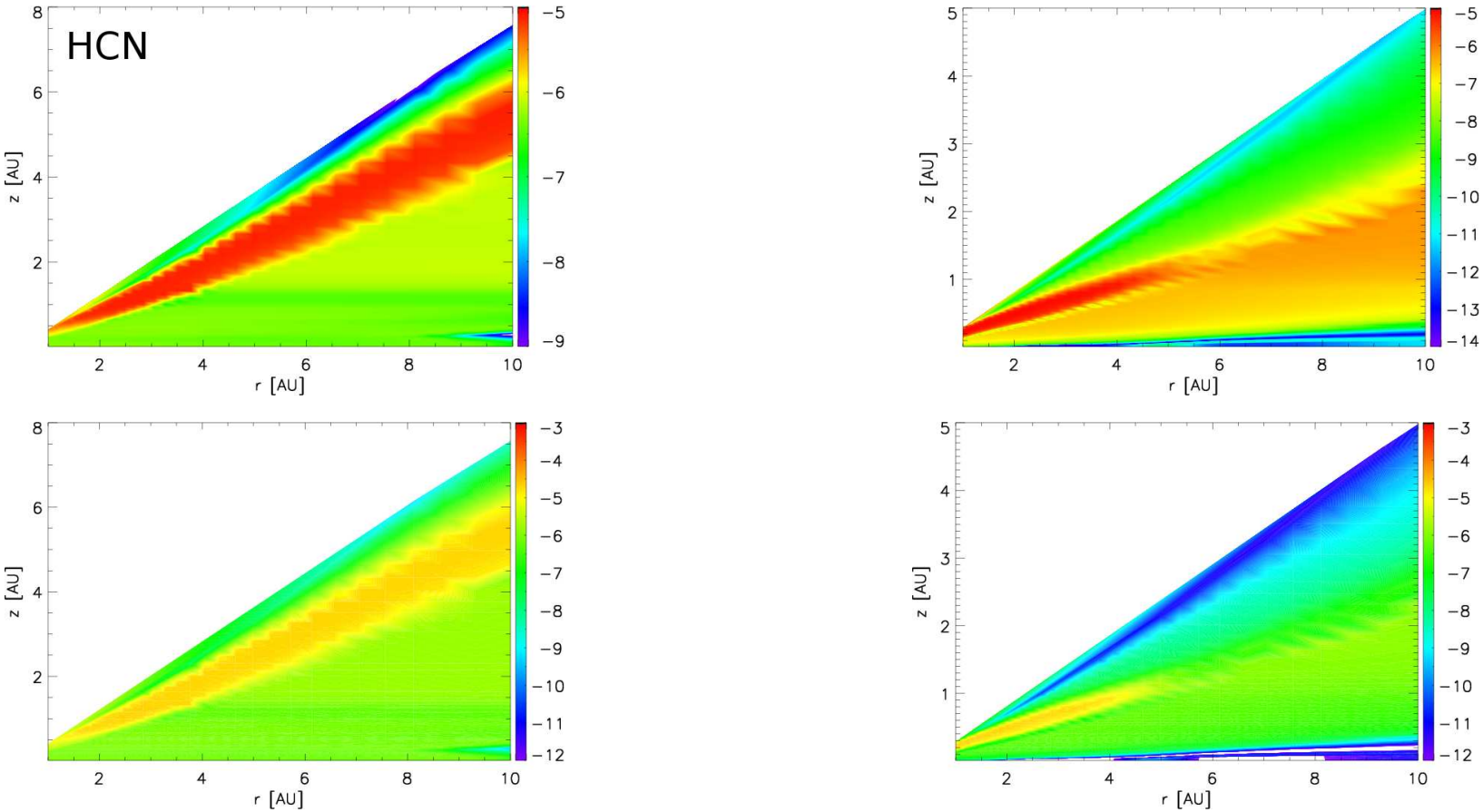

Figure 4.7: Comparison of 10^{-7} $M_\odot$ yr^{-1} (left) and 10^{-8} $M_\odot$ yr^{-1} (right) molecular distributions of HCN, with natural maximum abundance variation (top) and constrained abundance variation (bottom).

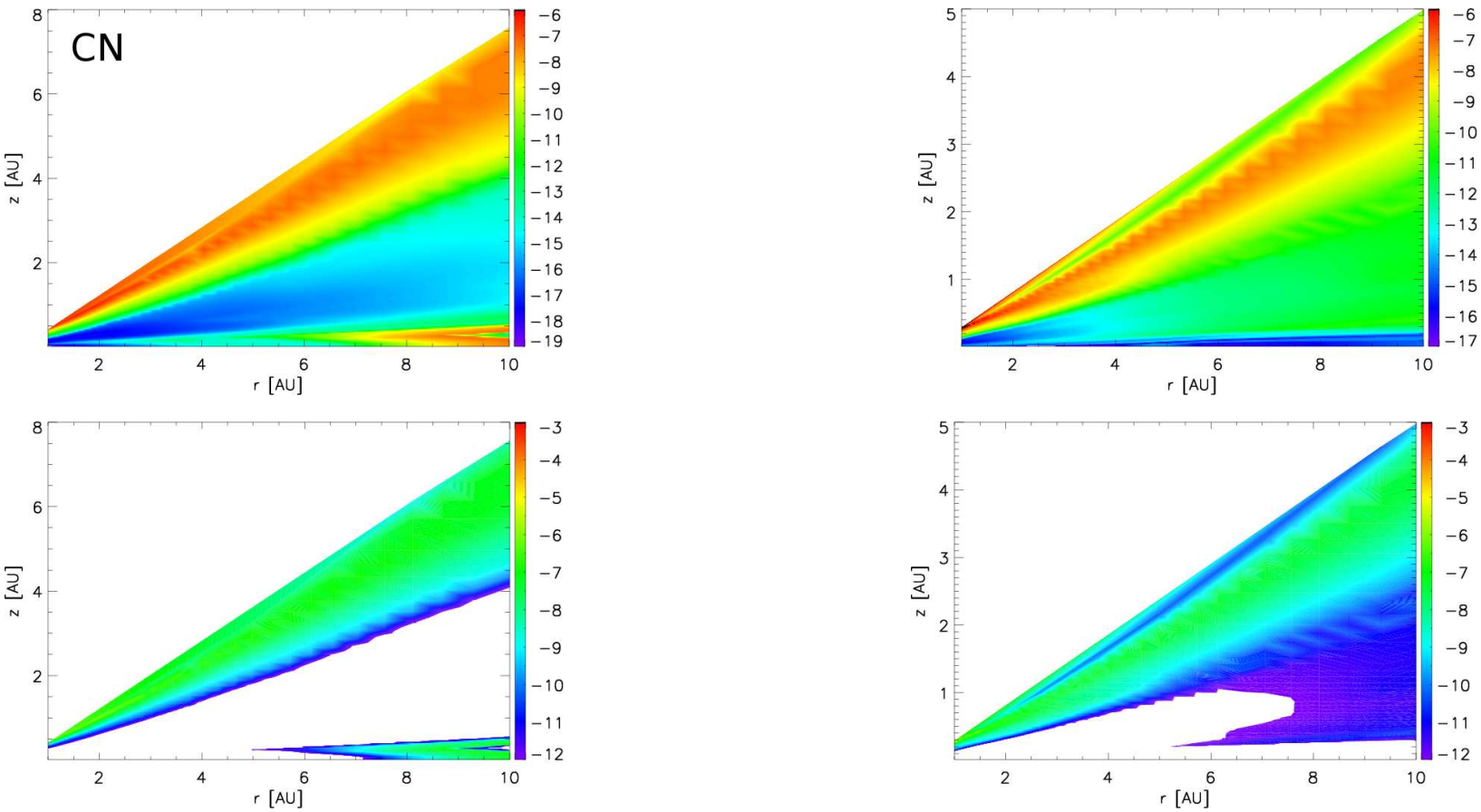

Figure 4.8: Comparison of 10^{-7} $M_\odot$ yr^{-1} (left) and 10^{-8} $M_\odot$ yr^{-1} (right) molecular distributions of CN, with natural maximum abundance variation (top) and constrained abundance variation (bottom).

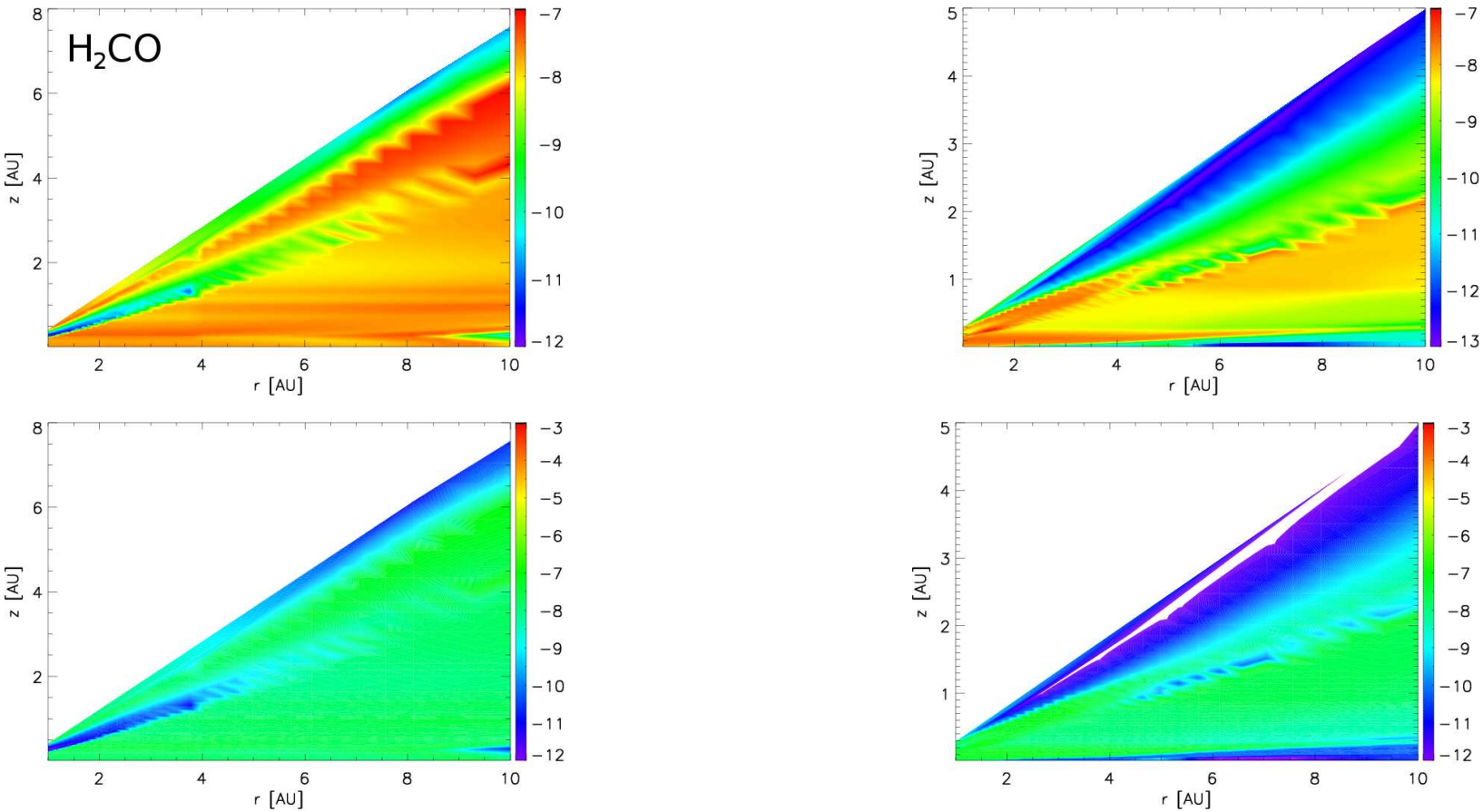

Figure 4.9: Comparison of 10^{-7} $M_\odot$ yr^{-1} (left) and 10^{-8} $M_\odot$ yr^{-1} (right) molecular distributions of H_2CO, with natural maximum abundance variation (top) and constrained abundance variation (bottom).

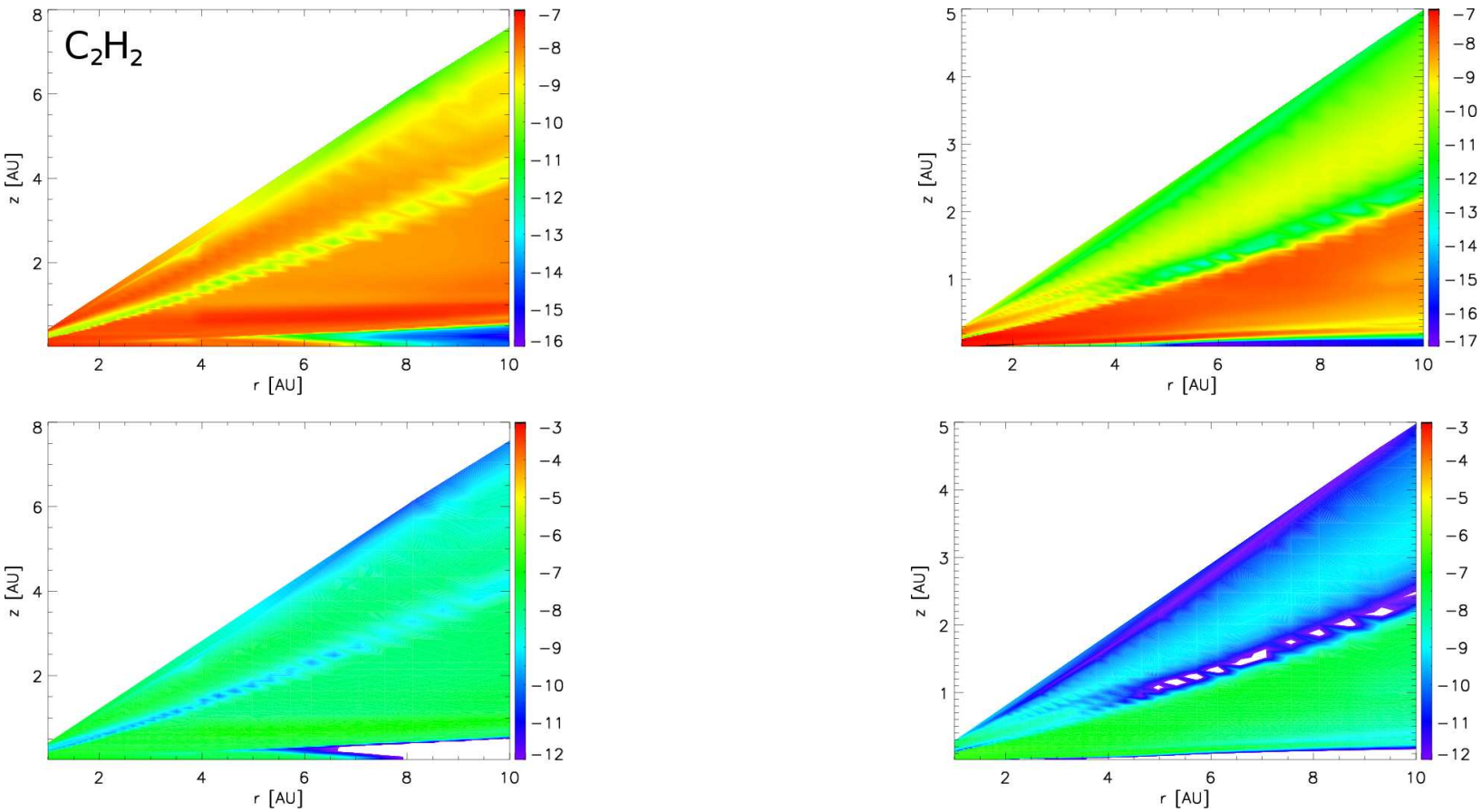

Figure 4.10: Comparison of 10^{-7} $M_\odot$ yr^{-1} (left) and 10^{-8} $M_\odot$ yr^{-1} (right) molecular distributions of C_2H_2, with natural maximum abundance variation (top) and constrained abundance variation (bottom).

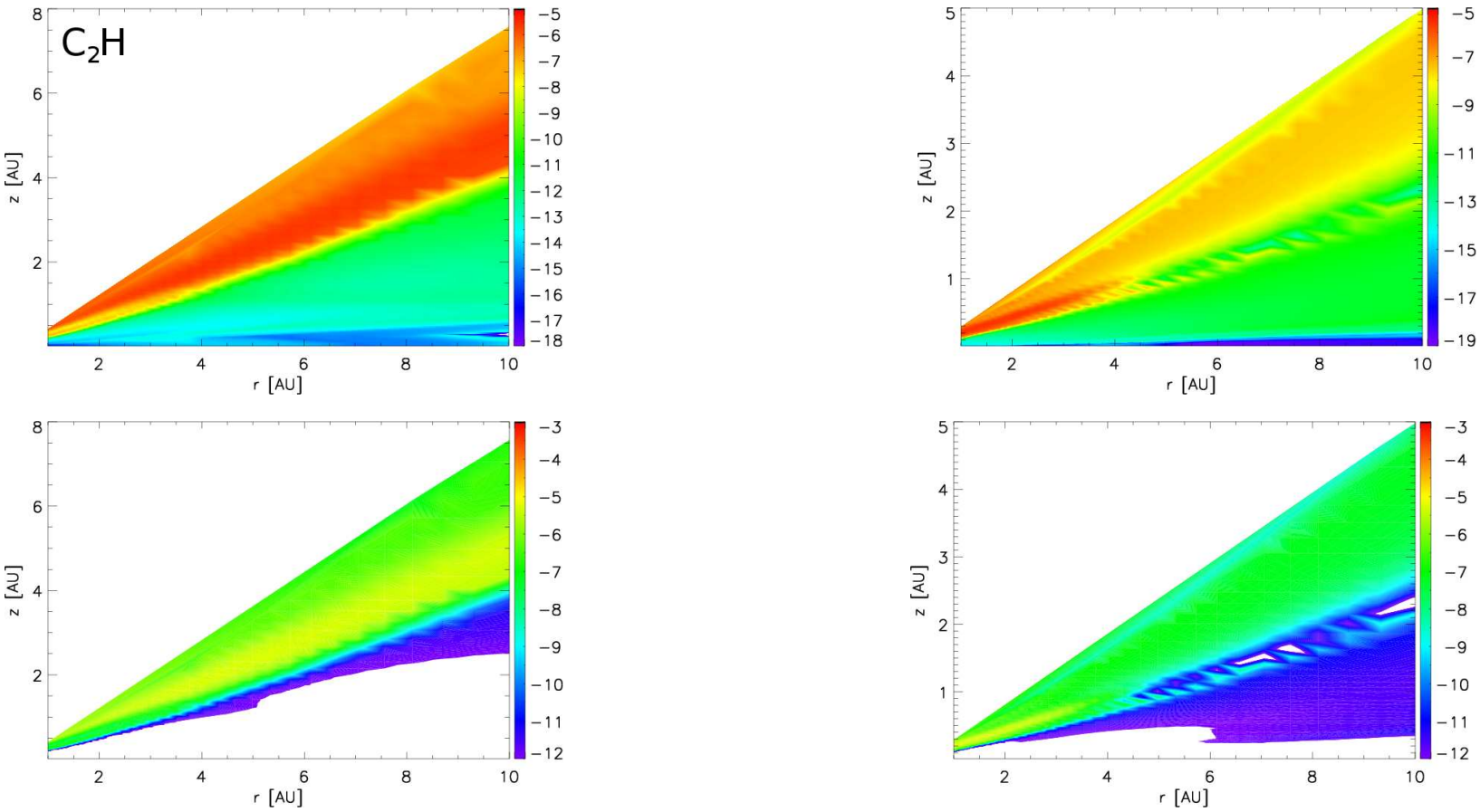

Figure 4.11: Comparison of 10^{-7} $M_\odot$ yr^{-1} (left) and 10^{-8} $M_\odot$ yr^{-1} (right) molecular distributions of C_2H, with natural maximum abundance variation (top) and constrained abundance variation (bottom).

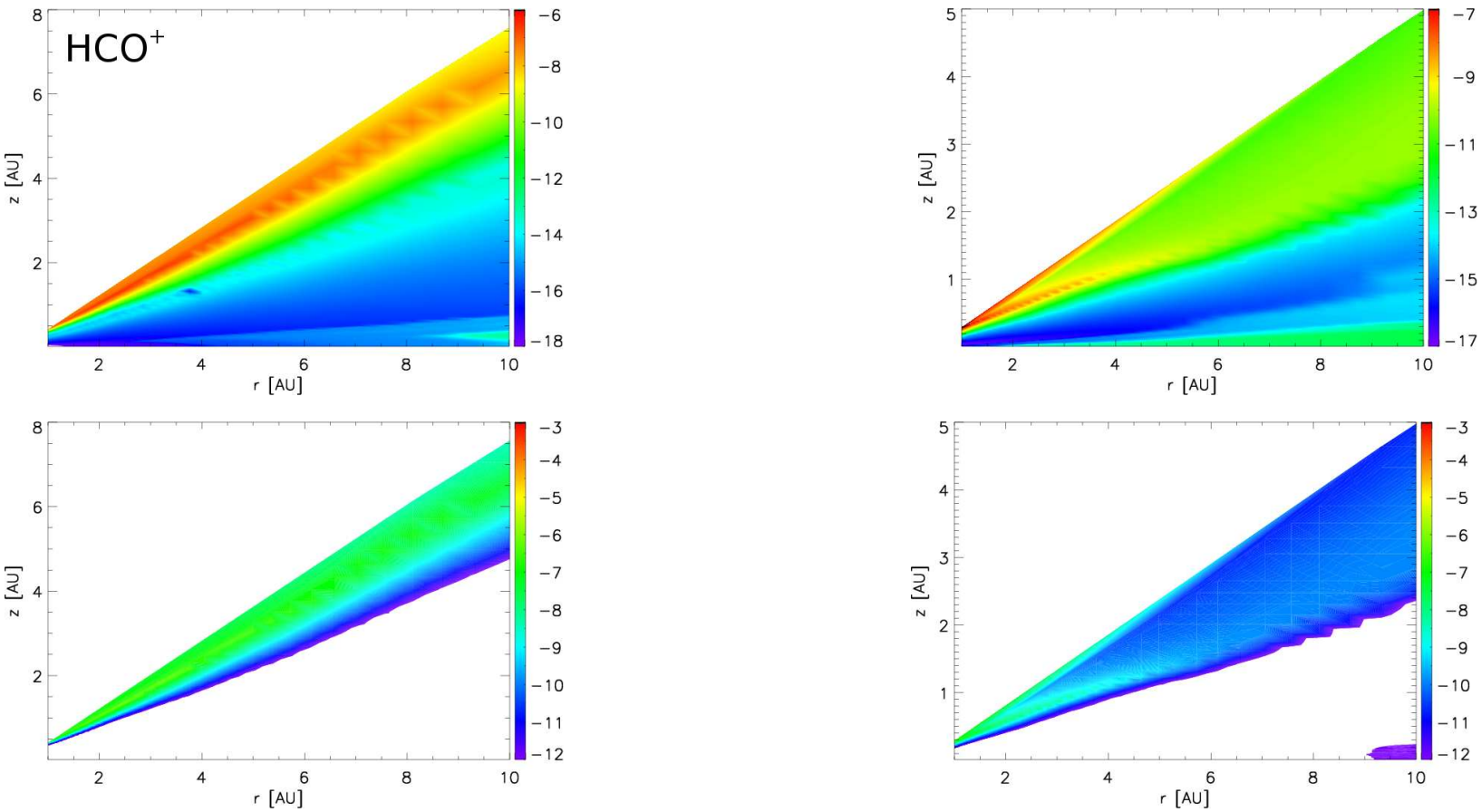

Figure 4.12: Comparison of 10^{-7} $M_\odot$ yr^{-1} (left) and 10^{-8} $M_\odot$ yr^{-1} (right) molecular distributions of HCO^+, with natural maximum abundance variation (top) and constrained abundance variation (bottom).

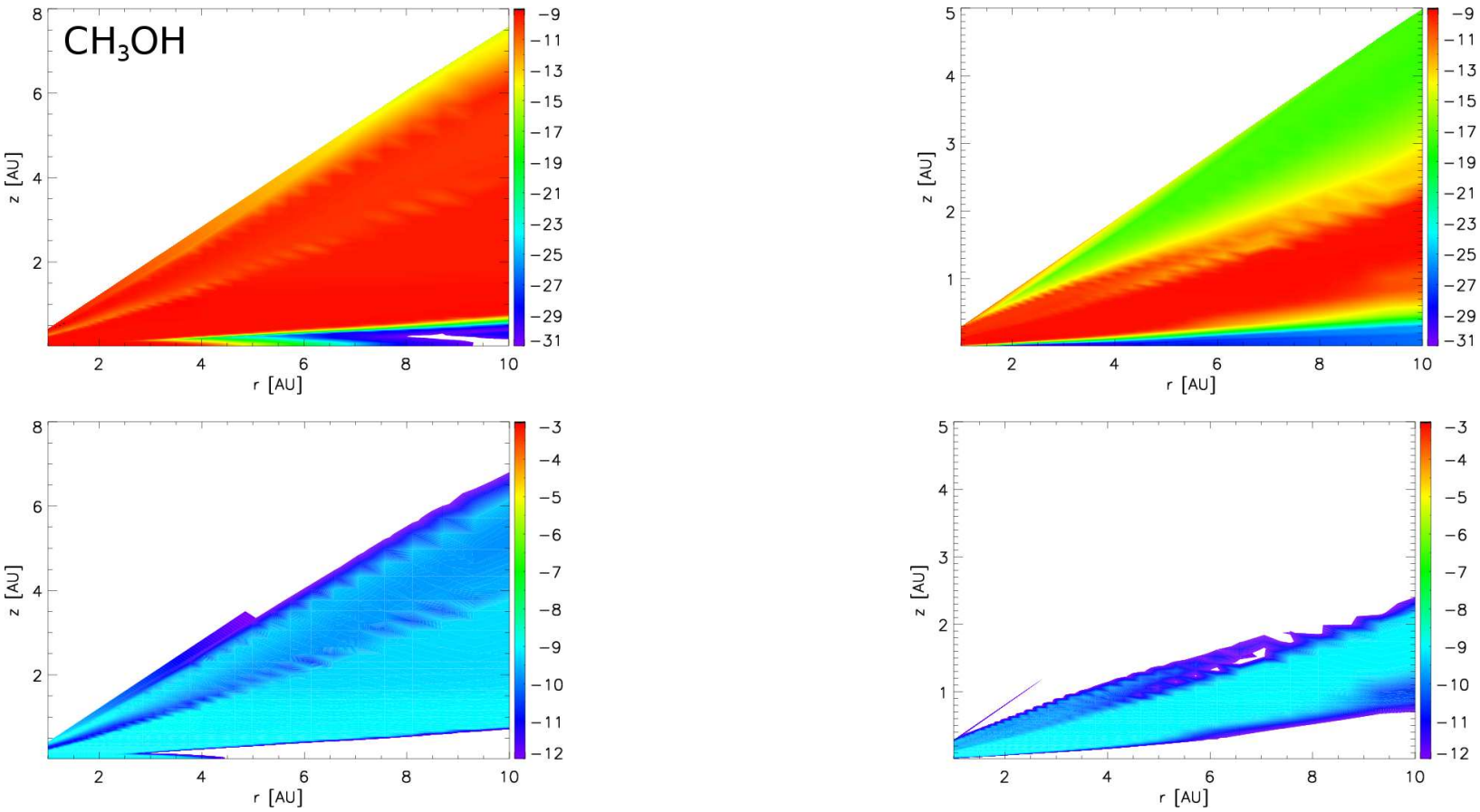

Figure 4.13: Comparison of 10^{-7} $M_\odot$ yr^{-1} (left) and 10^{-8} $M_\odot$ yr^{-1} (right) molecular distributions of CH_3OH, with natural maximum abundance variation (top) and constrained abundance variation (bottom).

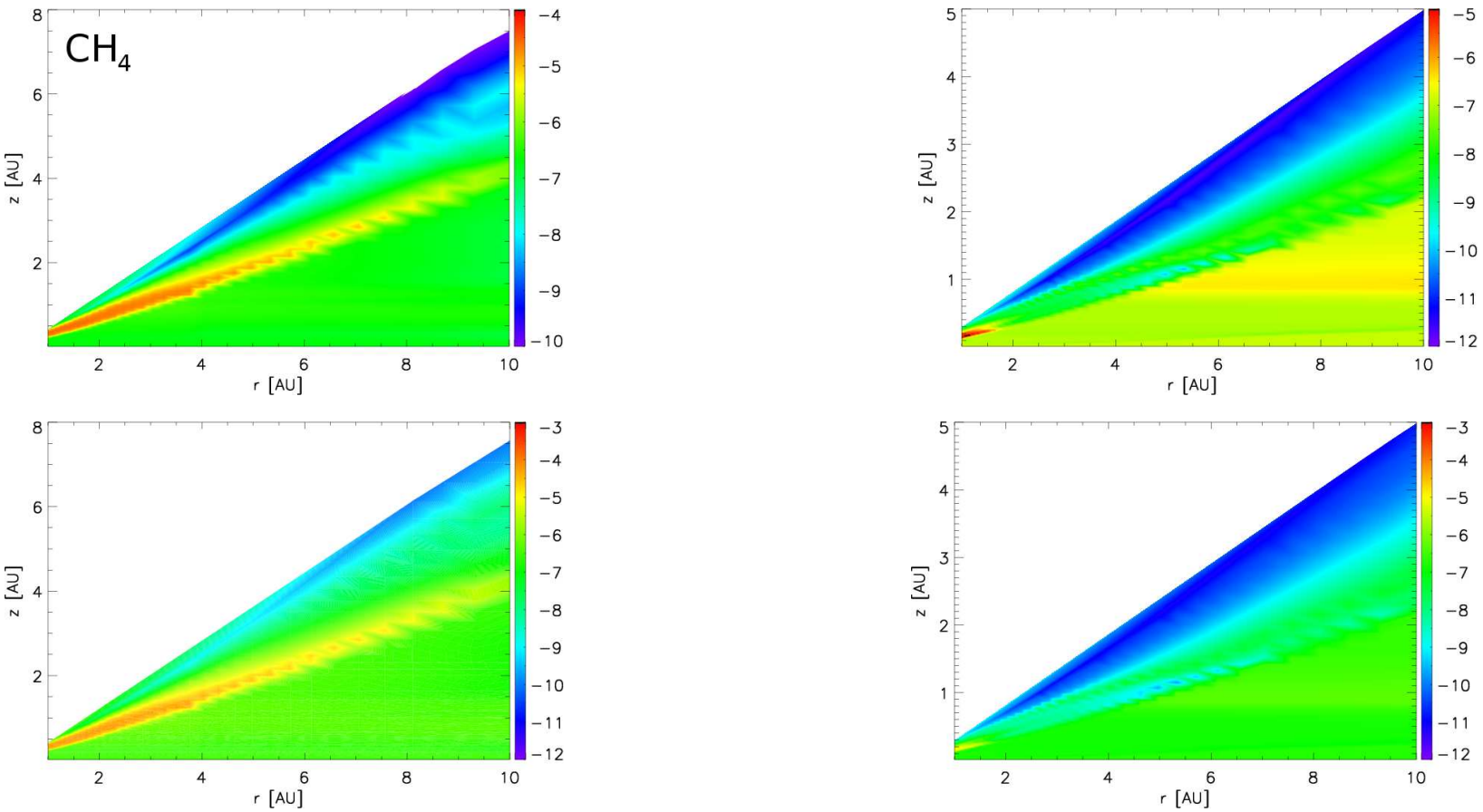

Figure 4.14: Comparison of 10^{-7} $M_\odot$ yr^{-1} (left) and 10^{-8} $M_\odot$ yr^{-1} (right) molecular distributions of CH_4, with natural maximum abundance variation (top) and constrained abundance variation (bottom).

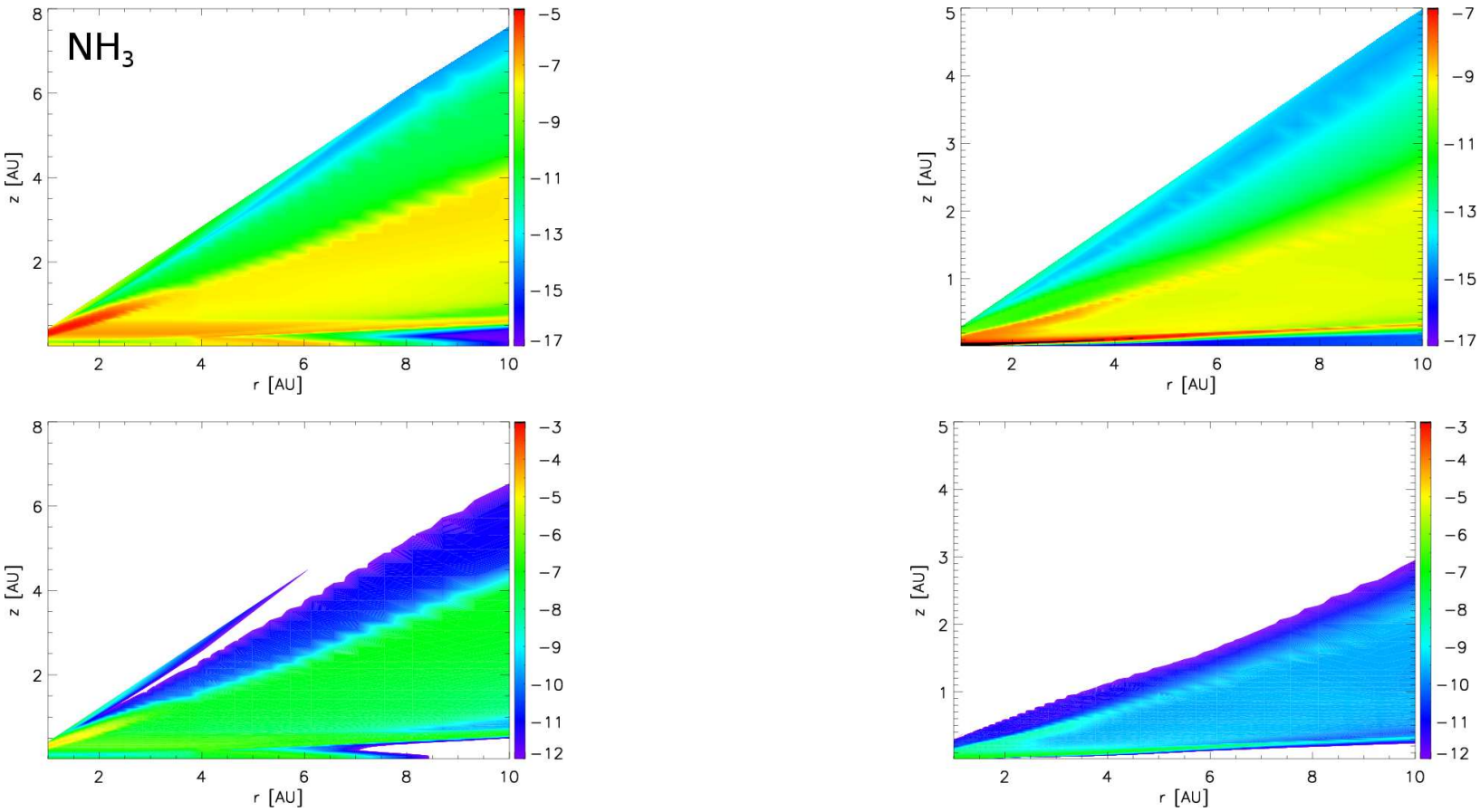

Figure 4.15: Comparison of 10^{-7} $M_\odot$ yr^{-1} (left) and 10^{-8} $M_\odot$ yr^{-1} (right) molecular distributions of NH_3, with natural maximum abundance variation (top) and constrained abundance variation (bottom).

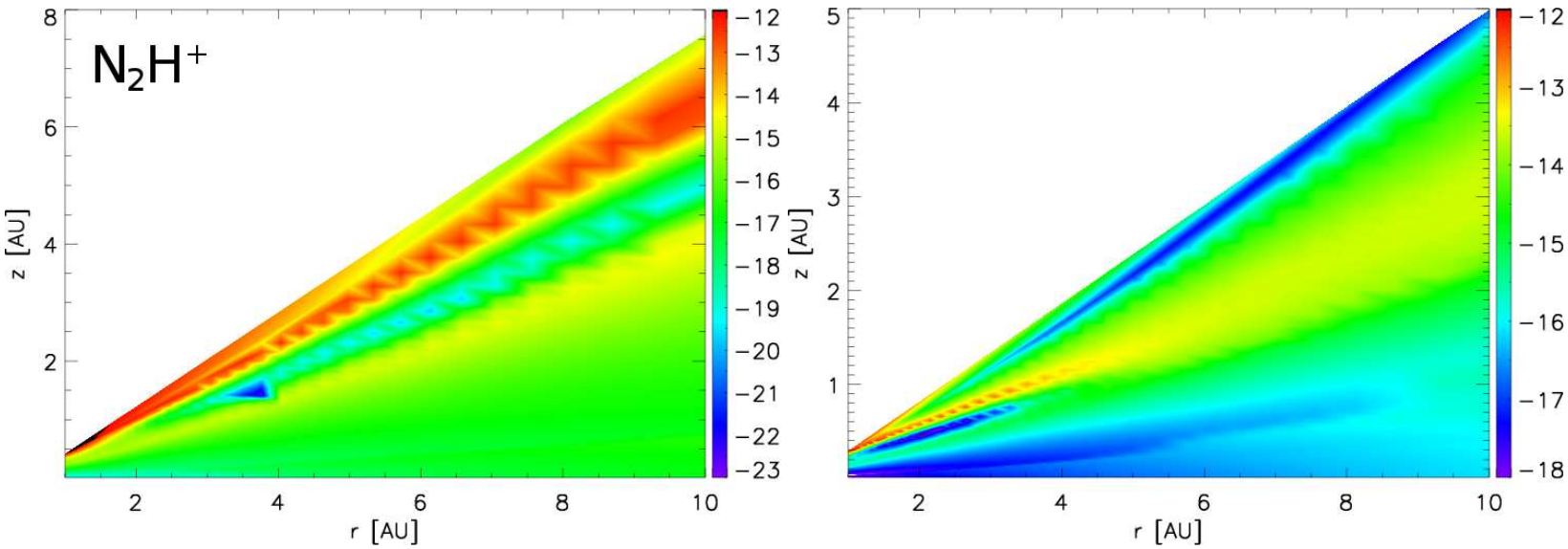

Figure 4.16: Comparison of 10^{-7} $M_\odot$ yr^{-1} (left) and 10^{-8} $M_\odot$ yr^{-1} (right) molecular distributions of N_2H^+.

4.2.3 Comparison of molecular abundances in the midplane

The point at which the disk temperature matches the desorption temperature ($\tau_{\rm ads} = \tau_{\rm des}$) is known as the "snow-line", and can occur at different radii and heights from the midplane for each species. Molecules are frozen-out and the gas-phase abundance is negligible beyond this snow-line radius ($\tau_{\rm ads} < \tau_{\rm des}$). By definition, the snow-line is associated with the midplane. The binding energies (in K) for some species were given in Tables 2.4 and 2.5. As Figure 2.3 showed, temperature increases less rapidly with decreasing radius in the 10^{-8} $M_\odot$ yr^{-1} disk compared with the 10^{-7} $M_\odot$ yr^{-1} disk. The resulting snow-lines for each of the molecules are therefore located closer to the star in the 10^{-8} $M_\odot$ yr^{-1} disk. Table 4.3 lists the snow-lines for both disks and their binding energies originally from Table 2.4.

Table 4.3: Snow-lines in units of AU and binding energies ($E_{\rm D}$) in K for the twelve species at the midplane for both 10^{-7} $M_\odot$ yr^{-1} and 10^{-8} $M_\odot$ yr^{-1} disks.

Molecule	10^{-7} $M_\odot$ yr^{-1} snow-line (AU)	10^{-8} $M_\odot$ yr^{-1} snow-line (AU)	$E_{\rm D}$ (K)
CO	> 10	> 10	855
CO_2	6	2	2990
H_2O	4	< 1	4800
HCN	10	3	1760
OH	9	2	1259
CN	8	2	1510
H_2CO	9	6	1760
C_2H_2	7	5	2400
C_2H	6	3	1460
CH_3OH	6	2	4930
NH_3	8	3	2790
CH_4	> 10	> 10	1090

Figures 4.17 to 4.28 display the same molecular distributions for both disks, but this time restricted to $z \leq 1$ AU. Plots of the variation in adsorption, desorption and

accretion timescales at the midplane for each of the neutral species are also shown. The ionic radials HCO^+ and N_2H^+ are ignored in this subsection since their desorption and adsorption are associated with their neutral counterparts HCO and N_2H, which have not been observed to date. Depleted regions in the gas (coloured blue-purple) are seen for most species whose snow-lines are inside a radius of 10 AU; the exceptions being CO, HCN and CH_4 in the 10^{-7} $M_\odot$ yr^{-1} disk with snow-lines outside of 10 AU.

A molecule's return to the gas is dependent on its binding energy and the temperature. Molecules with the lowest binding energies (e.g. CO) are volatile and return to the gas at larger radii than those with larger binding energies (e.g. H_2O, CO_2 and CH_3OH). The difference between 10^{-7} $M_\odot$ yr^{-1} and 10^{-8} $M_\odot$ yr^{-1} snow-line positions at the midplane can vary between species, and occurs as a result of the behavior of the $\exp -\left(\frac{E_D(T)}{T}\right)$ term in the thermal evaporation rate Equation (2.25), in relation to rate of temperature increase with decreasing radius in each disk. The desorption rate dominates over adsorption with increasing temperature and decreasing radius since desorption has an exponential dependence with temperature, whereas the adsorption rate dependence is only linear. Species with the highest binding energies (H_2O and CH_3OH) remain frozen even inside 1 AU in the 10^{-8} $M_\odot$ yr^{-1} disk.

4.2.4 Gas-grain interaction discrepancies

It is important to note that binding energies are not by any means definitive. The set of molecular binding energies used in this model are one of many variations of values extracted from the literature. On top of models with different underlying temperature distributions, chemical models may be implemented with different molecular binding energies, resulting in contrasting snow-lines and onsets of molecular chemical processing in the gas. With this in mind, it is important to utilize the latest, most up-to-date values where possible since they have major consequences on the chemical evolution.

The model of gas-grain interaction used here is likely to be too simplistic since desorption is not a binary process and its temperature dependency is likely much more complex. Nevertheless all current models continue to adhere to this basic binary process, with the addition of non-thermal photodesorption processes.

The complex chemical makeup of grains also adds to this problem. Recent models have incorporated a separate ice-mantle chemistry process occurring in grains in addition to grain-surface reactions and surface recombination chemistry (e.g. Willacy & Woods 2009; Heinzeller et al. 2011). The temperature gradient is so abrupt in some inner regions of the disk that molecules are mass-thermally desorbed over unrealistically short distances, translating to gas-phase abundances which increase by many orders of magnitude. Further understanding of the dynamical relationship between the gas and grain medium is important.

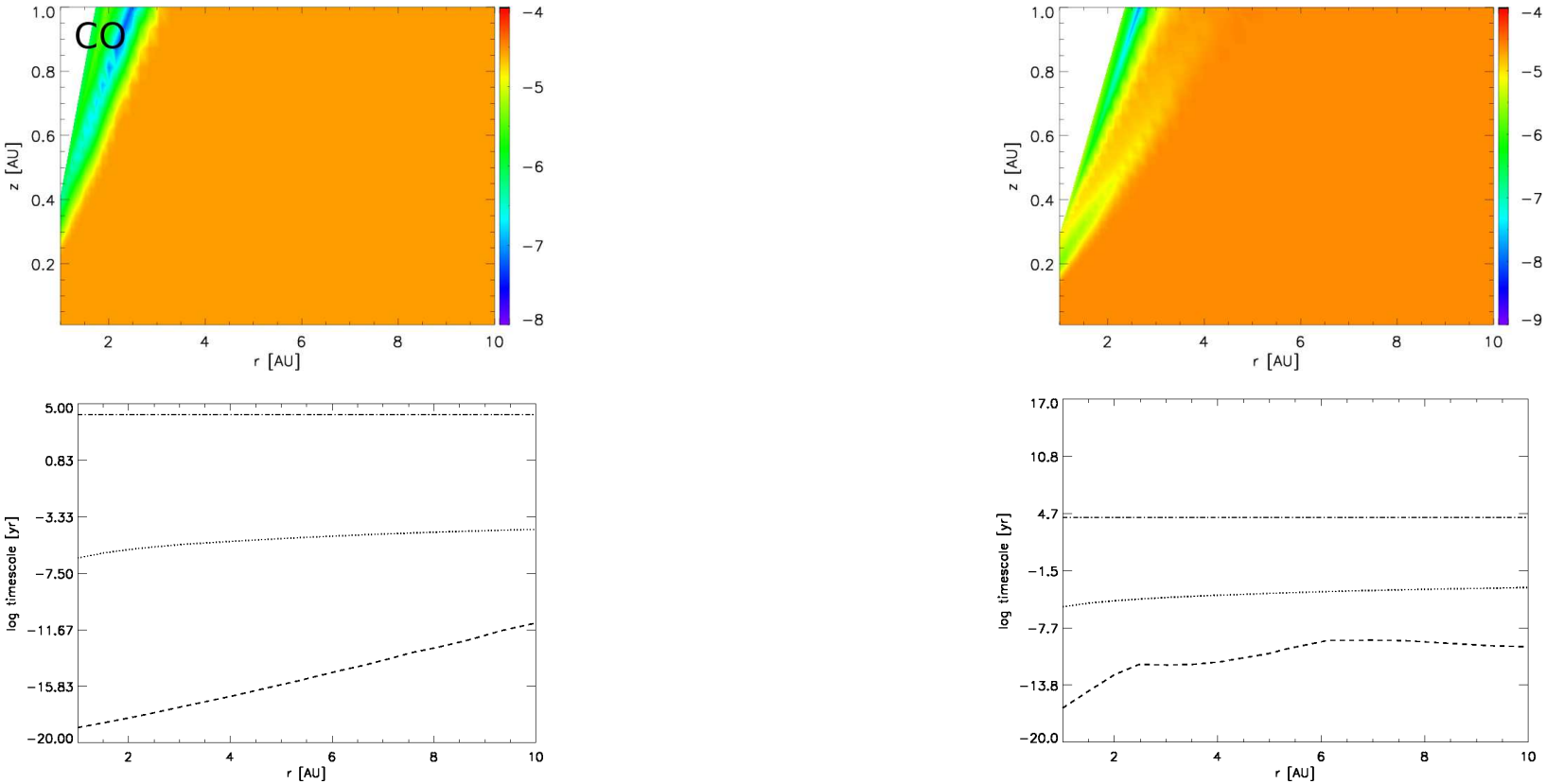

Figure 4.17: *Toprow* : Comparison of 10^{-7} $M_\odot$ yr^{-1} (left) and 10^{-8} $M_\odot$ yr^{-1} (right) molecular distributions of CO between the midplane and $z = 1$ AU. *Bottomrow* : Adsorption (dotted line), desorption (dashed line) and calculation (dot-dashed line) timescales in the 10^{-7} $M_\odot$ yr^{-1} (left) and 10^{-8} $M_\odot$ yr^{-1} (right) disk for CO.

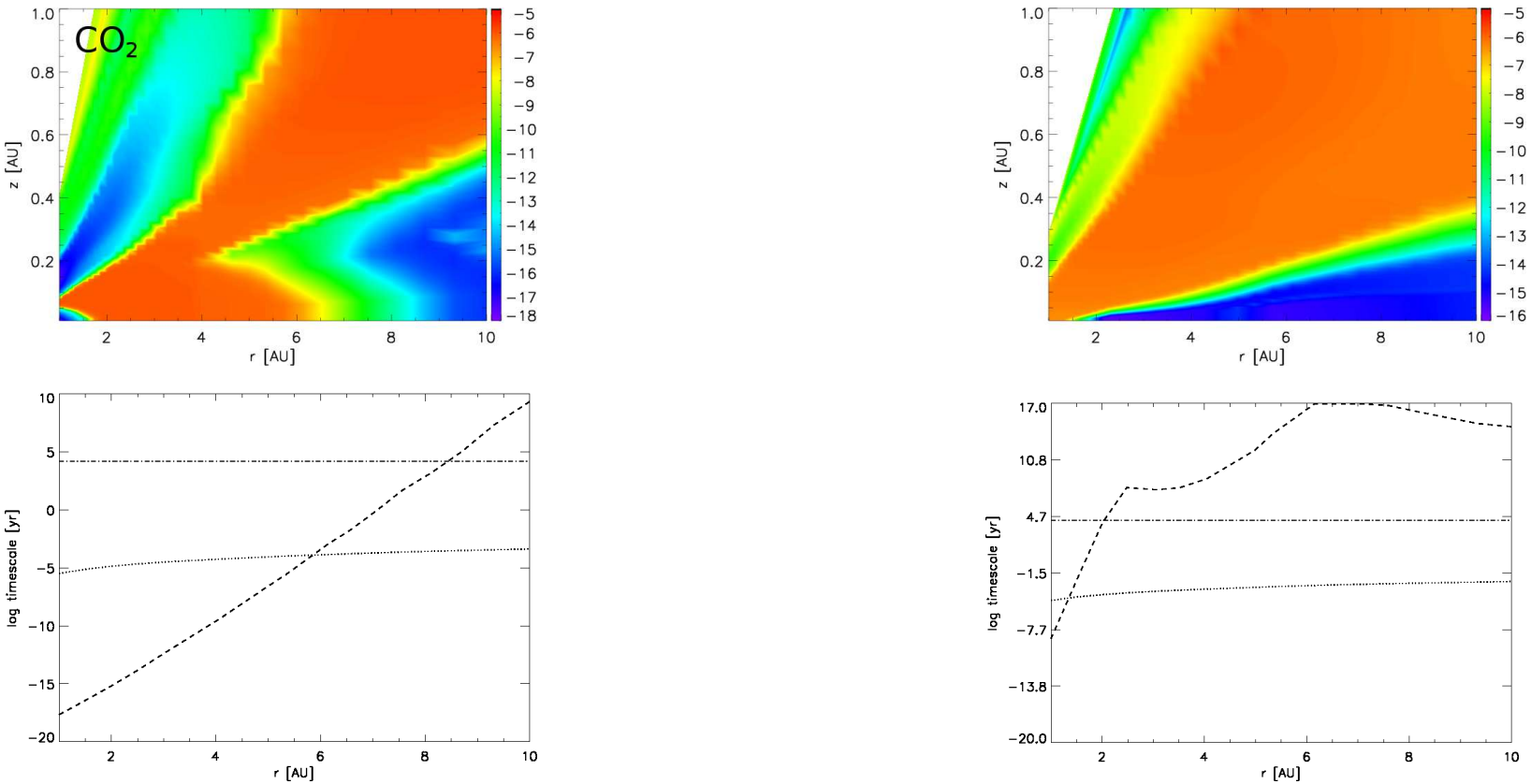

Figure 4.18: *Toprow* : Comparison of 10^{-7} $M_\odot$ yr^{-1} (left) and 10^{-8} $M_\odot$ yr^{-1} (right) molecular distributions of CO_2 between the midplane and z = 1 AU. *Bottomrow* : Adsorption (dotted line), desorption (dashed line) and calculation (dot-dashed line) timescales in the 10^{-7} $M_\odot$ yr^{-1} (left) and 10^{-8} $M_\odot$ yr^{-1} (right) disk for CO_2.

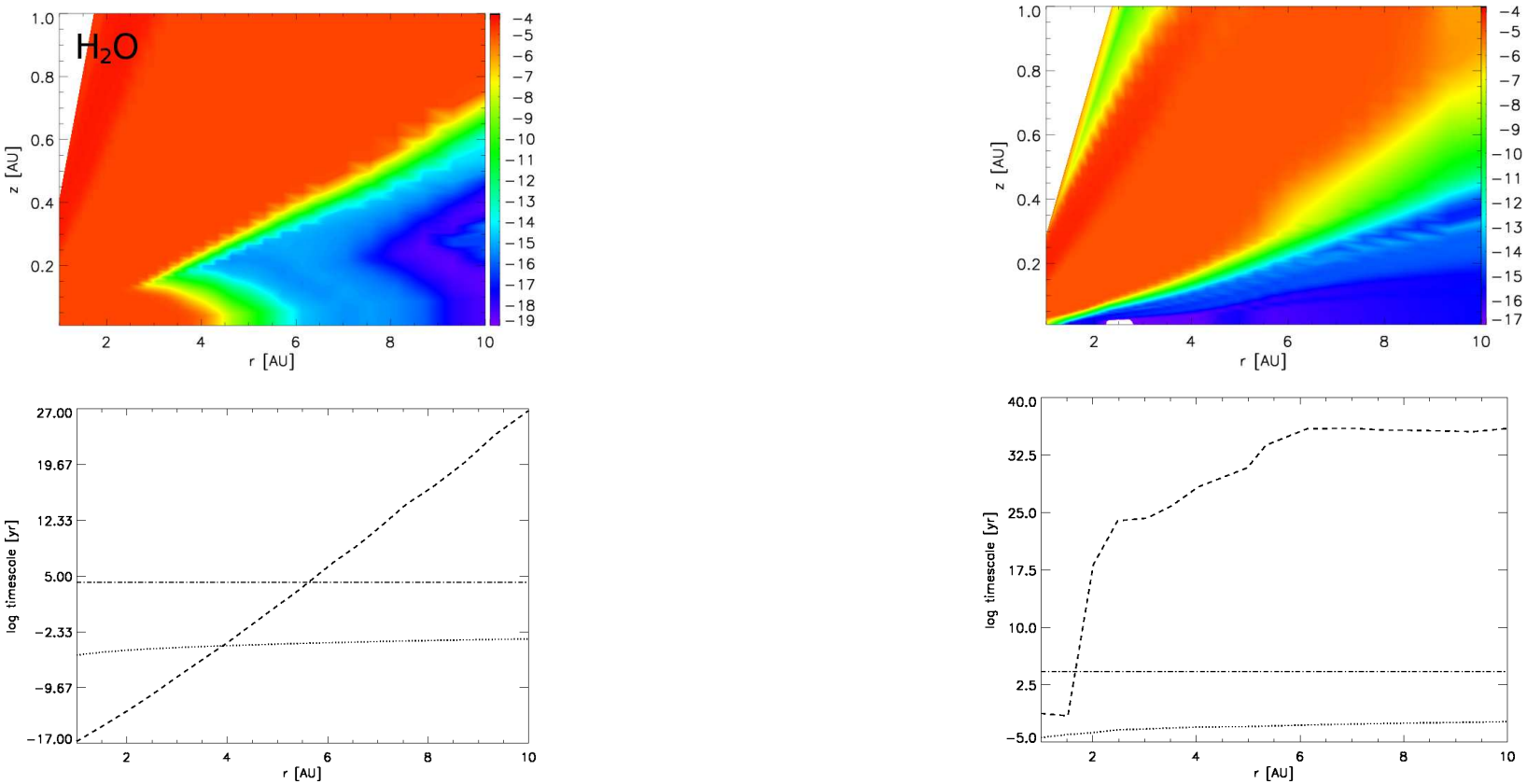

Figure 4.19: *Toprow* : Comparison of 10^{-7} $M_\odot$ yr^{-1} (left) and 10^{-8} $M_\odot$ yr^{-1} (right) molecular distributions of H_2O between the midplane and z = 1 AU. *Bottomrow* : Adsorption (dotted line), desorption (dashed line) and calculation (dot-dashed line) timescales in the 10^{-7} $M_\odot$ yr^{-1} (left) and 10^{-8} $M_\odot$ yr^{-1} (right) disk for H_2O.

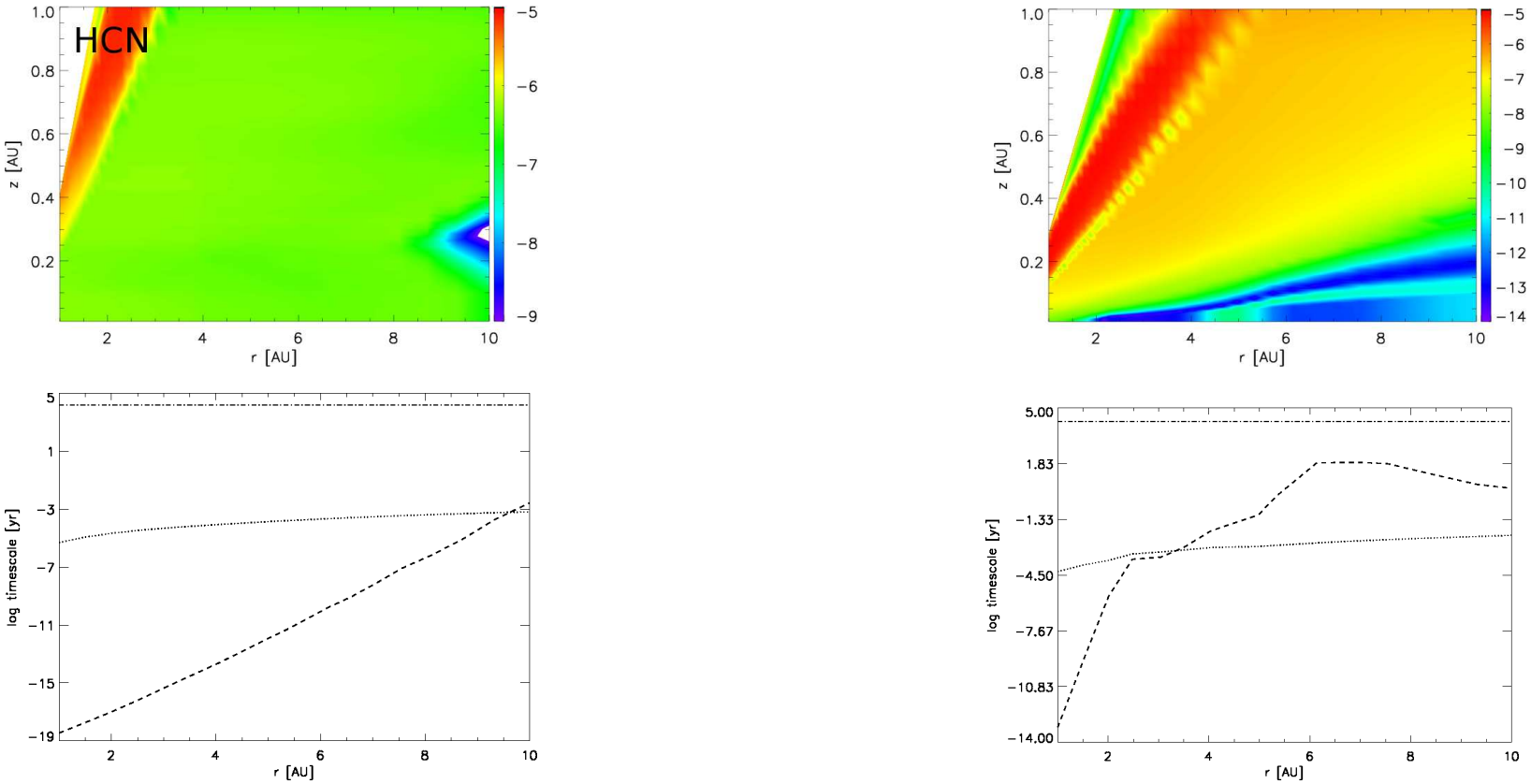

Figure 4.20: *Toprow* : Comparison of 10^{-7} $M_\odot$ yr^{-1} (left) and 10^{-8} $M_\odot$ yr^{-1} (right) molecular distributions of HCN between the midplane and z = 1 AU. *Bottomrow* : Adsorption (dotted line), desorption (dashed line) and calculation (dot-dashed line) timescales in the 10^{-7} $M_\odot$ yr^{-1} (left) and 10^{-8} $M_\odot$ yr^{-1} (right) disk for HCN.

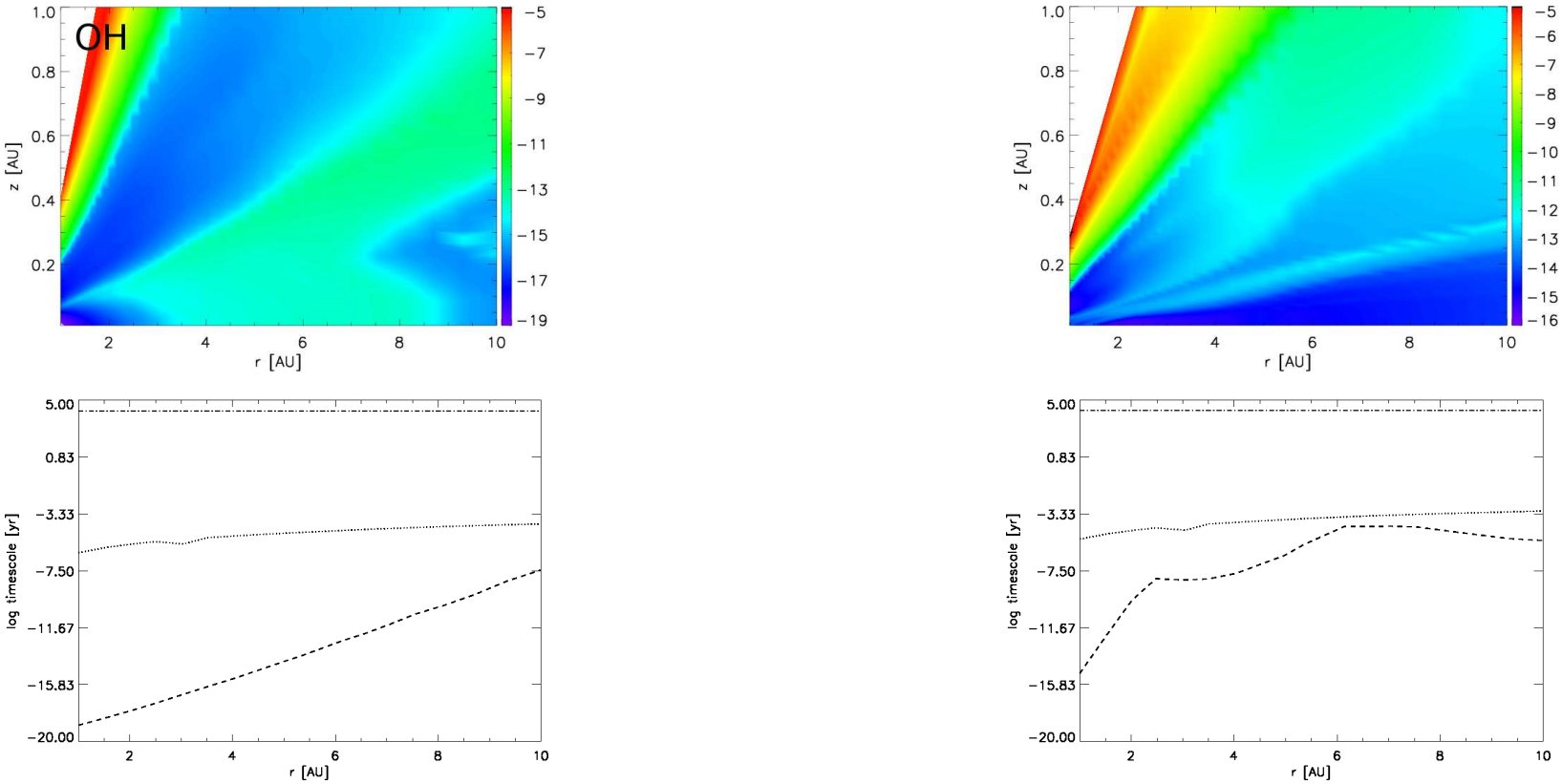

Figure 4.21: *Toprow* : Comparison of 10^{-7} $M_\odot$ yr^{-1} (left) and 10^{-8} $M_\odot$ yr^{-1} (right) molecular distributions of OH between the midplane and z = 1 AU. *Bottomrow* : Adsorption (dotted line), desorption (dashed line) and calculation (dot-dashed line) timescales in the 10^{-7} $M_\odot$ yr^{-1} (left) and 10^{-8} $M_\odot$ yr^{-1} (right) disk for OH.

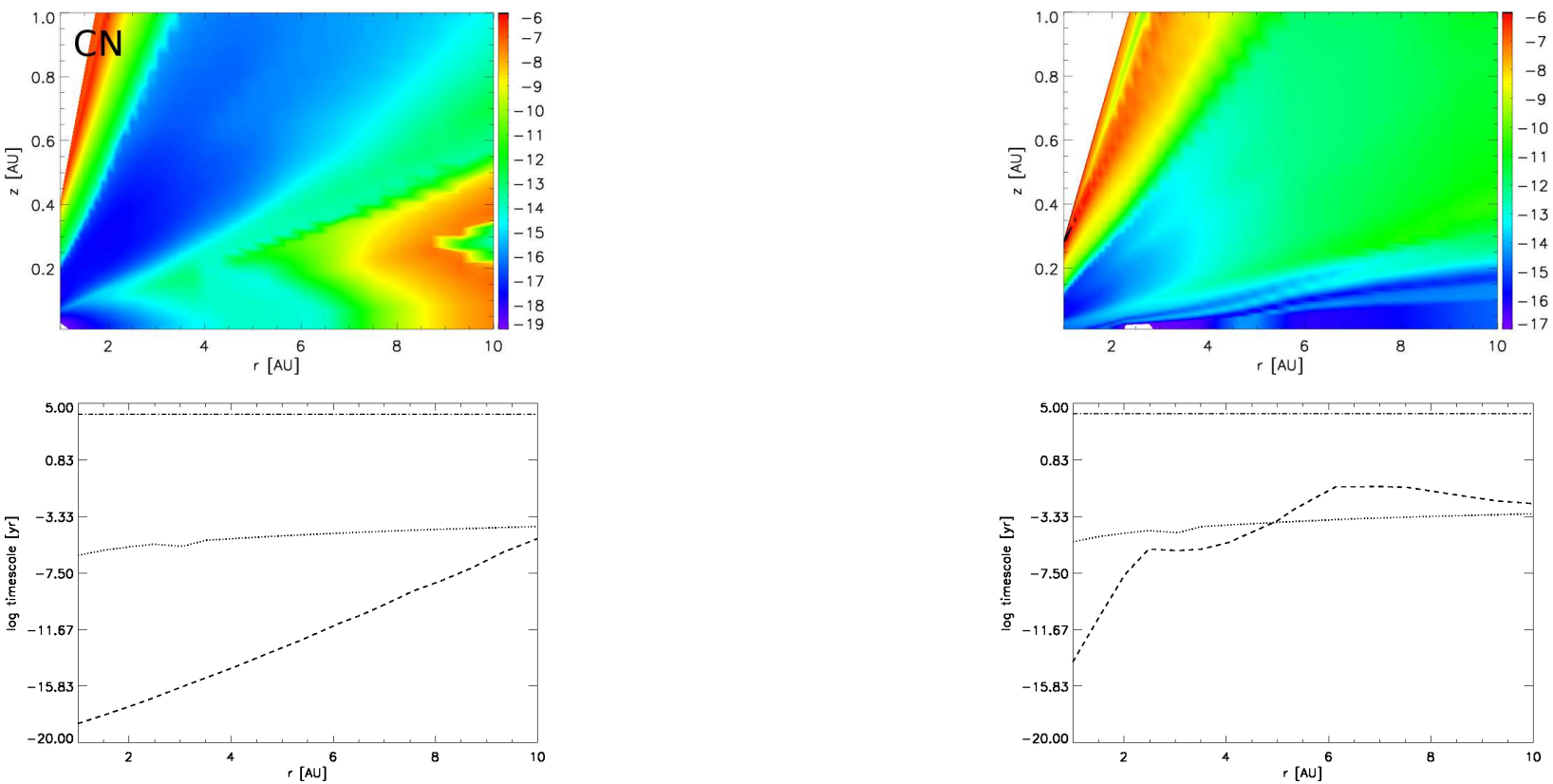

Figure 4.22: *Toprow* : Comparison of 10^{-7} $M_\odot$ yr^{-1} (left) and 10^{-8} $M_\odot$ yr^{-1} (right) molecular distributions of CN between the midplane and $z = 1$ AU. *Bottomrow* : Adsorption (dotted line), desorption (dashed line) and calculation (dot-dashed line) timescales in the 10^{-7} $M_\odot$ yr^{-1} (left) and 10^{-8} $M_\odot$ yr^{-1} (right) disk for CN.

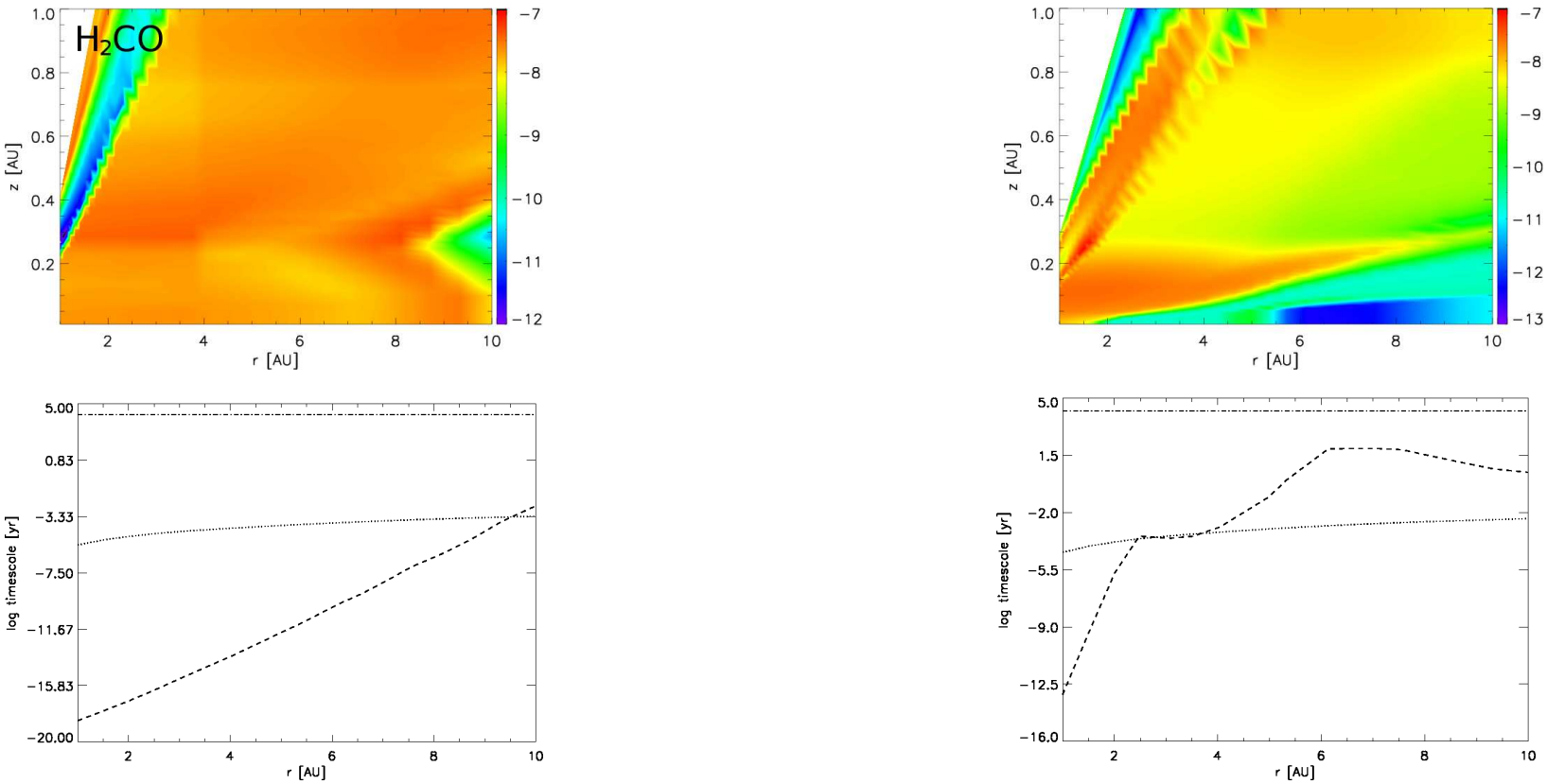

Figure 4.23: *Toprow* : Comparison of 10^{-7} $M_\odot$ yr^{-1} (left) and 10^{-8} $M_\odot$ yr^{-1} (right) molecular distributions of H_2CO between the midplane and $z = 1$ AU. *Bottomrow* : Adsorption (dotted line), desorption (dashed line) and calculation (dot-dashed line) timescales in the 10^{-7} $M_\odot$ yr^{-1} (left) and 10^{-8} $M_\odot$ yr^{-1} (right) disk for H_2CO.

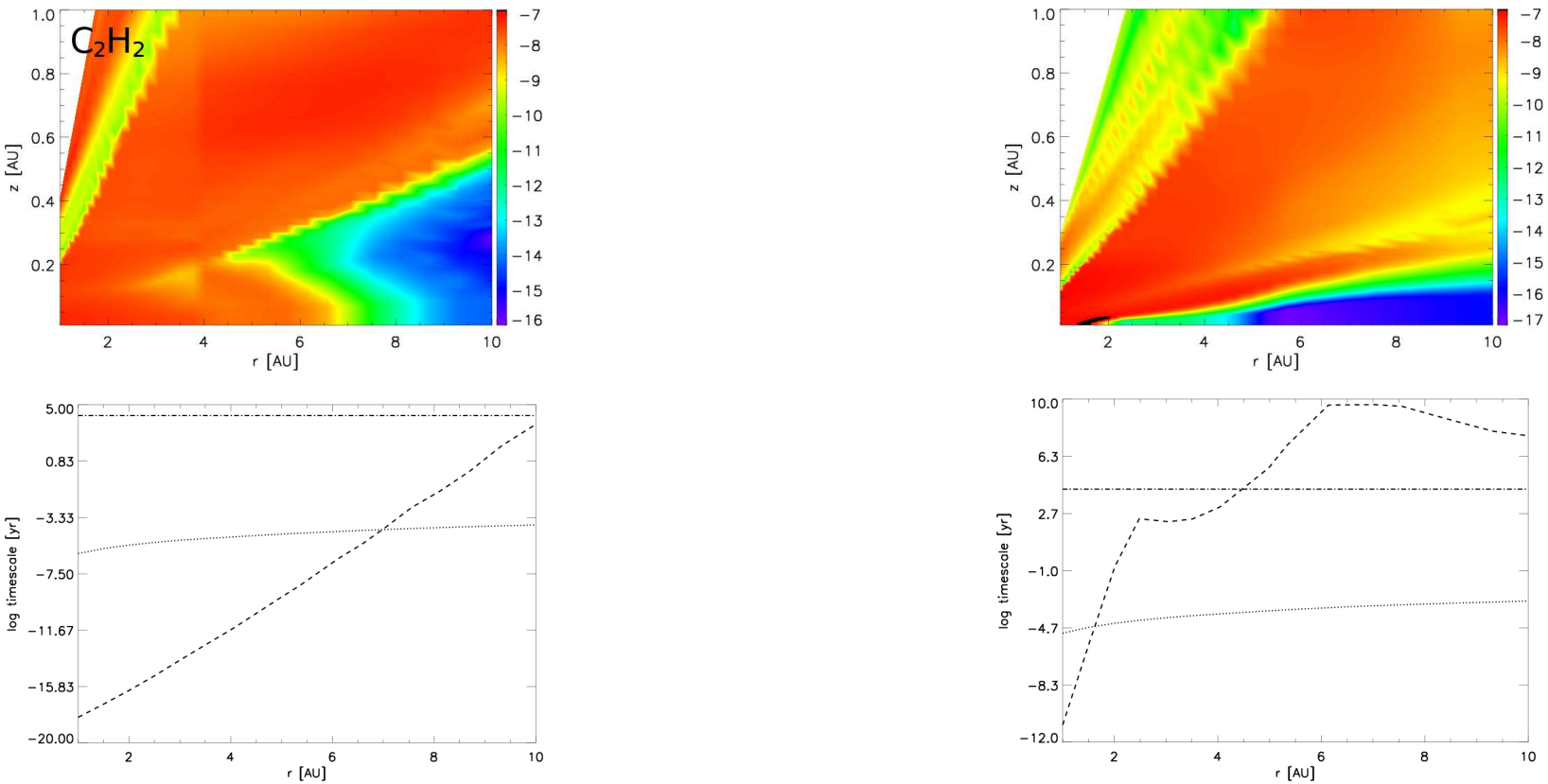

Figure 4.24: *Toprow* : Comparison of 10^{-7} $M_\odot$ yr^{-1} (left) and 10^{-8} $M_\odot$ yr^{-1} (right) molecular distributions of C_2H_2 between the midplane and z = 1 AU. *Bottomrow* : Adsorption (dotted line), desorption (dashed line) and calculation (dot-dashed line) timescales in the 10^{-7} $M_\odot$ yr^{-1} (left) and 10^{-8} $M_\odot$ yr^{-1} (right) disk for C_2H_2.

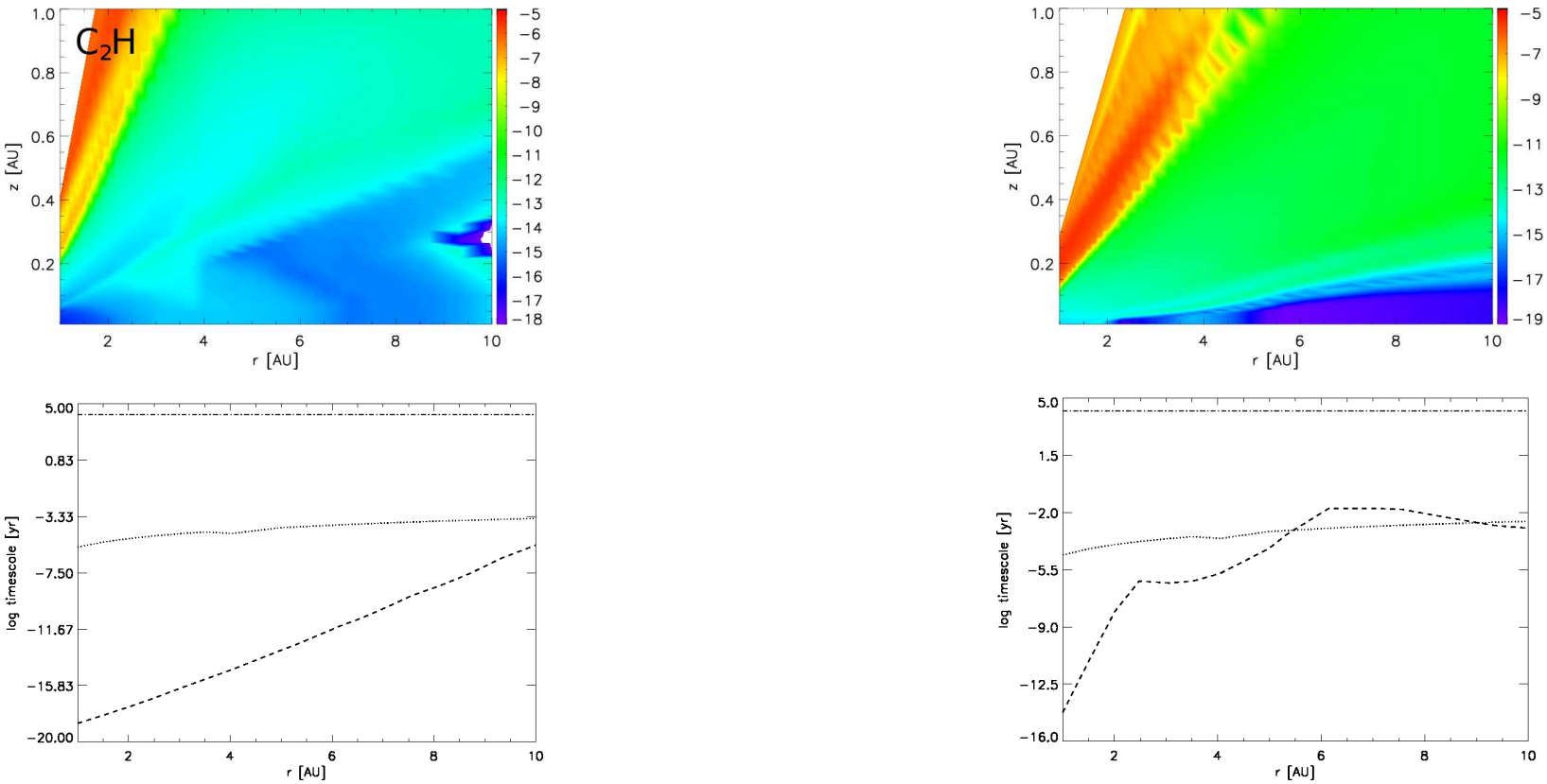

Figure 4.25: *Toprow* : Comparison of 10^{-7} $M_\odot$ yr^{-1} (left) and 10^{-8} $M_\odot$ yr^{-1} (right) molecular distributions of C_2H between the midplane and z = 1 AU. *Bottomrow* : Adsorption (dotted line), desorption (dashed line) and calculation (dot-dashed line) timescales in the 10^{-7} $M_\odot$ yr^{-1} (left) and 10^{-8} $M_\odot$ yr^{-1} (right) disk for C_2H.

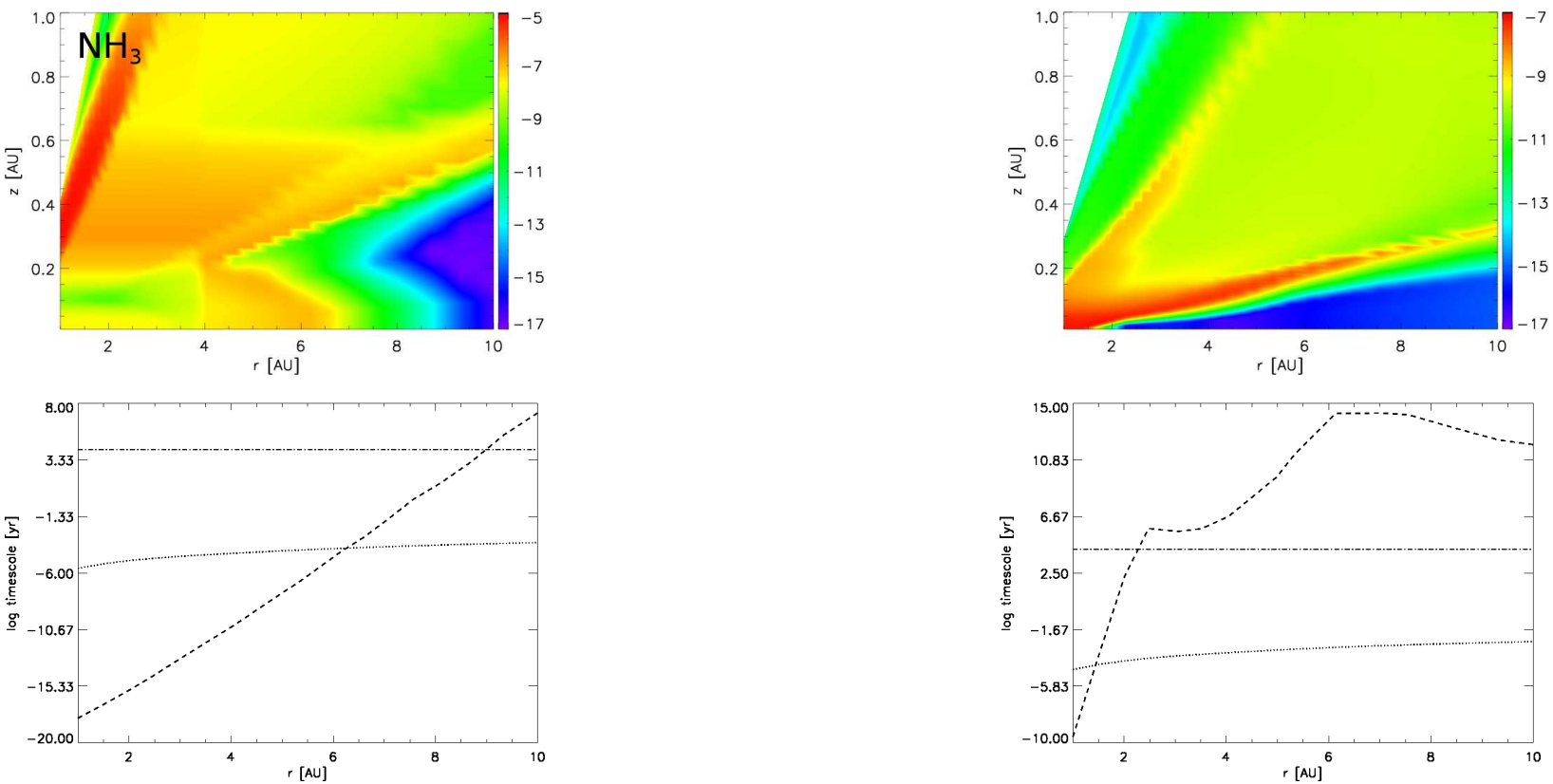

Figure 4.26: *Toprow* : Comparison of 10^{-7} $M_\odot$ yr^{-1} (left) and 10^{-8} $M_\odot$ yr^{-1} (right) molecular distributions of NH_3 between the midplane and $z = 1$ AU. *Bottomrow* : Adsorption (dotted line), desorption (dashed line) and calculation (dot-dashed line) timescales in the 10^{-7} $M_\odot$ yr^{-1} (left) and 10^{-8} $M_\odot$ yr^{-1} (right) disk for NH_3.

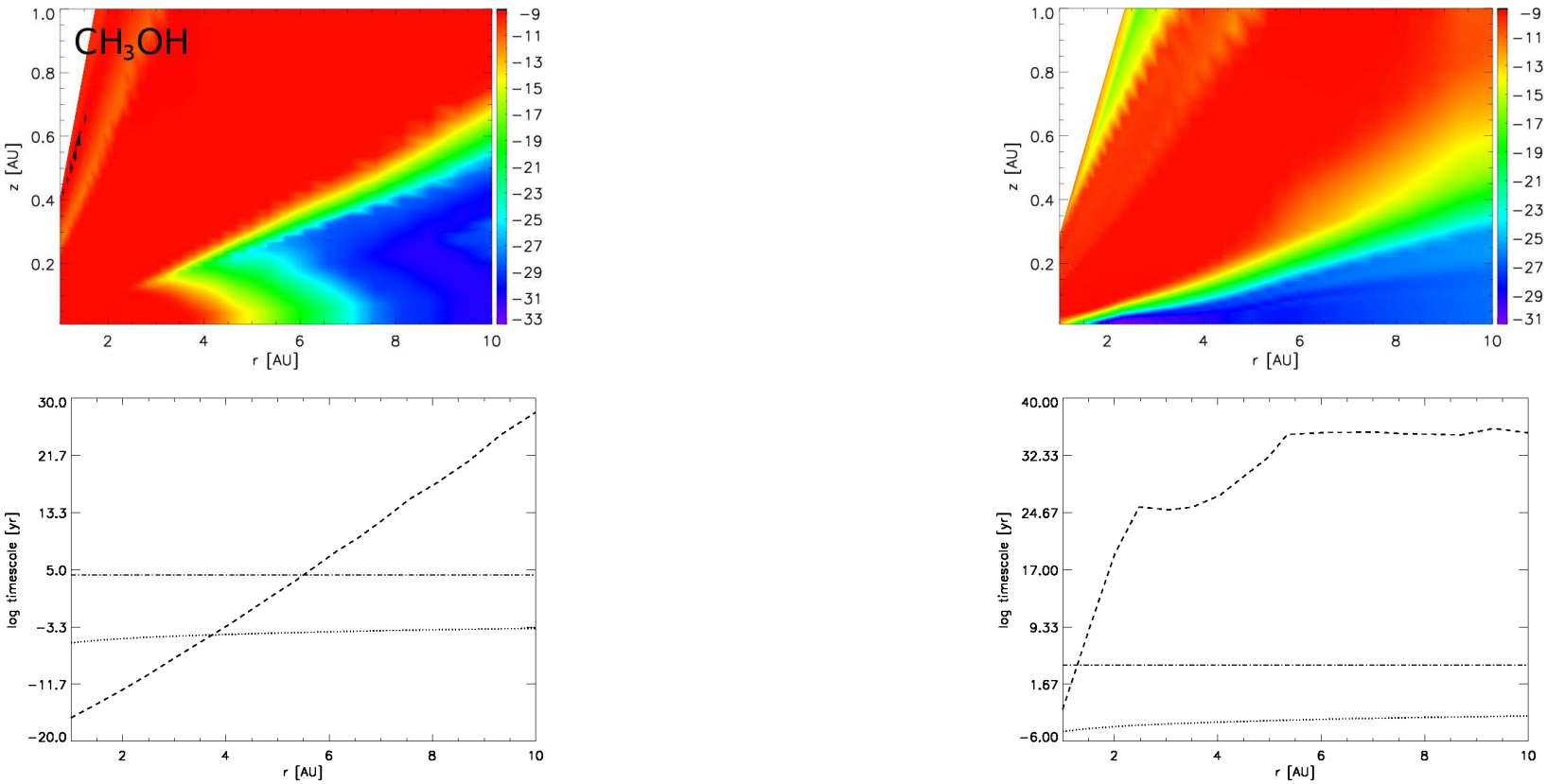

Figure 4.27: *Toprow* : Comparison of 10^{-7} $M_\odot$ yr^{-1} (left) and 10^{-8} $M_\odot$ yr^{-1} (right) molecular distributions of CH_3OH between the midplane and $z = 1$ AU. *Bottomrow* : Adsorption (dotted line), desorption (dashed line) and calculation (dot-dashed line) timescales in the 10^{-7} $M_\odot$ yr^{-1} (left) and 10^{-8} $M_\odot$ yr^{-1} (right) disk for CH_3OH.

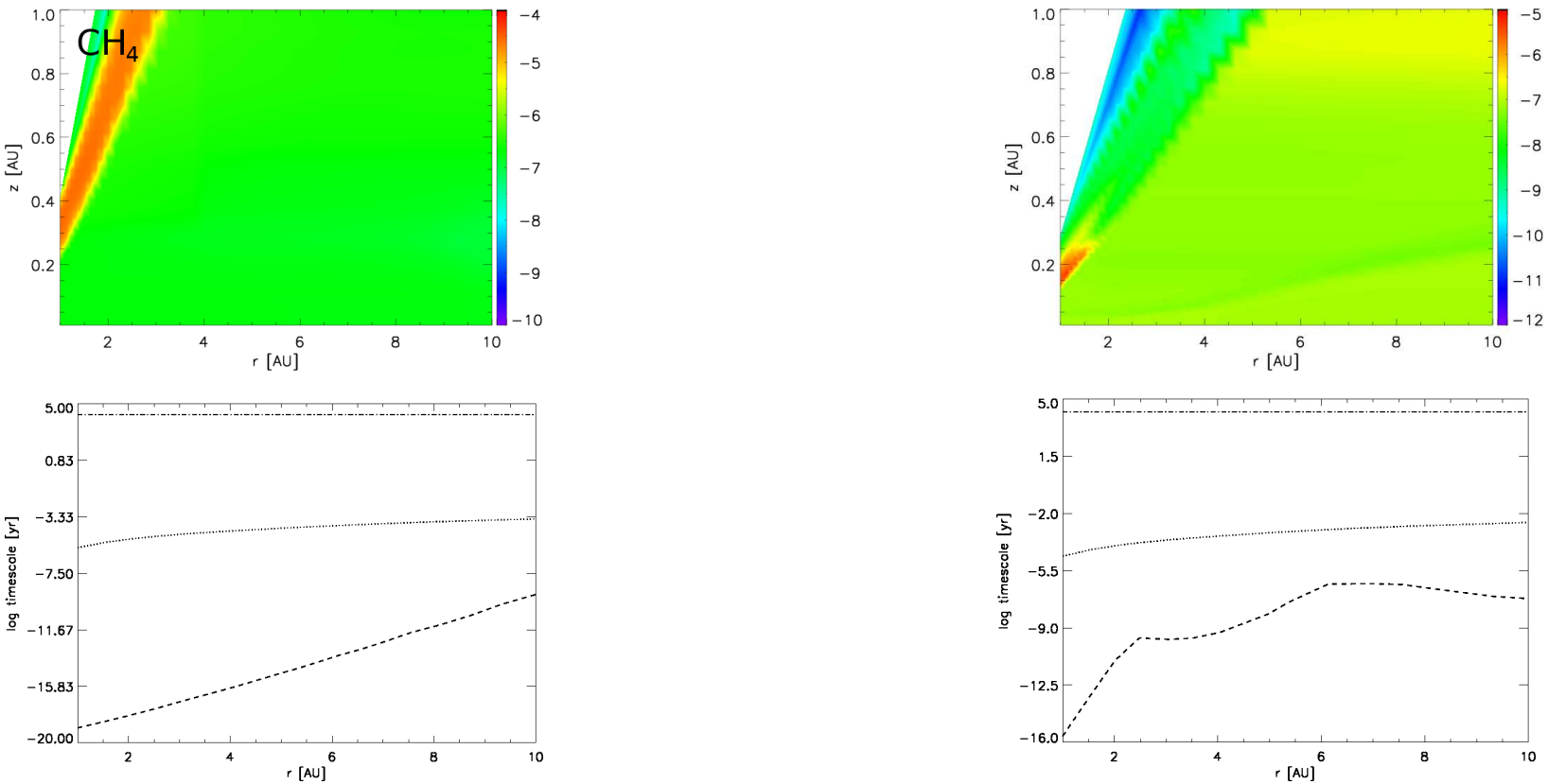

Figure 4.28: *Top* : Comparison of 10^{-7} $M_\odot$ yr^{-1} (left) and 10^{-8} $M_\odot$ yr^{-1} (right) molecular distributions of CH_4 between the midplane and $z = 1$ AU. *Bottom* : Adsorption (dotted line), desorption (dashed line) and calculation (dot-dashed line) timescales in the 10^{-7} $M_\odot$ yr^{-1} (left) and 10^{-8} $M_\odot$ yr^{-1} (right) disk for CH_4.

4.2.5 10^{-7} $M_\odot$ yr^{-1} and 10^{-8} $M_\odot$ yr^{-1} column densities

4.2.5.1 Column density comparisons

Figure 4.29 displays the molecular column density profiles for 10^{-7} $M_\odot$ yr^{-1} and 10^{-8} $M_\odot$ yr^{-1}. They are estimated by vertically integrating the molecular fractional abundances through the disk column from the surface to the midplane. The majority of 10^{-8} $M_\odot$ yr^{-1} column densities are smaller than 10^{-7} $M_\odot$ yr^{-1} since the H_2 gas density is a factor of $\sim 10^3$ lower in the 10^{-8} $M_\odot$ yr^{-1} disk. These column densities are weighted by the gas density which increases from the surface towards the midplane; that is, molecules most abundant near the midplane in chemically active zones, and at the midplane which have been thermally desorbed back to the gas. Molecules with the largest column densities are CO, H_2O, HCN, CO_2 and CH_4, which are the most abundant molecules in the chemical model. The profiles of molecules which fluctuate indicate changes in the most dominant chemical reactions involving that species.

Table 4.4 compares the column density values of CO, H_2O and HCN at 1 and 10 AU with some other chemical models which assume either 10^{-7} or 10^{-8} $M_\odot$ yr^{-1}, and the $\alpha = 0.01$ prescription. Comparisons between models are generally difficult since they each vary in their physical, radiative and chemical complexity as well as initiation (see Table 2.1, Chapter 2 of this thesis). These are limited to those closest to our disk parameters discussed in Chapter 2. Irrespective of this, reasonable agreement is found with most of the models. Specifically these molecules are found to be the most abundant in their respective initial abundances and chemical models, and are less likely to be affected by variations in physical or chemical approach, hence it is not surprising that they are similar. Heinzeller et al. (2011) values are taken from their "UV-old" model which most closely resembles the one used here, although they do still consider grain-surface chemistry. Values from Agúndez et al. (2008) are lower since their column densities are taken exclusively from simulated

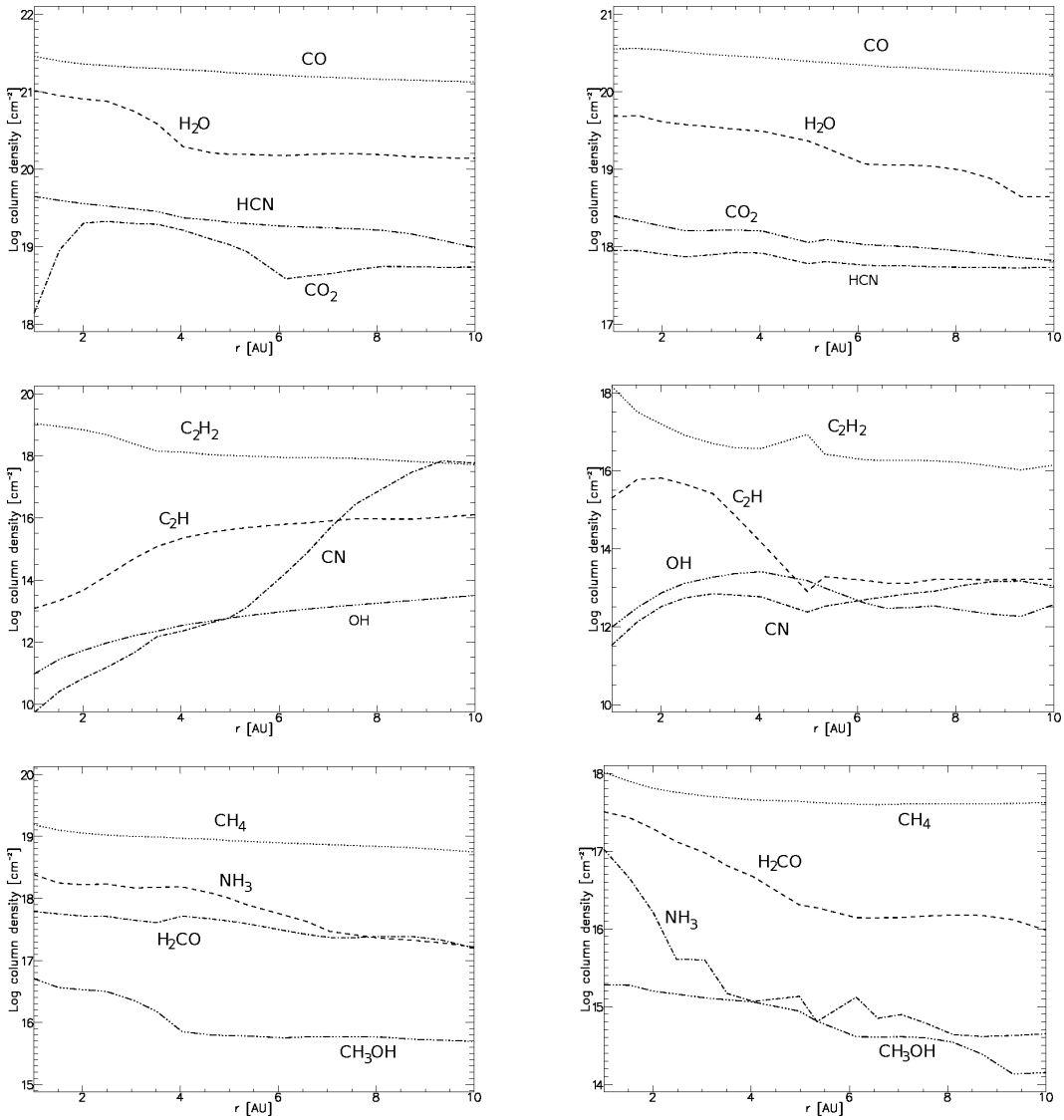

Figure 4.29: Logarithmic column density profiles of some species from the 10^{-7} $M_\odot$ yr^{-1} (left column) and 10^{-8} $M_\odot$ yr^{-1} (right column) accretion disks.

CO-depleted PDRs, whilst others presented here involve integration through the entire vertical column of their modelled disks. Willacy & Woods (2009) additionally estimated column densities for $T > 150$ K regions (denoted Willacy & Woods 2009 - PDR) associated with numerous optically-thin inner disk IR-observations, and hence compare more closely with Agúndez et al. (2008).

Table 4.4: Comparison of calculated vertical column densities (cm^{-2}) for CO, H_2O and HCN at r = 1 and 10 AU, with models that assume 10^{-7} $M_\odot$ yr^{-1} and 10^{-8} $M_\odot$ yr^{-1} and α = 0.01 prescriptions.

Model	SA rate ($M_\odot$ yr^{-1})	1 AU			10 AU		
		CO	H_2O	HCN	CO	H_2O	HCN
Thesis	1(-07)	2.9(21)	1.0(21)	4.4(19)	1.3(21)	1.4(20)	9.7(18)
Markwick et al. (2002)	1(-07)	3.2(21)	1.6(22)	2.5(20)	1.0(21)	–	5.0(17)
Thesis	1(-08)	3.6(20)	4.8(19)	8.9(17)	1.7(20)	4.4(18)	5.4(17)
Agúndez et al. (2008)	1(-08)	–	2.0(17)	2.0(16)	–	–	–
Woitke et al. (2009)	1(-08)	1.0(15)	1.0(14)	–	–	–	–
Willacy & Woods (2009)-Full	1(-08)	1.1(21)	4.1(21)	1.1(20)	3.6(20)	2.5(16)	4.2(14)
Willacy & Woods (2009)-PDR	1(-08)	1.6(19)	1.3(19)	4.4(16)	3.6(20)	2.5(16)	4.2(14)
Walsh et al. (2010)	1(-08)	2.3(21)	1.7(21)	2.0(17)	3.6(20)	4.3(15)	7.1(14)
Heinzeller et al. (2011)	1(-08)	1.9(21)	2.8(22)	5.2(19)	2.0(20)	5.4(15)	8.0(14)

4.2.5.2 Molecular D/H ratios

Another probe of early chemical and dynamical processes in the solar system, particularly with regards to the inner r < 10 AU planet-forming regions, is the determination of molecular D/H ratios - a detailed review can be found in Willacy & Woods (2009). One recent example is the HDO/H_2O ratio, which is pivotal in distinguishing between the "wet" or "dry" Earth hypotheses used to constrain the possible origins of water on our planet (although Thi et al. (2010) dispute this ratio is a suitable tracer).

Although the mechanism for deuterium enrichment is similar in molecular clouds and the low temperature environment of disks, D/H ratios have been found to be lower in the latter. It is generally accepted that D/H ratios decrease with increasing temperature since the energy differences in forward and reverse reactions becomes less significant (see Equations (2.23) and (2.24) of this thesis).

Sub-mm observations in various disks with JMCT (e.g. van Dishoeck et al. 2003) and the SMA (e.g. Kessler et al. 2002; Qi et al. 2008) established DCO^+/HCO^+ and DCN/HCN ratios ranging between ~ 0.01 - 0.03 and 0.02 respectively. DCN

was recently observed in TW Hya using ALMA-Band 6 receivers by Öberg et al. (2012) who determined DCN/HCN ratios of $\sim 10^{-2}$. This is lower than the DCN/HCN ratio value of 0.04, identical to the general D/H ratio of 10^{-2} determined by observations from the colder dark-cloud environment of TMC-1 (Roberts et al. 2002a), but higher than the cosmic, atomic D/H ratio of the local galactic disk, 1.5×10^{-5} (Linsky et al. 2006).

To date, all sub-mm observations of molecular D/H ratios in disks have probed only the colder outer $r > 50$ AU (e.g. Kessler et al. 2002; Qi et al. 2008). Although IR receivers such as the Keck Interferometer (Gibb et al. 2007) and Spitzer Space Telescope (e.g. Lahuis et al. 2006b) are capable of determining ratios in these planet-forming regions, they are only likely to probe specifically warmer surface regions where D/H ratios are much lower. ALMA is the receiver which will have the spatial and spectral resolution inside a radius of 10 AU to resolve deuterated abundances whose emission resides from the colder midplane zones, where D/H ratios are likely enhanced.

HDO/H_2O, DCN/HCN and CH_3D/CH_4 ratio enhancements over the cosmic value have also been determined from the observations of solar system comets (e.g. Meier et al. 1998; Hutsemékers et al. 2008; Gibb et al. 2012), primitive meteorites, our Moon, Mars (e.g. Novak et al. 2007; Villanueva et al. 2011), the giant planets Jupiter and Saturn (Ben Jaffel et al. 1998; Lellouch et al. 2001) along with the Saturn's water vapour-releasing moon, Enceladus (Petit et al. 2012). Since D/H ratios have been shown to increase with distance from the Sun, each case should reflect the physical and chemical conditions in which they formed. More recent data from a larger sample of comets (e.g. 103P/Hartley 2) have also confirmed a wide spread of deuterated diversity (depletions as well as enhancements) (Gibb et al. 2012). This suggests that comets formed in different regions of the solar system can be classified according to the regions where they formed, and that Uranus and Neptune were once much closer to Saturn's current distance from the Sun ~ 15 AU (see Petit

et al. 2012). A recent review of D/H values in comets can be found in Mumma & Charnley (2011). Nevertheless, the origin of deuterated material in our solar system, whether it be of interstellar or protostellar origin, is yet to be agreed on amongst the scientific community.

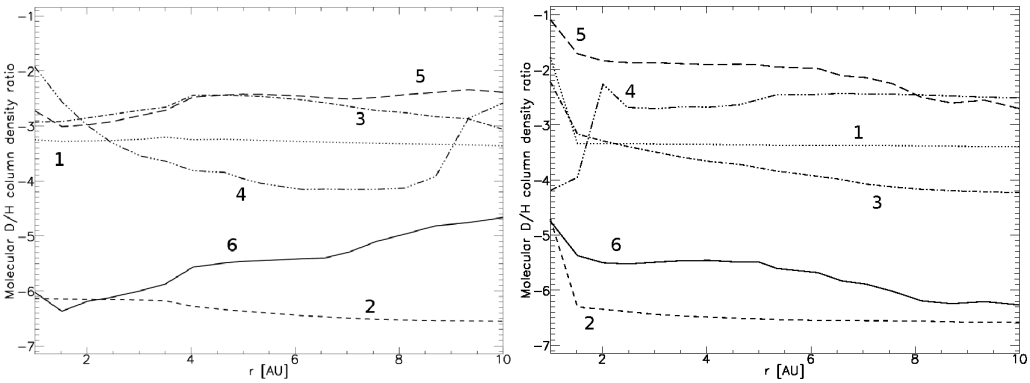

Figure 4.30: 10^{-7} $M_\odot$ yr^{-1} (left panel) and 10^{-8} $M_\odot$ yr^{-1} (right panel) D/H ratio column density profiles for: (1) HDO/H_2O, (2) D_2O/H_2O, (3) DCN/HCN, (4) DCO^+/HCO^+, (5) $HDCO/H_2CO$, and (6) D_2CO/H_2CO.

Figure 4.30 displays the D/H ratio column density profiles of some commonly observed molecules from the 10^{-7} and 10^{-8} $M_\odot$ yr^{-1} disk. The majority of molecular ratios remain more or less constant from r = 10 AU to 1 AU for 10^{-7} $M_\odot$ yr^{-1}. These include HDO/H_2O, $HDCO/H_2CO$ and DCN/HCN $\sim 10^{-3}$, and $D_2O/H_2O \sim 10^{-6}$. Those which fluctuate are: (i) DCO^+/HCO^+ which is around 10^{-3} at r = 10 AU, but then decreases to 10^{-4} at 8 AU and steadily increases to 10^{-2} at 1 AU, and (ii) D_2CO/H_2CO, which starts at 10^{-5} and steadily drops to 10^{-6} by 1 AU.

The profile behaviour in the 10^{-8} $M_\odot$ yr^{-1} disk is different. For example, the ratios at 1 AU are larger by an order of magnitude for all except DCO^+/HCO^+ which is 2 orders smaller $\sim 10^{-4}$, and $HDCO/H_2CO$ which is 2 orders larger at 10^{-1}. There appears to be a common sharp increase in the ratio between r = 1.5 AU and 1 AU, which is attributed to the shift of grain to gas-phase molecular D/H ratios where molecules are returned to the gas. The exception is DCO^+/HCO^+ which decreases

from 10^{-2} at 2 AU to 10^{-4} at 1 AU. Here, CO is photoionized to CO^+ by cosmic-rays, and the rate of the most dominant formation reaction for HCO^+, $CO^+ + H_2 \rightarrow HCO^+ + H$ is faster than the deuterated analogue channel $CO^+ + HD \rightarrow DCO^+ + H$.

Those species which show little or no change in D/H ratio profiles have accretion transport timescales which are shorter than the chemical reaction timescales that would otherwise deplete or transfer the deuterated species elsewhere. The 10^{-8} $M_\odot$ yr^{-1} profiles are similar to the molecular D/H radial column density variations in Figure 10 of Willacy & Woods (2009), despite their different physical assumptions.

Table 4.5 compares the HDO/H_2O, DCN/HCN and DCO^+/HCO^+ ratios at the midplane with that of Table 4 in Willacy & Woods (2009), observations in disks, comets, Mars, Enceladus and the Earth (i.e. the Vienna Standard Mean Ocean Water Value, VSMOW). It is seen that the D/H ratio for all three molecules at the midplane reduces with decreasing radius, apart from DCO^+/HCO^+ which is increased as a result of the rate difference between ion-neutral reactions with CO^+, H_2 and HD. The DCO^+/HCO^+ and DCN/HCN values from the model are lower than disk observations, which is expected since they are constrained to $r > 50$ AU regions where D/H ratios are higher. The HDO/H_2O values at $r = 1$ AU for 10^{-7} and 10^{-8} $M_\odot$ yr^{-1} accretion disks fit closest to the planetary values, in particular the VSMOW which is identical to the 10^{-8} $M_\odot$ yr^{-1} value. Cometary values fluctuate between 10^{-3} and 10^{-4}, correlating with the HDO/H_2O values from any of the three radii in the model.

The results extracted from Willacy & Woods (2009) are a combination of gas-phase and grain-abundance molecules, since they do not provide gas-phase abundances beyond 5 AU. This may not be the best scenario for comparison because their 10^{-8} $M_\odot$ yr^{-1} model is "heavier" and more complex since they additionally consider grain-surface reactions and ice-mantles on grains. Grain and gas D/H ratios for neutral species are identical in this work since thermal desorption and

Table 4.5: Comparisons between HDO/H_2O, DCN/HCN and DCO^+/HCO^+ ratios at the midplane, and those from Woods & Willacy (2009), sub-mm disk observations, eight comets, Enceladus, Mars and Earth (VSMOW).

Model/Reference	Radius (AU)/Object	HDO/H_2O	DCN/HCN	DCO^+/HCO^+
10^{-7} $M_\odot$ yr^{-1}	1	5.9(-04)	1.3(-03)	1.9(-02)
	5	4.1(-04)	4.6(-03)	2.6(-04)
	10	2.5(-03)	2.3(-03)	3.4(-03)
10^{-8} $M_\odot$ yr^{-1}	1	1.6(-04)	2.4(-03)	1.6(-04)
	5	2.4(-03)	2.8(-02)	4.7(-03)
	10	3.4(-03)	2.4(-02)	5.3(-03)
Woods & Willacy (2009)	1	1.0(-02)	5.5(-06)	–
	5	9.6(-03)	3.0(-03)	–
	10	9.5(-03)	3.0(-02)	2.3(-02)
van Dishoeck et al. (2003)	TW Hya	–	–	3.5(-02)
Guilloteau et al. (2006)	DM Tau	–	–	4.0(-03)
Qi et al. (2008)	TW Hya	–	1.7(-02)	1.0(-02) - 1.0(-01)
Oberg et al. (2012)	TW Hya	–	1.0(-02)	–
Eberhardt et al. (1995)	Comet/P Halley	6.2(-04)	–	–
Meier et al. (1998)	Hale-Bopp	6.6(-04)	2.3(-03)	–
Bocklee-Morvan et al. (1998)	Hyakutake	5.8(-04)	–	–
Hutsemekers et al. (2008)	C/2002 T7 (LINEAR)	5.0(-04)	–	–
Villanueva et al. (2009)	8P/Turtle	8.2(-04)	–	–
Hartogh et al. (2011)	103P/Hartley 2	3.2(-04)	–	–
Bocklee-Morvan et al. (2012)	C/2009 P1 (Garradd)	2.1(-04)	–	–
Gibb et al. (2012)	C/2007 N3 (LULIN)	1.1(-03)	–	–
Waite et al. (2009)	Enceladus	2.9(-04)	–	–
Owen et al. (1988)	Mars	8.5(-04)		
Various	Earth (VSMOW)	1.6(-04)	–	–

freeze-out are the only two considered processes; DCO^+/HCO^+ is different to its neutral grain counterpart, GDCO/GHCO as grain-surface recombination is also incorporated. The ratios from Willacy & Woods (2009) are larger, likely owing to higher initial molecular cloud ratios and slight variations in binding energies.

4.3 Investigation: Modelling from 10^{-7} $M_\odot$ yr^{-1} to 10^{-8} $M_\odot$ yr^{-1}

There have been many previous studies of protoplanetary disk chemical modelling which consider a stellar accretion rate of either 10^{-7} $M_\odot$ yr^{-1} (e.g. Markwick et al. 2002, Millar et al. 2003, Semenov et al. 2004), 10^{-8} $M_\odot$ yr^{-1} (e.g. Willacy & Woods 2009, Semenov et al. 2010, Walsh et al. 2010) and 10^{-9} $M_\odot$ yr^{-1} (e.g. Vasyunin et al. 2011). Comparisons have also been made between observations and models with stellar accretion rates of 10^{-7} $M_\odot$ yr^{-1}, 10^{-8} $M_\odot$ yr^{-1} and 10^{-9} $M_\odot$ yr^{-1} (e.g. D'Alessio et al. 1999).

Numerous observations have shown that protoplanetary disks vary from faster to slower accretion rates with the median stellar accretion rate $\sim 10^{-8}$ $M_\odot$ yr^{-1} (Hartmann et al. 1998) and this is set as the benchmark in all recent models (the so called "fiducial" models). In Section 4.2, the resulting molecular distributions of 10^{-7} $M_\odot$ yr^{-1} and 10^{-8} $M_\odot$ yr^{-1} disks from a similar physical calculation and identical initial chemistry were discussed. However, all previous investigations to date have failed to attempt modelling from a higher to lower accretion rate, particularly concerning the inner $r \leq 10$ AU, and thus more accurately simulate the chemical evolution in the planet-forming region of a protoplanetary disk. Ideally, a fully-coupled physical and chemical transition is the most desirable outcome, but iteratively calculating the density, temperature and optical depth parameters for each timestep is beyond the scope of this investigation. Instead, a basic benchmark investigating how the chemistry evolves can be modelled. A single iteration can be performed where the calculation is run for a period of time under the physical conditions of a higher stellar accretion rate, and this chemical output is input into the calculation of the lower accretion rate for another period of time.

In this investigation, the 10^{-8} $M_\odot$ yr^{-1} calculation is run as a function of the initial abundance values listed in Tables 2.4 and 2.5 in Section 2 (termed Model A),

and is compared to a calculation which begins from the 10^{-7} $M_\odot$ yr^{-1} disk structure, and the chemical output is used as input for a 10^{-8} $M_\odot$ yr^{-1} (termed Model B) calculation. Each of the 10^{-7} $M_\odot$ yr^{-1} and 10^{-8} $M_\odot$ yr^{-1} sub-calculations in Model B are run for the same time over the entire grid as their separate 10^{-7} $M_\odot$ yr^{-1} and 10^{-8} $M_\odot$ yr^{-1} (Model A) counterparts discussed in Section 4.3.2 and 4.3.3.

Figure 4.31 displays the Model B calculation process from the outer radius of 25 AU to the inner radius of 1 AU. This method requires starting the calculation at the same radius in the 10^{-8} $M_\odot$ yr^{-1} disk, as opposed to initially calculating along the line of radial accretion flow as in the 10^{-7} $M_\odot$ yr^{-1} simulation.

Any differences between Models A and B will occur at the midplane where adsorption and desorption processes are dominant, and in chemically active layers just above the midplane, where the chemical, adsorption, desorption and calculation timescales are competitive and comparable. The left panels of Figures 4.32 to 4.35 depict the molecular distribution sensitivity profiles between Model A and B for the twelve species, and the right panels show their column density profiles for 1 AU $\leq r \leq$ 10 AU, which are weighted by the denser midplane. The resulting differences in the column density profiles of Models A and B are then addressed in terms of these sensitivity profiles, which are constrained between the midplane and z = 1 AU; these being the densest disk regions which contribute most to the column density.

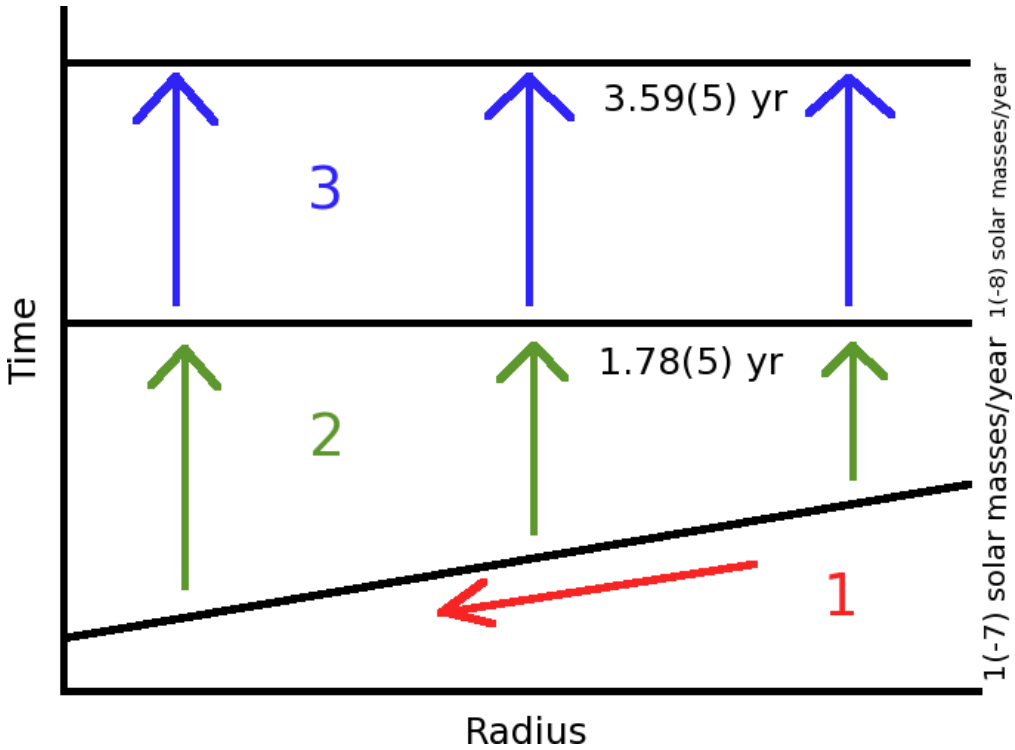

Figure 4.31: Schematic diagram of Model B process as a function of calculation time. Phases 1 and 2 display the portion of simulation spent in the 10^{-7} $M_\odot$ yr^{-1} disk, of which the line with red arrow represents the accretion calculation period along the line of radial accretion flow. Every grid point is run for an additional calculation time until the entire grid is calculated for 1.78×10^5 years (green arrows). Using the resulting chemical data from 10^{-7} $M_\odot$ yr^{-1}, the model then proceeds in the 10^{-8} $M_\odot$ yr^{-1} disk (Phase 3) and simulated at each radius (blue arrows) for 1.81 $\times 10^5$ years. 3.59×10^5 years depicts the total calculation time of Model B.

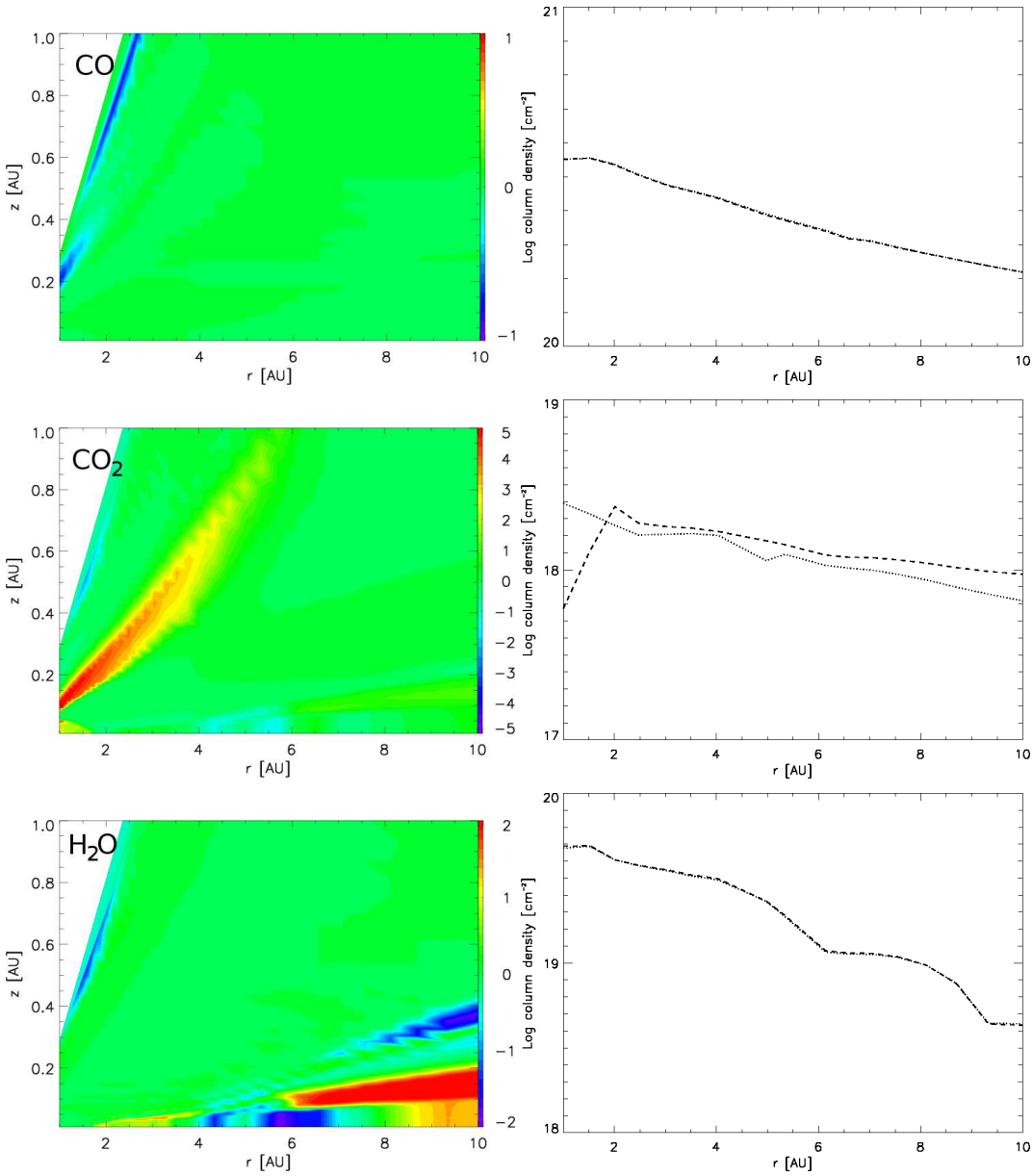

Figure 4.32: Left: Logarithmic molecular distribution sensitivities between Models A (MA) and B (MB) for CO, CO_2 and H_2O. MA/MB sensitivities > 1 depict higher abundances in Model A, whilst sensitivities < 1 represent higher abundances in Model B. Right: Corresponding column density profiles for Model A (dotted line) and Model B (dashed line).

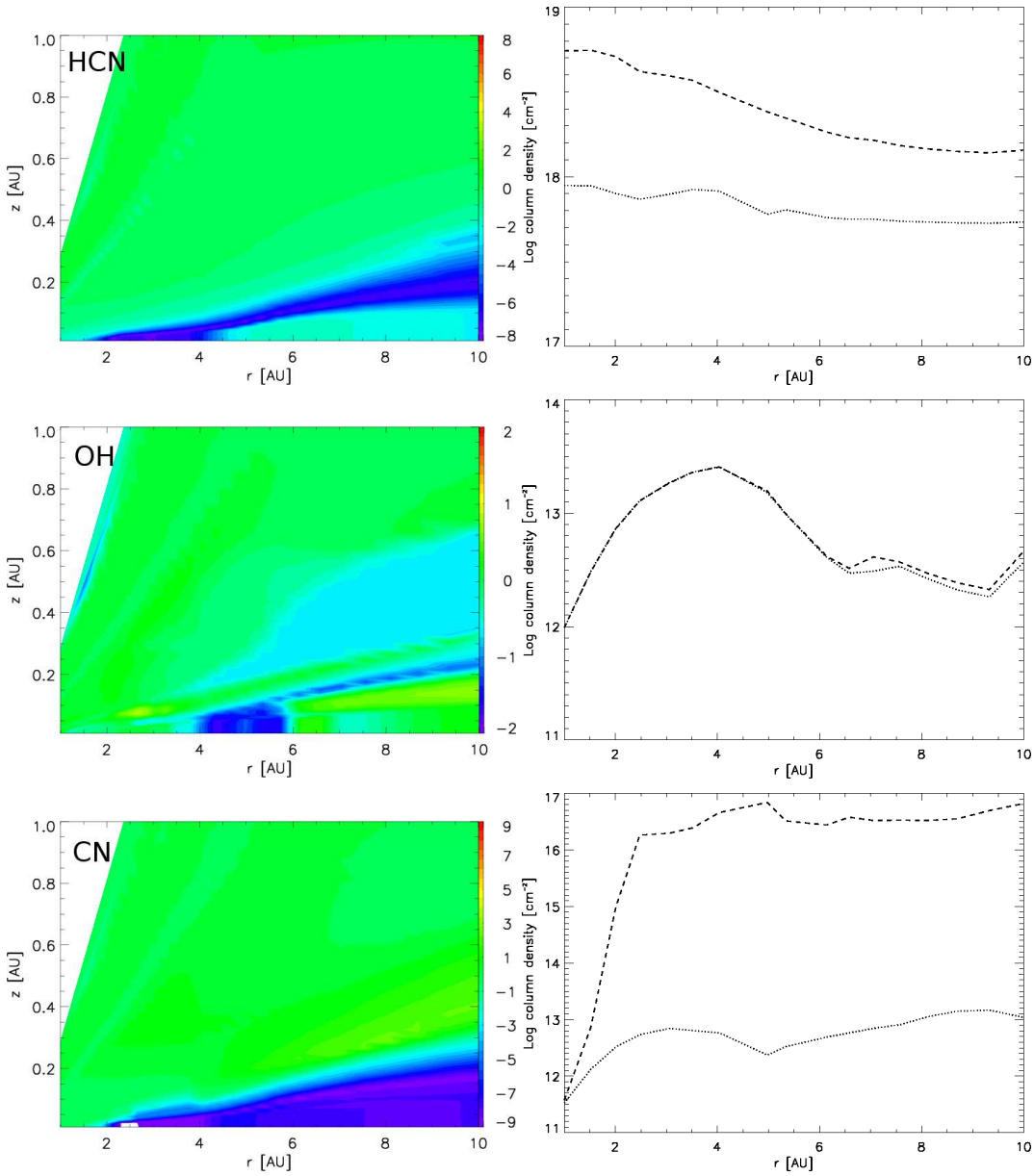

Figure 4.33: Left: Logarithmic molecular distribution sensitivities between Models A (MA) and B (MB) for HCN, OH and CN. MA/MB sensitivities > 1 depict higher abundances in Model A, whilst sensitivities < 1 represent higher abundances in Model B. Right: Corresponding column density profiles for Model A (dotted line) and Model B (dashed line).

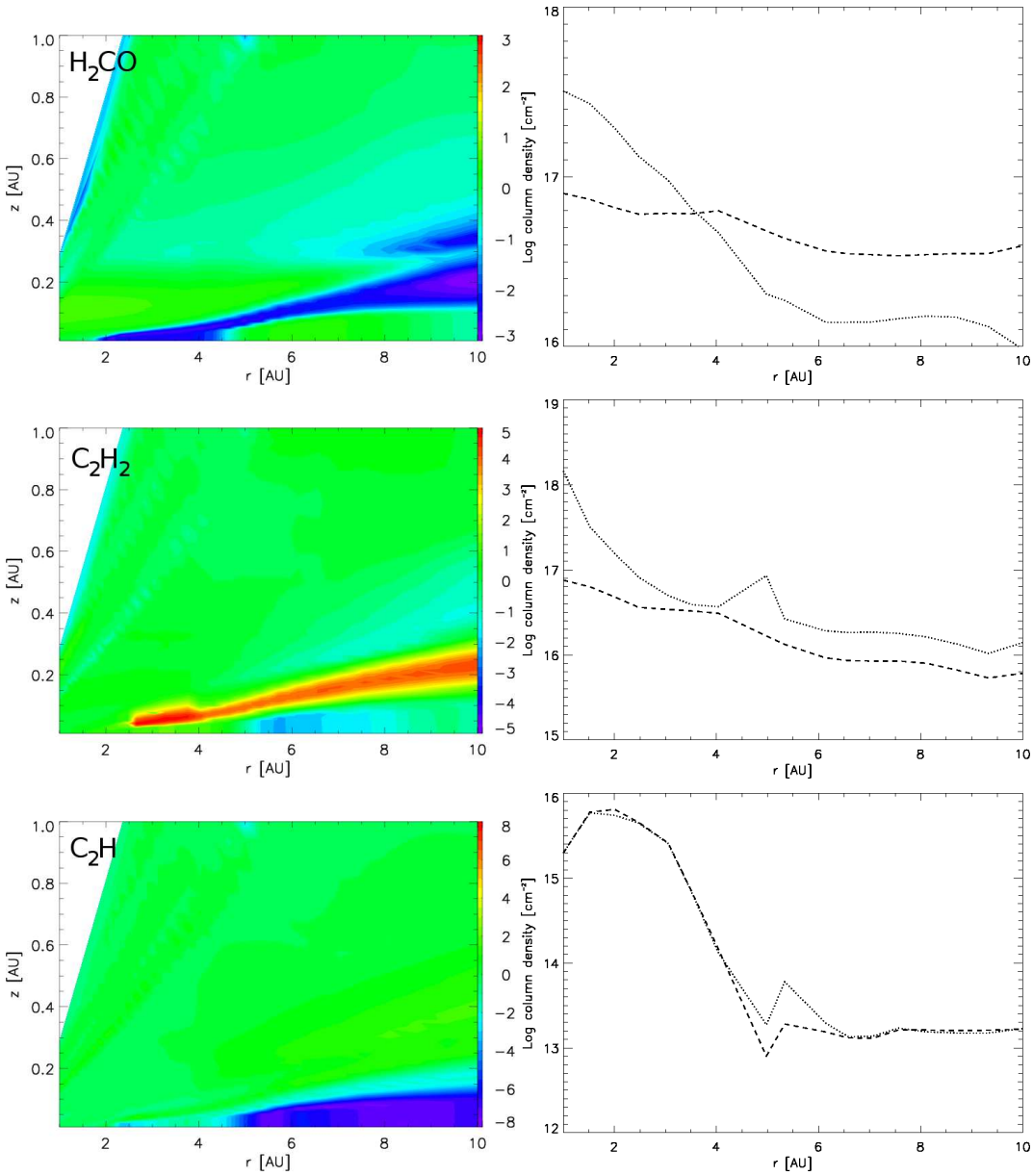

Figure 4.34: Left: Logarithmic molecular distribution sensitivities between Models A (MA) and B (MB) for H_2CO, C_2H_2 and C_2H. MA/MB sensitivities > 1 depict higher abundances in Model A, whilst sensitivities < 1 represent higher abundances in Model B. Right: Corresponding column density profiles for Model A (dotted line) and Model B (dashed line).

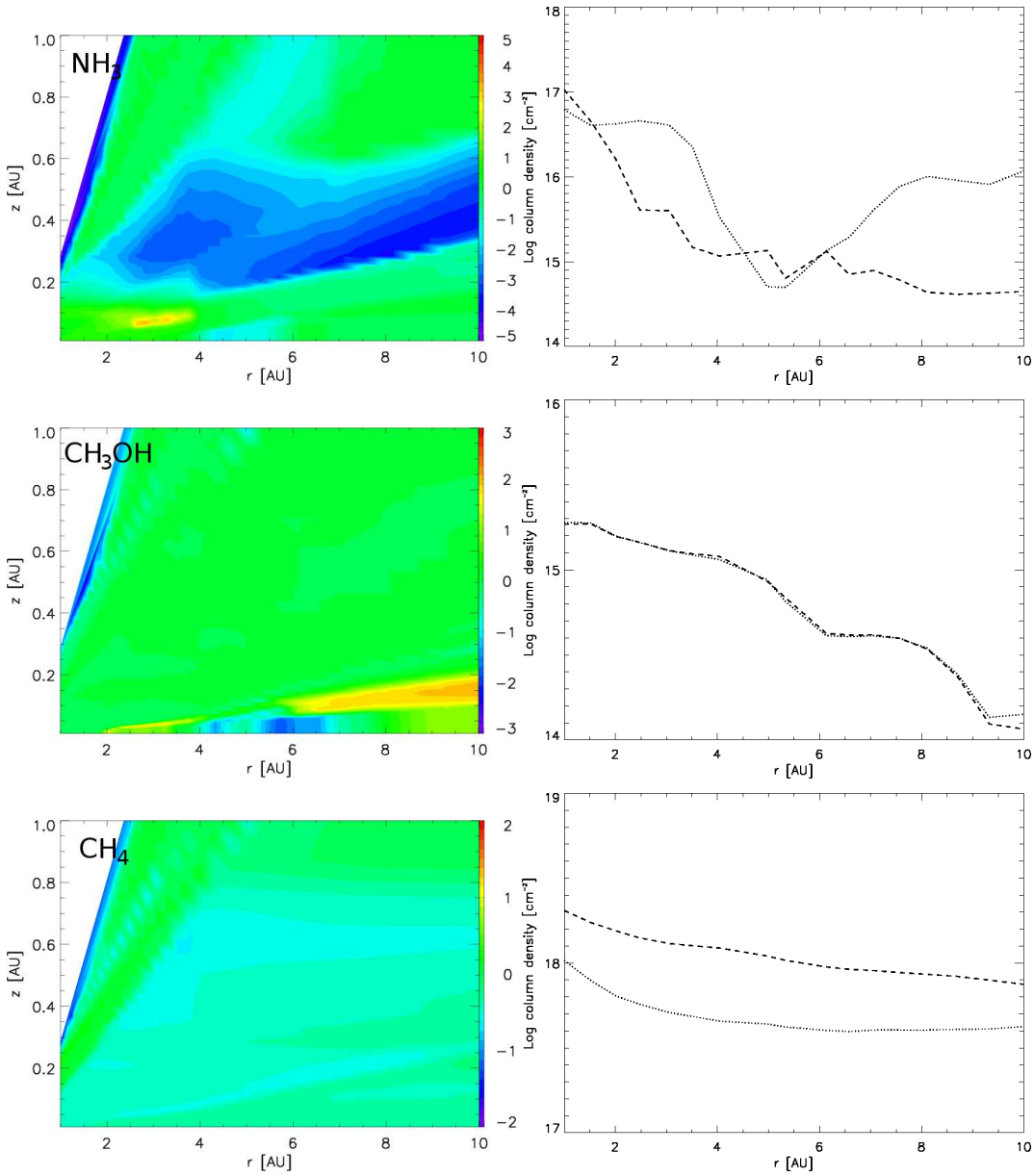

Figure 4.35: Left: Logarithmic molecular distribution sensitivities between Models A (MA) and B (MB) for C_2H, NH_3, CH_3OH and CH_4. MA/MB sensitivities > 1 depict higher abundances in Model A, whilst sensitivities < 1 represent higher abundances in Model B. Right: Corresponding column density profiles for Model A (dotted line) and Model B (dashed line).

As before, column densities are calculated by integrating the molecular abundances vertically from the surface to the midplane. The sensitivity, S, is defined by:

$$S = \frac{\text{Model A abundance}}{\text{Model B abundance}}. \tag{4.1}$$

Regions coloured green represent a sensitivity, S of $10^0 = 1$, i.e. no difference. Those coloured yellow to red portray $S > 1$ regions, whilst blue to purple regions denote $S < 1$. The sensitivity range for each of the distributions are set equidistantly either side of 10^0 to provide a clear sense of how these ratios effect the corresponding Model A and Model B column densities. The results of each molecule are described in turn.

The first notable differences occur at the midplane region inside the 10^{-7} $M_\odot$ yr^{-1} snow-line but outside the 10^{-8} $M_\odot$ yr^{-1} snow-line. Here, in Model B, three outcomes are possible:

(i) A molecule can be returned into the gas, but undergoes minimal chemical processing in the 10^{-7} $M_\odot$ yr^{-1} epoch, preserving its abundance. It is then completely frozen back out (i.e. $\tau_{des} > \tau_{ads}$) in the 10^{-8} $M_\odot$ yr^{-1} epoch within τ_{acc} and τ_{calc}. Molecules fitting this criteria are CO_2, H_2O, NH_3, C_2H_2 and have S values ~ 1 at the midplane.

(ii) A molecule is desorbed and preserved in the 10^{-7} $M_\odot$ yr^{-1} epoch as in (i), but is only partially frozen out in the 10^{-8} $M_\odot$ yr^{-1} epoch because $\tau_{ads} \sim \tau_{des}$. The molecule satisfying this criteria is HCN and H_2CO.

(iii) A molecule is desorbed, but undergoes chemical processing in the 10^{-7} $M_\odot$ yr^{-1} epoch which reduces its abundance, before being frozen back out in the 10^{-8} $M_\odot$ yr^{-1} epoch, albeit to a lesser extent since there is less to freeze back out. The molecule obeying this scenario is CN, which becomes embroiled in HCN formation and destruction reactions.

CO and CH_4 remain in the gas-phase inside a radius of 10 AU during the entire

Model B calculation, so the competition between adsorption and desorption processes at the midplane are not important for these molecules. They show no degree of sensitivity at the midplane, but the CH_4 is sensitive further up in a more chemically active zone.

Sensitivity bands also exist in chemically active layers above the midplane for certain molecules, and beyond the 10^{-8} $M_\odot$ yr^{-1} snow-line. Here, differences in the initial abundances of Model B, compared to the initial abundance of Model A, can alter the chemical evolution, either though the same 10^{-8} $M_\odot$ yr^{-1} reaction channels, or by activating different 10^{-8} $M_\odot$ yr^{-1} chemical reaction channels to those in Model A. In either case the result is a final Model B molecular abundance which is different to Model A.

The bluer ($S < 1$) bands in CN, HCN, H_2CO and NH_3 distributions are all such examples of initial abundances which are larger in Model B. Whereas H_2CO and NH_3 gas-phase reaction and grain-interaction pathways are unaltered, HCN peaks in Model B at $S \sim 10^{-8}$ primarily because there is more CN available from HC_3N to rapidly form it via endothermic reactions with H_2. At the same time, the cosmic-ray dissociation back to CN is then enhanced. Chemical reactions which break the CN triple bond are incapable of rivaling photodissociation due to the large activation energies required, so the enhanced reaction channel in Model B is exclusive to cyano-species.

The yellow-red ($S > 1$) bands in the distributions of CO_2, C_2H_2 and CH_3OH are all examples of lower initial abundances in Model B. As in Model A, C_2H_2 and CH_3OH abundances do not vary in the 10^{-8} $M_\odot$ yr^{-1} epoch. CO_2 increases from an initial abundance of 10^{-13} to 10^{-10} at the end of the 10^{-8} $M_\odot$ yr^{-1} epoch, since firstly the general ionic fraction is higher and dissociative recombination from HCO_2^+ is more prevalent, and secondly the endothermic destruction reaction, $H_2 + CO_2 \rightarrow H_2O + CO$ is less effective. However this is still lower than the Model A steady-state abundance of 10^{-6}, resulting in a red region with $S \sim 10^4$.

CH_4 is the only molecule of the twelve of which grain interaction is not important inside a radius of 10 AU and yet still shows a slight degree of sensitivity ($\sim 10^{-1}$). This sensitivity, although not obviously significant, is exemplified at the midplane since the gas-phase abundance of CH_4 is larger than most other species whose snow-lines reside inside 10 AU; particularly in the 10^{-8} $M_\odot$ yr^{-1} epoch. Combined with the fact that column densities are weighted by the denser midplane, the Model B column density of CH_4, averaging $\sim 3 \times 10^{18}$ cm^{-2}, is a around factor of 3 larger than the Model A column density, $\sim 1 \times 10^{18}$ cm^{-2}.

4.3.1 Uncertainties in sensitivity

Most of these molecular enhancements or depletions in Model B are translated to the corresponding column density profiles. Unfortunately, the correlation between sensitivity and column densities is not always so straightforward. In addition to the individual uncertainties of the 10^{-7} $M_\odot$ yr^{-1} and 10^{-8} $M_\odot$ yr^{-1} molecular distributions discussed in Section 4.3.1, discrepancies between certain "blobs" of differing sensitivity and the resultant column densities do exist which cannot be explained by the given reasons alone.

Redder or bluer blobs occur in localized regions where adsorption or desorption processes either change drastically at the midplane, or suddenly become important in the chemically active layers. One example is the CO_2, H_2O, OH, CH_3OH and NH_3 $S \sim 10^{-2}$ region between the radii of 4 – 6 AU at the midplane. Here, the initial abundance in Model B is higher than that of Model A, but the re-adsorption channel which should be active in the 10^{-8} $M_\odot$ yr^{-1} epoch is ineffective at freezing these molecules back out. One plausible reason is that τ_{ads} and τ_{des} are too similar for the solver to calculate the readsorption rate. RTOL and ATOL values, assigned as 10^{-9} and 10^{-11} respectively, may be set too high to tolerate the rapidly changing abundance which readsorption brings here, hence the solver bypasses these calculations altogether. Nevertheless, the sensitivity of these blobs are too small and localized

to appear in the Model B column density profiles.

4.3.2 Summary

In this investigation, the molecular distributions of ten molecules (CO, CO_2, H_2O, HCN, H_2CO, C_2H_2, C_2H, NH_3, CH_3OH and CH_4) from two simulations, Model A and Model B, have been compared and discussed, focusing particularly on the inner 1 AU $\leq r \leq$ 10 AU region. Molecules which show the greatest differences in column density, i.e. CN, HCN, H_2CO and NH_3, appear to be most sensitive to changes in the initial abundances of a simulation which considers a mass stellar accretion rate of 10^{-8} $M_\odot$ yr^{-1}. These differences occur at and around the colder, denser midplane, where sub-mm emission is expected. The column density of CN is enhanced by 4 orders of magnitude in the region 2 AU $\leq r \leq$ 10 AU, using the initial abundances from a 10^{-7} $M_\odot$ yr^{-1} calculation, compared with the initial abundances used from a pre-stellar core model. HCN is enhanced by roughly a factor of 7 throughout 1 AU $\leq r \leq$ 10 AU. H_2CO switches from enhancement to depletion at $r \sim 4$ AU, and vice-versa with $NH_3 \sim r = 5$ AU.

4.3.3 Column density values

Table 4.6 presents a tabulated summary of the calculated Model A and Model B column density values, at $r = 1, 5$ and 10 AU, for each of the twelve species. Ideally the Model B values should be compared to column density estimates constrained from current observational data of inner PPDs, to see whether they are in closer agreement than the MA values. Unfortunately, this is difficult since observations of inner disks are currently limited to the hot ($T \sim 1000$ K), less-dense IR-emitting surface regions (e.g. Salyk et al. 2008, Pontoppidan et al. 2010b, Salyk 2011). As Section 4.4 explained, the differences in the column density values are attributed to deeper regions around the midplane, which ALMA may be able to probe one fully

operational. Until then, scientists are restricted to ALMA simulators.

Table 4.6: Model A (MA) and Model B (MB) column density values at $r = 1, 5$ and 10 AU.

Species	1 AU		5 AU		10 AU	
	MA	MB	MA	MB	MA	MB
CO	3.6(20)	3.6(20)	2.4(20)	2.4(20)	1.7(20)	1.7(20)
CO_2	2.5(18)	5.9(17)	1.1(18)	1.5(18)	6.6(17)	9.4(17)
H_2O	4.8(19)	4.9(19)	2.3(19)	2.3(19)	4.4(18)	4.3(18)
OH	9.8(11)	9.8(11)	1.5(13)	1.6(13)	3.7(12)	4.6(12)
HCN	8.9(17)	5.5(18)	6.0(17)	2.4(18)	5.4(17)	1.4(18)
CN	3.4(11)	3.8(11)	2.4(12)	6.9(16)	1.1(13)	6.6(16)
H_2CO	3.2(17)	8.0(16)	2.0(16)	4.8(16)	9.6(15)	3.9(16)
C_2H_2	1.5(18)	7.5(16)	8.6(16)	1.7(16)	1.4(16)	6.1(15)
C_2H	2.0(15)	2.0(15)	8.0(12)	1.9(13)	1.7(13)	1.7(13)
NH_3	1.1(17)	6.2(16)	1.4(15)	5.1(14)	4.5(14)	1.2(16)
CH_3OH	1.9(15)	1.9(15)	8.7(14)	8.6(14)	1.4(14)	1.2(14)
CH_4	1.0(18)	2.0(18)	4.4(17)	1.1(18)	4.2(17)	7.5(17)

4.4 ALMA simulations

The molecules which have been observed in numerous protoplanetary disks were summarized in Section 4.3, along with the wavelength regimes associated with their emission. IR emission originates from vibrational transitions in the hotter surface disk regions, whilst sub-mm emission is generated from rotational transitions in cooler, deeper disk regions. The next question is, is it possible for the sensitivities discussed in Section 4.3 to be observed in protoplanetary disks? Such sensitivities may be translated to differences in observed molecular emission lines of Models A and B. And which transition lines in particular? Since these differences contributing most to the column density profiles, reside at the denser $r \leq 10$ AU midplane (30 – 40 K), ALMA is the most appropriate observational tool for potentially detecting

and resolving these sensitivities.

To date, ALMA is not fully operational to begin observing a specific project such as this. Instead, software packages are used to mimic the physical and chemical structures of observable disks, along with the physical and angular distances to the source, and in turn estimate the resulting molecular line intensity observed. One such piece of software is the Common Astronomy Software Applications (CASA) package, of which a basic 1-D LTE CASA analytical algorithm is used here (C. Walsh; private communication – C.Walsh converted the fractional abundance, gas density and temperature values provided by the author to integrated intensity, optical depth and emissivity values via her algorithm. The author of this thesis has then presented and interpreted the following results of this conversion). This algorithm has also been used in Walsh et al. (2013).

4.4.1 Rotational transitions

ALMA detects in the sub-mm range (100 μm – 1 mm) of the electromagnetic spectrum. Sub-mm emission originates from the rotational transitions of a molecule. Molecules rotate with energies in discrete levels, and by convention, the particular rotational state of a molecule is given by its rotational angular momentum quantum number level, J, and $J = 0$ depicts the unexcited ground state, i.e. no rotational excitation, with increasing values representing higher, more excited states. Molecules typically decay from a J+1 state to J (i.e. $\Delta J = 1$) and accordingly emit a unique energy signature which is observed as a molecular transition line in the sub-mm regime. One commonly observed example is the J = 4-3 transition line of HCO^+ (van Zadelhoff et al. 2002).

Some lines are more intense than others, probing regions of higher molecular abundance with a correspondingly larger number of transitions, depending on the temperature, density and optical depth of the observed region. For linear polyatomic molecules such as HCN whose rotation consists of two identical moments of inertia,

the relationship between the energy E_J at a level J is expressed as:

$$E_J = BhcJ(J+1), \tag{4.2}$$

where B is a rotational constant unique to each molecule (m^{-1}), h is the Planck constant and c the speed of light. Realistically, one would also need to consider centrifugal distortion due to rotation, but this is commonly ignored for simplicity. The relationship for molecules with two different moments of inertia is more complex, and requires the assignment of separate quantum numbers to each moment of inertia. H_2CO is one example, which is defined as a prolate symmetric top (Brunken et al. 2003).

4.4.2 LTE level populations

The transition strength depends on the number of molecules in a given rotational level, or the population density. Radiative transfer algorithms are used to calculate the level populations, in terms of the fractional abundances and local physical parameters. These can vary from basic 1-D programs which consider Local Thermodynamic Equilibrium (LTE) (e.g. Gómez & D'Alessio 2000), to more complex 2-D non-LTE codes (see van Zadelhoff et al. 2002). In this investigation, Local Thermodynamic Equilibrium (LTE) is assumed, which is generally applicable for inner disks (van Zadelhoff 2002) where the sensitivities for HCN and H_2CO occur. In LTE, the rates of molecular collisions greatly exceed the rates of absorption and emission of energy. Firstly the density n is large enough for molecules to be collisionally excited above a critical density n_{cr}:

$$n_{cr} = \frac{A_{ul}}{\sum_i K_{ui}} \quad \mathrm{cm}^{-3}. \tag{4.3}$$

where A_{ul} is the Einstein coefficient (s^{-1}) for the spontaneous emission associated with the transition from an upper level u to lower level l, and $\sum_i K_{ui}$ depicts the sum of all collisional rate coefficients from a level u to all other possible levels i (van

Zadelhoff 2002). Secondly, the population densities n_u and n_l are determined from the Boltzmann distribution, i.e.

$$\frac{n_u}{n_l} = \frac{g_u}{g_l} \exp\left(-\frac{h\nu_{ul}}{kT_{\rm ex}}\right), \tag{4.4}$$

where k is the Boltzmann constant, $T_{\rm ex}$ is the excitation (rotational) temperature, $h\nu_{ul}$ the energy difference between u and l, and g_u and g_l are the statistical weights, or degeneracies of the u and l states, equal to $2J + 1$, the total number of sub-states for a given value of J. In LTE, populations are dominated by collisions, depending only on the local temperature. Hence $T_{\rm ex} = T_{\rm gas}$, i.e.:

$$T_{\rm gas} = -\frac{h\nu_{ul}}{k}\left[\log \frac{g_l n_u}{g_u n_l}\right]^{-1}. \tag{4.5}$$

Thus, in LTE, the relative level populations at each grid point in the disk can be determined from the gas temperature and transition energy alone. Not only does the $\frac{n_{\rm u}}{n_{\rm l}}$ ratio increase with gas temperature and decreasing radius, but the populations of higher level J states also increases. The most populous J state, $J_{\rm max}$ for a given molecule in LTE can be estimated from the expression:

$$J_{\rm max} = \left(\frac{kT_{\rm gas}}{2Bhc}\right)^{1/2} - \frac{1}{2}, \tag{4.6}$$

which is established by differentiating the Boltzmann distribution expression in Equation (4.4) w.r.t. J, and setting $\frac{dN}{dJ} = 0$, where $N = ng$.

4.4.3 Solving molecular line radiative transfer

Once the relative level populations are known, the molecular line intensities can be evaluated by solving the basic radiative transfer equation. In this investigation, the vertical ray-tracing method in van Zadelhoff (2002, Sect. 4.4.4) and Nomura & Millar (2005, Sect. 4, Eqns. 10-15) is adopted and radiative transfer is solved in the vertical z-direction of the disk, assuming the disk to be face-on:

$$\frac{dI_{ul}}{dz} = -\alpha_{ul}(I_{ul} - S_{ul}). \tag{4.7}$$

Here, the source function S_{ul} is defined by:

$$S_{ul} = \frac{j_{ul}}{\alpha_{ul}} = \frac{1}{\alpha_{ul}} n_u A_{ul} \Phi_{ul} \frac{h\nu_{ul}}{4\pi}, \tag{4.8}$$

where j_{ul} is the emission coefficient, and the extinction coefficient, α_{ul}, assigned to a molecule which absorbs and consequently excites from a lower$l$ to upper u level, is defined by:

$$\alpha_{ul} = \rho\kappa_\nu + (n_l B_{lu} - n_u B_{ul})\Phi_{ul} \frac{h\nu_{ul}}{4\pi}. \tag{4.9}$$

The symbols A_{ul} and B_{ul} are the Einstein coefficients for spontaneous and stimulated emission for the transition u to l, and B_{lu} is the Einstein coefficient for absorption. The symbol κ_ν represents the dust opacity at a frequency ν_{ul}, which in this model consists of a dusty medium with graphite and olivine silicate components coated in water-ice (Eqs. 15a-19 Adams & Shu 1985). The function $\Phi_{ij}(\nu)$ depicts a Voigt profile, which is the line profile of a given transition as a result of convoluted Gaussian and Lorentzian broadened lines (van Zadelhoff et al. 2002). The molecular gas density, or abundance relative to the total gas density, ρ, is defined by:

$$\rho = \frac{n(\mathrm{X})}{n(\mathrm{H_2}) + n(\mathrm{H}) + n(\mathrm{H^+}) + n(\mathrm{He}) + n(\mathrm{He^+})}, \tag{4.10}$$

where X depicts the absolute abundance of a species. The α and j values are calculated at each grid point as a function of radius r and height z in the disk. At each radius r, α_{ul} is integrated in the vertical direction to determine the optical depth, τ_ν at each point:

$$\tau_\nu = \int_{z_{\min}}^{z_{\max}} \alpha_\nu dz. \tag{4.11}$$

The optical depth τ_ν is assumed to equal zero facing the observer and increases in the z-direction through the disk away from the observer. Then, starting from the surface furthest away from the observer where τ_{nu} is a maximum, the emergent integrated intensity, I_{ul} is calculated by integrating the emissivity j_{ul} through z towards the surface where $\tau_\nu = 0$, weighted by the optical depth and Φ_{ij}:

$$I_{ul} = \int_{z_{\max}}^{z_{\min}} j_{ul} \exp(-\tau_{ul}) dz. \tag{4.12}$$

I_{ul} is usually presented in units of erg s^{-1} cm^{-2} sr^{-1}km s^{-1}. The final step is repeated for each radius r, and for each rotational transition and corresponding energy.

4.4.3.1 Summary

A 1-D CASA ALMA algorithm is used to simulate the molecular line intensities of a species from the modelled disk described in Chapter 2, using the molecular abundances from Section 4.3. LTE is assumed since the region considered is the high temperature, high density region of the inner disk, and molecules are thermalized since collisional processes are efficient. Using a vertical-ray tracing method, the analytical process can be described in five-steps:

- Evaluate the level populations in LTE by inputting the gas temperature from the model into the Boltzmann distribution at each point in the disk
- Calculate the extinction and emission coefficients at each point in the disk using the fractional abundance of the species, and the physical parameters associated with the model used
- Integrate the extinction coefficient at each radius in the vertical direction to calculate the optical depth
- Integrate the emission coefficient, weighted by the optical depth to calculate the integrated intensity at each radius.

4.4.4 HCN and H_2CO integrated line intensities

In Section 4.3 it was shown that HCN and H_2CO were sensitive to a change in initial abundance and resulted in a marked difference in the column density profiles. Figures 4.36 to 4.42 compare the 1-D and 1+1D Model A and Model B integrated intensity (unconvolved emission) profiles for HCN and H_2CO, for a number of transitions. Since simulated molecular transitions of disks to date are restricted to those

which are feasible for ALMA Early Science, i.e. ALMA bands 3, 6, 7 and 9, the bands shown for HCN are: J=1-0 (Figure 4.36), J=3-2 (Figure 4.37), J=4-3 (Figure 4.38), J=7-6 (Figure 4.39) and J=8-7 (Figure 4.40). For H_2CO these are: $J_K=3_{03}$-2_{02} (Figure 4.41), $J_K=4_{04}$-3_{03} (Figure 4.42), $J_K=5_{05}$-4_{04} (Figure 4.43), $J_K=9_{09}$-8_{08} (Figure 4.44) and $J_K=10_{010}$-9_{09} (Figure 4.45).

Each of the figures are constrained to a radius inside 10 AU, and the 1+1D colour contour distribution plots span over exactly an order of magnitude which, in most cases corresponds to the maximum difference in integrated intensity. Intensity values inside 1 AU indicate extrapolation to the nearest order of magnitude by the graphical software used to plot these distributions. These are characterized by circular spots coloured red in the centre of the Model A and Model B plots, purple in the J=1-0 sensitivity plots and green in the others.

Unlike the molecular distributions shown in the previous sections, intensity is weighted by the density, temperature and emissivity which all increase with decreasing radius, and so intensity peaks at the smallest considered radius, 1 AU. Regions at larger radii which may have appeared to show the greatest sensitivity in the molecular distributions are compromised by this weighting and therefore display smaller differences in intensity profiles to those at smaller radii. This is because sensitivities are augmented with decreasing radius.

The sensitivity plots for HCN are set to range from 1.0 (red) to 0.7 (purple). Sensitivity does not exceed 1.0 since the Model B abundance and column density profile is always greater than Model A inside a radius of 10 AU. Sensitivities in all five transitions begin to decrease from 1.0 at a radius of 6 AU, and reach their lowest value at 1 AU. This corresponds to a deviation in the line intensity profiles. The sensitivity range for H_2CO is from 1.4 to 0.7 for the $J_K=3_{03}$-2_{02} transition, and 1.5 to 0.7 for the four higher transitions, since Model A intensities are higher than Model B for $r > 3$ AU.

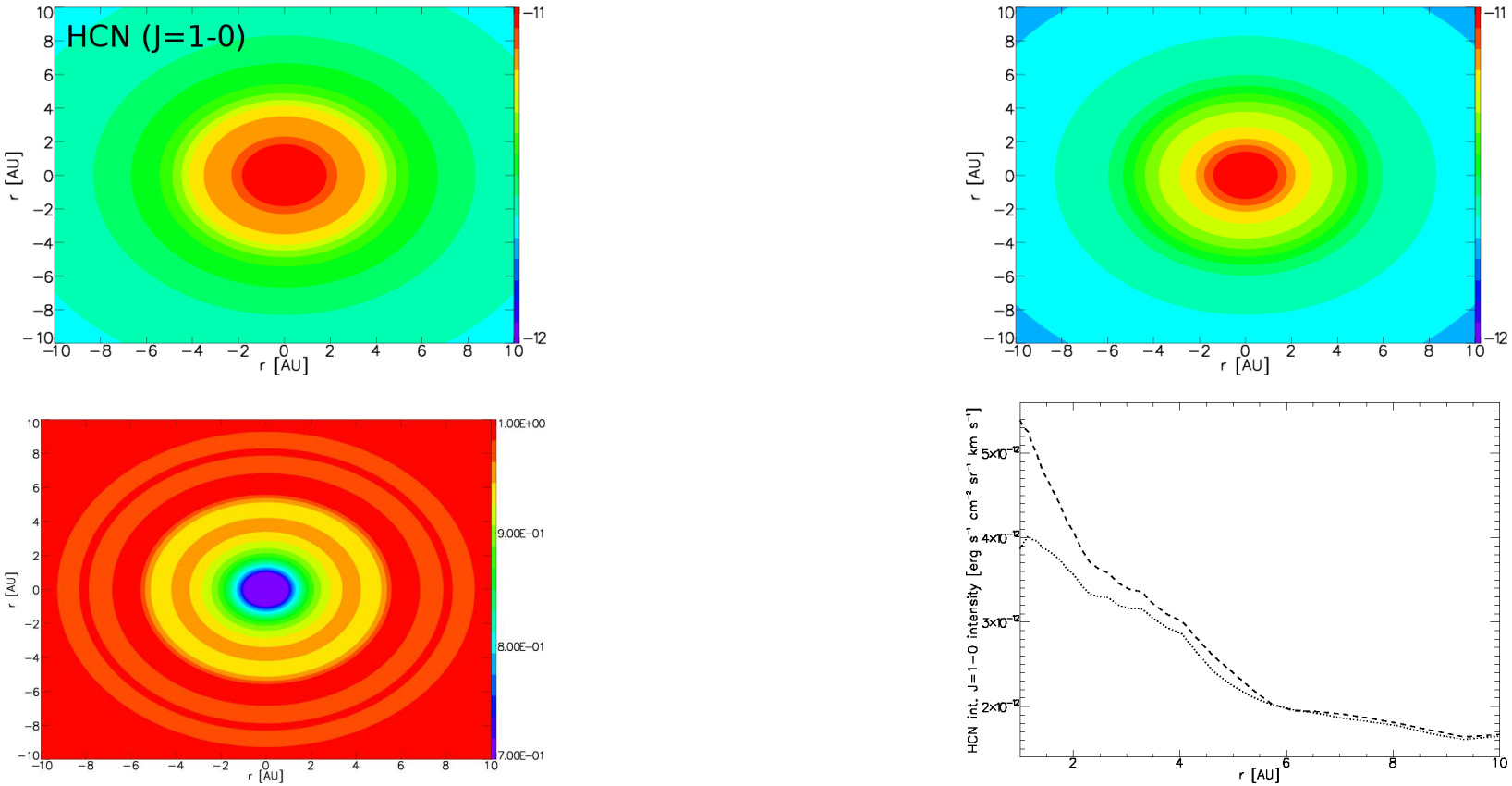

Figure 4.36: Top left: 1+1D Model A integrated J=1-0 intensity of HCN. Top right: 1+1D Model B integrated J=1-0 intensity of HCN. Bottom left: 1+1D integrated J intensity sensitivity between Models A and B. Bottom right: J=1-0 line profiles from Model A (dotted line) and Model B (dashed line).

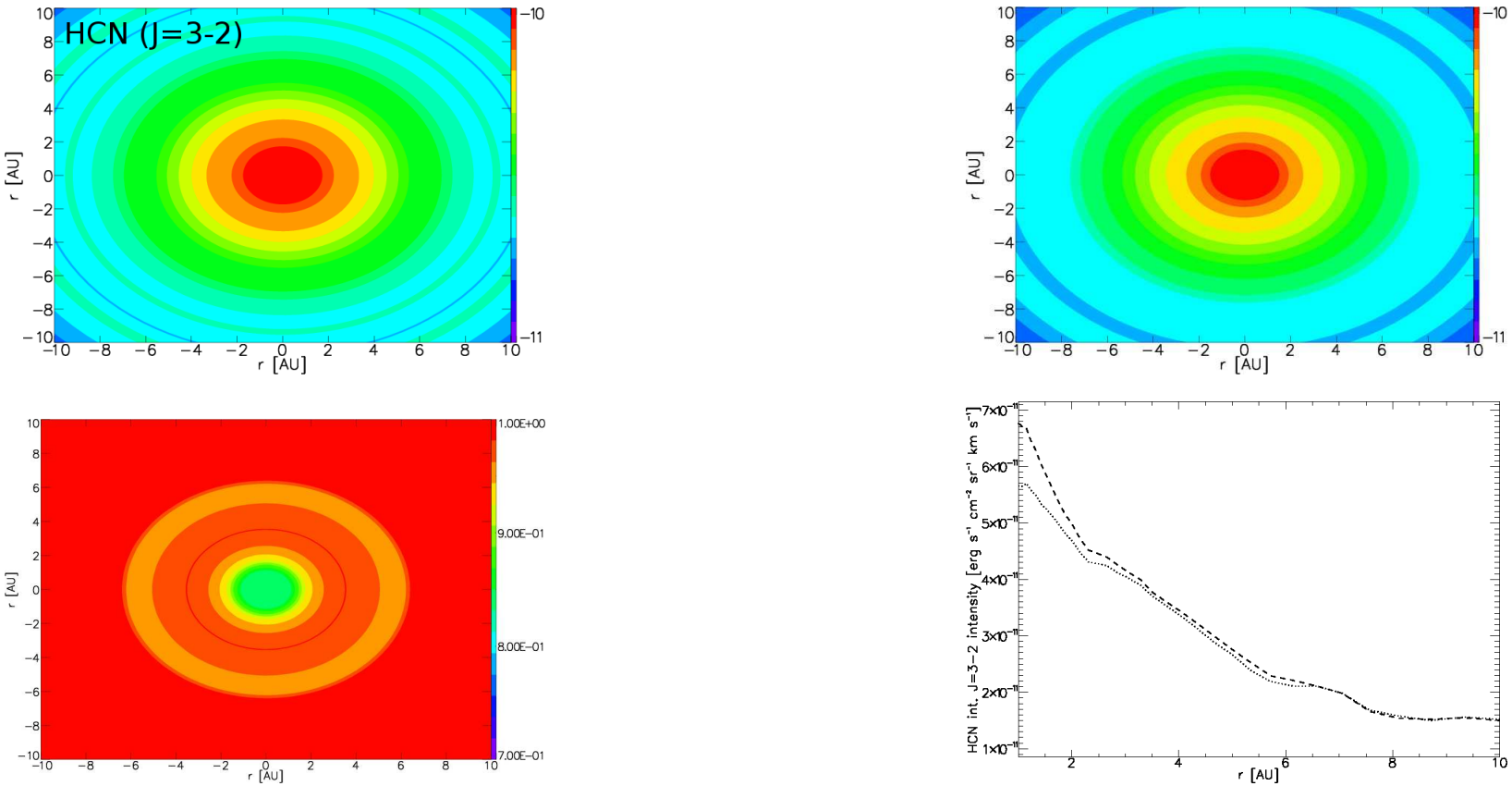

Figure 4.37: Top left: 1+1D Model A integrated J=3-2 intensity of HCN. Top right: 1+1D Model B integrated J=3-2 intensity of HCN. Bottom left: 1+1D integrated J intensity sensitivity between Models A and B. Bottom right: J=1-0 line profiles from Model A (dotted line) and Model B (dashed line).

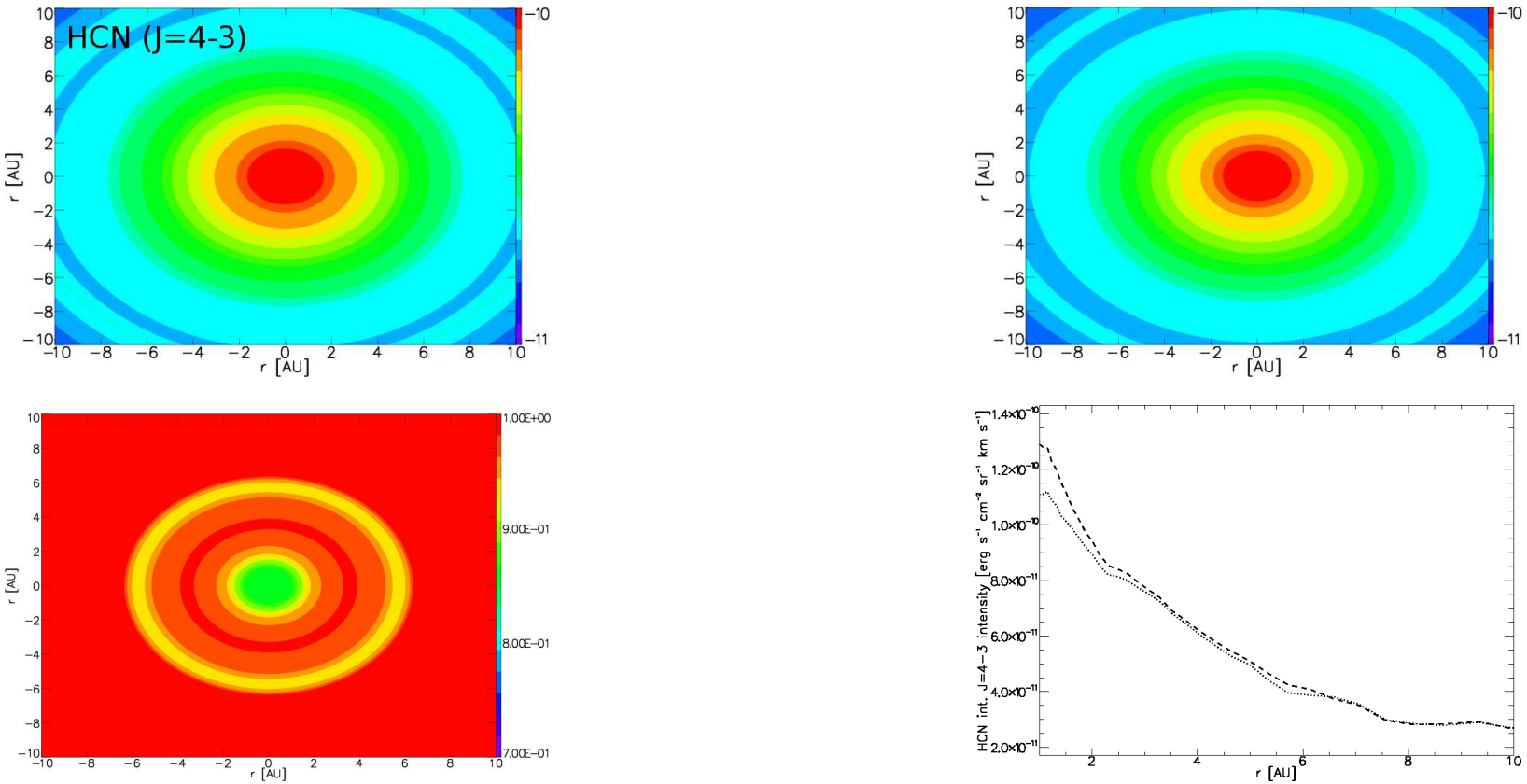

Figure 4.38: Top left: 1+1D Model A integrated J=4-3 intensity of HCN. Top right: 1+1D Model B integrated J=4-3 intensity of HCN. Bottom left: 1+1D integrated J intensity sensitivity between Models A and B. Bottom right: J=4-3 line profiles from Model A (dotted line) and Model B (dashed line).

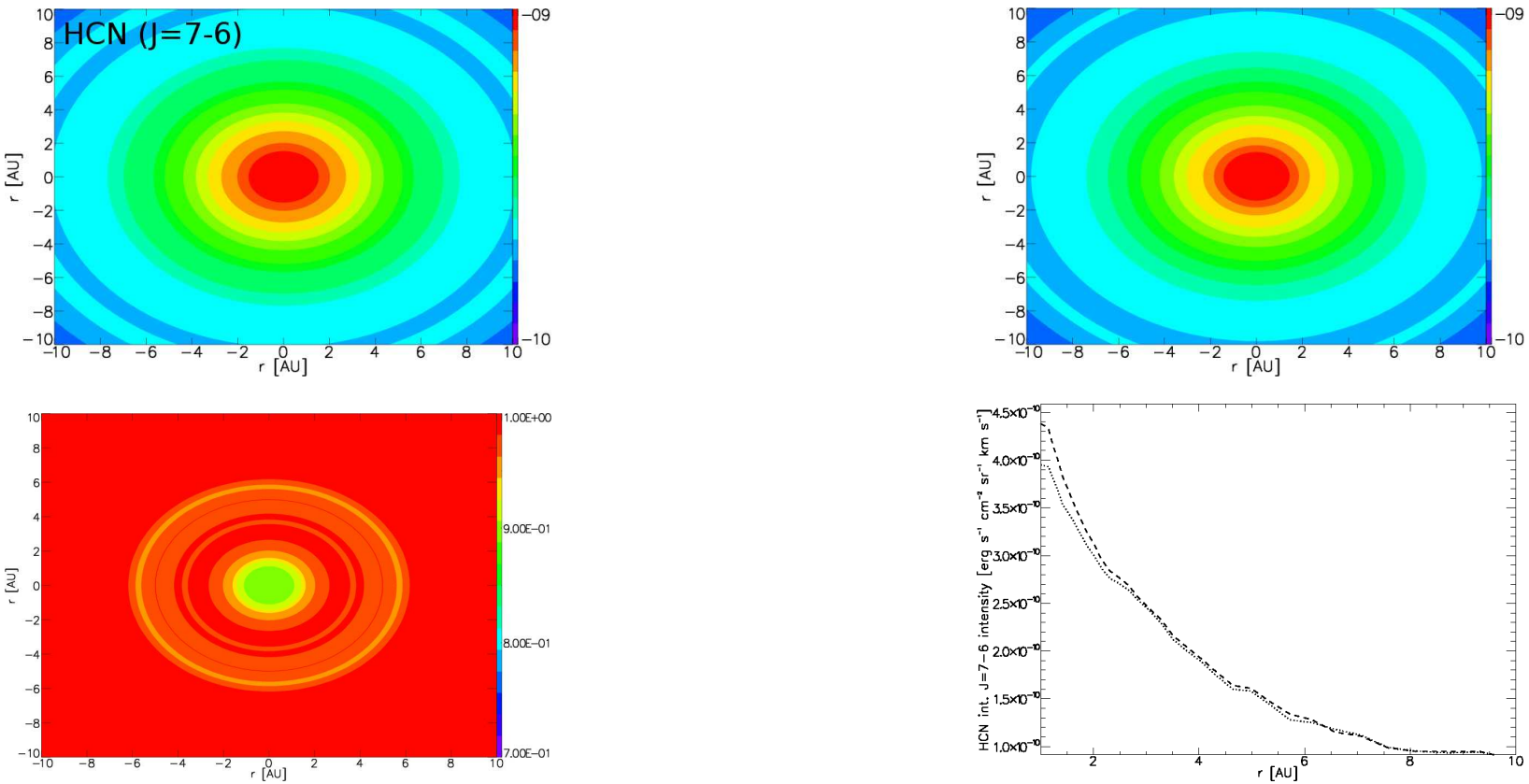

Figure 4.39: Top left: 1+1D Model A integrated J=7-6 intensity of HCN. Top right: 1+1D Model B integrated J=7-6 intensity of HCN. Bottom left: 1+1D integrated J intensity sensitivity between Models A and B. Bottom right: J=7-6 line profiles from Model A (dotted line) and Model B (dashed line).

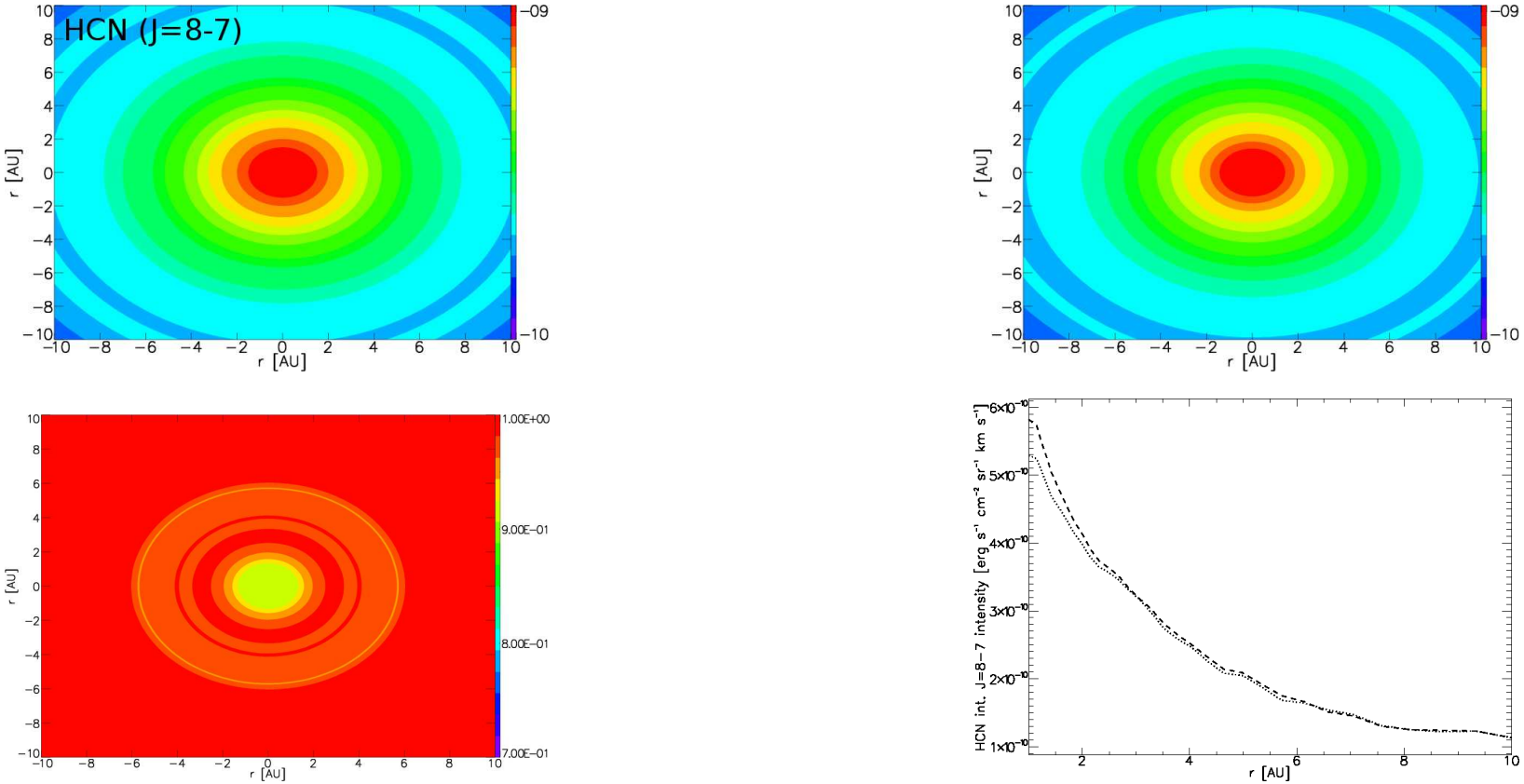

Figure 4.40: Top left: 1+1D Model A integrated J=8-7 intensity of HCN. Top right: 1+1D Model B integrated J=8-7 intensity of HCN. Bottom left: 1+1D integrated J intensity sensitivity between Models A and B. Bottom right: J=8-7 line profiles from Model A (dotted line) and Model B (dashed line).

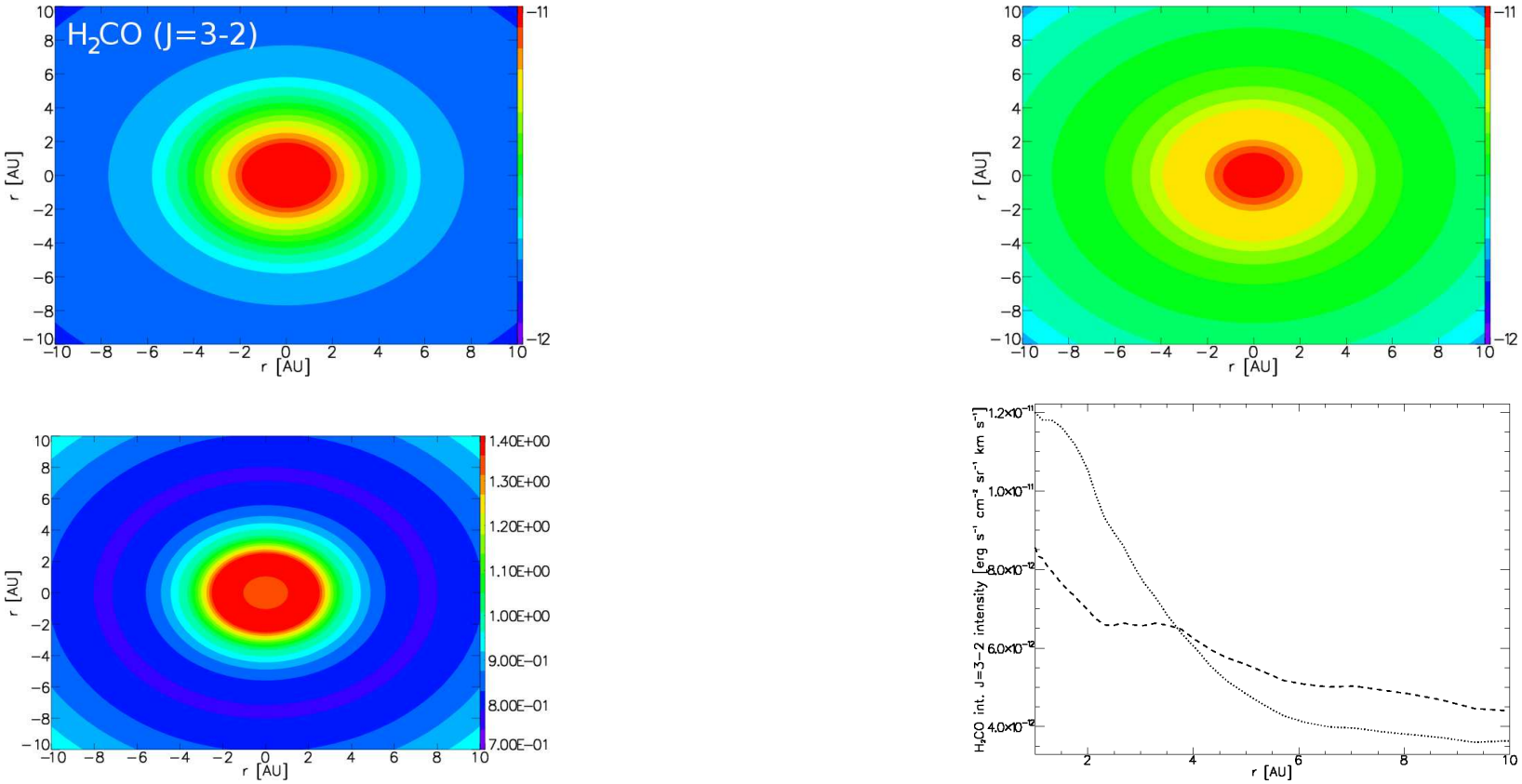

Figure 4.41: Top left: 1+1D Model A integrated $J_K=3_{03}$-2_{02} intensity of H_2CO. Top right: 1+1D Model B integrated $J_K=3_{03}$-2_{02} intensity of H_2CO. Bottom left: 1+1D integrated $J_K=3_{03}$-2_{02} intensity sensitivity between Models A and B. Bottom right: $J_K=3_{03}$-2_{02} line profiles from Model A (dotted line) and Model B (dashed line).

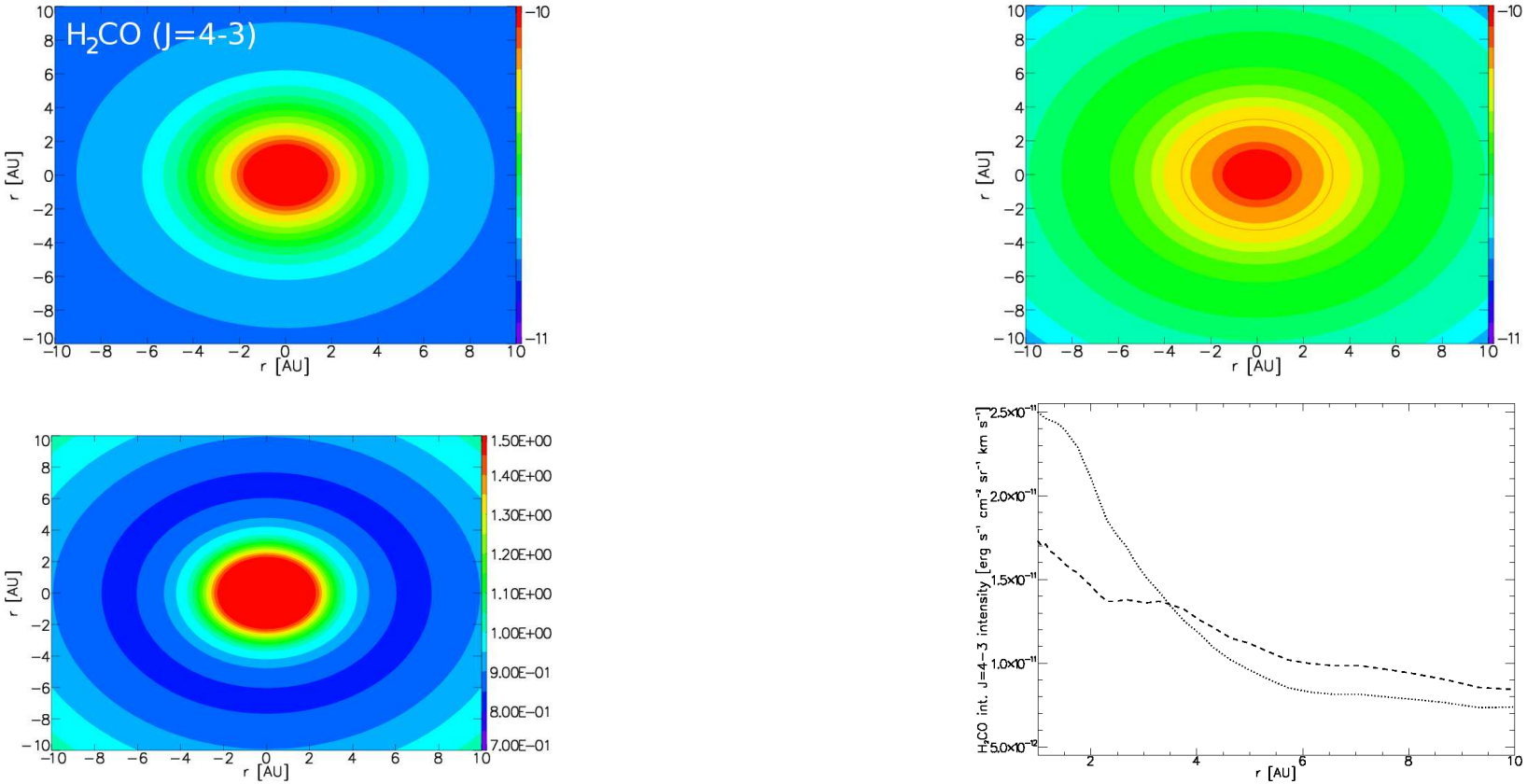

Figure 4.42: Top left: 1+1D Model A integrated J_K=4_{04}-3_{03} intensity of H_2CO. Top right: 1+1D Model B integrated J_K=4_{04}-3_{03} intensity of H_2CO. Bottom left: 1+1D integrated J_K=4_{04}-3_{03} intensity sensitivity between Models A and B. Bottom right: J_K=4_{04}-3_{03} line profiles from Model A (dotted line) and Model B (dashed line).

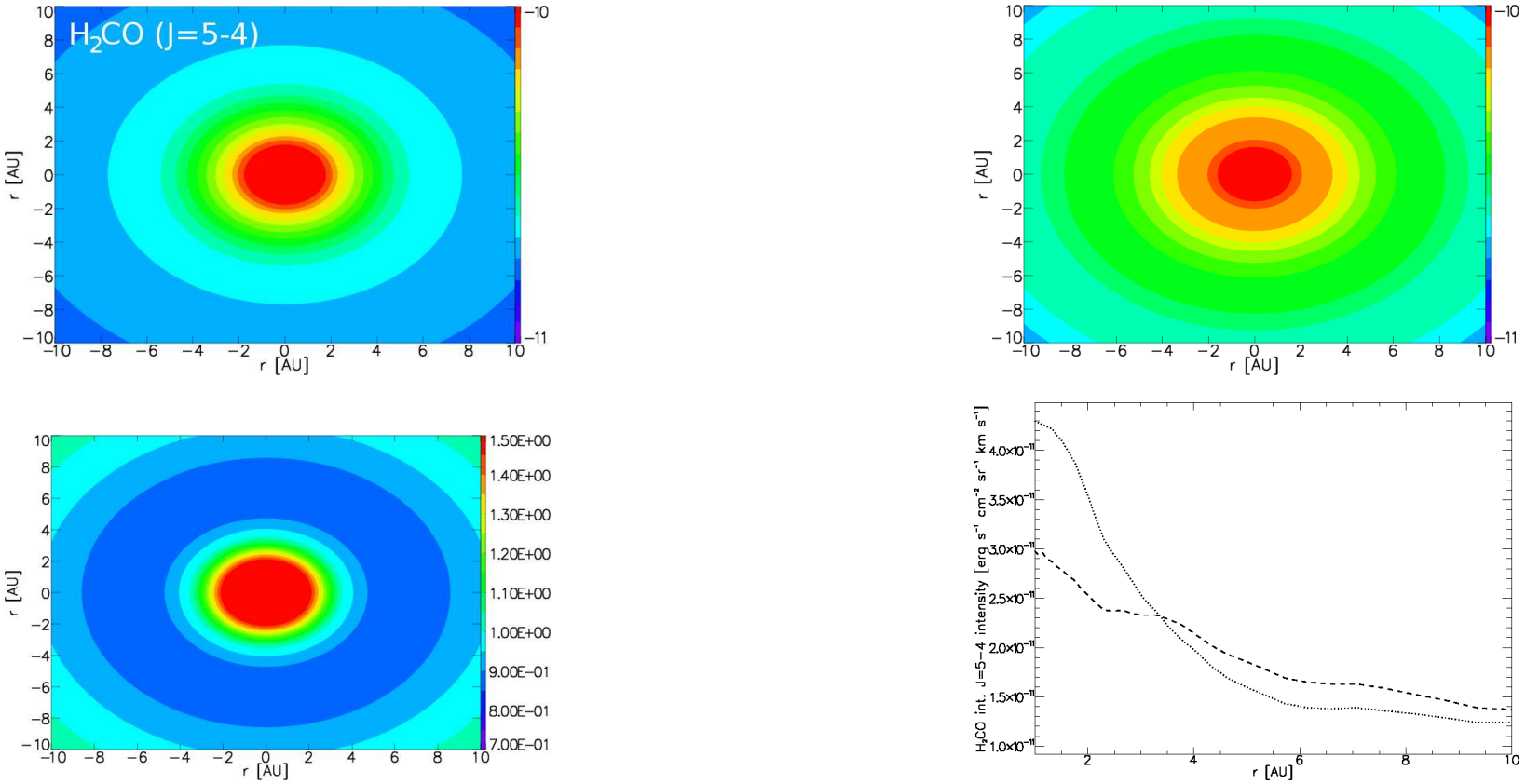

Figure 4.43: Top left: 1+1D Model A integrated J_K=5_{05}-4_{04} intensity of H_2CO. Top right: 1+1D Model B integrated J_K=5_{05}-4_{04} intensity of H_2CO. Bottom left: 1+1D integrated J_K=5_{05}-4_{04} intensity sensitivity between Models A and B. Bottom right: J_K=5_{05}-4_{04} line profiles from Model A (dotted line) and Model B (dashed line).

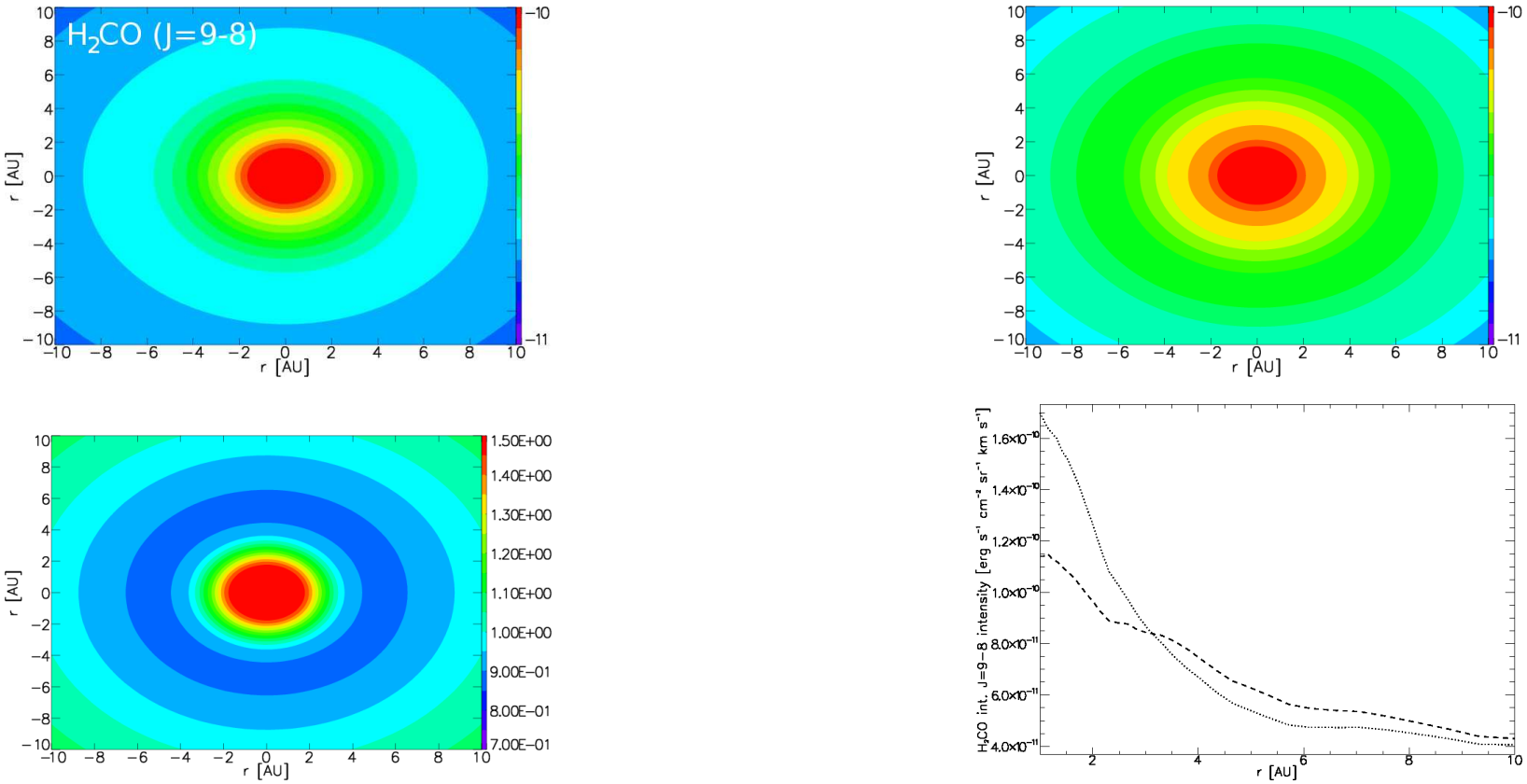

Figure 4.44: Top left: 1+1D Model A integrated J_K=9_{09}-8_{08} intensity of H_2CO. Top right: 1+1D Model B integrated intensity of H_2CO. Bottom left: 1+1D integrated J_K=9_{09}-8_{08} intensity sensitivity between Models A and B. Bottom right: J_K=9_{09}-8_{08} line profiles from Model A (dotted line) and Model B (dashed line).

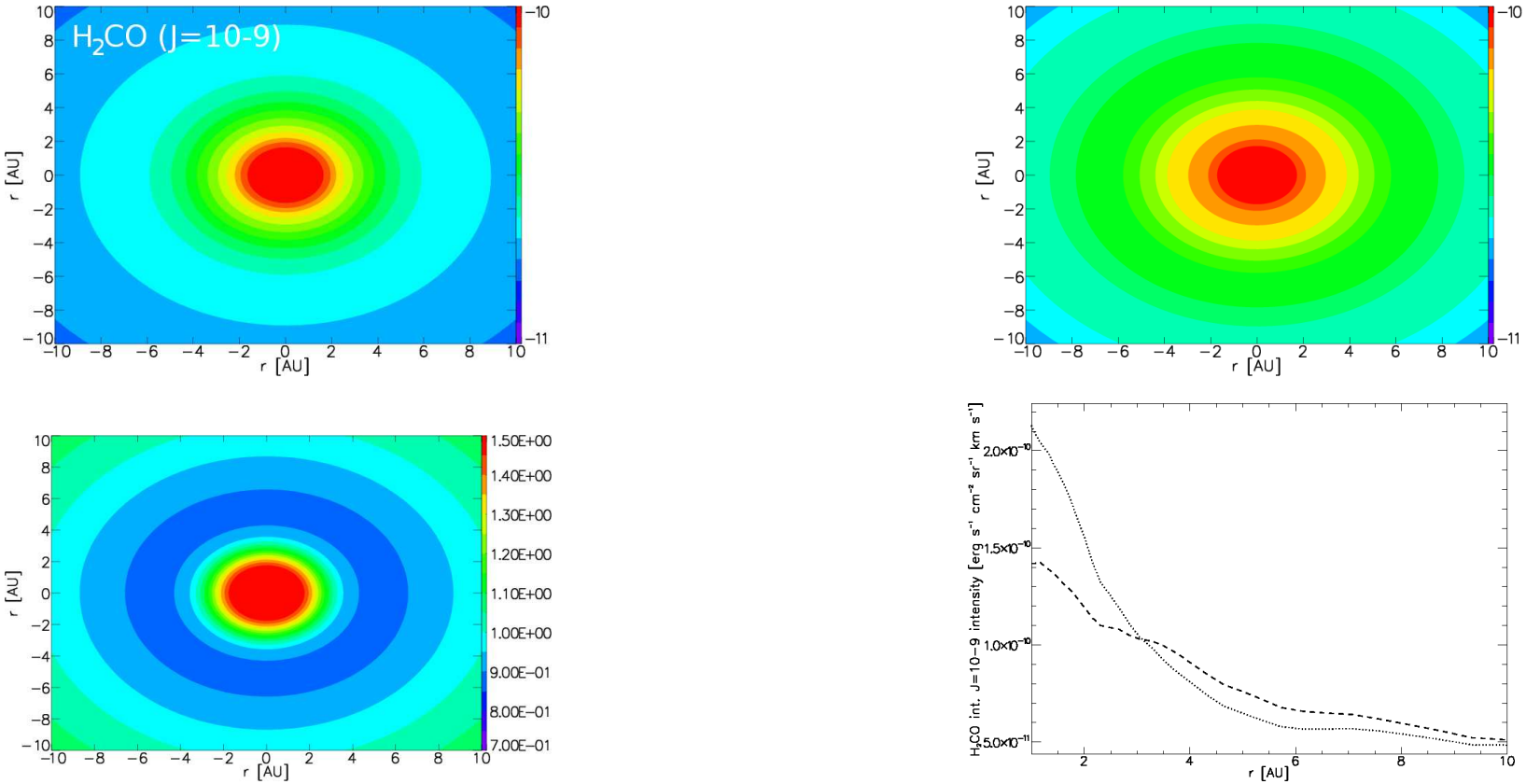

Figure 4.45: Top left: 1+1D Model A integrated J_K=10_{010}-9_{09} intensity of H_2CO. Top right: 1+1D Model B integrated J_K=10_{010}-9_{09} intensity of H_2CO. Bottom left: 1+1D integrated J_K=10_{010}-9_{09} intensity sensitivity between Models A and B. Bottom right: J_K=10_{010}-9_{09} line profiles from Model A (dotted line) and Model B (dashed line).

4.4.5 Optical depth and emissivity: origin of emission

The optical depth τ and emissivity α are functions of the molecular abundance with respect to the total gas density. The optical depth of the disk is zero at the surface facing the observer and increases with depth, reaching a maximum value at the disk surface facing away from the observer. The $\tau = 1$ level is chosen arbitrarily as a boundary between optically thin ($\tau < 1$) and optically thick ($\tau > 1$) zones of the disk.

The optical depth decreases slightly with decreasing radius since the $\exp(-1/T_{\rm ex})$ term from the Boltzmann expression dominates the density term in the extinction coefficient expression. In the vertical z direction from the surface, optical depth increases and emissivity decreases through the disk. The most optically thick and least emitting zones reside in the surface regions facing away from the observer. There is no emission from the disk underside apart from the Model A J=1-0 HCN transition.

The regions where the HCN abundance difference between Model B and Model A is greatest is located in the optically thick midplane. This translates to Model B optical depths which are around ten times larger than those of Model A in the optically thick zone. The difference in Model A and Model B abundances decrease with height, and the optical depths are considerably closer in the optically thin region. The result is a more extreme and steeper Model B optical depth profile from the optically thick to optically thin regime. The optical depth difference is not as profound for H_2CO, with Model A optical depths around a factor of 2 larger inside a radius of 3 AU, and inverting to a lesser extent beyond this radius due to the density weighting. This inversion at $\sim$ 3 AU for H_2CO closely maps the Model A and Model B column density profiles in Figure 4.34.

Regardless of this fact, the molecular emission from the optically thick regions of Models A and B are too low to contribute to the intensity. Figures 4.43 and 4.44 compare the Model B emissivity as a function of radius and height for each of the five transitions of HCN and H_2CO. It is seen that most of the peak emission origi-

nates from a confined region just above the midplane and borders on the optically thick/optically thin $\tau = 1$ surface boundary where there is a sudden sharp increase in emissivity. These lines are optically thin since there is minimal extinction from layers above. HCN peak emission is located notably further from the midplane than H_2CO, in both cases tracing the $\tau = 1$ line closely.

For HCN, the τ=1 line and peak emissivity migrates further from the midplane with higher order transitions. At $r = 1$ AU for example, the J=1-0 $\tau = 1$ surface is located ~ 0.1 AU above the midplane, but is found at ~ 0.2 AU for the J=8-7 transition. The H_2CO τ=1 line also migrates upward but from Figure 4.44 is only noticeable at larger radii, i.e. $r > 2$ AU.

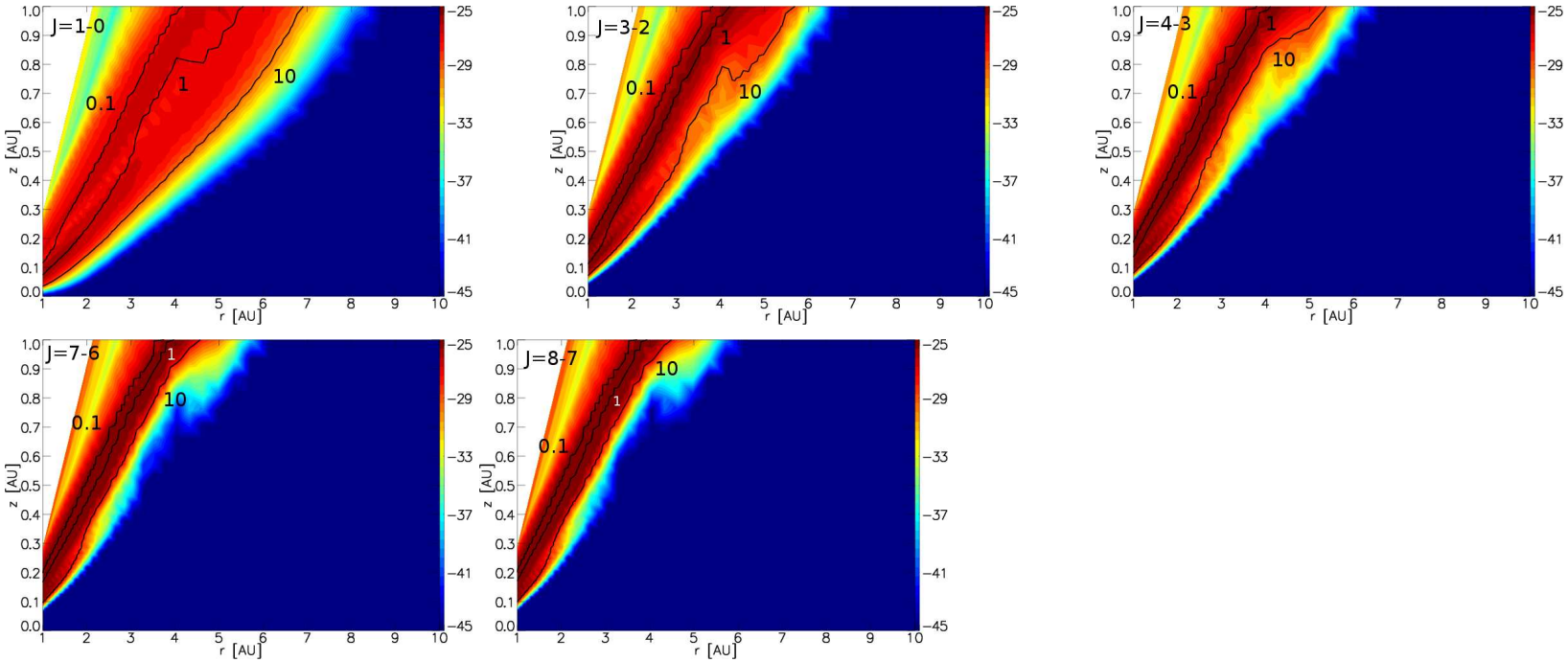

Figure 4.46: Model B emissivity distribution plots as a function of radius (1 to 10 AU) and height (0 to 1 AU) for each of the five transitions of HCN. The τ = 0.1, 1 and 10 contour lines are also plotted.

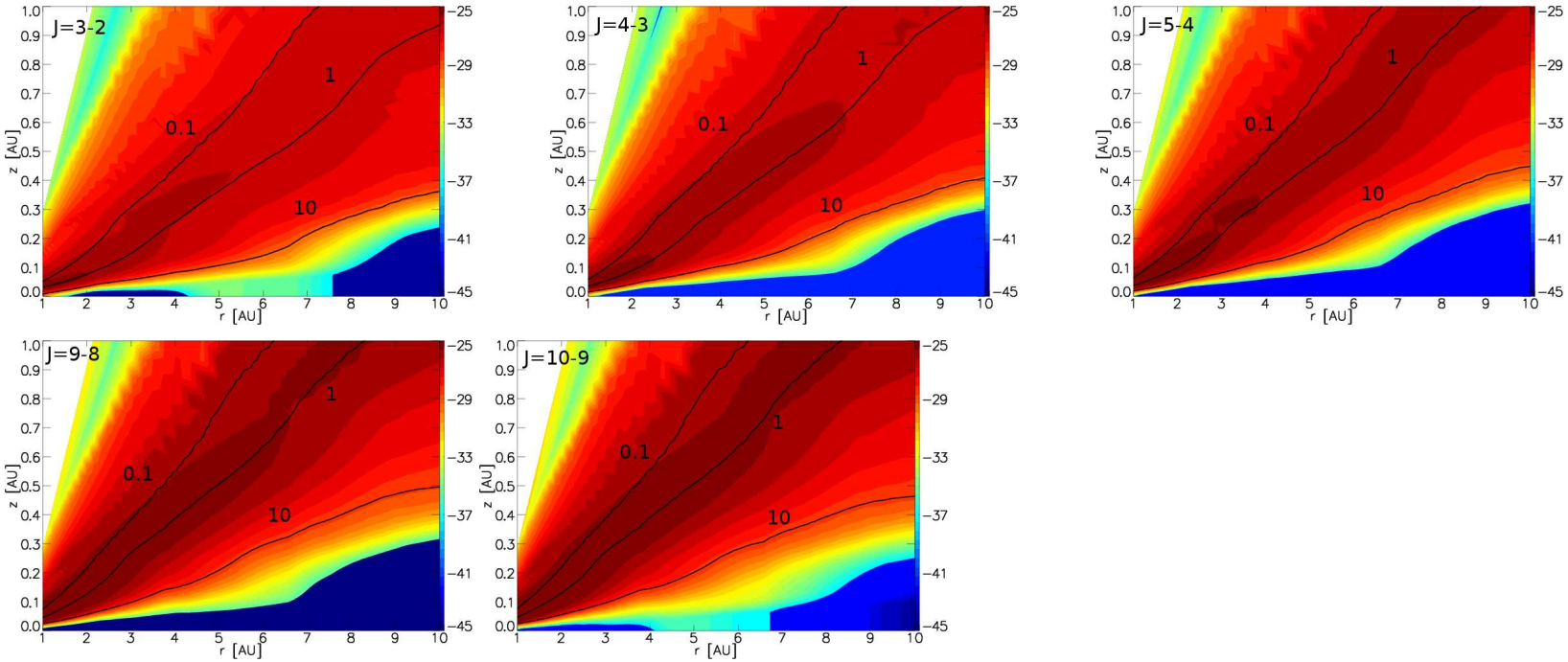

Figure 4.47: Model B emissivity distribution plots as a function of radius (1 to 10 AU) and height (0 to 1 AU) for each of the five transitions of H_2CO. The $\tau = 0.1$, 1 and 10 contour lines are also plotted.

4.4.6 Tracing temperature, density and abundance

Level populations are governed by the abundance in different temperature regions. Higher temperatures for a given abundance produce more populated higher order energy levels (and thus higher level transitions) with respect to lower energy levels. Thus the higher level transitions will become more intense than lower level ones with increasing temperature. The emission of all transitions is greatly reduced where there is a sharp fall in density towards the disk surface, irrespective of temperature increase since the total molecular population decreases. This occurs where $\tau < 0.1$.

Since emission of HCN and H_2CO peak in different regions of the disk along with each transition peaking at a different height depending on radius, each transition represents a unique temperature, density and abundance in the disk. Figures 4.48 and 4.49 display the magnitude of the relationship between the peak Model B emissivity values ($\tau \sim 1$) and temperature, total gas density and abundance at a radius of 1 AU and 5 AU. Axes have been scaled to magnify the temperature, density and fractional abundance range. Sections where the plot is vertical represent adjacent transitions which probe the same region, e.g. the J=8-7 and J=7-6 HCN transition lines at r = 5 AU.

The most notable correlations are with temperature, where the temperature gradient is more significant than that of density or fractional abundance, and the peak emissivity between transition lines is greatest. The adjacent transitions with the greatest difference in temperature, density and fractional abundance are the J=3-2 and J=4-3 HCN transition lines at r = 1 AU which probes a disk region with a temperature difference of 60 K, a density difference of 6.15×10^{10} g cm^{-3} and fractional abundance difference of 4.22×10^{-6}. Adjacent lines of H_2CO do not probe differences of this magnitude at either radius since the temperature, density and fractional abundance gradients are smaller nearer the midplane. Although the adjacent lines of HCN at r = 5 AU depict larger differences than H_2CO, they are not as great as

those at 1 AU.

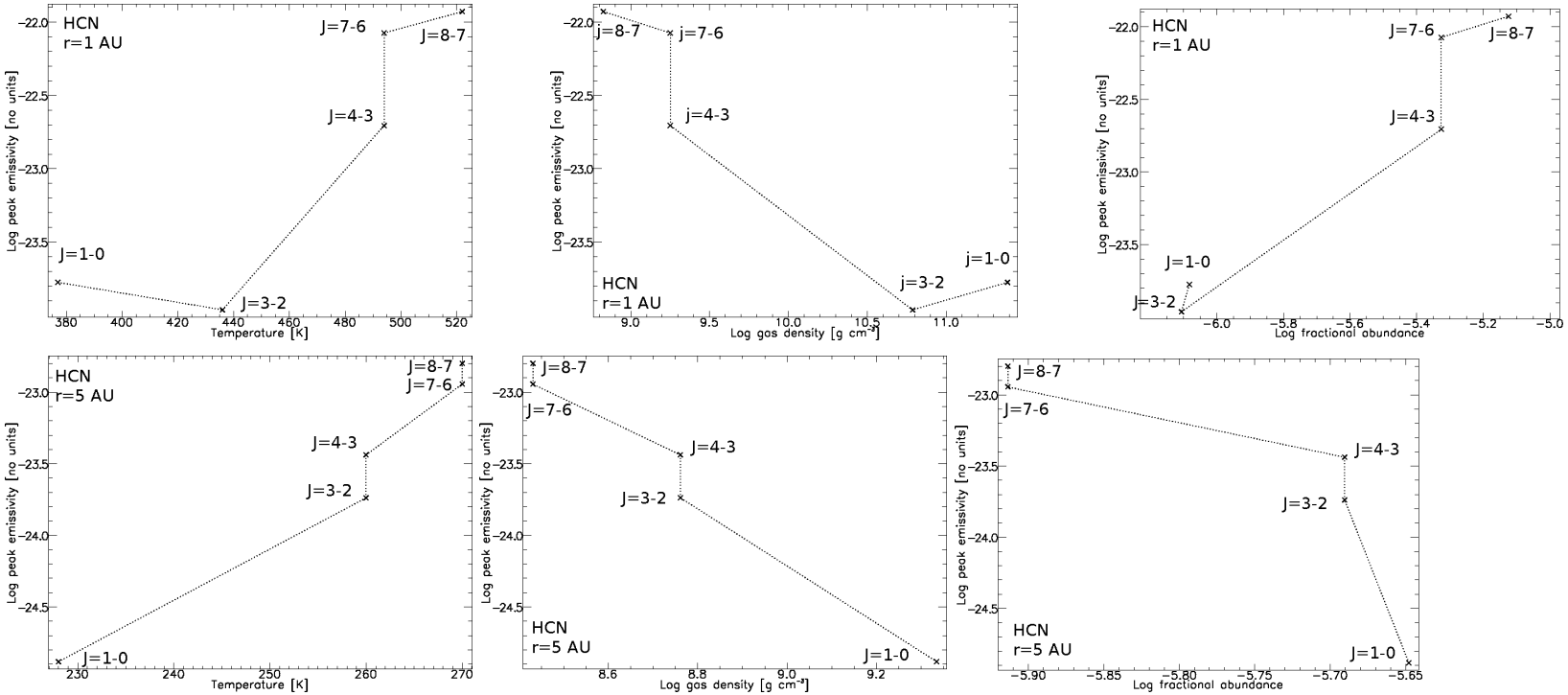

Figure 4.48: Peak transition emissivity against temperature (left column), gas density (middle column) and fractional abundance (right column) plots for HCN at r = 1 AU (top row) and 5 AU (bottom row).

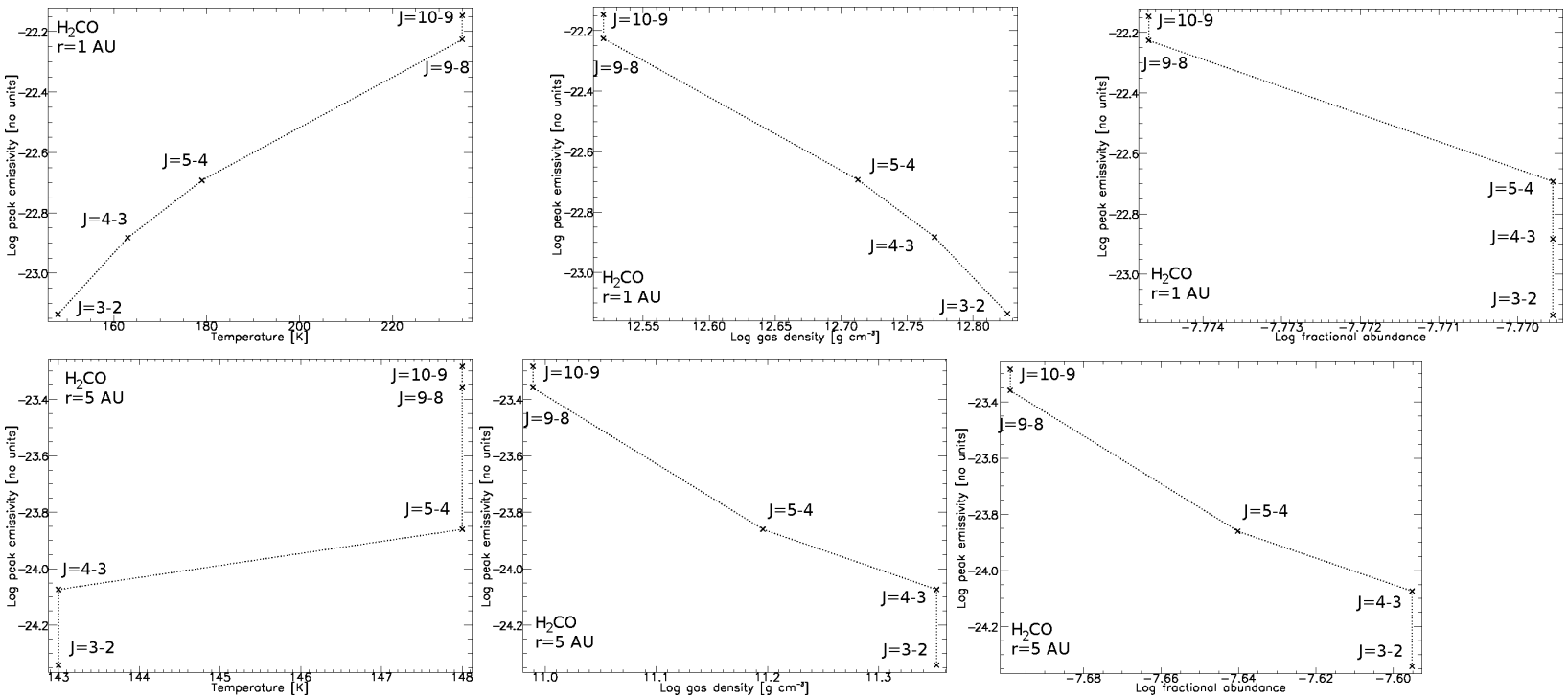

Figure 4.49: Peak transition emissivity against temperature (left column), gas density (middle column) and fractional abundance (right column) plots for H_2CO at $r = 1$ AU (top row) and 5 AU (bottom row).

4.4.7 Model A and Model B intensity sensitivity

Figures 4.50 and 4.51 compare the Model A and Model B emissivity, optical depth and intensity profiles for the lowest J=1-0 and highest J=8-9 HCN transitions and $J_K=3_{03}$-2_{02} and $J_K=10_{010}$-9_{09} H_2CO transitions as a function of disk depth at 1 AU. Slight variations in the Model A and Model B emissivity and intensity profiles for both molecules are visible.

Model A and Model B intensity differences are shown to correlate strongly with emissivity, and sensitivities are different for each transition. As Figure 4.52 shows, the relative HCN sensitivity is largest in the J=1-0 transition and decreases with increasing transition number. Nevertheless, the higher order, more intense transitions weight the actual intensity difference (ΔI) between Model A and Model B above that of the J=1-0 transition. The greatest difference in intensity is associated with the most intense J=8-7 HCN transition, with the intensity of Model B higher than that of Model A. Since the Model B abundance of H_2CO is lower than Model A at 1 AU, the resulting intensities follow suit; instead the H_2CO intensity of Model A is larger than Model B. For H_2CO, the greatest intensity difference is associated with the most intense $J_K=10_{010}$-9_{09} transition.

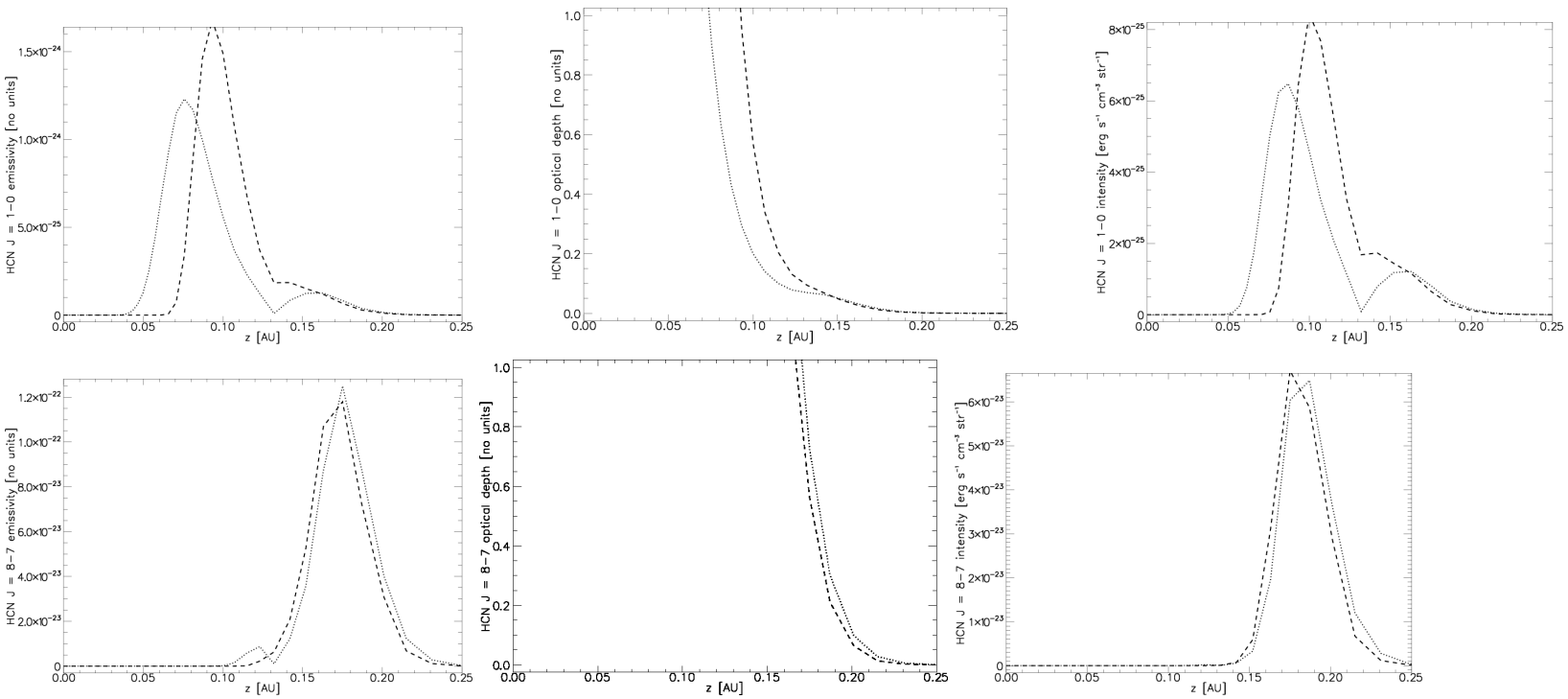

Figure 4.50: Emissivity (left column), optical depth (middle column) and integrated intensity (right column) plots as a function of disk depth for J=1-0 (top row) and J=8-7 (bottom row) HCN transitions at r = 1 AU. At this radius, the emissivity, τ = 1 layer and integrated intensity peaks migrate further from the midplane with higher order transitions.

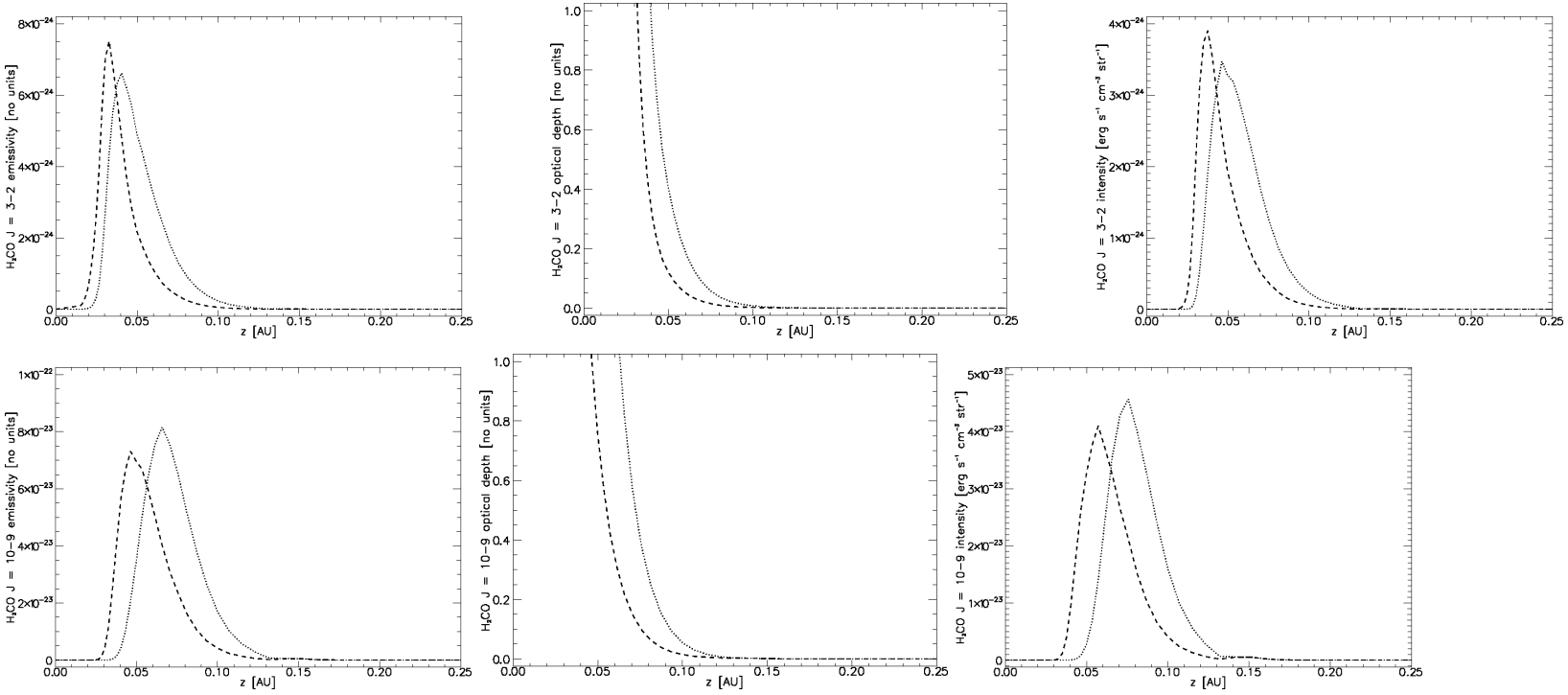

Figure 4.51: Emissivity (left column), optical depth (middle column) and integrated intensity (right column) plots as a function of disk depth for J_K=3_{03}-2_{02} (top row) and J_K=10_{010}-9_{09} (bottom row) H_2CO transitions at r = 1 AU. At this radius, the emissivity, τ = 1 layer and integrated intensity peaks remain around the same height above the midplane for both transitions.

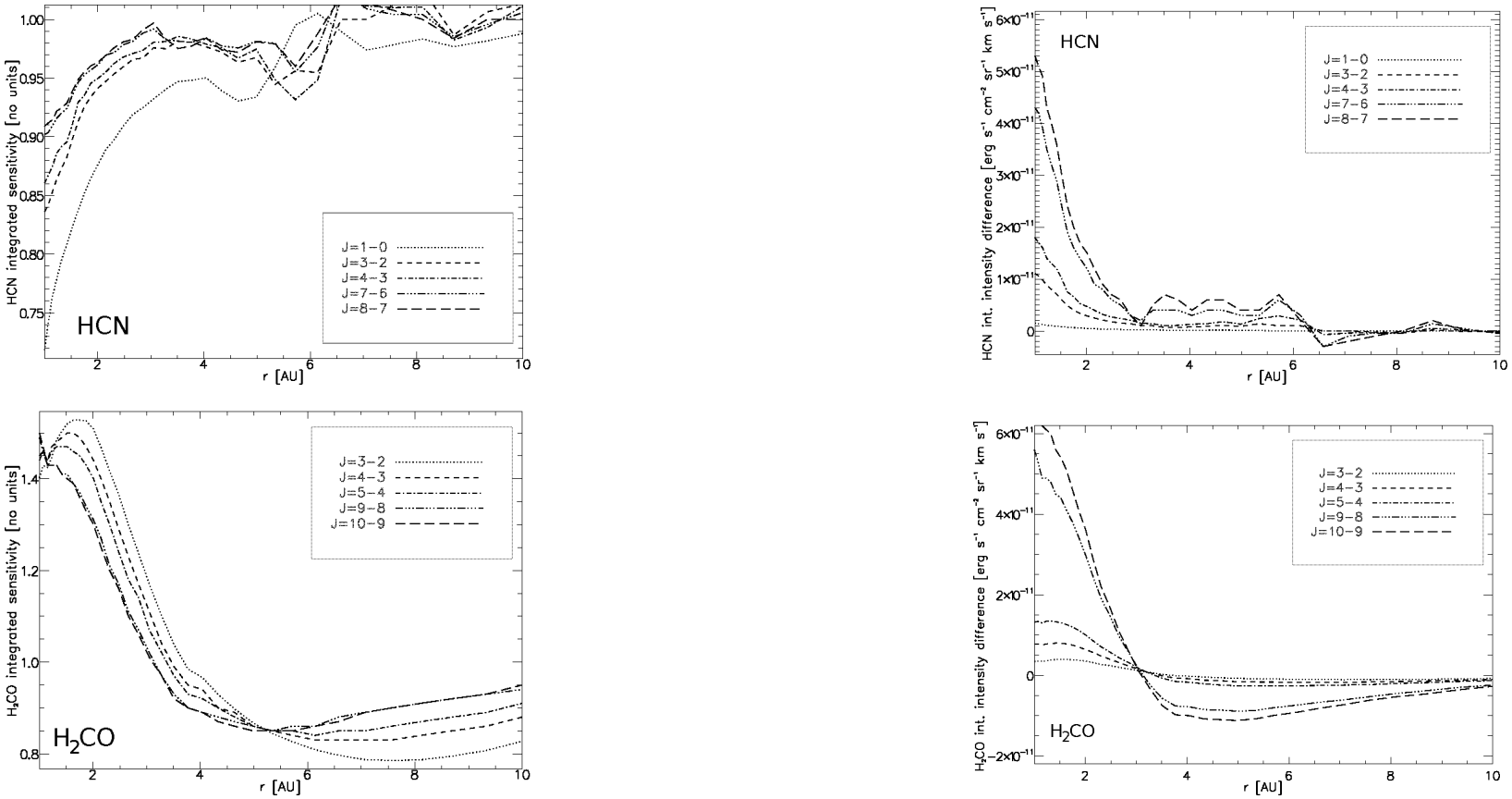

Figure 4.52: Sensitivity profiles (left) and integrated intensity differences (right) between Models A and B for each of the five feasible HCN (top) and H_2CO (bottom) transitions. Although the J=1-0 HCN transition shows the largest degree of sensitivity, the J=9-8 HCN transition displays the greatest intensity difference which is amplified with decreasing radius. For H_2CO this is more complex.

4.4.8 Brightness temperature

Table 4.7 lists frequency values alongside each rotational transition of HCN and H_2CO taken from the Splatalogue database for astronomical spectroscopy[1], and the particular ALMA band the frequency values can be detected in.

Table 4.7: Frequency values for each of the five HCN and H_2CO transitions. The ALMA band that these frequencies correspond to are also listed.

Molecule	J/J_K	ν (GHz)	ALMA band
HCN	8-7	708.877	9
	7-6	620.304	9
	4-3	354.505	7
	3-2	265.886	6
	1-0	88.632	3
H_2CO	10_{010}-9_{09}	716.938	9
	9_{09}-8_{08}	647.082	9
	5_{05}-4_{04}	362.736	7
	4_{04}-3_{03}	290.623	7
	3_{03}-2_{02}	218.222	6

With these frequency values in mind, it is possible to convert the integrated intensity value for each transition outlined in Section 4.4.7 to a brightness temperature, T_B, by using the Rayleigh-Jeans approximation:

$$T_{\rm B} = \frac{c^2 I_\nu}{2k_{\rm B}\nu^2\Delta v} \quad {\rm K}, \tag{4.13}$$

where $k_{\rm B}$ is the Boltzmann constant, c is the speed of light and Δv is the velocity linewidth. Figure 4.53 presents the logarithmic brightness temperature distributions of each of the five Model A and Model B transitions of HCN and H_2CO assuming a velocity linewidth Δv of 1 km s^{-1} as in Nomura et al. (2009). Figure 4.54 presents the temperature factor differences between the brightness and surface temperature

[1] www.splatalogue.net

of the 10^{-8} $M_\odot$ yr^{-1} disk which is the hottest region of the disk, and where most of the radiation eminates.

The plots show that the brightness temperatures of HCN are larger than H_2CO, which is expected since the peak emission of HCN resides closer to the hotter disk surface than H_2CO. The brightness temperatures of both molecules at the modelled source are significantly lower than the disk surface temperature since T_B is a measure of the molecular line strength, and not the continiuum emission which is related to the disk gas temperature. The factor difference between T_B and the surface temperature is generally smaller with increasing transition for HCN (apart from J=1-0), but larger with increasing transition for H_2CO. For example at 1 AU, the most intense Model A J=8-7 HCN line has T_B = 1.6 K, whilst for the most intense Model A J=10-9 H_2CO line, T_B = 0.82 K. The surface temperature at this radius is 559 K, so this particular HCN and H_2CO transition contributes 0.28% and 0.15% of the total emission from the surface respectively.

T_B differences between Models A and B trace both the column density and integrated intensity difference since T_B is directly proportional to the integrated intensity (Equation 4.14). Indeed, T_B therefore also increases with higher-order transition, and in most cases the differences between Models A and B are magnified (Figure 4.55).

In summary, both HCN and H_2CO brightness temperatures for each transition are a factor $\sim 10^{-3}$ smaller than the hottest surface region of the 10^{-8} $M_\odot$ yr^{-1} disk, which correlates to $\sim 10^{-3}$ of the total emission at each radius. Since in reality the temperature of the $\tau = 1$ and peak emission region is lower than the disk surface, the factor differences for each transition shown in Figure 4.54 are likely to be even larger, more so for H_2CO since the $\tau = 1$ line is located deeper down in the inner disk (Figure 4.47) than HCN (Figure 4.46).

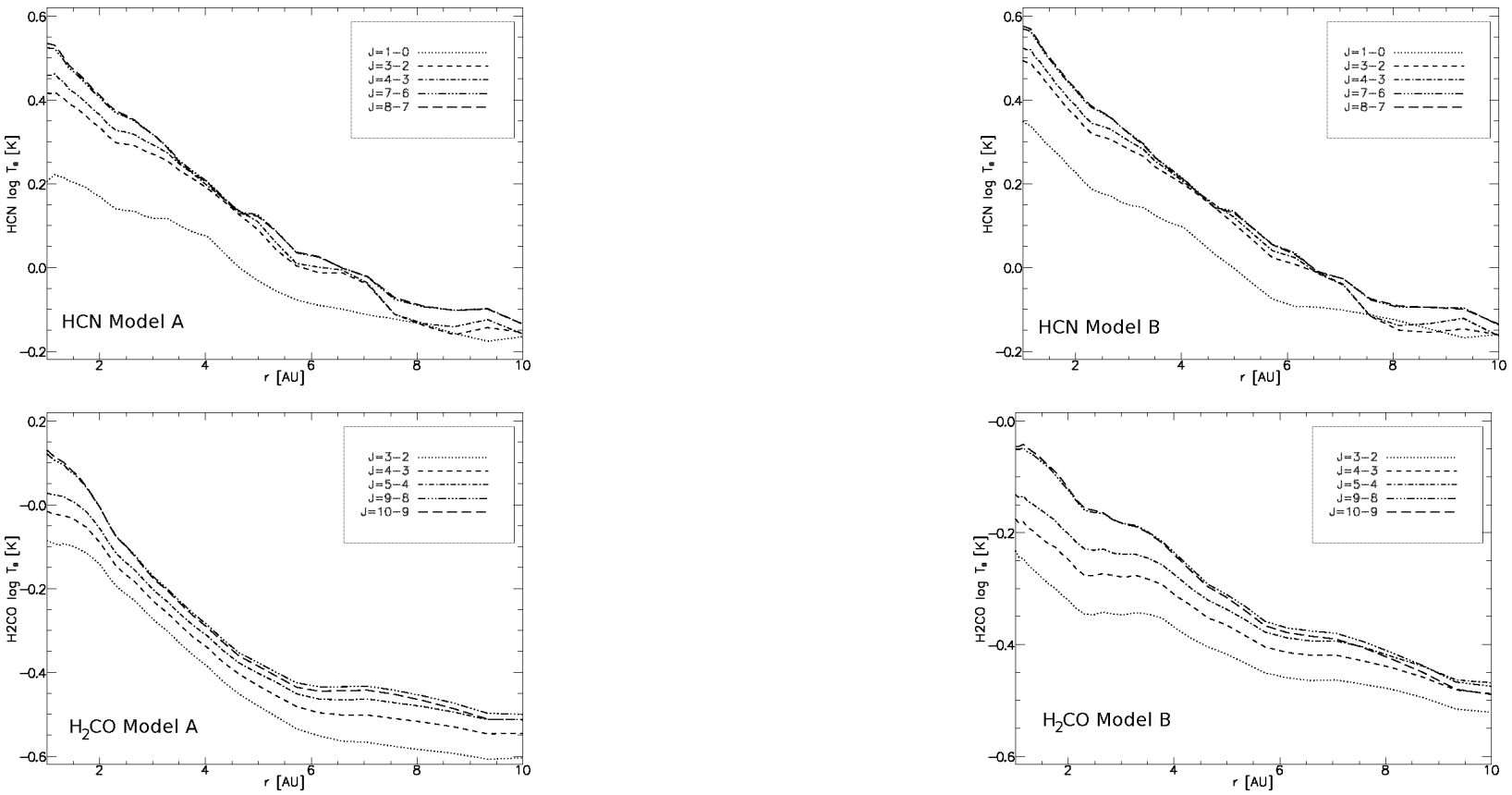

Figure 4.53: Logarithmic brightness temperature distributions of each of the five Model A (left) and Model B (right) transitions of HCN (top) and H_2CO (bottom).

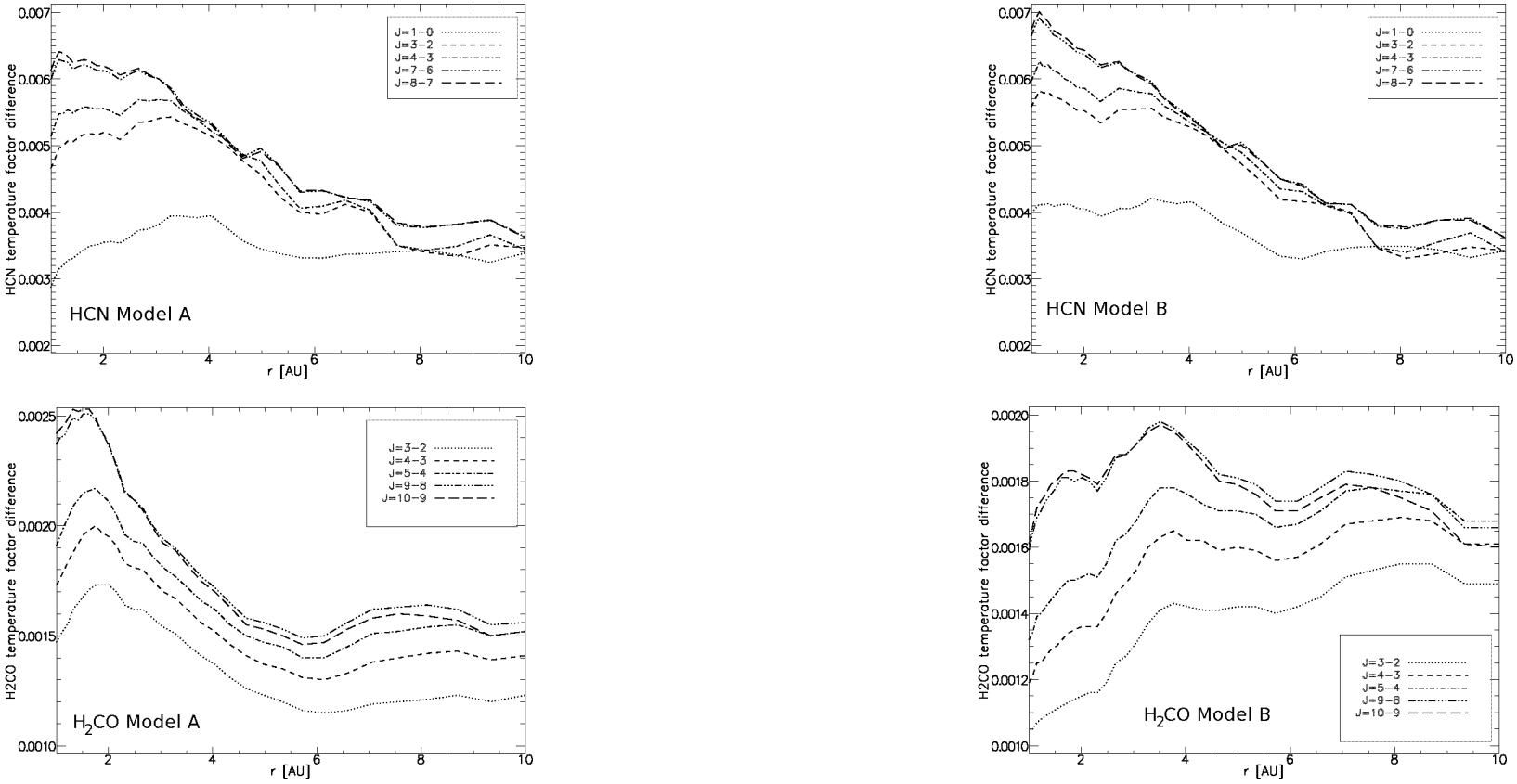

Figure 4.54: HCN (top) and H_2CO (bottom) factor differences between brightness temperature and disk surface temperature in K for Models A (left) and B (right) as a function of radius.

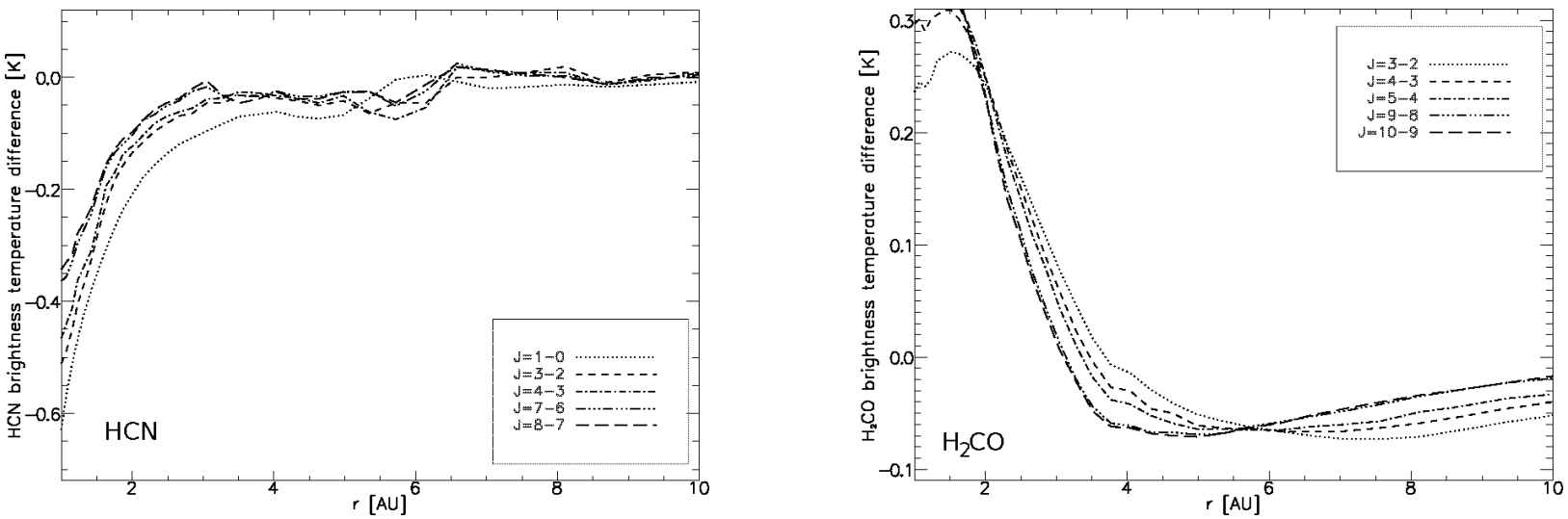

Figure 4.55: HCN (left) and H_2CO (right) brightness temperature differences between Models A and B (Model A – Model B). Negative values indicate higher values in Model B.

4.4.9 Current and future ALMA detection

It is possible to "convolve" the integrated intensity maps to a typical beam size of ALMA, by using the CASA Convolve 2D Simulator[2]. This will produce a set of integrated intensity maps linked to ALMA's beam size in units of mJy/beam or mJy km s^{-1} for a given velocity linewidth. Spectral emission line studies of molecular transition lines in other disk models or from ALMA observations are usually presented as plots of the brightness temperature against velocity linewidth (e.g. Fig. 9 of van Zadelhoff et al. 2003), mJy/beam against frequency (e.g. Pineda et al. 2012), or presented as tables of integrated intensities in units of K km s^{-1} (e.g. van Zadelhoff et al. 2003). Brightness tempertures of a few Kelvin, down to milliKelvin are typical of molecular line strengths as measured at the receiver for single-dish telescopes (e.g. Thi et al. 2004).

Detecting and resolving lines on the scales discussed in this chapter requires the smallest possible angular and spatial resolution. Under ALMA's current array configuration[3] of 32 x 12 m antennas, the maximum baseline achievable is 1.091 km. By using the relationship between the angular resolution α, frequency ν, the speed of light c and baseline B:

$$\alpha = 1.22 \times 206265 \times \frac{c}{\nu B} \quad \text{arcsec}, \tag{4.14}$$

and using the parallax equation to determine the spatial resolution or beam size L,

$$L = \alpha D \quad \text{AU}, \tag{4.15}$$

where D is the distance to the disk from the observer, it is possible to approximate the integrated intensity over a single beam size L (= $r_{\rm max}$ - $r_{\rm min}$) to estimate a surface flux $F_{\rm ul}$ as in Nomura & Millar (2005, Eq. 13):

$$F_{ul} = \frac{1}{4\pi D^2} \int_{r_{\rm min}}^{r_{\rm max}} 2\pi r dr I_{ul} \quad \text{ergs}^{-1}\text{cm}^{-2}\text{kms}^{-1}. \tag{4.16}$$

[2]http://casa.nrao.edu/docs/casaref/image.convolve2d.html

[3]www.almascience.eso.org

This can be converted to a brightness temperature T_B or to mJy/beam as measured at the receiver's end via the CASA Convolve 2D Simulator. One can then gauge the integration or observing time required to detect the transition emission as a detection limit under the current ALMA configuration by using the ALMA Sensitivity Calculator[4] (ASC), which will determine whether the observation is feasible or not. Here, one can set the velocity resolution (e.g. 1 km s^{-1}) and the number of antennas to use. Nomura et al. (2009) performed such a calculation with the 145 GHz J_K=3_0-2_0 CH_3OH line assuming a distance D of 140 pc.

ALMA's eventual full use of 50 antennas of the 12 m array, and a maximum baseline of ~ 16 km will enable a maximum angular resolution of ~ 5 milliarcseconds for 950 GHz (the highest detectable frequency in Band 10). This is equivalent to a spatial resolution of just 0.7 AU if a typical distance to the disk of 140 pc is considered. In the case of the highest HCN transition (J=8-7), this is an angular resolution of 6.6 milliarcseconds and a spatial resolution of 0.93 AU.

Convolving the integrated intensity maps presented in this chapter, estimating the observing times for each transition under the current and future maximum ALMA baseline, and in particular correlating the brightness temperature difference between Models A and B with different observing times, are all cases for future work.

4.4.10 Comparisons with J_{max}

Equation (4.6) enables one to compare the values of the most populous J-states, at a given point and temperature, to the most intense transitions considered here for HCN (J=8-7) and H_2CO (J_K=10_{010}-9_{09}). With this knowledge, it is possible not only to determine how far the transitions differ from J_{max}, but also get an idea of whether it is possible for ALMA to detect these transition lines in the future, based on the LTE assumptions considered.

[4] www.almascience.eso.org/proposing/sensitivity-calculator

The Boltzmann distribution suggests that transitions from J_{max} are likely to be the most intense lines which can be observed. Table 4.10 lists some Model B J_{max} values calculated with Equation (4.6) at points in the disk for HCN and H_2CO, where the emissivity is at its highest value for one of the two molecules (denoted by the J_{max} value in bold). The peak emissivity of the HCN J=8-7 transition line at

Table 4.8: J_{max} values for HCN and H_2CO, for various heights at r = 1 AU and 5 AU where emissivity peaks for one of the two molecules (denoted by the J_{max} value in bold). Gas temperatures (in K) are also shown.

r	z	T_{gas}	J_{max}(HCN)	J_{max}(H_2CO)
1	1.75×10^{-1}	522	**11**	22
1	4.64×10^{-2}	235	7	**14**
5	1.23	270	**8**	16
5	5.34×10^{-1}	148	6	**11**

r = 5 AU equals J_{max} at this point in the disk, meaning that one is likely seeing the most populous and intense transition. Each of the H_2CO transition lines are under the estimated J_{max} values for that point, so one is not likely viewing the most intense H_2CO transition.

To view the most intense HCN emission (T > 500 K) corresponding to a minimum J_{max} value of 11, a receiver would need to detect a 1.064 THz signal. That is, future ALMA Band 11 antennas with a proposed 1.0 – 1.6 THz receiver[5]. This is currently not in the cycle-0 or cycle-1 list of operations and may be planned at a later stage. To date, there have been no observations of a H_2CO J_K=11_{011}-10_{010} transition and its emission frequency, thus a detection prediction cannot be made at this time.

[5]http://www.physics.ox.ac.uk/almaband11/

4.4.11 Discussion: general uncertainties and comparisons with other works

The results provide an initial indication of how the emissivity, integrated intensity and brightness temperature distributions of HCN and H_2CO vary and probe different regions of a modelled protoplanetary disk. The results are in agreement with the idea that higher order transition lines probe increasingly higher warmer molecular layers of the disk (e.g. Aikawa et al. 2002); that is if one assumes LTE which is applicable for the inner regions (e.g. Nomura et al. 2009). Indeed, the peak emissivities are a function of temperature and density and are therefore reliant on the assumptions of the model. Different models will produce different emissivity distributions, integrated intensity and brightness temperature values, dependent on their degree of complexity. For example, the inclusion of X-ray heating may well be significant in increasing the disk temperature deeper down and modifying the peak emissivity of certain transitions, and larger grain-sizes will make the disk more optically-thin.

The HCN emissivity results presented here may be overestimated by many orders of magnitude by neglecting the vastly superior photodissociation and photodesorption rates which the inclusion of stellar UV and X-ray photoprocesses bring, and the excessive freeze-out up to much higher temperatures nearer the surface as a result of fixing the dust temperature to that of the gas, which preserves a higher proportion of HCN than is usual at the expense of CN (e.g. Walsh et al. 2010). The same can be interpreted for H_2CO, with some models (e.g. Willacy & Woods 2009) suggesting a higher degree of processing to simpler molecules in the regions discussed here.

Since the calculation is performed from a radius of 25 AU, the intensity flux contribution from outer regions of the disk is ignored altogether. Although the in-

ner disk emits a higher regional flux, most of the integrated emission originates from the outer disk due to the larger surface area. One of the major calculation steps bypassed here is the flux density (Equation 4.17) integrated over a larger radius beyond 25 AU.

Common interferometric observations of the $C^{12}O$ J=2-1 transition line in T Tauri disks such as TW Hya (D = 56 pc), DM Tau (D = 140 pc) and LkCa15 (D ~ 140 pc) have shown these disks to be ~ 225 AU (Weinberger et al. 2002), 800 AU and 650 AU (Simon et al. 2000) in radius respectively. Hence the flux density $F_{\rm ul}$ simulating the distance to these disks from this model is too low to be useful. Other models which begin calculations from a few hundred AU, determined from the point where their disk densities are close to the ISM critical density value (e.g. r = 373 AU in Aikawa et al. 2002, 305 AU in Walsh et al. 2010, where $n_{\rm crit} \sim 10^{-18}$ g cm^{-3}) suffer less since the integrated flux density is more resolvable and comparable with observations. The extent of detecting the differences between the intensities of Models A and B would be served better by estimating the flux density out to a radius of a few hundred AU. Other models which confirm similar sensitivities due to differences in chemical history may be more suitable to address this question.

There have been many studies of molecular isotopologues in disks, such as ^{13}CO which has been shown to probe lower, colder regions of disks than ^{12}CO (Aikawa et al. 2002). Along with $C^{18}O$ observations, there is general consensus of a common vertical temperature gradient structure in disks (e.g. Piétu et al. 2007). Similar studies of $^{12}HCO^+$ and $^{13}HCO^+$ have also drawn similar conclusions, albeit much closer to the midplane (Aikawa et al. 2002). Deuterated analogues have both been modelled and observed (as discussed previously) with particular emphasis on the molecular D/H ratios which decline with increasing temperature. Most observations have established DCO^+/HCO^+ ratios, with two DCN/HCN observations from TW Hya, but to this date neither HDCO or D_2CO have been observed in disks.

In spite of all of this, sub-mm observations have so far been constrained to the

outer $r > 50$ AU regions of disks, and theoretical algorithms similar to the one presented in this chapter have have only considered non-LTE (e.g. van Zadelhoff et al. 2003) which is not applicable for the inner disk. This makes it particularly difficult to compare the results shown here with observations and other works. Until observations with ALMA are conducted at the higher resolutions required to resolve the innermost disk regions, comparisons to modelled results from the inner disk along with abundances and ratios established from solar system cometary material cannot be determined. Future work should be directed at determining if HCN and H_2CO isotopologue and deuterated ratios alter in any way by changing the chemical inputs as performed in Models A and B; more so for the latter since the chemical model used in this work assumes different pathways for the formation of deuterated molecules, and the overall 10^{-7} $M_\odot$ yr^{-1} disk temperature is higher than 10^{-8} $M_\odot$ yr^{-1} which may further reduce the D/H ratio.

4.5 Observational constraints of stellar accretion rate vs protoplanetary disk age

The previous investigation assumed a total calculation time of 1.78×10^5 and 1.81×10^5 years for the 10^{-7} $M_\odot$ yr^{-1} and 10^{-8} $M_\odot$ yr^{-1} disks respectively over the entire disk between $r = 1$ AU to 25 AU (discussed in Section 2.3.6). One can assume that the calculations in both disks were performed for the same length of time. For Model B, the calculation was performed over a total time of 3.59×10^5 years at each radius; i.e. double the length of time of either separate calculation.

But how do the calculation timescales set by Equation (2.17) compare with constraints set from observations? Understanding the evolution of stellar accretion rate with time is clearly an important aspect of protoplanetary disks since it pieces together another part of the jigsaw which connects the simpler chemistry in disks to the more complex chemistry in planets like our own. This relationship is thought to

be the only indicator of gas mass flow limits in the inner regions of disks (Hartmann 2005). Although the relationship between stellar accretion rate and other parameters such as disk mass (e.g. Hartmann et al. 2006) and viscosity (e.g. Hueso & Guillot 2005) is generally plausible, the exact link with disk age has proved difficult to constrain from observations primarily due to a lack of older star samples (Hartmann 2005). Jones et al. (2012) discussed a method for approximating the disk age, and have shown it to be that of the stellar age within a reasonable fit. The method was based on a collection of observational disk data available from the literature, which notes that the stellar age, disk mass and stellar accretion rate are all measurable. In Hartmann et al. (1998) a relationship, established from UV and optical luminosity measurements in Taurus and Chamaeleon I molecular clouds, was proposed:

$$\log \dot{M} = -8.0 - 1.4 \log t_{\rm age}, \tag{4.17}$$

where $t_{\rm age}$ is in units of years. Neglecting the estimates of errors on $\log \dot{M} = 0.6$ and $\log t = 0.3$ (p4; Hartmann et al. 1998) for simplicity, then the age of a T Tauri protoplanetary disk with a stellar mass accretion rate of 10^{-7} $M_\odot$ yr^{-1} can be estimated to be:

$$\log t = 6 - \frac{1}{1.4} \longrightarrow t \approx 1.93 \times 10^5 \quad \text{yr}. \tag{4.18}$$

Similarly the age of a disk with a stellar mass accretion rate of 10^{-8} $M_\odot$ yr^{-1} is approximately:

$$\log t = 6 \longrightarrow t \approx 10^6 \quad \text{yr}. \tag{4.19}$$

Assuming the stellar accretion rate slows directly from 10^{-7} $M_\odot$ yr^{-1} to 10^{-8} $M_\odot$ yr^{-1}, and that these ages represent the beginning of these epochs, then the duration, τ_1, of evolution spent in 10^{-7} $M_\odot$ yr^{-1} is the difference between the 10^{-7} $M_\odot$ yr^{-1} and 10^{-8} $M_\odot$ yr^{-1} ages, i.e.

$$\tau_1 = 8.07 \times 10^5 \quad \text{yr}. \tag{4.20}$$

Following the same principle, the duration, τ_2, spent under the physical conditions of 10^{-8} $M_\odot$ yr^{-1} is estimated from the age difference between 10^{-8} $M_\odot$ yr^{-1} and 10^{-9}

$M_\odot$ yr^{-1}:

$$\tau_2 = 4.18 \times 10^6 \quad \text{yr.} \tag{4.21}$$

The combined value of 4.99×10^6 yr represents a total hypothetical calculation time from 10^{-7} $M_\odot$ yr^{-1} to 10^{-8} $M_\odot$ yr^{-1} if Equation (4.15) is considered.

In the previous investigation, the influence of the mass accretion rate on the chemistry was studied, by allowing the accretion rate to vary from 10^{-7} $M_\odot$ yr^{-1} to 10^{-8} $M_\odot$ yr^{-1}, using the accretion times directly calculated from Equation (2.20), and extending the calculation until all points in the disk grid were run for the same length of time. In this investigation, the accretion rate is allowed to vary from 10^{-7} $M_\odot$ yr^{-1} to 10^{-8} $M_\odot$ yr^{-1}, incorporating the duration times taken from the accretion rate-to-age relation from Hartmann et al. (1998). Although CN, HCN, H_2CO and NH_3 were found to be particularly sensitive to the alteration of input abundances from those taken from a pre-stellar core model to those from 10^{-7} $M_\odot$ yr^{-1}, the motivation here is to see if these same molecules are still sensitive to the adjustments in the calculation timescale of each epoch which are consistent with observations resulting in Equation (4.18).

4.5.1 Method of re-evaluating the calculation timescale

Figure 4.56 summarizes the process in re-evaluating the calculation timescales in accordance with this investigation. This simulation, referred hereon as Model C, again focuses on a calculation which starts from a radius of 25 AU and finishes at 1 AU. The calculation begins with the 10^{-7} $M_\odot$ yr^{-1} disk grid by following the same modelled process of accretion discussed in Section 2.3.6 and 2.4.4, until a calculation time of 1.78×10^5 years has elapsed i.e. the length of time a gas parcel accretes from a radius of 25 AU to 1 AU (Phase 1). The method for adopting the times in Equations (4.21) and (4.22) involve extending the calculation for each radial grid point after Phase 1 is completed, until the entire 10^{-7} $M_\odot$ yr^{-1} disk grid

has been calculated for 8.07×10^5 years (Phase 2), and then continued under the 10^{-8} $M_\odot$ yr^{-1} disk at each point for 4.18×10^6 yr (Phase 3).

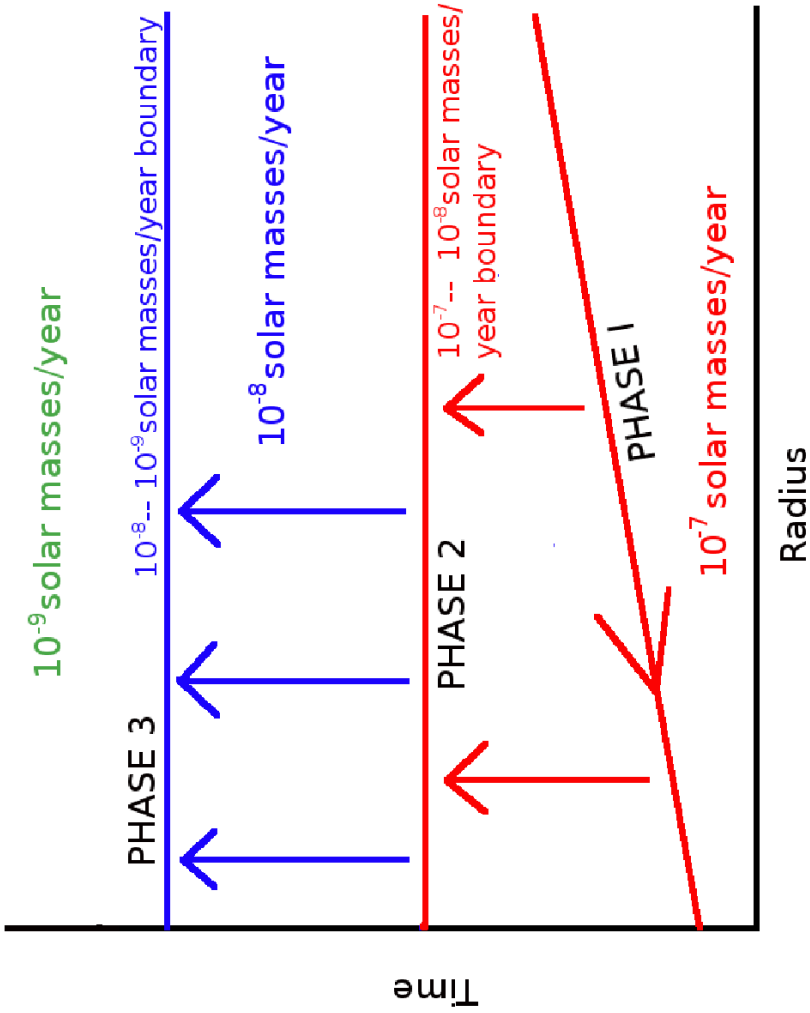

Figure 4.56: Schematic of the Model C calculation process.

4.5.2 Results

Once again particular attention is paid to the 1 AU $\leq r \leq$ 10 AU planet-forming region of each stellar accretion disk. Figure 4.57 compares the resulting Model C column densities (dashed line) of CN, HCN, H_2CO and NH_3 to those of Model B (dotted line) from Section 4.3.

Each of the four molecules display profile differences. The largest differences are in CN and NH_3 on the scale of orders of magnitude, whereas HCN and H_2CO are a few factors different.

Whilst the Model C profiles of HCN, H_2CO and NH_3 fluctuate to a greater extent, CN looks similar to that of Model A (Figure 4.33). The calculation times in each of the 10^{-7} $M_\odot$ yr^{-1} and 10^{-8} $M_\odot$ yr^{-1} disks are enhanced by a factor of $\sim$ 4.5 and 23 respectively, which is a combined enhancement factor of $\sim$ 14. This essentially means that chemistry (τ_{chem}) has 14 times longer to react at each disk grid point. Changes in Model B and Model C column densities are therefore attributed to chemical abundances in Model B not being in steady-state ($\tau_{chem} > \tau_{calc}$), whether that be specifically in the 10^{-7} $M_\odot$ yr^{-1} or 10^{-8} $M_\odot$ yr^{-1} sub-calculation, or both.

Table 4.11 compares the Model B and Model C HCN column density values at r = 1 AU and r = 10 AU, with values from other works previously listed in Table 4.4 which model with a 10^{-8} $M_\odot$ yr^{-1} disk. The difference between the Model C

Table 4.9: Comparison of Model B and Model C HCN column density values at r = 1 and 10 AU with values from other works as previously listed in Table 4.4.

Model/Work	r = 1 AU	r = 10 AU
Model B	5.6(18)	1.4(18)
Model C	1.1(19)	1.4(18)
Woods & Willacy (2009)-Full	1.1(20)	4.2(14)
Walsh et al. (2010)	2.0(17)	7.1(14)
Heinzeller et al. (2011)	5.2(19)	8.0(14)

HCN value at $r = 1$ AU and that from Walsh et al. (2010) is larger compared with Model B, but closer to the larger values established in Willacy & Woods (2009) and Heinzeller et al. (2011). At $r = 10$ AU, Model B and Model C values are the same, both around 4 orders of magnitude larger than the other three works.

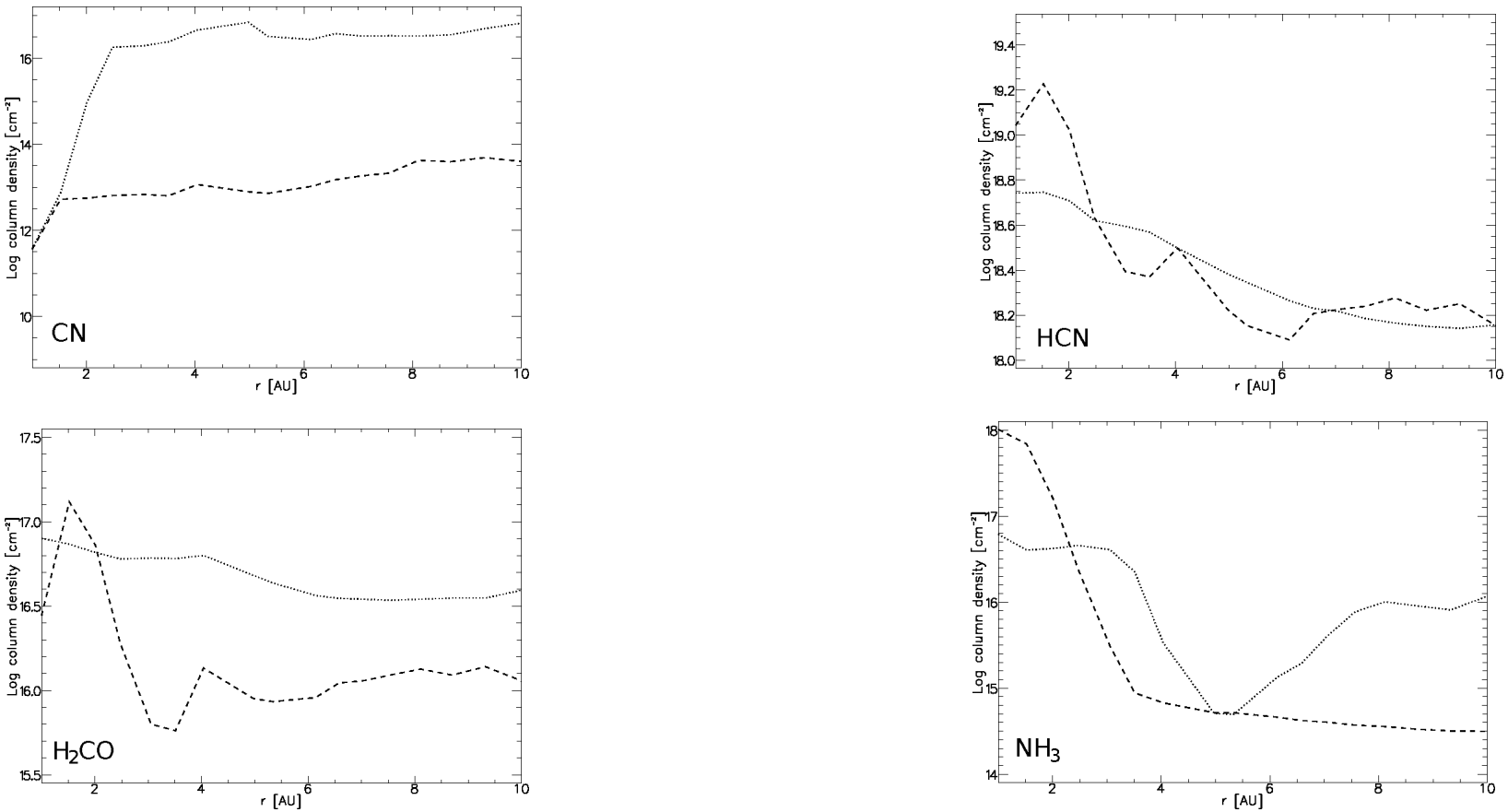

Figure 4.57: Logarithmic column density comparisons between Model B (dotted line) and Model C (dashed line) for CN, HCN, H_2CO and NH_3.

4.5.3 Uncertainties in Model C column densities and future work

A number of other assumptions and approximations have been made in this investigation. Firstly, one needs to address the validity of the linear stellar accretion rate–age approximation incorporated from Hartmann et al. (1998) (Equation 4.18). This investigation has discounted the potential variability in mass accretion rate decay due to the noted uncertainty in errors on log $t_{\rm age}$ and log $\dot{M}$ (see Section 2.2 of Hartmann et al. 1998).

The stellar sample in Hartmann et al. (1998) was determined initially from a sample of $\sim$ 40 K5-M2 pre-main sequence stars. This was later added to from Muzerolle et al. (2000) and Calvet et al. (2004) (see Figure 2 of Hartmann 2005). Although a general decrease of stellar accretion rate with disk age was established, the number of samples decreased with age. But of those older samples, a sharper decline with age also existed, which may point to either some form of non-steady episodic accretion burst behavior in the inner disk beyond 1 Myr (e.g. Zhu et al. 2009), rapid giant planet formation or episodically enhanced photoevaporation processes (Clarke et al. 2001). A larger sample of observed older stars confirming this sharper decline with age may well steepen the line, in which case, the proposed Model C column densities may be invalidated, or solely constrained to the initial "young" star samples in Hartmann et al. (1998). ALMA in particular will have the ability to observe a greater variety of pre-main sequence stars known to harbor protoplanetary disks from a greater special type range in a given region, and therefore strengthen the understanding of how the stellar accretion rate decreases with age.

A second important assumption is limiting the chemical calculation between the radii of 1 to 25 AU. The initial reasons for ignoring the inward accretion from contributing radii beyond 25 AU was to speed up computational time, knowing that very little chemical activity is expected since temperatures rarely exceed 10 – 20 K. Another reason is due to the discrepancy in the temperature increasing with radius beyond 25 AU which is an inherent fault in the model (Hideko Nomura, private

communication); with the risk of unrealistic desorption and chemical processing in the gas at distances where most of the species should be frozen out. A calculation beginning from a much larger radius would not be a problem with the use of a more recent model (e.g. see Nomura et al. 2007).

An important future study is to determine the extent of CN, HCN, H_2CO and NH_3 column density sensitivity from a greater variety of calculation times in both 10^{-7} $M_\odot$ yr^{-1} and 10^{-8} $M_\odot$ yr^{-1} epochs. This particular investigation has constrained the calculation time to a single set of results established from collated observational data. However, performing over many different calculation timescales will establish the behaviour of abundance and column density variance with time and may provide a unique chemical tracing tool in determining disk age.

An additional study would be to incorporate the more recent work of Jones et al. (2012), who noted that the disk age can be approximated to be that of the stellar age. By collating observational data of most T Tauri sources and their associated protoplanetary disk found from the literature, they concluded that a stellar age = disk age best-line fit describes the spread of stellar accretion rate versus stellar age to a reasonable degree, where:

$$t_{\rm disk} = \frac{M_{\rm disk}}{\dot{M}} \quad \text{yr.} \tag{4.22}$$

Here, $t_{\rm disk}$ and $M_{\rm disk}$ are the disk age and mass respectively. It is possible to compare between the values obtained in Equations (4.19) and (4.20), and the $t_{\rm disk}$ values from Equation (4.23), if the total disk mass between two adjacent radial grid points is calculated. This alternative method would require a 10^{-9} $M_\odot$ yr^{-1} physical disk to work with, and is a case for future work.

Finally, it should be noted that a numerical integration error from the model itself cannot be discounted. To eliminate the possibility of a lack of calculation sensitivity as the cause, one must repeat this investigation for smaller values of RTOL and ATOL, to see if an avoidance of small abundances affects the final distributions of CN, HCN, H_2CO and NH_3. This will only become important if the abundance

of these molecules is affected by molecules below the ATOL value, which does not seem to be the case. A basic benchmark test of H_2CO abundance variation with different RTOL and ATOL values is discussed in Appendix A.

4.5.4 Summary

From CN, HCN, H_2CO and NH_3, the molecules CN and NH_3 appear to show the largest degree of sensitivity upon altering the chemical calculation from a prescribed calculation time discussed in Section 4.3, to one which correlates more with observations whilst evolving from 10^{-7} $M_\odot$ yr^{-1} to 10^{-8} $M_\odot$ yr^{-1}. However, do CN and NH_3 show a general sensitivity to a change in calculation timescale, and thus the duration of chemical evolution from 10^{-7} $M_\odot$ yr^{-1} to 10^{-8} $M_\odot$ yr^{-1}, and the age of the disk? This should be investigated in the future.

CHAPTER 5

Conclusions and future work

5.1 Summary

This thesis has investigated the evolution of inner chemistry ($r \leq 10$ AU) over time within a modelled protoplanetary disk (PPD) surrounding a low-mass T Tauri star; a phase our own solar system went through some 4.5–4.6 billion years ago. To achieve this, a 1+1D physical model of a PPD was combined with an extensive chemical model to perform time-dependent calculations over the modelled disk grid.

5.1.1 Model

The physical model was taken from Nomura (2002), who self-consistently calculated the density and temperature profile of an axisymmetric PPD surrounding a typical T Tauri star as a function of radius r and height z, with parameters $M_* = 0.5\ M_\odot$, radius $R_* = 2\ R_\odot$ and $T_* = 4000$ K. The model is based on the standard accretion disk model of Lynden-Bell & Pringle (1974), utilizing the α-prescription discussed in Shakura & Sunyaev (1973) to represent the kinematic viscosity in the PPD. The α-viscous parameter of 0.01 is adopted for all points in the disk. Two sources of disk heating are considered: stellar UV heating from the hypothetical stellar source ($r = z = 0$), and viscous dissipation from the midplane ($z = 0$). The height of the disk at each radius is determined according to the typical gas density of a molecular cloud which the PPD is assumed to be encased in. Nomura (2002) set this to be 3.8×10^{-22} g cm^{-3}. The modelled disk is flared, such that the maximum disk height, $z_{\rm max}$, increases with r, and radial accretion is assumed according to the thin-disk approximation (Ilgner et al. 2004). Gas and dust are assumed to be well-mixed, and have identical temperature distributions over the entire disk. The hottest disk regions are found close to the star and near the disk surface, whilst the coldest regions are located further from the star, and at the midplane. The surface density distribution is determined by equating the expression for the gravitational energy of radially accreting mass to the expression for the viscous heating rate.

The gas-phase chemical network is taken from a reduced version of the RATE95 UMIST database (Millar et al. 1997). It consists of 3894 reaction coefficients, involving 395 species from 7 elements H, He, C, N, O, S and Fe. To this, a deuterated network from Roberts & Millar (2000a,b), and a gas-grain interaction network from Hasegawa et al. (1992) is added. Gas-phase reactions include two-body processes, UV photochemistry and cosmic-ray ionization. The cosmic-ray ionization rate, per H_2 molecule, is set to 1.3×10^{-17} s^{-1}. Gas-grain interactions include freeze-out and

thermal-desorption, and dissociative recombination of cations on grain-surfaces. In total, there are 9659 reactions. The initial reference abundances implemented into the model are calculated from a pre-stellar core model at a fixed temperature of 10 K (see Markwick-Kemper (2005) for details).

5.1.2 Objectives

The objectives were to use this model to:

- Compare between the cosmic-ray ionization rate distributions of the plane-parallel attenuator (e.g. Semenov et al. 2004) and the isotropic attenuator (Umebayashi & Nakano 2009).
- Determine how the isotropically–attenuated cosmic-ray ionization rate compares with the radionuclide ionization rate along the midplane.
- Compare between the computed chemical abundances at the midplane with and without radionuclides, as a function of the radionuclide ionization rate.
- Compare the $r \leq 10$ AU chemical distributions of a physical disk with a stellar accretion rate of 10^{-7} $M_\odot$ yr^{-1} and 10^{-8} $M_\odot$ yr^{-1}.
- Noting that stellar accretion rate reduces with time (e.g. Hartmann et al. 1998), compare between the chemical distributions of: (i) a 10^{-8} $M_\odot$ yr^{-1} simulation using the initial pre-stellar core reference abundances, and (ii) a 10^{-8} $M_\odot$ yr^{-1} which incorporates the chemical abundances from a previous 10^{-7} $M_\odot$ yr^{-1} simulation.
- Determine abundant molecules which are most sensitive to this change.
- Repeat the previous investigation by constraining the calculation time according to the $\log \dot{M} = -8.0 - 1.4 \log t_{\rm age}$ relation from Hartmann et al. (1998), and determine any molecules which are sensitive.

- Convert the results to potentially observable parameters via the use of a 1-D LTE ALMA algorithm, taking note of the constraints of this particular model.

5.1.3 Findings

The first set of investigations primarily focused on the potential effects of radionuclides along the midplane, influenced by the knowledge that radionuclides may have been abnormally abundant in our early solar system compared with the interstellar medium. The most ionizing of these radionuclides is thought to have been ^{26}Al.

It is currently not known if other PPDs share this excess, and since it is impossible to observe radionuclides directly, one must look to other ways of tracing their presence. One possibility is that the chemistry they influence may be detectable. The motivation therefore exists to determine which molecules are most affected by the presence of radionuclides. The primary investigation in chapter 3 established that the most sensitive species were relatively low ($\leq 10^{-20}$) abundant hydrocarbon cations such as CHD_2OH^+ and CH_3CN^+. But the molecules showing the overall greatest changes were relatively abundant ($\geq 10^{-7}$) neutrals such as C_4H_2, HC_3N, C_3H, HCN, CH_4, C_2H_2 and N_2. Of these, HCN and C_2H_2 have already been detected in PPDs.

The second set of investigations are motivated from observations which suggest that T Tauri systems vary from faster to slower accretion rates. Stellar accretion rates of 10^{-7} $M_\odot$ yr^{-1} and 10^{-8} $M_\odot$ yr^{-1} are important periods to study from the perspective of identifying the chemical ingredients involved in planetary formation. The resulting chemical distribution of the 10^{-8} $M_\odot$ yr^{-1} disk was reminiscent of a later epoch which is optically thinner than a epoch equivalent to 10^{-7} $M_\odot$ yr^{-1}, in that molecules are more prone to photodissociation from the deeper-penetrating radiation field.

Inputting the 10^{-7} $M_\odot$ yr^{-1} calculated chemical abundances into 10^{-8} $M_\odot$ yr^{-1} resulted in differences to the abundances of CN, HCN, H_2CO and NH_3, over the standalone 10^{-8} $M_\odot$ yr^{-1} simulation. The chemical distributions revealed that the differences were attributed to layers at or around the midplane, and this translated to the column density profiles since most of the disk mass resides there. The location of the disparities suggested that only a sub-mm receiver with sufficient resolution to probe the $r < 10$ AU regions had the potential to observe these differences – ALMA.

Of course, ALMA is not yet fully operational to begin observations of this precision. Utilizing instead the CASA 1-D ALMA algorithm, a conversion was made from the two distinct 10^{-8} $M_\odot$ yr^{-1} abundance distributions of two feasibly observable molecules HCN and H_2CO, to a set of integrated intensity distributions for five rotational transitions of each molecule, each as a function of disk emissivity and optical depth. It was found that the highest feasible rotational transitions of HCN and H_2CO (J = 8–7 and $J \rightarrow$ 10–9 respectively) show the greatest overall integrated intensity differences inside a radius of 10 AU. Although the general peak emission of HCN was found to reside closer to the hotter disk surface than H_2CO, the difference in the location of peak emission between the two models was deemed negligible. For both molecules it was also determined that the peak intensities associated with the highest J transitions and differences were below J_{max} at radii 1 and 5 AU; the highest conceivable transition and intensity in the LTE approximation. These intensities were converted to brightness temperatures via the Rayleigh-Jeans approximation and compared with the surface temperature distribution of the 10^{-8} $M_\odot$ yr^{-1} disk. Due to the constraints of an outer calculation radius at 25 AU for this particular model, it was deemed impossible to estimate a useful integrated flux for the modelled disk, since most of the flux is generated > 25 AU. This, of course will not be a problem with other models whose calculations start from much larger radii, e.g. 100–400 AU. Until then, it remains unanswered whether these differences are

observable or not.

In a final investigation, the 10^{-7} $M_\odot$ yr^{-1} and 10^{-8} $M_\odot$ yr^{-1} simulations were re-evaluated according to the approximate stellar-accretion rate–age relation, $\log \dot{M} = -8.0 - 1.4 \log t_{\rm age}$, from Hartmann et al. (1998). Having repeated the previous investigation, it was found that CN, HCN and H_2CO and NH_3 were all sensitive to the change in calculation time, with CN and NH_3 showing sensitivities over an order of magnitude. This suggests CN and NH_3 may be suitable tracers of calculation time, and possibly disk age. Further analysis with different calculation times, and comparing with the results from the more recent, alternative method proposed in Jones et al. (2012) will be required, in addition to simulations with different RTOL and ATOL values to eliminate the possibility of numerical inaccuracies within the model itself as the cause.

5.2 Future work

The scope of potential further work in this field is summarized in this section, and is broken down into three categories.

5.2.1 General

- Use as chemically-complete a network as possible in later works (e.g. Walsh et al. 2012).
- Incorporate temperature limits for endothermic reactions.
- Implement the most up-to-date binding energies for the set of gas-grain interaction reactions in the chemical model.
- Perform the accretion calculation following a Lagrangian method, i.e. all accretion streamlines converge at smaller radii.

- Determine how the Magnetic Reynolds number, Re_M, alters between 10^{-7} $M_\odot$ yr^{-1} and 10^{-8} $M_\odot$ yr^{-1}.
- Model the chemistry for different stellar accretion rates with different grain-sizes.
- Model the chemistry with different density distributions and α-viscous parameters such as 0.025 (e.g. Willacy & Woods 2009).
- Enforce self-shielding processes at the disk surface into this model.
- Include non-spherical grain geometry and grain sputtering processes, and determine how this affects the chemistry for the 10^{-7} $M_\odot$ yr^{-1} and 10^{-8} $M_\odot$ yr^{-1} disks.
- Model more complex transport processes such as vertical-mixing, and stellar winds with chemistry (e.g. Heinzeller et al. 2011).
- Investigate the thermal ionization of heavy metals such as Mg^+ and K^+ (e.g. Ilgner & Nelson 2006b).
- Study in depth the charge-distribution of grains with a large chemical network.
- An updated physical model, i.e. Nomura et al. (2007), which considers both UV and X-ray heating, Lα radiation, and separate gas and dust temperature distributions.
- Incorporating stellar UV and X-ray photochemical reactions, or, for the latter, determining the X-ray ionization rate at each point in the disk as a function of the cosmic-ray ionization rate.
- Utilize anionic species such as H^-, CN^-, C^-, and doubly-ionized cations such as C^{2+} and Mg^{2+}.

- Restrict accretion to surface regions and areas of the warm-molecular layer where the disk is magnetorotationally unstable, and even model outward-moving transport processes along the midplane.
- Investigate episodic accretion bursts of $\sim 10^{-4}$ $M_\odot$ yr^{-1} by adjusting the calculation times for grid points around the midplane.
- Modelling a 3-D turbulent disk with as chemically-complete a network as possible (very demanding).

5.2.2 Radionuclides

- Compare the chemistry with and without radionuclides fully for the 1+1D grid.
- Compare the chemistry with and without radionuclides when S_X is set to 0.3.
- Compare the chemistry with and without radionuclides in the 10^{-8} $M_\odot$ yr^{-1} disk.
- Model the chemistry with cosmic-rays omitted.
- Implement a set of induced photochemical and ionization reactions for each individual species in the chemical network, e.g.

  $$\mathrm{CO} + \mathrm{RADPHOT} \rightarrow \mathrm{C} + \mathrm{O},$$

  where RADPHOT represents the 1.809 MeV photon emitted from the relaxation of the ^{26}Mg nucleus, itself formed from ^{26}Al decay.
- Model the attenuation of energy isotropically emitted from ^{26}Al decay, either encased in a grain, or freely in the gas.
- Explicitly model the desorption potential from grains as a result of absorption of energy from radionuclide decay.

5.2.3 Stellar accretion rate evolution and disk age

- Determine whether the abundance differences in CN, HCN, H_2CO, NH_3 are observable or not.
- Calculate and compare the chemistry with the more recent method discussed in Jones et al. (2012), where the stellar age = disk age.
- Determine whether CN and NH_3 traces the calculation time, and perhaps disk age.
- Thorough analysis of the deuterated molecules enlisted in the chemical network and their potential differences between the two distinct 10^{-8} $M_\odot$ yr^{-1} simulations; particularly the D/H ratios, such as DCO^+/HCO^+.
- Studying the set of feasible J-transitions of HCO^+ in a similar way to which HCN and H_2CO have been analyzed using the 1-D CASA algorithm.
- Utilizing a non-LTE 2-D algorithm, which may be more appropriate for HCN.
- Performing the 10^{-7} $M_\odot$ yr^{-1} to 10^{-8} $M_\odot$ yr^{-1} calculation to a higher iteration, i.e. a 2nd order iteration represents running firstly from 10^{-7} $M_\odot$ yr^{-1} to an intermediate 5×10^{-7} $M_\odot$ yr^{-1}; see Figure 5.1. The ultimate (but computationally demanding) procedure is to model between a different set of physical disk prescriptions at each calculation timestep, i.e. with different density, temperature and opacity parameters.
- Expanding the analysis to later accretion rates and epochs, e.g. 10^{-9} $M_\odot$ yr^{-1}, 10^{-10} $M_\odot$ yr^{-1}, 10^{-11} $M_\odot$ yr^{-1} etc. Note that a comparison of molecular snowlines has already been studied for these accretion rates; see Oka et al. (2011).
- Model how the dead-zone evolves over time between these stellar accretion rate disks, coupled with dust-coagulation processes which proceed with time, in turn reducing the disk opacity.

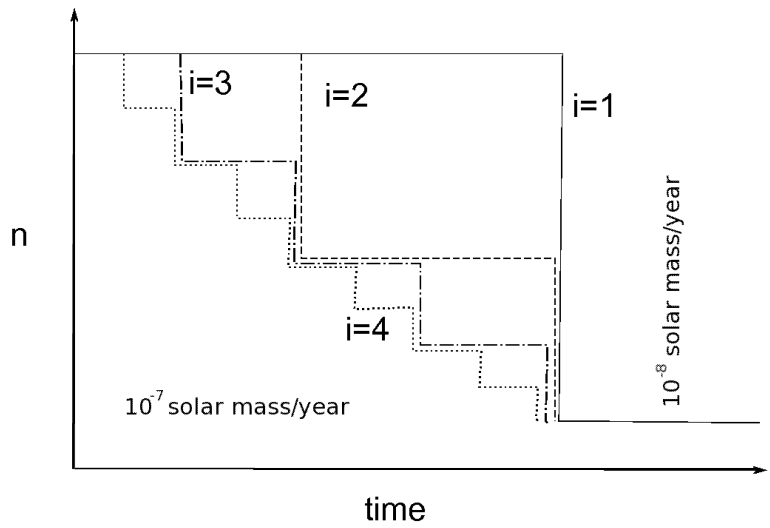

Figure 5.1: Schematic illustration of how the number density may be iterated to the *i*th order from 10^{-7} $M_\odot$ yr^{-1} to 10^{-8} $M_\odot$ yr^{-1}. This work has focused on i = 1. i = 2 might involve iterating firstly from 1×10^{-7} $M_\odot$ yr^{-1} to 5×10^{-7} $M_\odot$ yr^{-1} (an intermediate number density), and then to 1×10^{-8} $M_\odot$ yr^{-1} and so on for larger values of i.

5.3 Conclusions

This section lists the main conclusions of this thesis.

- The isotropic attenuator derived in Umebayashi & Nakano (2009) attenuates cosmic-rays over more of the disk than the plane-parallel attenuator, but does not increase the extent of attenuation.

- Abundant molecules ($\sim 10^{-7}$) which are enhanced with the inclusion of radionuclides at the midplane, are C_4H_2, HC_3N and C_3H. Those which are depleted are HCN, C_2H_2, CH_4 and N_2, each with an abundance difference of $\sim$ 1%. The first two depeleted molecules, HCN and C_2H_2, have already been detected in PPDs at sub-mm wavelengths associated with colder, outer disk regions, but may also be associated with the inner disk midplane, which ALMA could probe.

- CN, HCN, H_2CO and NH_3 all appear to be sensitive to a change in the initial abundances of a 10^{-8} $M_\odot$ yr^{-1} accretion disk.
- The J=8-7 HCN and J_K=10_{010}-9_{09} H_2CO transitions may trace the evolution of the stellar accretion rate in other PPDs, but must be studied further using a model which begins its calculation at $r \sim$ 100–400 AU.
- CN and NH_3 may trace the calculation time and the disk age of a PPD, with possible unique column density signatures for each stellar accretion rate.

APPENDIX A

Benchmark testing of the model

A description of both the physical and chemical model used in this thesis is discussed in Sections 2.3 and 2.4. This same physical model has been previously described and utilized in Millar et al. (2003). The authors combine the physical model of a 10^{-7} $M_\odot$ yr^{-1} disk along with a chemical model which was taken originally from Willacy et al. (1998) and discussed in Markwick et al. (2002); the main difference being that the Willacy et al. (1998) chemical model excludes a deuterated network unlike the one used in this thesis.

Millar et al. (2003) presented molecular distributions of H_2CO and C_2H for the inner $r \leq 10$ AU and $z \leq 1$ AU of their 10^{-7} $M_\odot$ yr^{-1} disk model. For comparison, these are presented alongside equivalent molecular distributions from the combined physical and chemical model used in this thesis (Figure A.1).

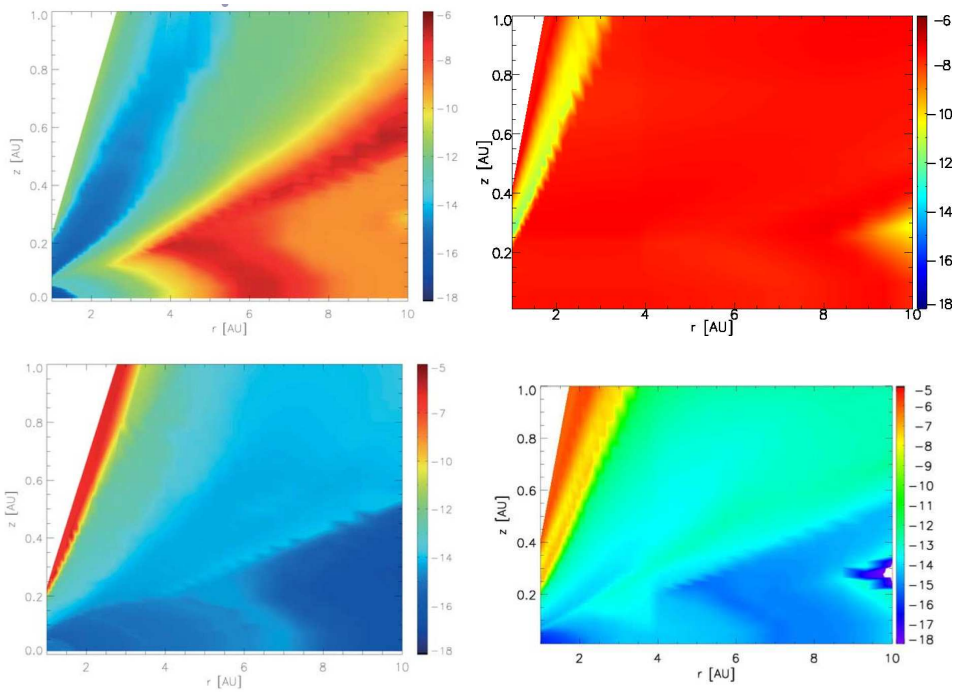

Figure A.1: 10^{-7} $M_\odot$ yr^{-1} logarithmic abundance distribution maps of H_2CO (top row) and C_2H (bottom row) from Millar et al. (2003) [left], and this thesis [right].

One can see that both C_2H profiles are essentially the same regardless of the different chemical networks. The H_2CO profiles are however remarkably different. The Millar et al. (2003) distribution varies from more abundant 10^{-6} and 10^{-8} (red to orange) regions in the deeper $r \geq 4$ AU, to less abundant 10^{-12} to 10^{-18} bands towards the surface. Yet the distribution in this thesis essentially remains unchanged at 10^{-8} (red), albeit a thin 10^{-12} yellow-green band just below the surface which is an otherwise common feature in both distributions.

One possible reason for this discrepancy is that the relative and absolute tolerances (RTOL and ATOL respectively) set in the LSODE differential calculator (see Section 2.4.4) are different. In this thesis, RTOL and ATOL are set to 10^{-9} and 10^{-11} respectively over the entire disk grid, whereas RTOL and ATOL are set to approximately 10^{-14} and 10^{-16} in the Millar et al. (2003) calculation, preferring instead to run over a substantially longer time. Figure A.2 compares the H_2CO and H_2O final

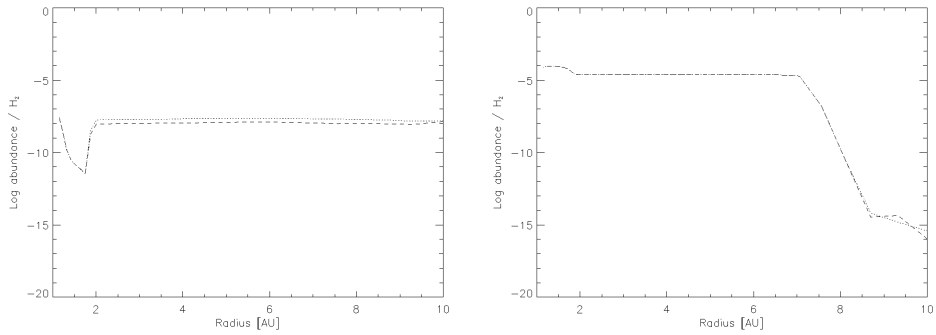

Figure A.2: Logarithmic abundance profiles of H_2CO (left) and H_2O (right) at a disk height $z = 0.5$ AU where RTOL and ATOL is set to 10^{-9} and 10^{-11} respectively (dotted line), and 10^{-14} and 10^{-16} respectively (dashed line).

abundance profiles after 10^6 yr for calculations performed with firstly RTOL $=10^{-9}$ and ATOL $= 10^{-11}$, and secondly RTOL $= 10^{-14}$ and ATOL $= 10^{-16}$; in both cases at a constant height of $z = 0.5$ AU.

Figure A.2 shows no difference between the profiles, suggesting the accuracy of the calculation does not affect the steady-state abundance of these or any of the focused species in this thesis, and that the difference in the H_2CO distribution is a chemical one. No difference over an order of magnitude exists between the two calculations over the entire disk grid.

The chemical discrepancy could be due to the treatment of reducing the chemical network used in this thesis, removing reactions which may otherwise destroy H_2CO, or the effects of deuterated species, and particularly analogues such as HDCO and D_2CO which compete for destruction, preserving more H_2CO due to H-D exchange reactions. Thus, in the case of H_2CO in particular it is difficult to produce the results of the Millar et al. (2003) calculation since they use a different chemical network to the one used in this thesis. It must also be noted that there is no benchmark test to be made as such of the 10^{-8} $M_\odot$ yr^{-1} disk used in this thesis since it has not been used in any previous work.

APPENDIX B

The Standard Accretion Disk Model

An accretion disk is commonly modelled as a thin disk of gas particles, rotating around a star of mass M_* with radius R_* (e.g. Lynden-Bell & Pringle 1974; Pringle 1981). It is used to explain how a star is able to accrete from its surrounding disk whilst conserving overall angular momentum. Accretion disks rotate in a differential manner, with some matter spiraling inward, losing energy and angular momentum. In response, neighbouring matter spirals outward to larger radii, sweeping up the lost angular momentum.

The particles are assumed to rotate at a given radius r from the star, with a Keplarian angular velocity $\Omega(r)$ given by:

$$\Omega(r) = \left(\frac{GM_*}{r^3}\right)^{1/2} \quad \mathrm{s}^{-1}, \tag{B.1}$$

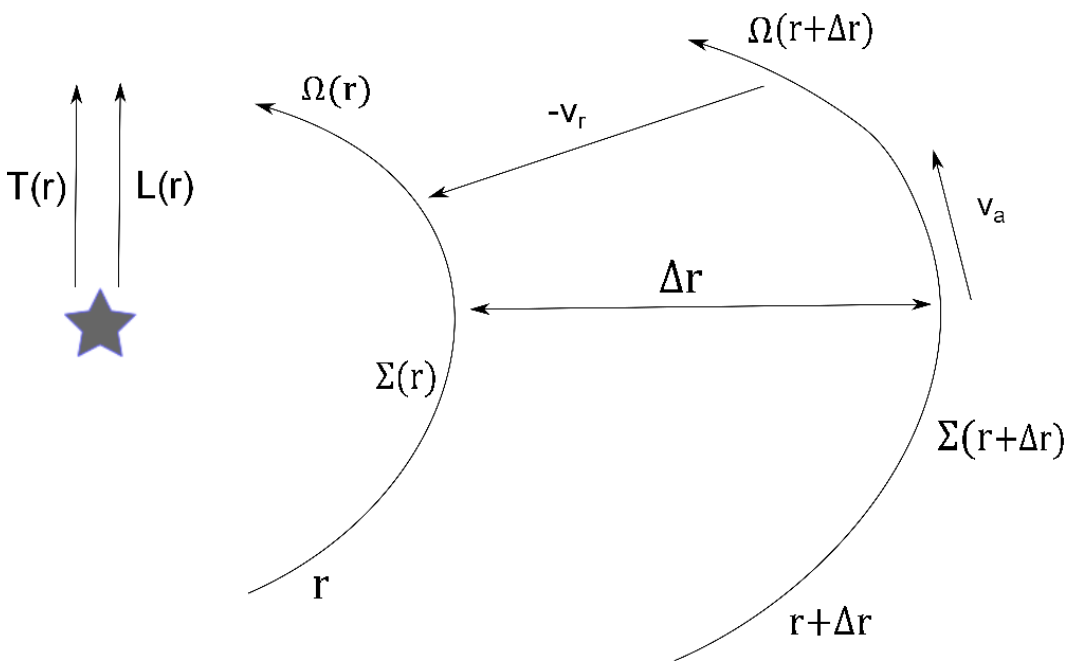

Figure B.1: Schematic diagram of the parameters used in the Standard Accretion Disk Model as discussed in this Appendix.

where G is the gravitational constant. The instantaneous velocity in the azimuthal rotating plane, $v_a(r)$, is then:

$$v_a(r) = r\Omega(r) \quad \text{cms}^{-1}. \tag{B.2}$$

This accretion disk is principally defined by its surface density Σ at a radius r at a time t. If one considers the rotation of an annulus of gas between an inner radius r and outer radius $r+\Delta r$, then the mass M of the annulus is given by:

$$M = 2\pi r \Delta r \Sigma(r,t) \quad \text{g}. \tag{B.3}$$

Then, the angular momentum of the annulus is:

$$L = 2\pi r \Delta r \Sigma(r,t) r^2 \Omega(r) \quad \text{gcm}^2\text{s}^{-1}. \tag{B.4}$$

The rate of change of annulus mass at a given radius r is equal to the net flow of mass falling into it from adjoining annuli, moving at a negative radial drift velocity

$v_{\rm r}$ towards the disk centre:

$$\frac{\partial}{\partial t}(2\pi r\Delta r\Sigma) = 2\pi r v_{\rm r}(r,t)\Sigma(r,t) - 2\pi(r+\Delta r)v_{\rm R}(r+\Delta r,t)\Sigma(r+\Delta r,t). \tag{B.5}$$

Tending to the limit $\Delta r \to 0$, this becomes:

$$r\frac{\partial\Sigma(r,t)}{\partial t} + \frac{\partial}{\partial r}[r\Sigma(r,t)v_{\rm R}(r,t)] = 0. \tag{B.6}$$

Similarly, conservation of angular momentum yields

$$r\frac{\partial}{\partial t}[\Sigma(r,t)r^2\Omega(r)] + \frac{\partial}{\partial r}[r\Sigma(r,t)v_{\rm r}(r,t)r^2\Omega] = \frac{1}{2\pi}\frac{\partial T(r)}{\partial t}, \tag{B.7}$$

where T(r) is the viscous torque applied on the inner material from the outer material, itself given by:

$$T(r) = 2\pi r\nu\Sigma(r,t)r^2\frac{d\Omega(r)}{dt}. \tag{B.8}$$

The parameter, ν, is known as the kinematic viscosity. Combining Equations (A.2), (A.6), (A.7) and (A.8) generates an expression for the evolution of the surface density with time:

$$\frac{\partial\Sigma(r,t)}{\partial t} = \frac{3}{r}\frac{\partial}{\partial r}\left[r^{1/2}\frac{\partial}{\partial r}(\nu\Sigma(r,t)r^{1/2})\right] \quad \mathrm{gcm^{-2}s^{-1}}. \tag{B.9}$$

The parameter ν may be a function of local disk variables r, Σ and t. Hence Equation (A.9) is a non-linear diffusion equation for $\Sigma(r,t)$.

The radial structure of the thin accretion disk due to viscosity is thought to change on a timescale $t_{\rm vis} \sim r^2/\nu$. The disk can be considered "steady" if all other dynamical timescales exceed $t_{\rm vis}$, i.e. the disk structure does not change during calculation time. Then the $\partial/\partial t$ terms in Equations (A.6) and (A.7) can be set to zero. Integrating Equation (A.6) with respect to radius leads to:

$$r\Sigma(r)v_r(r) = \dot{M}, \tag{B.10}$$

where $\dot{M}$ is defined as the mass flow or accretion rate, constant through each point in the disk. It is given by:

$$\dot{\mathbf{M}} = \mathbf{2\pi r\Sigma(r)(-v_r(r))}, \tag{B.11}$$

either in units of $M_\odot$ yr^{-1} or g s^{-1}. Similarly integrating Equation (A.7) in the same way gives:

$$r\Sigma(r)v_r(r)r^2\Omega(r) = \frac{1}{2\pi}(T(r) + C), \tag{B.12}$$

where C is a constant of integration. Substituting Equation (A.8) into Equation (A.12) yields:

$$-\nu\Sigma(r)\frac{d\Omega(r)}{dr} = (-v_r(r))\Sigma(r)\Omega(r) + \frac{C}{2\pi r^3}. \tag{B.13}$$

The constant C is defined as the steady influx of angular momentum through the disk:

$$C = -\dot{M}(T(r)M_*R_*)^{1/2}, \tag{B.14}$$

as a function of the star's parameters to first order (Pringle 1981). Merging Equations (A.1) and (A.14) into Equation (A.13) then forms the expression:

$$\nu\Sigma(r) = \frac{\dot{M}}{3\pi}\left[1 - \left(\frac{R_*}{r}^{1/2}\right)\right]. \tag{B.15}$$

The viscous dissipation, $D(r)$ is given by:

$$D(r) = \frac{1}{2}\nu\Sigma(r)\left(r\frac{d\Omega(r)}{dr}\right)^2. \tag{B.16}$$

Substituting Equation (A.13) in terms of $\nu\Sigma(r)$, along with Equation (A.14), into Equation (A.16) gives:

$$D(r) = \frac{3GM_*\dot{M}}{4\pi r^3}\left[1 - \left(\frac{R_*}{r}\right)^{1/2}\right]. \tag{B.17}$$

The viscosity ν follows the α-prescription of Shakura & Sunyaev (1973), and is defined by:

$$\nu = \alpha c_s H, \tag{B.18}$$

where c_s is the sound speed in the disk, H is the scale height, and α is a dimensionless parameter < 1.

Finally, equating Equations (A.15) and (A.16) in terms of $D(r)$, and substituting in Equation (A.18) gives the result:

$$\mathbf{\frac{3GM_*\dot{M}}{8\pi r^3}\left[1 - \left(\frac{R_*}{r}\right)\right] = \frac{9}{4}\Sigma\alpha c_s^2\Omega.} \tag{B.19}$$

The term on the left represents the gravitational release of energy due to accretion and the right side, thermal heating via viscous dissipation:

$$\mathbf{Q}_{\mathrm{vis}} = \frac{\mathbf{9}}{\mathbf{4}}\boldsymbol{\Sigma}\alpha\mathbf{c}_{\mathrm{s}}^{\mathbf{2}}\boldsymbol{\Omega}. \tag{B.20}$$

Rearranging Equation (A.19) in terms of Σ gives:

$$\boldsymbol{\Sigma} = \frac{\mathbf{1}}{\mathbf{6}}\frac{\mathbf{GM}_{*}\dot{\mathbf{M}}}{\boldsymbol{\pi}\mathbf{r}^{\mathbf{3}}\alpha\mathbf{c}_{\mathbf{s}}^{\mathbf{2}}\boldsymbol{\Omega}}\left[\mathbf{1} - \left(\frac{\mathbf{R}_{*}}{\mathbf{r}}\right)^{\mathbf{1/2}}\right] \quad \mathrm{gcm}^{-2}. \tag{B.21}$$

Equations highlighted in bold are referred to in the main text of the thesis.

APPENDIX C

Radiative equilibrium and transfer

In this model, radiative equilibrium is assumed at all points in the disk (i.e. emitted and absorbed radiation are balanced). The full expression is given by:

$$4\pi \int_0^\infty \kappa_\nu B_\nu[T(r,\Theta)]d\nu = \int_0^\infty \kappa_\nu J_\nu(r,\Theta)d\nu, \tag{C.1}$$

where κ_ν is the monochromatic absorption opacity, ν is the photon frequency, B_ν is the Planck function:

$$B_\nu(T) = \frac{2h\nu^3}{c^2}\left[\left(\exp\left(\frac{h\nu}{k_B T}\right) - 1\right)^{-1}\right], \tag{C.2}$$

and the mean intensity, J_ν, is a result of integrating the total mean specific intensity, I_ν over all solid angles:

$$J_\nu(r,\Theta) = \frac{1}{4\pi}\int_0^{2\pi}\int_{-1}^{1} I_\nu(r,\Theta;\mu,\phi)d\mu d\phi. \tag{C.3}$$

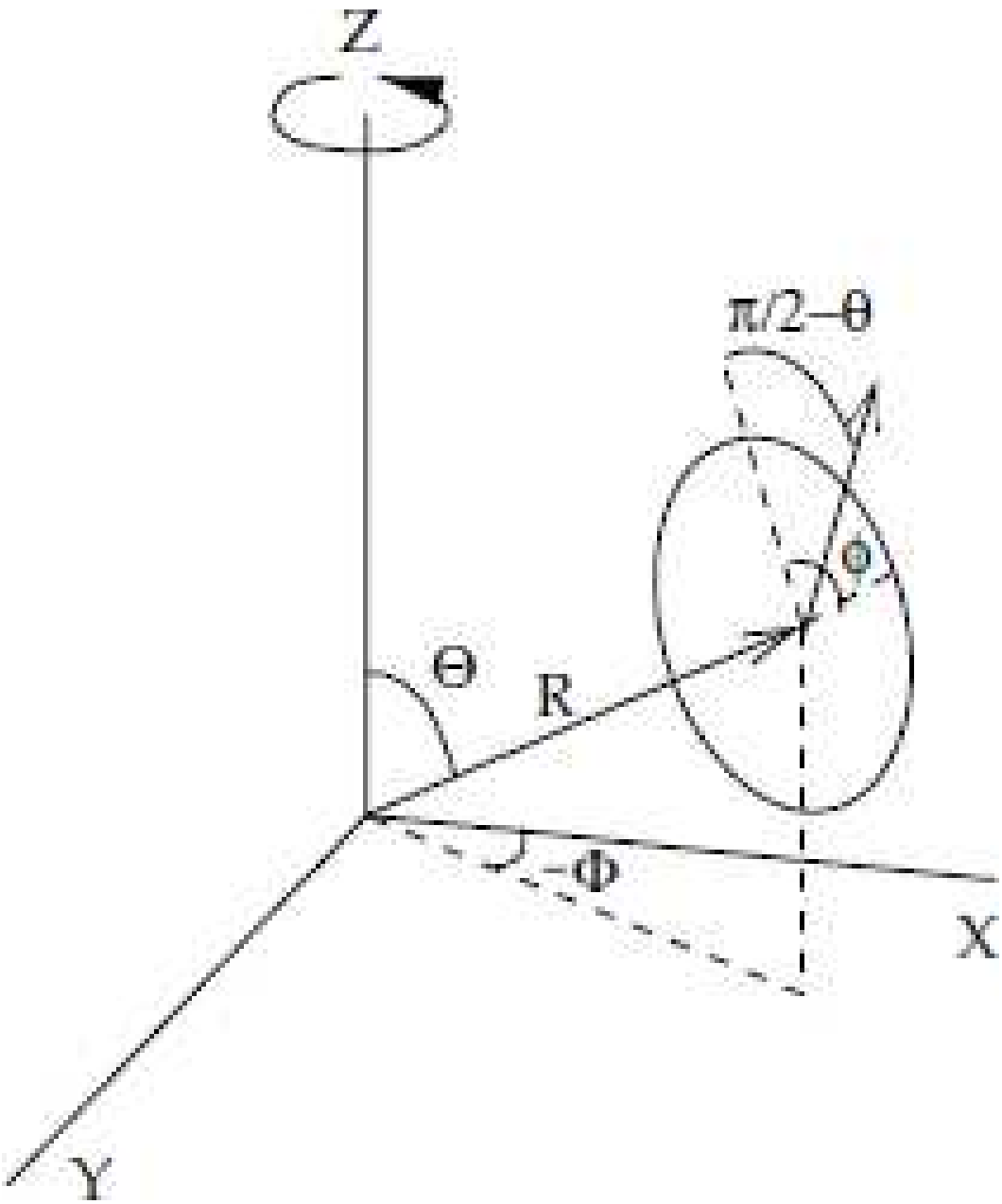

Figure C.1: Spherical coordinate system used to describe the 2-D radiation field, taken from Dullemond & Turolla (2000). The Φ angle is not considered here.

To outline the solid angle terms in Equation C.3, the spherical coordinate system from Dullemond & Turolla (2000) is adopted, and is shown in Figure C.1. Briefly, the radiation field consists of a set of spatial coordinates (R, Θ) and ray direction coordinates (μ, ϕ). $R \equiv (X^2 + Y^2)^{1/2}$, and Θ is the angle from the z-axis such that $\Theta = \tan^{-1}(X/Z)$. The ϕ angle is defined in such a way that $\phi = 0$ is parallel to the midplane of the disk ($Z = 0$, $\Theta = \pi/2$). The θ angle is gauged such that $\theta = \pi/2$ points in the outward-pointing R direction. A hypothetical angle, μ, is then defined as $\cos\theta$. Thus, the specific intensity is labelled as $I_\nu(R, \Theta; \mu, \phi)$.

The total specific intensity, I_ν, consists of three components:

$$I_\nu = I_\nu^* + I_\nu^{\rm vis} + I_\nu^{\rm th}, \tag{C.4}$$

where I_ν^* and $I_\nu^{\rm vis}$ represent, respectively, the specific intensity of radiation from the stellar source, and the viscous dissipation process at the midplane of the disk. The third term represents the specific intensity of thermal dust grain emission (Efstathiou & Rowan-Robinson 1990; Nomura 2002). Radiative scattering is neglected in this model for simplicity. Each of the intensity components are expressed as a function of the specific optical depth, $\tau_\nu(R, \Theta)$ and source temperature, T:

$$I_\nu^*(R, \Theta; \mu, \phi) = B_\nu(T_*) \exp\left[-\tau_\nu(R, \Theta)\right], \tag{C.5}$$

for the stellar source, and:

$$I_\nu^{\rm vis}(R, \Theta; \mu, \phi) = B_\nu[T_{\rm vis}(R)] \exp\left[-\tau_\nu(R, \Theta)\right], \tag{C.6}$$

for the specific intensity due to viscous dissipation from the midplane, which satisfies the boundary condition:

$$I_\nu^{\rm vis}(R) \begin{cases} > 0 & \text{for } Z{=}0, \theta{=}\frac{\pi}{2} \\ = 0 & \text{otherwise,} \end{cases} \tag{C.7}$$

and finally:

$$I_\nu^{\rm th}(R, \Theta; \mu, \phi) = \int_0^s \kappa_\nu(R', \Theta')\rho(R', \Theta') \times B_\nu[T(R', \Theta')] \exp\left[-\tau_\nu(R', \Theta')\right] ds', \tag{C.8}$$

where:

$$\tau_\nu(R,\Theta) = \int_0^s = \kappa_\nu(R',\Theta')\rho(R',\Theta')\, ds', \tag{C.9}$$

for the specific intensity from hypothetical dust grains where $I^{\rm th}$ is integrated along the ray s from the radiation source (R', Θ') to a point in the disk (μ, θ).

Each of the terms are derived from the radiative transfer equation:

$$\frac{dI_\nu}{ds} = \rho\kappa_\nu(S_\nu - I_\nu), \tag{C.10}$$

where the source functions $S_\nu{}^* = S_\nu{}^{\rm vis} = 0$, and $S^{\rm th} = B_\nu$. Equations (B.5), (B.6) and (B.8) are solved via a short-characteristics method outlined in Appendix A2 of Nomura (2002). Equation (B.1) is solved via the iterative method discussed in Appendix A1 of Nomura (2002) which, together with the hydrostatic equation:

$$\frac{dP}{dZ} = c_s^2\frac{d\rho}{dZ} = -\rho g_Z, \tag{C.11}$$

is used to solve the density distribution via a fourth-order Runge-Kutta method. Then by solving with Equations (B.5) – (B.9) self-consistently, one finally arrives with the temperature distribution of the disk (see Nomura (2002) for details).

APPENDIX D

Initial abundances

Table D.1 lists the initial abundances of the entire gas-phase reduced chemical network, and grain and deuterated species. All abundances are relative to H_2. They are taken from the output of a dense-core model run at a temperature of 10 K (see Markwick-Kemper (2005) for details). They are ordered from highest to lowest abundance. Note that AE-B means $A \times 10^{-B}$, and that GX represents a species X frozen on to a grain.

Table D.1: Full list of initial abundances in this model relative to H_2.

Species	Abundance	Species	Abundance	Species	Abundance
H2	1.00E+00	NH3	4.55E-09	C3H4	5.05E-11
He	1.40E-01	GSO2	4.16E-09	C2S	4.85E-11
GH2O	2.43E-03	C3H	2.90E-09	C3S	4.74E-11
CO	6.78E-05	NH2	1.14E-09	DC3N	3.22E-11
H2O	2.36E-05	GHCN	1.07E-09	CH2D2	2.65E-11
HD	1.60E-05	CH3D	9.57E-10	H	2.50E-11
N2	9.29E-06	CH3OH	9.36E-10	HCO	1.70E-11
GH2	3.07E-06	C3H3	9.34E-10	HDCS	1.63E-11
D2	1.69E-06	GD2O	7.66E-10	NS	1.48E-11
HCN	1.65E-06	GC3N	5.79E-10	GC3H	1.32E-11
GHDO	1.08E-06	GCH3CN	5.48E-10	C2H3	1.29E-11
HNC	9.12E-07	GNH3	4.86E-10	GH2CO	1.24E-11
C4H2	3.57E-07	CH2	3.83E-10	GC4HD	1.10E-11
CO2	2.30E-07	C4H	2.79E-10	C3H2	1.05E-11
HC3N	1.43E-07	HCS	2.48E-10	GD2	1.04E-11
CH4	1.35E-07	CS	2.47E-10	O2	9.61E-12
CH3CN	1.20E-07	GHNC	2.30E-10	C2HD	9.48E-12
GFe	8.80E-08	DNC	2.23E-10	D2O	7.45E-12
OCS	7.64E-08	O	2.05E-10	HCNH+	7.39E-12
GCO	4.07E-08	C4HD	1.92E-10	GCH4	6.97E-12
C3N	2.22E-08	CH2DCN	1.55E-10	GC4H	6.01E-12
GC4H2	2.04E-08	GC2H2	1.47E-10	C	5.99E-12
C2H2	1.95E-08	S	1.39E-10	C2H	5.83E-12
H2CO	1.92E-08	DCN	1.35E-10	GCH3OD	4.39E-12
H2CS	1.39E-08	GN2	1.31E-10	HDCO	3.96E-12
HDO	1.05E-08	SO	1.03E-10	H2S	3.72E-12
Fe	1.00E-08	GHD	7.74E-11	GC3S	3.70E-12
GHC3N	9.90E-09	NO	7.25E-11	GC3H3	3.53E-12
GCH3OH	9.64E-09	NH	7.10E-11	GCH2DOH	3.24E-12
SO2	8.78E-09	CH3	7.06E-11	GDC3N	2.23E-12
GOCS	5.97E-09	N	6.76E-11	C2	2.00E-12
CH2CO	5.50E-09	GCH2CO	6.61E-11	CHD3	1.95E-12
GCO2	5.36E-09	GH2CS	5.88E-11	CHDCO	1.76E-12

Table D.1 (continued): Full list of initial abundances in this model relative to H_2.

Species	Abundance	Species	Abundance	Species	Abundance
NH2D	1.66E-12	GCH3D	4.95E-14	C3H4+	2.52E-15
NH4+	9.76E-13	C3H3D	4.76E-14	DCO	2.29E-15
H2C3N+	9.18E-13	H3CO+	3.42E-14	C3HD	2.14E-15
H4C2N+	8.22E-13	GNH2	2.69E-14	H3+	1.90E-15
C3D	7.11E-13	GC3H2	2.59E-14	HCND+	1.82E-15
GCH2DCN	7.06E-13	C3H3+	2.55E-14	C+	1.76E-15
GC2S	5.40E-13	GNS	2.40E-14	GC4D	1.60E-15
GC3H4	5.00E-13	GCHDCO	2.11E-14	D	1.57E-15
NHD	4.35E-13	CH3CN+	1.64E-14	HDS	1.46E-15
CH3OD	4.26E-13	DCS	1.62E-14	C2D	1.43E-15
C3O	4.10E-13	CH3CO+	1.41E-14	H3DC2N+	1.43E-15
GHCS	4.03E-13	HOCS+	1.40E-14	GCH2D2	1.37E-15
GCS	4.00E-13	ND	1.35E-14	GN	1.30E-15
CH2DOH	3.15E-13	GCH2	1.29E-14	GC2H	1.22E-15
C3H2D	2.91E-13	OCS+	9.38E-15	GCH2DOD	1.21E-15
HS	2.82E-13	GC2H3	8.38E-15	GC3H2D	1.09E-15
OH	2.00E-13	GS	7.75E-15	DCNH+	1.04E-15
GNH2D	1.77E-13	GNO	6.03E-15	GCN	1.03E-15
CNC+	1.68E-13	Fe+	5.86E-15	CCN+	9.47E-16
GSO	1.66E-13	NHD2	5.54E-15	GO2	7.97E-16
C3	9.22E-14	GC3O	4.93E-15	SO+	7.40E-16
GDCN	8.75E-14	GCH3	4.90E-15	GCHD2OH	7.31E-16
CH2D	8.20E-14	HCS+	4.84E-15	CH2CO+	7.26E-16
CD4	7.88E-14	GHCO	4.31E-15	GNH	6.97E-16
D2CS	7.49E-14	HCO+	4.12E-15	GNHD2	5.91E-16
C4D	7.41E-14	GO	3.93E-15	NH3D+	5.41E-16
GC2HD	7.15E-14	CH3OH2+	3.35E-15	HDC3N+	5.38E-16
GHDCS	6.91E-14	GC3D	3.26E-15	He+	5.18E-16
CN	6.82E-14	H3CS+	2.99E-15	GC3H3D	4.71E-16
H3O+	6.36E-14	GH2S	2.81E-15	ND2	3.34E-16
GDNC	5.65E-14	C2H2D	2.70E-15	GD2CS	3.16E-16
C4H2+	5.62E-14	C2H4+	2.63E-15	D2CO	3.10E-16
CHD	5.26E-14	GHDCO	2.57E-15	N2H+	2.68E-16

Table D.1 (continued): Full list of initial abundances in this model relative to H_2.

Species	Abundance	Species	Abundance	Species	Abundance
H2NC+	2.33E-16	NH3+	1.19E-17	CH2DOH+	2.39E-20
C3H5+	2.26E-16	CH5+	1.18E-17	HD2CS+	2.34E-20
HC3S+	1.68E-16	CH2DCO+	1.11E-17	HC2O+	2.21E-20
GC2	1.66E-16	O2+	1.07E-17	N+	1.71E-20
H2CS+	1.59E-16	GNHD	1.03E-17	GDS	9.32E-21
GC3	1.55E-16	HCO2+	8.83E-18	HD2+	9.22E-21
CH3+	1.50E-16	C3H2D+	7.72E-18	H2S2+	8.96E-21
C4	1.23E-16	GCH2D	5.70E-18	HCN+	8.07E-21
GC	1.17E-16	NO+	5.41E-18	GCHD2	8.02E-21
CH2DOD	1.17E-16	GC3HD	5.30E-18	GND2	7.79E-21
HC2S+	1.16E-16	GCD3OH	5.06E-18	OH+	7.02E-21
CHD2	1.16E-16	H2DCS+	4.63E-18	NH+	6.69E-21
H+	1.14E-16	CD3	4.32E-18	C3O+	6.19E-21
GCHD3	1.01E-16	GCD4	4.07E-18	GD	5.43E-21
GH	9.17E-17	DOCS+	3.95E-18	NH2D+	4.65E-21
S+	7.37E-17	C3S+	3.32E-18	DSO+	4.18E-21
CHD2OH	7.09E-17	CH3OHD+	3.09E-18	DC3O+	4.01E-21
CH3OH+	7.03E-17	HNS+	3.01E-18	C2HD+	3.67E-21
GHS	6.89E-17	H3S+	2.56E-18	GOD	3.45E-21
H4C4N+	6.03E-17	C3H3D+	2.18E-18	CD	3.42E-21
C2H3+	5.35E-17	C3H2+	1.95E-18	CN+	3.12E-21
H2DO+	4.99E-17	GC2H2D	1.75E-18	N2+	3.08E-21
CH	4.06E-17	GCHD	1.71E-18	C2O+	3.08E-21
C2H2+	3.85E-17	H2D+	1.61E-18	DCO2+	2.47E-21
DS	3.83E-17	NH2D2+	1.54E-18	GCD3OD	1.94E-21
OD	2.79E-17	C3H+	1.43E-18	HD2CO+	1.93E-21
C4HD+	2.68E-17	CH2DOH2+	1.14E-18	CH4+	1.62E-21
GDCS	2.62E-17	DCO+	1.13E-18	H2DS+	1.51E-21
GOH	2.25E-17	HC3N+	1.11E-18	CH2+	1.43E-21
CH2DCN+	2.14E-17	GHDS	1.10E-18	C4H+	1.32E-21
HC3O+	1.78E-17	GC4	1.00E-18	C4+	1.27E-21
HSO+	1.48E-17	ND3	9.57E-19	C3HD+	1.20E-21
H2DCO+	1.38E-17	HS+	9.17E-19	CS+	1.05E-21

Table D.1 (continued): Full list of initial abundances in this model relative to H_2.

Species	Abundance	Species	Abundance	Species	Abundance
CO+	9.75E-22	CH3D+	1.14E-23	CD2+	6.00E-27
CH+	9.42E-22	D3+	9.49E-24	CHD2OD+	2.04E-27
CH3D2+	9.12E-22	DC2O+	9.33E-24	CD3OHD+	1.23E-27
SO2+	9.08E-22	GCD	9.17E-24	CD3+	9.22E-28
CH2DOHD+	8.65E-22	C3HDO+	9.05E-24	ND3+	6.61E-28
DNS+	8.51E-22	CH2DOD+	9.04E-24	D3S+	5.05E-29
D2CS+	7.76E-22	HDS+	5.56E-24	CHD2OD2+	2.98E-29
CH3OD2+	6.86E-22	CHD2OH+	5.47E-24	CD3OD+	1.49E-29
C2H+	5.58E-22	HDS2+	3.54E-24	S2	2.94E-31
NHD3+	5.25E-22	CHD2+	2.99E-24	CD3OD2+	1.07E-31
C3+	4.44E-22	CHD4+	2.40E-24	GS2	4.77E-34
C3N+	3.67E-22	D2+	1.83E-24		
H2DC3O+	3.37E-22	NHD+	1.60E-24		
D3CS+	3.16E-22	CD3OH2+	1.58E-24		
C3D+	3.14E-22	OD+	1.54E-24		
GCD3	2.98E-22	HD2S+	6.19E-25		
DC3N+	2.74E-22	CHD+	4.79E-25		
GD2S	2.71E-22	DCN+	4.32E-25		
CHD2OH2+	2.53E-22	ND4+	3.51E-25		
D+	2.07E-22	CH2D2+	3.15E-25		
CD3OD	1.88E-22	ND+	2.05E-25		
C2+	1.54E-22	C4D+	1.96E-25		
C7+	1.54E-22	CHDOHD+	1.88E-25		
HDCO+	1.39E-22	CH2DOD2+	1.69E-25		
DSO2+	1.25E-22	C2D+	1.08E-25		
D2NC+	9.72E-23	C2S+	1.08E-25		
CH2D3+	5.92E-23	D3CO+	1.07E-25		
O+	4.95E-23	CD+	7.90E-26		
CO2+	3.04E-23	D2S+	6.10E-26		
HDO+	2.27E-23	CD3OH+	3.84E-26		
NHD2+	1.49E-23	ND2+	3.58E-26		
DS+	1.41E-23	D2O+	2.44E-26		
HD+	1.37E-23	D2CO+	1.09E-26		

APPENDIX E

Isotropic attenuation of cosmic-rays

Cosmic-rays have previously been modelled entering a PPD vertically from one plane, i.e. a plane-parallel treatment. In reality however, cosmic-rays will enter isotropically (i.e. from all directions). Therefore, their attenuation must be modelled accordingly.

One such method was discussed in Umebayashi & Nakano (2009). In this Appendix, some of the important steps and assumptions are highlighted. Briefly, if one adopts the cylindrical coordinates (r, ϕ, z), then the column density, $\chi(r, \phi, z; \theta, z)$ can be defined from the disk surface to a point (r, θ, z) along a line in the direction (θ, ψ), where θ is the angle from the z-axis, and ψ is the projected angle on the (r,ψ) plane from the radial direction r. Therefore:

$$\chi(r, \phi, z; \theta, \psi) = \int_z^\infty \rho(r', \phi', z') \sec\theta dz'. \tag{E.1}$$

Here, ρ is the disk density, and r' and ϕ' represent the r and ϕ coordinates respectively at a height z' on the line. They are approximately given by:

$$r' \approx r + (z' - z)\tan\theta\cos\psi, \tag{E.2}$$

and

$$\phi' \approx \phi + \frac{z' - z}{r}\tan\theta\sin\psi, \tag{E.3}$$

presuming that $|z'\text{-}z| \,/\, r \times \tan\theta << 1$. Since most of the attenuating disk matter resides at the midplane (i.e. $|z| \,/\, r << 1$), then a significant portion of the flux comes from $\theta \neq 0$:

$$\chi(r,\phi,z;\theta,\psi) \approx \sec\theta \int_z^\infty \Bigg[\rho(r,\phi,z') + \frac{\partial\rho(r,\phi,z')}{\partial r}(z' - z) \times \tan\theta\cos\psi + \frac{\partial\rho(r,\theta,z')}{\partial}\frac{z' - z}{r}\tan\theta\sin\psi\Bigg]dz'. \tag{E.4}$$

For the remaining $\theta = 0$ flux, the column density in the z direction is:

$$\chi(r,\phi,z) \equiv \chi(r,\phi,z;\theta = 0,\psi) = \int_z^\infty \rho(r,\phi,z')dz'. \tag{E.5}$$

The cosmic-ray ionization rate at (r,ϕ,z) is then:

$$\zeta_{\rm CR}(r,\phi,z) = \frac{\zeta^0_{\rm CR}}{4\pi}\int_{\psi=0}^{2\pi}\int_{\theta=0}^{\pi/2}\exp\left(-\frac{\chi(r,\phi,z;\theta,\psi)}{\lambda_{\rm CR}}\right)\times\sin\theta d\theta d\psi. \tag{E.6}$$

Here, $\zeta^0_{\rm CR}$ is the unattenuated interstellar cosmic-ray ionization rate, usually set to 1.3×10^{-17} s^{-1}, and $\lambda_{\rm CR}$ is the characteristic attenuation length of cosmic-rays, equal to 96 g cm^{-2}. Noting that the second and third terms in Equation (E.4) are negligible (see Umebayashi & Nakano 2009), then substituting Equation (E.4) into (E.6) gives:

$$\zeta_{\rm CR}(r,\phi,z) \approx \frac{\zeta^0_{\rm CR}}{2}\int_0^{\pi/2}\exp\left(-\frac{\chi(r,\phi,z)}{\lambda_{\rm CR}}\sec\theta\right)\sin\theta d\theta. \tag{E.7}$$

By expanding $\sec\theta$ and $\sin\theta$ terms in a power series, separate high and low column density expressions emerge. For the high column density limit ($\chi(r,\phi,z)/\lambda_{\rm CR} >> 1$):

$$\zeta_{\rm CR}(r,\phi,z) \approx \frac{\zeta^0_{\rm CR}}{2}\exp\left(-\frac{\chi(r,\phi,z)}{\lambda_{\rm CR}}\right)\frac{\lambda_{\rm CR}}{\chi(r,\phi,z)}. \tag{E.8}$$

For the low column density limit ($\chi(r,\phi,z)/\lambda_{\rm CR} << 1$):

$$\zeta_{\rm CR}(r,\phi,z) \approx \frac{\zeta^0_{\rm CR}}{2}\exp\left(-\frac{\chi(r,\phi,z)}{\lambda_{\rm CR}}\right). \tag{E.9}$$

Umebayashi & Nakano (2009) adopt an empirical formula for Equation (E.7), which satisfies the asymptotic limits of Equations (E.8) and (E.9):

$$\zeta_{\rm CR}(r,\phi,z) \approx \frac{\zeta^0_{\rm CR}}{2}\exp\left(-\frac{\chi(r,\phi,z)}{\lambda_{\rm CR}}\right)\times\left[1+\left(\frac{\chi(r,\phi,z)}{\lambda_{\rm CR}}\right)^{\gamma}\right]^{-1/\gamma}. \tag{E.10}$$

Figure 4 in Umebayashi & Nakano (2009) presents the results of the numerical integration process. They determine the power-law value, $\gamma = 3/4$.

Finally assuming that cosmic-rays additionally penetrate from the other side of the disk, the full expression expands to:

$$\begin{aligned}\zeta_{\rm CR}(r,z) \;&\approx\; \frac{\zeta^0_{\rm CR}}{2}\left\{\exp\left(-\frac{\chi(r,z)}{\lambda_{\rm CR}}\right)\right\}\left[1+\left(\frac{\chi(r,z)}{\lambda_{\rm CR}}\right)^{3/4}\right]^{-4/3} \\ &+\; \exp\left(-\frac{\Sigma(r)-\chi(r,z)}{\lambda_{\rm CR}}\right)\times\left[1+\left(\frac{\Sigma(r)-\chi(r,z)}{\lambda_{\rm CR}}\right)^{3/4}\right]^{-4/3} \quad {\rm s}^{-1}, \end{aligned} \tag{E.11}$$

where $\zeta_{\rm CR}(r,z)$ is additionally a function of the surface density, $\Sigma(r)$.

References

Adams, F. C., Lada, C. J., & Shu, F. H. 1987, ApJ, 312, 788

Adams, F. C., Lada, C. J., & Shu, F. H. 1988, ApJ, 326, 865

Adams, F. C. & Shu, F. H. 1985, ApJ, 296, 655

Agúndez, M., Cernicharo, J., & Goicoechea, J. R. 2008, A&A, 483, 831

Aikawa, Y. & Herbst, E. 1999, A&A, 351, 233

Aikawa, Y., Momose, M., Thi, W., et al. 2003, PASJ, 55, 11

Aikawa, Y., Ohashi, N., Inutsuka, S.-i., Herbst, E., & Takakuwa, S. 2001, ApJ, 552, 639

Aikawa, Y., van Zadelhoff, G. J., van Dishoeck, E. F., & Herbst, E. 2002, A&A, 386, 622

Allen, M. & Robinson, G. W. 1977, ApJ, 212, 396

Amelin, Y., Krot, A. N., Hutcheon, I. D., & Ulyanov, A. A. 2002, Science, 297, 1678

Bai, X.-N. 2011, ApJ, 739, 50

Bai, X.-N. & Goodman, J. 2009, ApJ, 701, 737

Balbus, S. A. & Hawley, J. F. 1991, ApJ, 376, 214

Bates, D. R. & Spitzer, Jr., L. 1951, ApJ, 113, 441

Bell, K. R. & Lin, D. N. C. 1994, ApJ, 427, 987

Ben Jaffel, L., Vidal-Madjar, A., Gladstone, G. R., et al. 1998, in Astronomical Society of the Pacific Conference Series, Vol. 143, The Scientific Impact of the Goddard High Resolution Spectrograph, ed. J. C. Brandt, T. B. Ake, & C. C. Petersen, 366

Bergin, E. A. 2009, ArXiv e-prints

Bergin, E. A., Aikawa, Y., Blake, G. A., & van Dishoeck, E. F. 2007, in Protostars and Planets V, ed. B. Reipurth, D. Jewitt, & K. Keil, 751–766

Bergin, E. A., Alves, J., Huard, T., & Lada, C. J. 2002, ApJL, 570, L101

Boogert, A. C. A., Pontoppidan, K. M., Knez, C., et al. 2008, ApJ, 678, 985

Boss, A. P. 2012, Annual Review of Earth and Planetary Sciences, 40, 23

Boss, A. P. & Keiser, S. A. 2010, ApJL, 717, L1

Boss, A. P. & Keiser, S. A. 2012, ApJL, 756, L9

Bottinelli, S., Boogert, A. C. A., van Dishoeck, E. F., et al. 2008, in IAU Symposium, Vol. 251, IAU Symposium, ed. S. Kwok & S. Sandford, 105–110

Brauer, F., Dullemond, C. P., & Henning, T. 2008a, A&A, 480, 859

Brauer, F., Henning, T., & Dullemond, C. P. 2008b, A&A, 487, L1

Bringa, E. M. & Johnson, R. E. 2004, ApJ, 603, 159

Brown, W. A. & Bolina, A. S. 2007, MNRAS, 374, 1006

Brunken, S., Muller, H. S. P., Lewen, F., & Winnewisser, G. 2003, Phys. Chem. Chem. Phys., 5, 1515

Burke, J. R. & Hollenbach, D. J. 1983, ApJ, 265, 223

Carr, J. S. & Najita, J. R. 2008, Science, 319, 1504

Carr, J. S. & Najita, J. R. 2011, ApJ, 733, 102

Carr, J. S., Tokunaga, A. T., & Najita, J. 2004, ApJ, 603, 213

Cecchi-Pestellini, C. & Aiello, S. 1992, MNRAS, 258, 125

Charnley, S. B., Kuan, Y., Chuang, Y., & Milam, S. N. 2010, LPI Contributions, 1538, 5587

Chiang, E. & Murray-Clay, R. 2007, Nature Physics, 3, 604

Chiang, E. I. & Goldreich, P. 1997, ApJ, 490, 368

Clarke, C. J., Gendrin, A., & Sotomayor, M. 2001, MNRAS, 328, 485

Cohen, M. 1983, ApJL, 270, L69

Collins, II, G. W. 1978, The virial theorem in stellar astrophysics

Cowie, L. L. & Songaila, A. 1986, ARA&A, 24, 499

D'Alessio, P., Calvet, N., Hartmann, L., Lizano, S., & Cantó, J. 1999, ApJ, 527, 893

D'Alessio, P., Canto, J., Calvet, N., & Lizano, S. 1998, ApJ, 500, 411

Desch, S. J. 2007, ApJ, 671, 878

Desch, S. J. & Mouschovias, T. C. 2001, ApJ, 550, 314

Dickman, R. L. 1978, ApJS, 37, 407

Diehl, R., Halloin, H., Kretschmer, K., et al. 2006, Nature, 439, 45

Diehl, R., Lang, M., Kretschmer, K., & Wang, W. 2008, , 52, 440

Dominik, C. & Dullemond, C. P. 2011, A&A, 531, A101

Dullemond, C. P., Brauer, F., Henning, T., & Natta, A. 2008, Physica Scripta Volume T, 130, 014015

Dullemond, C. P. & Monnier, J. D. 2010, ARA&A, 48, 205

Dullemond, C. P. & Turolla, R. 2000, A&A, 360, 1187

Duschl, W. J., Gail, H.-P., & Tscharnuter, W. M. 1996, A&A, 312, 624

Dutrey, A., Guilloteau, S., & Guelin, M. 1997a, A&A, 317, L55

Dutrey, A., Guilloteau, S., & Guelin, M. 1997b, A&A, 317, L55

Dutrey, A., Guilloteau, S., & Simon, M. 1994, A&A, 286, 149

Dutrey, A., Henning, T., Guilloteau, S., et al. 2007, A&A, 464, 615

Dzyurkevich, N., Flock, M., Turner, N. J., Klahr, H., & Henning, T. 2010, A&A, 515, A70

Efstathiou, A. & Rowan-Robinson, M. 1990, MNRAS, 245, 275

Ellinger, C. I., Young, P. A., & Desch, S. J. 2010, ApJ, 725, 1495

Evans, II, N. J. 1999, ARA&A, 37, 311

Ewen, H. I. & Purcell, E. M. 1951, Nature, 168, 356

Finocchi, F. & Gail, H.-P. 1997, A&A, 327, 825

Fitoussi, C., Duprat, J., Tatischeff, V., et al. 2008, Phys. Rev. C, 78, 044613

Fogel, J. K. J., Bethell, T. J., Bergin, E. A., Calvet, N., & Semenov, D. 2011, ApJ, 726, 29

Friedjung, M. 1985, A&A, 146, 366

Fromang, S., Terquem, C., & Balbus, S. A. 2002a, MNRAS, 329, 18

Fromang, S., Terquem, C., & Balbus, S. A. 2002b, MNRAS, 329, 18

Gammie, C. F. 1996, ApJ, 457, 355

Gaustad, J. E. 1963, ApJ, 138, 1050

Gibb, E. L., Bonev, B. P., Villanueva, G., et al. 2012, ApJ, 750, 102

Gibb, E. L., Whittet, D. C. B., Boogert, A. C. A., & Tielens, A. G. G. M. 2004, ApJS, 151, 35

Gilmour, J. & Middleton, C. 2009, Icarus, 201, 821

Gilmour, J. D. & Middleton, C. A. 2008, in Lunar and Planetary Institute Conference Abstracts, Vol. 39, Lunar and Planetary Institute Conference Abstracts, 1970–+

Girart, J. M., Rao, R., & Marrone, D. P. 2006, Science, 313, 812

Glassgold, A. E., Lucas, R., & Omont, A. 1986, A&A, 157, 35

Goldsmith, P. F. & Langer, W. D. 1978, ApJ, 222, 881

Gómez, J. F. & D'Alessio, P. 2000, ApJ, 535, 943

Gounelle, M. 2006, New Astronomy Review, 50, 596

Gounelle, M. & Meibom, A. 2007, ApJL, 664, L123

Guilloteau, S. & Dutrey, A. 1994, A&A, 291, L23

Hartmann, L. 2005, in Astronomical Society of the Pacific Conference Series, Vol. 341, Chondrites and the Protoplanetary Disk, ed. A. N. Krot, E. R. D. Scott, & B. Reipurth, 131–+

Hartmann, L., Ballesteros-Paredes, J., & Bergin, E. A. 2001, ApJ, 562, 852

Hartmann, L., Calvet, N., Gullbring, E., & D'Alessio, P. 1998, ApJ, 495, 385

Hartmann, L., D'Alessio, P., Calvet, N., & Muzerolle, J. 2006, ApJ, 648, 484

Hartmann, L. & Kenyon, S. J. 1996, ARA&A, 34, 207

Hasegawa, T. I. & Herbst, E. 1993, MNRAS, 261, 83

Hasegawa, T. I., Herbst, E., & Leung, C. M. 1992, ApJS, 82, 167

Hawley, J. F. & Balbus, S. A. 1991, ApJ, 376, 223

Hawley, J. F. & Stone, J. M. 1998, ApJ, 501, 758

Hayashi, C. 1961, PASJ, 13, 450

Hayashi, C. 1981, Progress of Theoretical Physics Supplement, 70, 35

Heinzeller, D., Nomura, H., Walsh, C., & Millar, T. J. 2011, ApJ, 731, 115

Herbst, E. & Klemperer, W. 1973, ApJ, 185, 505

Herrero, V. J., Gálvez, Ó., Maté, B., & Escribano, R. 2010, Physical Chemistry Chemical Physics (Incorporating Faraday Transactions), 12, 3164

Hewins, R. H. & Newsom, H. E. 1988, Igneous activity in the early solar system, ed. J. F. Kerridge & M. S. Matthews, 73–101

Hollenbach, D. & Salpeter, E. E. 1971, ApJ, 163, 155

Hueso, R. & Guillot, T. 2005, A&A, 442, 703

Huss, G. R. & Meyer, B. S. 2009, in Lunar and Planetary Inst. Technical Report, Vol. 40, Lunar and Planetary Institute Science Conference Abstracts, 1957

Hutsemékers, D., Manfroid, J., Jehin, E., Zucconi, J.-M., & Arpigny, C. 2008, A&A, 490, L31

Igea, J. & Glassgold, A. E. 1999, ApJ, 518, 848

Ilgner, M. 2012, A&A, 538, A124

Ilgner, M., Henning, T., Markwick, A. J., & Millar, T. J. 2004, A&A, 415, 643

Ilgner, M. & Nelson, R. P. 2006a, A&A, 445, 205

Ilgner, M. & Nelson, R. P. 2006b, A&A, 445, 223

Ilgner, M. & Nelson, R. P. 2006c, A&A, 455, 731

Ilgner, M. & Nelson, R. P. 2008, A&A, 483, 815

Jones, M. G., Pringle, J. E., & Alexander, R. D. 2012, MNRAS, 419, 925

Kastner, J. H., Zuckerman, B., Weintraub, D. A., & Forveille, T. 1997, Science, 277, 67

Keene, J. & Masson, C. R. 1990, ApJ, 355, 635

Kenyon, S. J. & Hartmann, L. 1987, ApJ, 323, 714

Kessler, J. E., Qi, C., & Blake, G. A. 2002, in Bulletin of the American Astronom-

ical Society, Vol. 34, American Astronomical Society Meeting Abstracts #200, 786

Khajenabi, F. 2012, Ap&SS, 337, 247

Klahr, H. 2004, ApJ, 606, 1070

Kobayashi, K., Kasamatsu, T., Kaneko, T., et al. 1995, Advances in Space Research, 16, 21

Koerner, D. W., Sargent, A. I., & Beckwith, S. V. W. 1993, , 106, 2

Lahuis, F., van Dishoeck, E. F., Boogert, A. C. A., et al. 2006a, ApJL, 636, L145

Lahuis, F., van Dishoeck, E. F., Boogert, A. C. A., et al. 2006b, ApJL, 636, L145

Larson, R. B. 1969, MNRAS, 145, 271

Larson, R. B. 2003, Reports on Progress in Physics, 66, 1651

Lay, O. P., Carlstrom, J. E., Hills, R. E., & Phillips, T. G. 1994, ApJL, 434, L75

Lee, T., Papanastassiou, D. A., & Wasserburg, G. J. 1977, ApJL, 211, L107

Leger, A., Jura, M., & Omont, A. 1985, A&A, 144, 147

Lellouch, E., Bézard, B., Fouchet, T., et al. 2001, A&A, 370, 610

Lepp, S. 1992, in IAU Symposium, Vol. 150, Astrochemistry of Cosmic Phenomena, ed. P. D. Singh, 471

Lewis, J. S., Barshay, S. S., & Noyes, B. 1979, , 37, 190

Lin, D. N. C. & Papaloizou, J. 1980, MNRAS, 191, 37

Linsky, J. L., Draine, B. T., Moos, H. W., et al. 2006, ApJ, 647, 1106

Lynden-Bell, D. & Pringle, J. E. 1974, MNRAS, 168, 603

MacPherson, G. J., Davis, A. M., & Zinner, E. K. 1995, Meteoritics, 30, 365

Mahoney, W. A., Ling, J. C., Jacobson, A. S., & Lingenfelter, R. E. 1982, ApJ, 262, 742

Markwick, A. J. & Charnley, S. B. 2004, Chemistry of Protoplanetary Disks (Astrobiology: Future Perspectives, by P.Ehrenfreund et al. Leiden Observatory, The Netherlands ASTROPHYSICS AND SPACE SCIENCE LIBRARY, Vol 305 Kluwer Academic Publishers, Dordrecht, p. 33), 33–+

Markwick, A. J., Ilgner, M., Millar, T. J., & Henning, T. 2002, A&A, 385, 632

Markwick-Kemper, A. J. 2005, in IAU Symposium, Vol. 231, Astrochemistry: Re-

cent Successes and Current Challenges, ed. D. C. Lis, G. A. Blake, & E. Herbst, 397–404

Matsumura, S., Pudritz, R. E., & Thommes, E. W. 2007, ApJ, 660, 1609

Meier, R., Owen, T. C., Jewitt, D. C., et al. 1998, Science, 279, 1707

Millar, T. J. 2005, in IAU Symposium, Vol. 231, Astrochemistry: Recent Successes and Current Challenges, ed. D. C. Lis, G. A. Blake, & E. Herbst, 77–86

Millar, T. J., Farquhar, P. R. A., & Willacy, K. 1997, A&AS, 121, 139

Millar, T. J., Nomura, H., & Markwick, A. J. 2003, Ap&SS, 285, 761

Miotello, A., Robberto, M., Potenza, M. A. C., & Ricci, L. 2012, ApJ, 757, 78

Moynier, F., Blichert-Toft, J., Wang, K., Herzog, G. F., & Albarede, F. 2011, ApJ, 741, 71

Mumma, M. J. & Charnley, S. B. 2011, ARA&A, 49, 471

Muzerolle, J., Calvet, N., Briceño, C., Hartmann, L., & Hillenbrand, L. 2000, ApJL, 535, L47

Najita, J., Carr, J. S., & Mathieu, R. D. 2003, ApJ, 589, 931

Najita, J. R., Crockett, N., & Carr, J. S. 2008, ApJ, 687, 1168

Nomura, H. 2002, ApJ, 567, 587

Nomura, H., Aikawa, Y., Nakagawa, Y., & Millar, T. J. 2009, A&A, 495, 183

Nomura, H., Aikawa, Y., Tsujimoto, M., Nakagawa, Y., & Millar, T. J. 2007, ApJ, 661, 334

Nomura, H. & Millar, T. J. 2004, A&A, 414, 409

Nomura, H. & Millar, T. J. 2005, A&A, 438, 923

Novak, R. E., Mumma, M. J., Villanueva, G., Bonev, B., & Disanti, M. 2007, LPI Contributions, 1353, 3283

Öberg, K. I., Boogert, A. C. A., Pontoppidan, K. M., et al. 2008a, in IAU Symposium, Vol. 251, IAU Symposium, ed. S. Kwok & S. Sandford, 127–128

Öberg, K. I., Boogert, A. C. A., Pontoppidan, K. M., et al. 2008b, ApJ, 678, 1032

Öberg, K. I., Qi, C., Wilner, D. J., & Hogerheijde, M. R. 2012, ApJ, 749, 162

Öberg, K. I., van Broekhuizen, F., Fraser, H. J., et al. 2005, ApJL, 621, L33

Ohishi, M. 2008, in IAU Symposium, Vol. 251, IAU Symposium, ed. S. Kwok &

S. Sandford, 17–26

Oka, A., Nakamoto, T., & Ida, S. 2011, ArXiv e-prints

Oppenheimer, M. & Dalgarno, A. 1974, ApJ, 192, 29

Penston, M. V. 1969, MNRAS, 144, 425

Perez-Becker, D. & Chiang, E. 2011, ApJ, 727, 2

Pestalozzi, M., Humphreys, E. M. L., & Booth, R. S. 2002, A&A, 384, L15

Petit, J.-M., Mousis, O., & Kavelaars, J. J. 2012, in EGU General Assembly Conference Abstracts, Vol. 14, EGU General Assembly Conference Abstracts, ed. A. Abbasi & N. Giesen, 9675

Phillips, A. C. 1994, The physics of stars

Piétu, V., Dutrey, A., & Guilloteau, S. 2007, A&A, 467, 163

Pineda, J. E., Maury, A. J., Fuller, G. A., et al. 2012, A&A, 544, L7

Podosek, F. A. & Swindle, T. D. 1988, Extinct radionuclides, ed. J. F. Kerridge & M. S. Matthews, 1093–1113

Pontoppidan, K. M., Boogert, A. C. A., Fraser, H. J., et al. 2008, ApJ, 678, 1005

Pontoppidan, K. M., Salyk, C., Blake, G. A., & Käufl, H. U. 2010a, ApJL, 722, L173

Pontoppidan, K. M., Salyk, C., Blake, G. A., et al. 2010b, ApJ, 720, 887

Pringle, J. E. 1981, ARA&A, 19, 137

Qi, C. 2001, PhD thesis, AA (California Institute Of Technology)

Qi, C., Wilner, D. J., Aikawa, Y., Blake, G. A., & Hogerheijde, M. R. 2008, ApJ, 681, 1396

Qi, C., Wilner, D. J., Calvet, N., et al. 2006, ApJL, 636, L157

Rank, D. M., Townes, C. H., & Welch, W. J. 1971, Science, 174, 1083

Rawlings, J. M. C., Hartquist, T. W., Menten, K. M., & Williams, D. A. 1992, MNRAS, 255, 471

Roberts, H., Fuller, G. A., Millar, T. J., Hatchell, J., & Buckle, J. V. 2002a, A&A, 381, 1026

Roberts, H., Herbst, E., & Millar, T. J. 2002b, MNRAS, 336, 283

Roberts, H. & Millar, T. J. 2000a, A&A, 364, 780

Roberts, H. & Millar, T. J. 2000b, A&A, 361, 388

Rodgers, S. D. & Charnley, S. B. 2003, ApJ, 585, 355

Ruffle, D. P. & Herbst, E. 2000, MNRAS, 319, 837

Rydgren, A. E. & Zak, D. S. 1987, PASP, 99, 141

Salyk, C. 2011, in IAU Symposium, Vol. 280, IAU Symposium

Salyk, C., Pontoppidan, K. M., Blake, G. A., et al. 2008, ApJL, 676, L49

Salyk, C., Pontoppidan, K. M., Blake, G. A., Najita, J. R., & Carr, J. S. 2011, ApJ, 731, 130

Sandford, S. A. & Allamandola, L. J. 1993, ApJ, 417, 815

Sano, T., Miyama, S. M., Umebayashi, T., & Nakano, T. 2000, ApJ, 543, 486

Sano, T. & Stone, J. M. 2002, ApJ, 577, 534

Semenov, D., Hersant, F., Wakelam, V., et al. 2010, A&A, 522, A42

Semenov, D. & Wiebe, D. 2011, ApJS, 196, 25

Semenov, D., Wiebe, D., & Henning, T. 2004, A&A, 417, 93

Semenov, D. A. 2011, in IAU Symposium, Vol. 280, IAU Symposium, 114–126

Shakura, N. I. & Sunyaev, R. A. 1973, A&A, 24, 337

Shalybkov, D. & Rüdiger, G. 2005, A&A, 438, 411

Shu, F. H. 1977, ApJ, 214, 488

Shu, F. H. 1982, The physical universe. an introduction to astronomy, ed. F. H. Shu

Shu, F. H., Adams, F. C., & Lizano, S. 1987, ARA&A, 25, 23

Simon, M., Dutrey, A., & Guilloteau, S. 2000, ApJ, 545, 1034

Simpson, J. P. 1975, A&A, 39, 43

Smith, I. W. M., Herbst, E., & Chang, Q. 2004, MNRAS, 350, 323

Solomon, P. M. & Klemperer, W. 1972, ApJ, 178, 389

Spitzer, L. 1968, Diffuse matter in space

Stepinski, T. F. 1992, in Lunar and Planetary Inst. Technical Report, Vol. 23, Lunar and Planetary Institute Science Conference Abstracts, 1359

Terebey, S., Shu, F. H., & Cassen, P. 1984, ApJ, 286, 529

Thi, W., van Zadelhoff, G., & van Dishoeck, E. F. 2004, A&A, 425, 955

Thi, W.-F., Woitke, P., & Kamp, I. 2010, MNRAS, 407, 232

Tielens, A. G. G. M. & Allamandola, L. J. 1987, in Astrophysics and Space Science Library, Vol. 134, Interstellar Processes, ed. D. J. Hollenbach & H. A. Thronson, Jr., 397–469

Tielens, A. G. G. M. & Hagen, W. 1982, A&A, 114, 245

Tscharnuter, W. M. & Gail, H.-P. 2007, A&A, 463, 369

Turner, N. J. & Sano, T. 2008, ApJL, 679, L131

Turner, N. J., Sano, T., & Dziourkevitch, N. 2007, ApJ, 659, 729

Umebayashi, T. & Nakano, T. 1980, PASJ, 32, 405

Umebayashi, T. & Nakano, T. 1981, PASJ, 33, 617

Umebayashi, T. & Nakano, T. 2009, ApJ, 690, 69

Urey, H. C. 1955, Proceedings of the National Academy of Science, 41, 127

van Dishoeck, E. F. 2009, Astrochemistry of Dense Protostellar and Protoplanetary Environments, ed. Thronson, H. A., Stiavelli, M., & Tielens, A., 187–+

van Dishoeck, E. F. & Black, J. H. 1986, ApJS, 62, 109

van Dishoeck, E. F. & Jørgensen, J. K. 2007, Astrophysics and Space Science, 313, 15

van Dishoeck, E. F., Thi, W.-F., & van Zadelhoff, G.-J. 2003, A&A, 400, L1

van Zadelhoff, G.-J. 2002, PhD thesis, , Leiden University, May 2002.

van Zadelhoff, G.-J., Aikawa, Y., Hogerheijde, M. R., & van Dishoeck, E. F. 2003, A&A, 397, 789

van Zadelhoff, G.-J., Dullemond, C. P., van der Tak, F. F. S., et al. 2002, A&A, 395, 373

van Zadelhoff, G.-J., van Dishoeck, E. F., Thi, W.-F., & Blake, G. A. 2001, A&A, 377, 566

Varnière, P., Bjorkman, J. E., Frank, A., et al. 2006, ApJL, 637, L125

Vasyunin, A. I., Wiebe, D. S., Birnstiel, T., et al. 2011, ApJ, 727, 76

Villanueva, G. L., Mumma, M. J., Novak, R. E., et al. 2011, in EPSC-DPS Joint Meeting 2011, 1506

Voshchinnikov, N. V., Semenov, D. A., & Henning, T. 1999, A&A, 349, L25

Wadhwa, M., Amelin, Y., Davis, A. M., et al. 2007, Protostars and Planets V, 835

Wakelam, V. 2009, in American Astronomical Society Meeting Abstracts, Vol. 214, American Astronomical Society Meeting Abstracts #214, 402.15

Walsh, C., Millar, T. J., & Nomura, H. 2010, ApJ, 722, 1607

Walsh, C., Millar, T. J., & Nomura, H. 2013, ApJL, 766, L23

Walsh, C., Nomura, H., Millar, T. J., & Aikawa, Y. 2012, ApJ, 747, 114

Wang, W., Lang, M. G., Diehl, R., et al. 2009, A&A, 496, 713

Wasserburg, G. J., Busso, M., Gallino, R., & Nollett, K. M. 2006, Nuclear Physics A, 777, 5

Watanabe, N., Nagaoka, A., Hidaka, H., et al. 2006, Planet. Space Sci., 54, 1107

Watson, W. D. 1976, Reviews of Modern Physics, 48, 513

Weinberger, A. J., Becklin, E. E., Schneider, G., et al. 2002, ApJ, 566, 409

Willacy, K., Klahr, H. H., Millar, T. J., & Henning, T. 1998, A&A, 338, 995

Willacy, K. & Woods, P. M. 2009, ApJ, 703, 479

Woodall, J., Agúndez, M., Markwick-Kemper, A. J., & Millar, T. J. 2007, A&A, 466, 1197

Woods, P. M. 2009, ArXiv e-prints

Woods, P. M. & Willacy, K. 2007, ApJL, 655, L49

Young, E. D., Simon, J. I., Galy, A., et al. 2005, Science, 308, 223

Young, K. H., Hunter, T. R., Wilner, D. J., et al. 2004, ApJL, 616, L51

Zhu, Z., Hartmann, L., & Gammie, C. 2009, ApJ, 694, 1045

Zsom, A., Ormel, C. W., Güttler, C., Blum, J., & Dullemond, C. P. 2010, A&A, 513, A57